2P

F. Wainscott 460

Final Report:

SELF-CONTAINED NAVIGATION EXPERIMENT

Contract Number NAS5-9683

Control Data Corporation Project Number 7638

July 10, 1969

Prepared for:

National Aeronautics and Space Administration
Goddard Space Flight Center
Greenbelt, Maryland

Edina Space and Defense Systems
CONTROL DATA CORPORATION
7200 France Avenue South
Minneapolis, Minnesota 55435

RD 2009

Final Report:

SELF-CONTAINED NAVIGATION EXPERIMENT

Contract Number NAS5-9683

Control Data Corporation Project Number 7638

July 10, 1969

Prepared for:

National Aeronautics and Space Administration
Goddard Space Flight Center
Greenbelt, Maryland

Edina Space and Defense Systems
CONTROL DATA CORPORATION
7200 France Avenue South
Minneapolis, Minnesota 55435

RD 2009

ABSTRACT

This report presents the results and conclusions of a series of experiments conducted for a Self-Contained Navigation System (SCNS) carried aboard the Applications Technology Satellite, ATS-III. The system, consisting of a flight model star sensor and auxiliary ground based data processing equipment, utilized star field mapping techniques to determine satellite attitude. In addition sightings made on both an ejected sphere and the moon were used to determine satellite orbital parameters.

The ATS-III satellite was launched into synchronous orbit on 6 November 1967. The SCNS equipment was initially operated on 2 March 1968. During the period between 13 March and 4 October 1968, 10 separate experimental operations were conducted.

Experiments were operated successfully for the determination of attitude. With the sun 45 degrees off the optical axis, useful data was obtained in full daylight when the scanning motion of the satellite directed the optical axis away from the sun. Scattered light from the sun masked star transit observations during one-half of the scan although the photomultiplier tube recovery rate permitted detection of stars as dim as visual magnitude +3.30 over the other half of the 0.6 second scan period.

Automatic reduction of the telemetered data, including star identification and attitude computation was accomplished. The standard deviation of the residuals for individual star transits was observed to be typically 60 arc seconds. The standard deviation of the derived attitude quantities varied within the range of 14 to 20 arc seconds for cases of good geometry. Position of star images within the slit were shown to be interpolative to a small fraction of the 7.6 arc minute slit width.

Difficulties were experienced in obtaining the precision required to

calculate orbital parameter from sightings of an ejected sphere. However, moon sightings were used as a substitute in conducting the navigation experiment. Satellite orbital position computed from moon transits was determined within an error band from -50 to + 40 kilometers over a 28 day interval when compared to a moon ephemeris.

FOREWORD

This report was prepared by the Research Division of Control Data Corporation for the National Aeronautics and Space Administration, Goddard Space Flight Center, under Contract NAS5-9683. The Control Data Project Engineer was William J. Lewis; however, during the data acquisition phase of the project Bruce D. Vannelli served as the Project Engineer. Control Data Corporation desires to particularly acknowledge the technical guidance of Forrest H. Wainscott of the ATS Project Office of the National Aeronautics and Space Administration, Technical Project Officer.

This report has been prepared in four chapters. Chapter 1 is concerned with the data acquisition system; Chapter 2, flight equipment performance; Chapter 3, determination of satellite attitude; and Chapter 4, determination of satellite orbit.

TABLE OF CONTENTS

TABLE OF CONTENTS (concluded)

LIST OF FIGURES

LIST OF FIGURES (continued)

LIST OF FIGURES (concluded)

LIST OF TABLES

SELF-CONTAINED NAVIGATION EXPERIMENT

INTRODUCTION

The Self-Contained Navigation System experiment had the following objectives:

(1) To determine the three axis attitude of the ATS-III spacecraft from star transit times as obtained from an on-board electro-optical star sensor. Data to be telemetered to a ground station for processing by Control Data.

(2) To determine the position of the spacecraft as a function of time by intermittently observing an ejected sphere against the background of stars over a period of two or more orbits. Also, to use the moon as a substitute for or in addition to the ejected spheres to determine the orbital parameters.

The SCNS operation equipment consisted of a flight model star sensor mounted within the ATS-III satellite and a ground-based data processing unit called a Star Data Formatter. Reduction of the star sensor raw data to provide satellite attitude navigational information was accomplished using Control Data 3600 and 6600 computers located at Control Data Corporation, Minneapolis, Minnesota.

Earlier documentation[1, 2] describes the flight and ground equipment and the applicable operational procedures. However, the following brief description of the SCNS operation principle is included here as an aid to the understanding of this report.

The flight equipment contains a star sensor and particle ejector. Basically, the sensor consists of a lens assembly, slit reticle and photomultiplier detector. Analog electronics process and deliver the photomultiplier output to the satellite telemetry system.

Radiation from stellar targets contained within the star sensor field

of view passes through the sensor aperture and is focussed by an optical system on an opaque reticle containing three transparent hair width slits. As the satellite rotates, the starlight is gated through the slits onto the cathode of the photomultiplier detector which, with its associated electronics, produces an analog pulse that is subsequently digitized and transmitted by wide band telemetry[1]. Digital data, corresponding to ingress and egress times for each pulse and necessary identifying remarks, are recorded on magnetic tape. The data is subsequently reformatted to be compatible with the FORTRAN language of the attitude computer program. This data is used as input to the computer program to provide attitude solutions.

Whereas, star sightings alone are necessary for attitude determination, ejected particle sightings provide the additional data required for orbit determination. The flight equipment contains three identical ball ejection mechanisms for this purpose.

The Star Data Formatter processes real-time data from the flight unit. This equipment routes analog data to an Ampex recorder, converts analog data to digital data, monitors data, and transfers digital data through the CTEC (Command Test Evaluation Console) to the SDS-910 Computer for preliminary processing and storage. Figure I-1 contains a flow diagram for the data acquisition of the ATS-III/SCNS experiment. Figure I-2 is a pictorial representation of the satellite and SCNS equipment.

The ATS-III satellite was launched into synchronous orbit on 6 November 1967. The SCNS equipment was initially operated on 2 March 1968. During the seven month period between March and October ten separate experiments were conducted. A summary of operational conditions is included as Appendix A.

---

1. During the experiment the Data Acquisition Facility at Rosman, North Carolina was utilized.

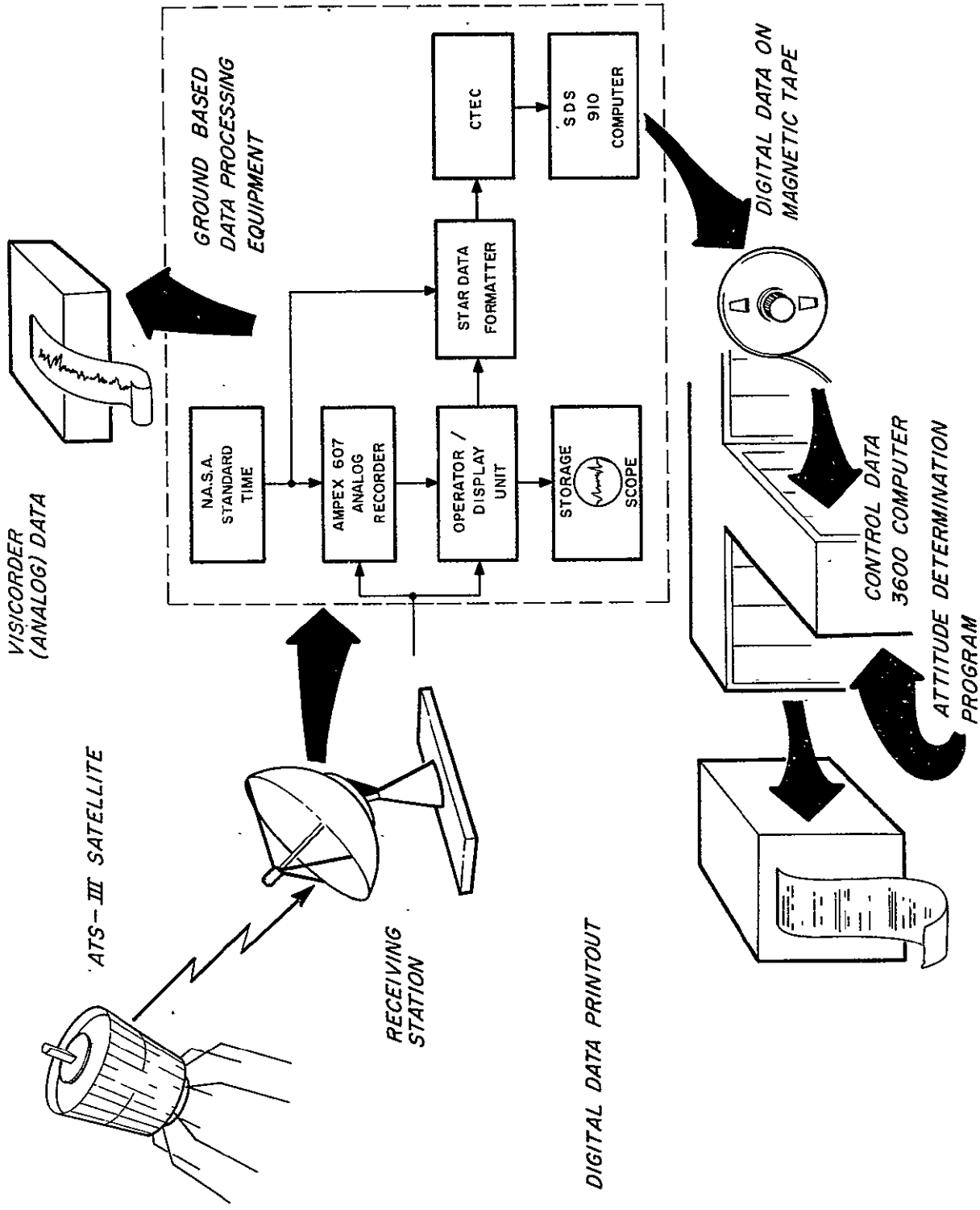

Figure I-1: Flow Diagram for Data Acquisition of ATS-III/SCNS

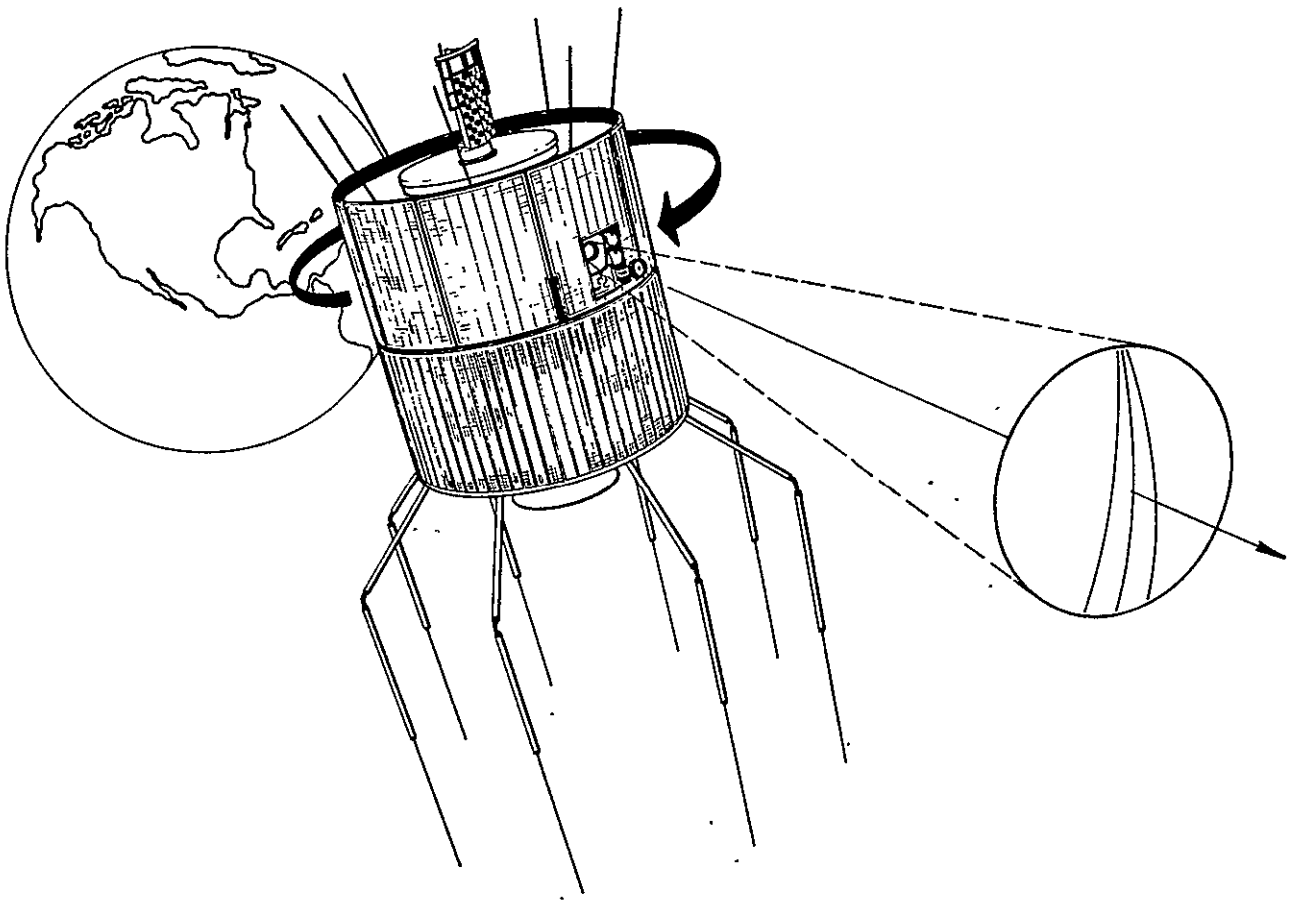

Figure I-2: ATS-III Satellite Showing the Self-Contained Navigation System Equipment

CHAPTER 1

EXPERIMENT DESCRIPTION

I. SCNS OPERATIONAL EQUIPMENT

The SCNS operational flight equipment is shown in Figure 1-1 and consists of four basic assemblies: the optical system, the detector, particle ejection assembly, and electronics assembly.

A. Optical System

The optical system is designed to focus star images on its image surface (slit plane) which is opague except for the three narrow slits shown in Figure 1-2. The light from images focused on any portion of these slits is transmitted through the opening to the cathode of the photomultiplier tube. The output voltage of the detector indicates the presence of a star image in the slit. Since the satellite rotates, the star images move across the slit plane normal to the center slit and at an inclined angle to the outer slits. The output signal for each star which crosses the slit pattern consists of three pulses with their separation dependent upon the zenith position of the star. This is illustrated in Figure 1-3.

The optical system includes the following items, each of which is shown in Figure 1-2.

- Cone: A fiberglass baffle included to prevent stray light from illuminating the lens assembly. The baffle configuration was constrained to fit within the skin of the spacecraft. As a consequence, the general shape became that of a frustrum of a cone.

- Objective Lens: An f/0.87 Super-Farron objective lens having a 30 degree field, a 76-mm focal length and a 40-mm diameter image plane.

  The lens assembly was an off-the-shelf item manufactured by the Farrand Optical Company. A computer automated ray trace was performed based upon patent disclosure information. The blur spot

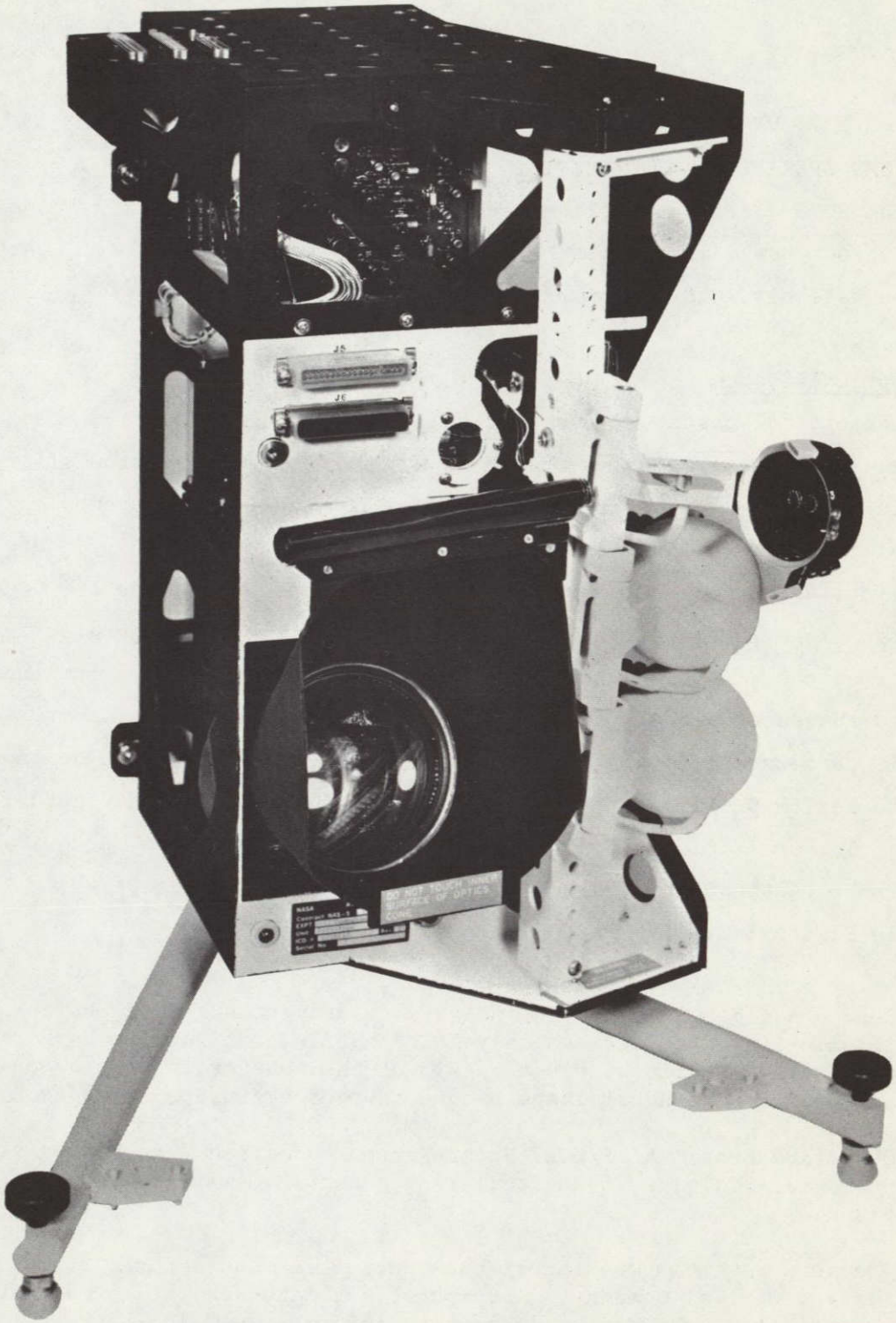

Figure 1-1: SCNS Operational Flight Equipment

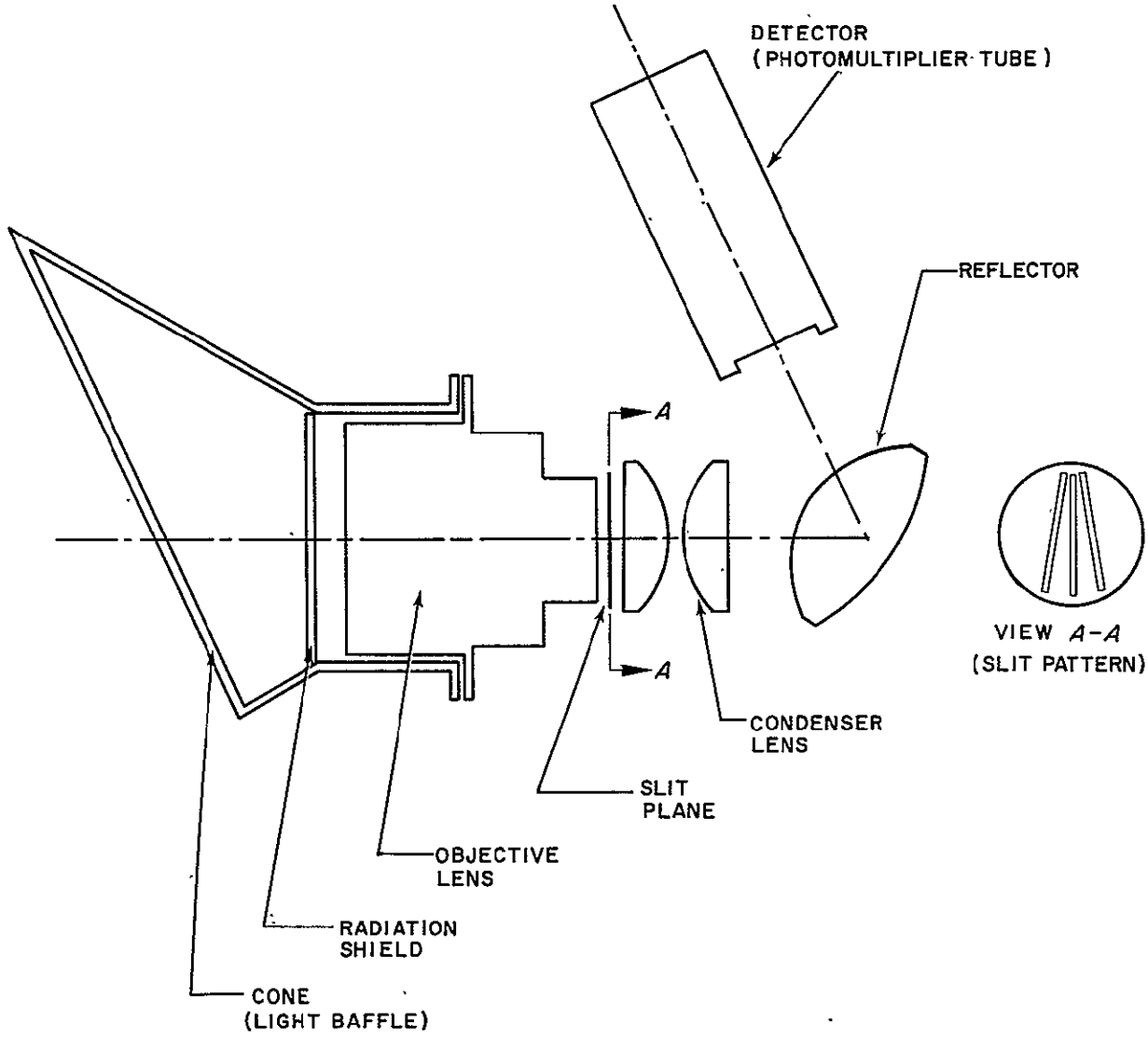

Figure 1-2: Flight Equipment Schematic Showing SCNS Optical Assembly and Detector

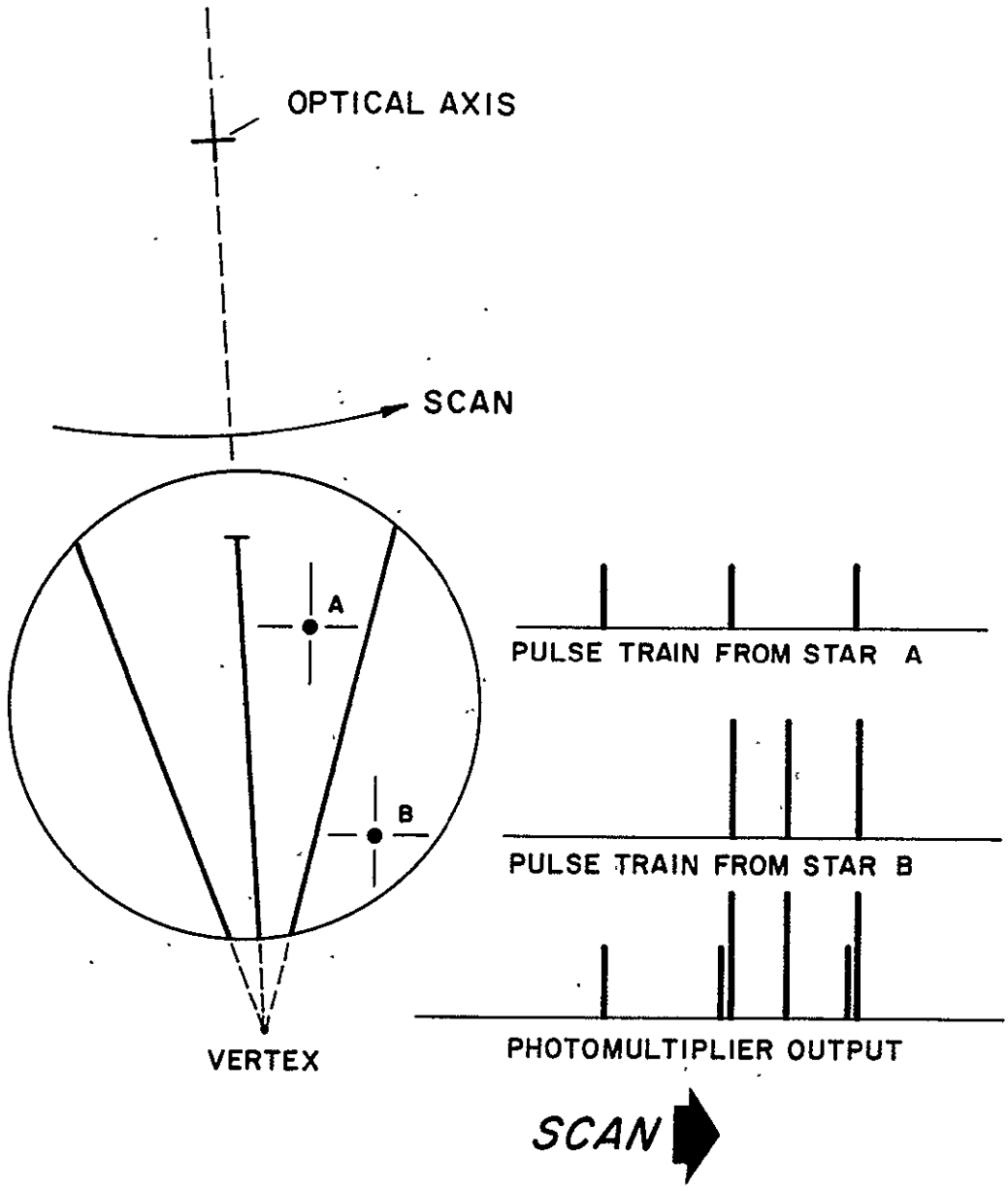

Figure 1-3: Pulse Separation for Two Candidate Stars Transiting the Slit Pattern

(image) diameter for an on-axis source was 5 arc minutes; for 7.5 degrees off-axis the blur spot diameter was 20 arc minutes and for 10 degrees it was 80 arc minutes.

- Slit Reticle: A vacuum-deposited opaque layer on a glass substrate having three translucent slits. The slits were designed to cover the entire 30 degree (40-mm) field of the objective and form an angle of 10.5 degrees having a vertex located 1.0675 inches above the optical axis.

  Actual measurements of the slit reticle indicated a value of 10.454 degrees ($\pm$ one arc minute) for the vertex angle and 1.075 $\pm$ .003 inches for the vertex-optical axis displacement. Based upon actual measurements the slit-to-slit separation angle is $11.^{\circ}102 \pm .02^{\circ}$. The rotational slit width at a point midway from the vertex is 7.6 arc minutes. A detailed analysis describing slit characterization is included in Appendix D.

- Radiation shield: An optically flat window of fused silica used to protect the objective lens from electron radiation damage.

- Condensor lens: Consists of two plano-ampheric lenses having a 40-mm diameter and a 34-mm focal length.

- Reflector: A 69-mm diameter, 46-mm focal length aspheric condensor having a reflective aluminum coating on its spherical convex back surface.

- Sunshade: The sunshade, designed as a cover for the open end of the optical system, was removed from the flight equipment prior to actual launch. This was done to preclude the possibility of a "fail-closed" condition and thus wipe out the experiment.

  The sunshade assembly consisted of a thin mylar shade (configured to roll up when released), a release mechanism, and an indicator switch. Its intended use was to prohibit direct sunlight from becoming incident upon the cathode during the de-spun launch phase of the satellite. Although referred to in References [1] and [2], it is not shown in Figure 1-2.

  Data taken during the experiment revealed a loss of sensor sensitivity to off-axis sources. Relatively bright stars having visual magnitudes around 1.5 lying five to ten degrees off the optical axis were not regularly detected. This was due principally to the severe vignetting of the Super-Farron lens. The effect is observed in Figure 1-4 which shows the light transmission characteristic of the SCNS optical system with off-axis position.

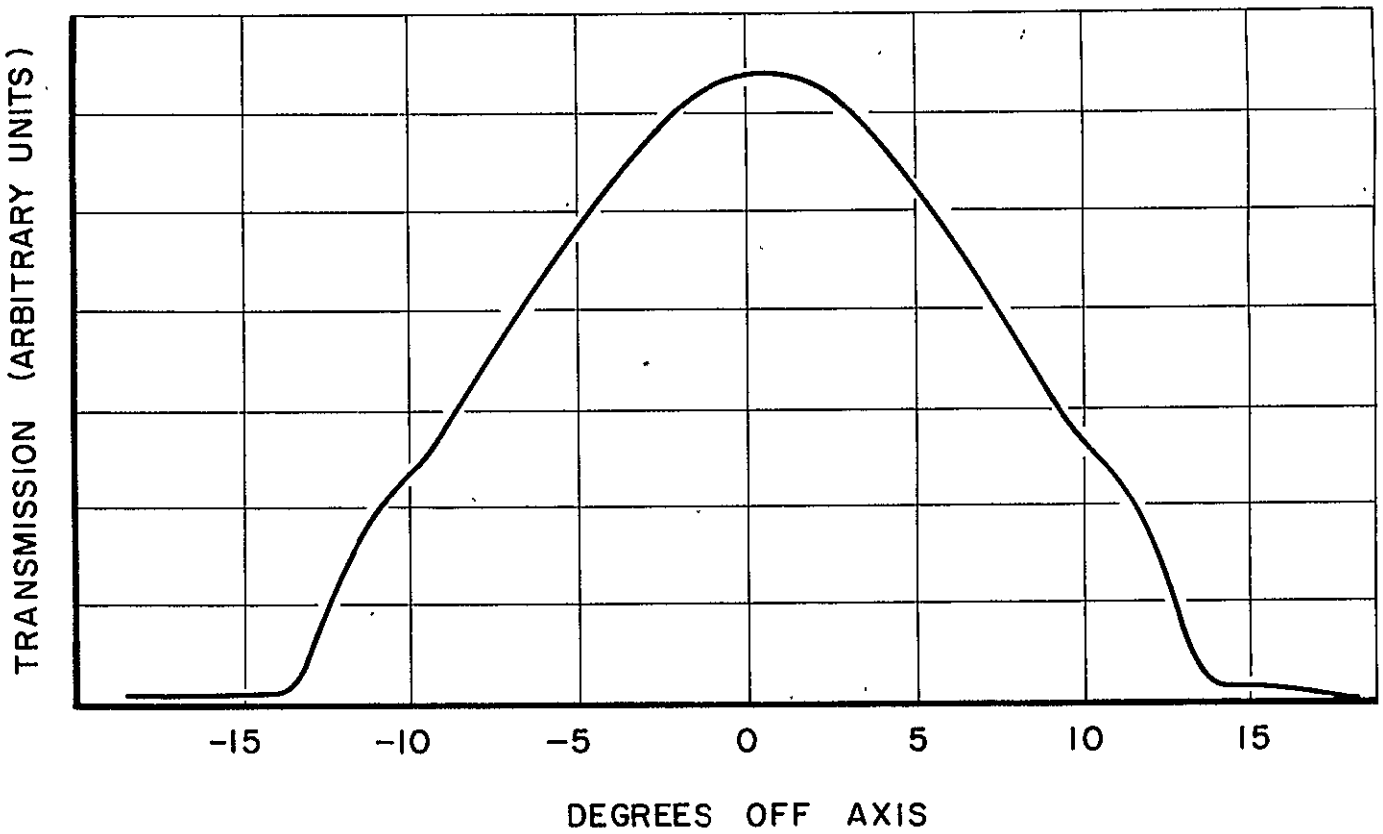

Figure 1-4: Transmission Characteristic of the SCNS Optical System

B. Detector

The detector selected was the model 541-E-01-14 photomultiplier tube manufactured by Electro-Mechanical Research, Inc. The PMT was used with an integral high voltage power supply. The detector contains a tri-alkali type cathode surface whose quantum efficiency at 4200 Angstroms is typically 0.25. Electrons emitted from the cathode are accelerated through a series of dynodes which both accelerate and emit electrons to produce a current gain from cathode to collecting anode of 1.5×10^6 to 1.5×10^7, depending upon voltage used. Both gains were employed at different times during the experiment.

C. System Electronics

The SCNS was designed to operate in one of two system operating states. The first, referred to as System 1, was designed to provide digital information only. The system did this by providing a digital pulse whenever the analog star pulse exceeded a fixed detection (or threshold) level. A step attenuator was used to deliver the analog star pulse to the threshold detector, which upon ground command, adjusted system gain in discrete steps. It thereby served the equivalent function of a variable threshold detector. Additional system sensitivity was obtained by adjusting the photomultiplier supply voltage.

System 2 output was analog only, and essentially reproduced the photomultiplier analog output pulse. Both systems amplified and filtered the detector output followed by a filter matched to the average slit dwell time of a star. The analog output of System 2 was telemetered to the ground data acquisition station where the star pulse information was digitized. The ground based data processing equipment circuitry was designed to produce digital pulses corresponding to a pre-set threshold crossing of the pulse rise and fall.

During certain phases of the experiment, particularly when the satellite passed from the earth's shadow into full sunlight, a significant increase in

spatial background noise caused the output to assume a variable baseline characteristic. This resulted in an inability to detect stars using a fixed baseline design. Modifications were subsequently made to the ground based data processing equipment to provide a variable threshold capability which utilized a baseline following circuit.

Since it was not possible to modify System 1 (and thereby provide a capability to detect stars under daylight conditions), this system fell into general disuse. All of the data obtained subsequent to the initial operation[2] of the SCNS equipment was obtained using System 2, modified to include the baseline following circuit.

D. Probe Ejection Mechanism

The navigation method of the Self-Contained Navigation System requires that a probe be ejected from the satellite at known velocity and direction, and positional measurements be taken during the orbit. Optical viewing constraints require that the probe be ejected at a velocity of 3 ft/sec. with an elevation angle of 45° south, and an azimuth normal to the satellite velocity vector. If the satellite spin velocity is 100 rpm and the probe release point is approximately 31 inches from the spin axis, the resultant tangential velocity is 27 ft/sec. The ejector is therefore required to compensate for this velocity component. Figure 1-5 shows the geometric interface between satellite and SCNS ejection mechanism.

Several ejector designs were evaluated, which resulted in the selection of the design illustrated in Figure 1-6. The probe, a three inch diameter spherical ball, is cupped in the throwing arm prior to and during ejection.

---

2. Initial operation occurred during early April 1968 when the satellite was in the earth's shadow. The resultant dark sky conditions produced a constant (non-varying) baseline.

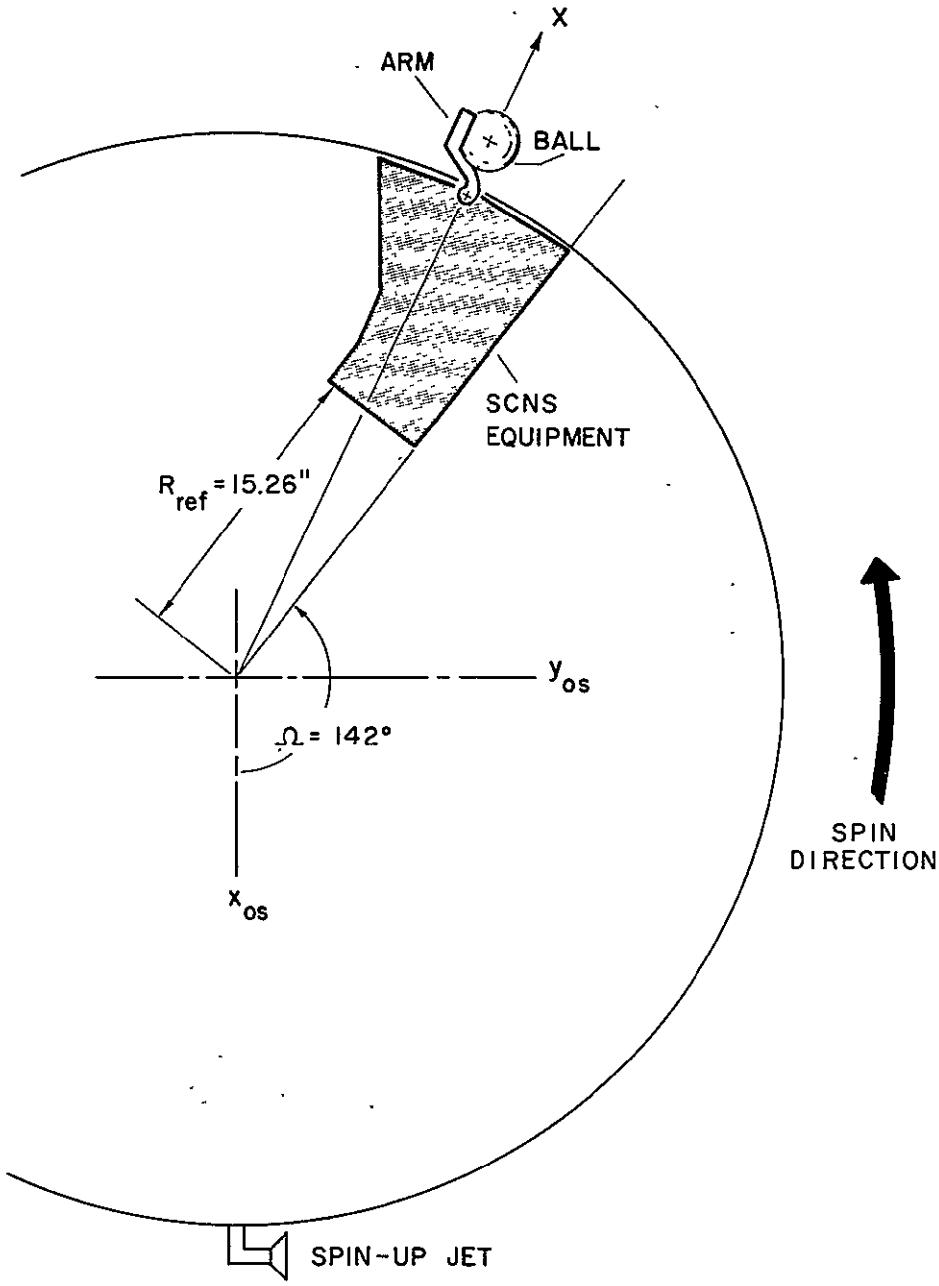

Figure 1-5: Satellite Interface with SCNS Ejection Mechanism

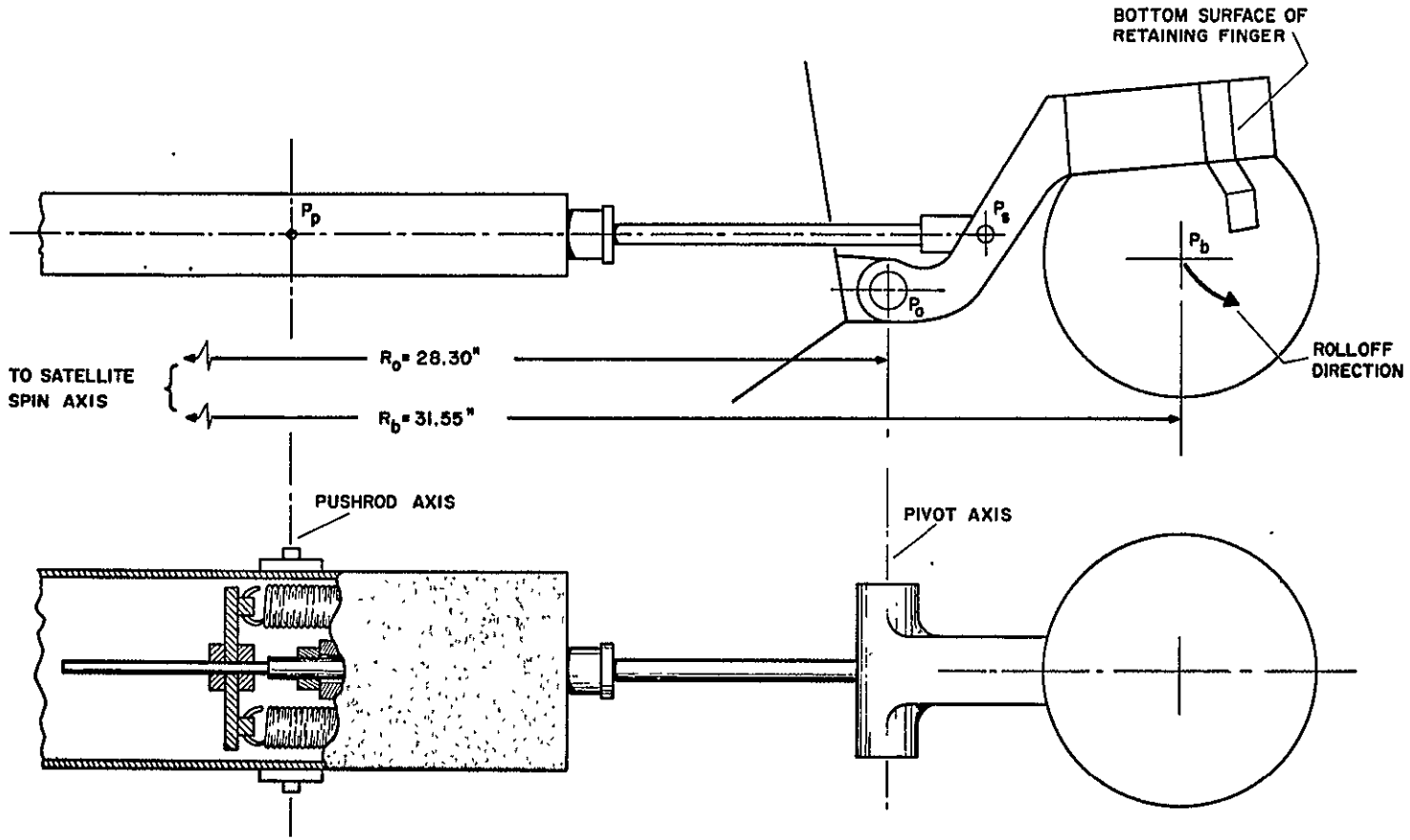

Figure 1-6: SCNS Ejection Mechanism

When the release switch is activated the springs and satellite centrifugal force accelerate the ejector to the released position. As illustrated in Figure 1-7, the ejector is designed to stop with an angle $\chi = 4.5$ degrees and with the pivot axis tilted about x^* axis by $\tau = 4.5$ degrees. If the y component of the ejector velocity entirely compensates the satellite tangential velocity, the x and z (parallel to the satellite spin axis) velocities are

$$v_x = v_{\dot{\theta}} \cos \tau \sin \chi = 2.1 \text{ ft/sec.} \quad (1)$$

$$V_z = \dot{v}_{\dot{\theta}} \sin \tau = 2.1 \text{ ft/sec.} \quad (2)$$

and the resultant speed is 3 ft/sec. with an azimuth angle of zero degrees and an elevation angle of 45 degrees.

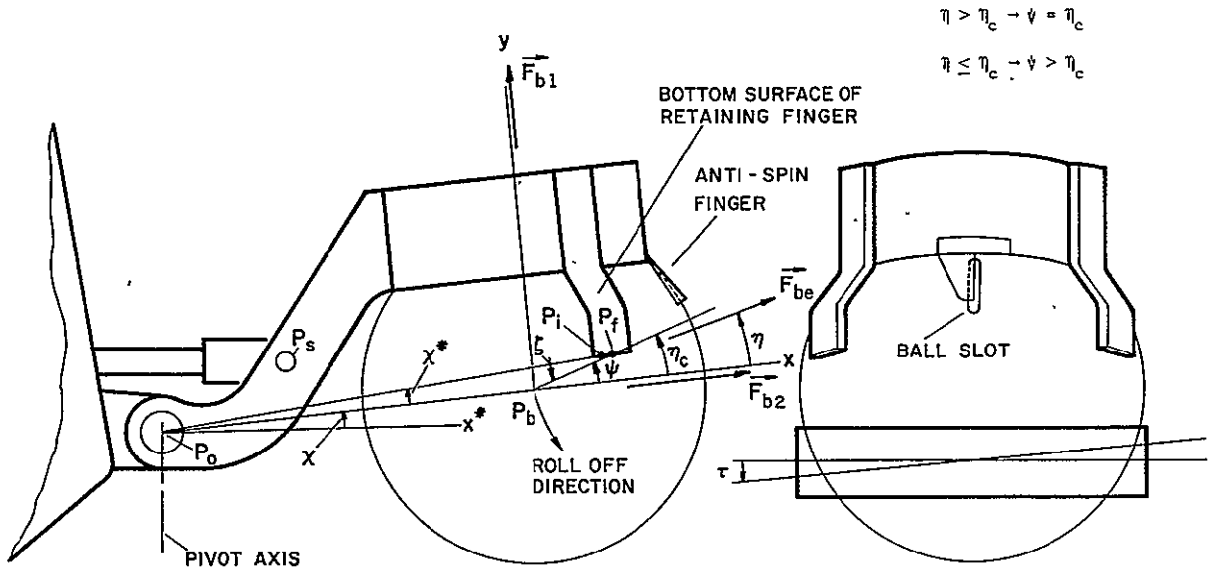

Figure 1-7: Ball Ejector Force Diagram

II. PRE-FLIGHT CHECK-OUT

Prior to installation within the ATS-III satellite, tests were conducted to obtain a measurement of response of the SCNS flight equipment to a calibrated artificial star and to a star field simulation.

The artificial star provided a close approximation to an AO-5 star in the range of wavelengths where SCNS is most sensitive. The desired intensity for a given magnitude was obtained by setting the distance from the artificial source aperture to the SCNS aperture. Star intensities were variable to 4th magnitude. The optical path for the source energy (adjustable to obtain desired intensity) reflects from a rotating mirror used to simulate the satellite scan motion. SCNS response to a simulated star at various off-axis positions within the field of view was evaluated by varying the vertical position of the source. The on-axis position corresponded to a declination angle of -25 degrees on the celestial sphere. A more detailed description of the tests conducted and their results is contained in reference [2]. Figure 1-8 shows a schematic diagram for the test configuration used.

Tests were also conducted to obtain a measurement of the SCNS response to the simulated stars contained in the Star Field Simulator (SFS). The SFS was designed, built and calibrated to provide four artificial stars, each having a different magnitude and off-axis position. The SFS was fixed to the SCNS optical assembly and simulated the satellite scanning motion through rotation of a mechanical chopping plate which gated the artificial starlight onto the SCNS optical system. The SFS also had the capability to adjust star intensities within the range of -1.5 to + 3.7 visual magnitude.

In addition to performing functional check-out and determining characteristic behavior for the SCNS flight equipment, the SFS pre-flight calibration and testing provided the theoretical (laboratory determined) limits of detectability for the different operational states possible. Information relative to SCNS response versus star magnitude was compiled as a nomograph which was

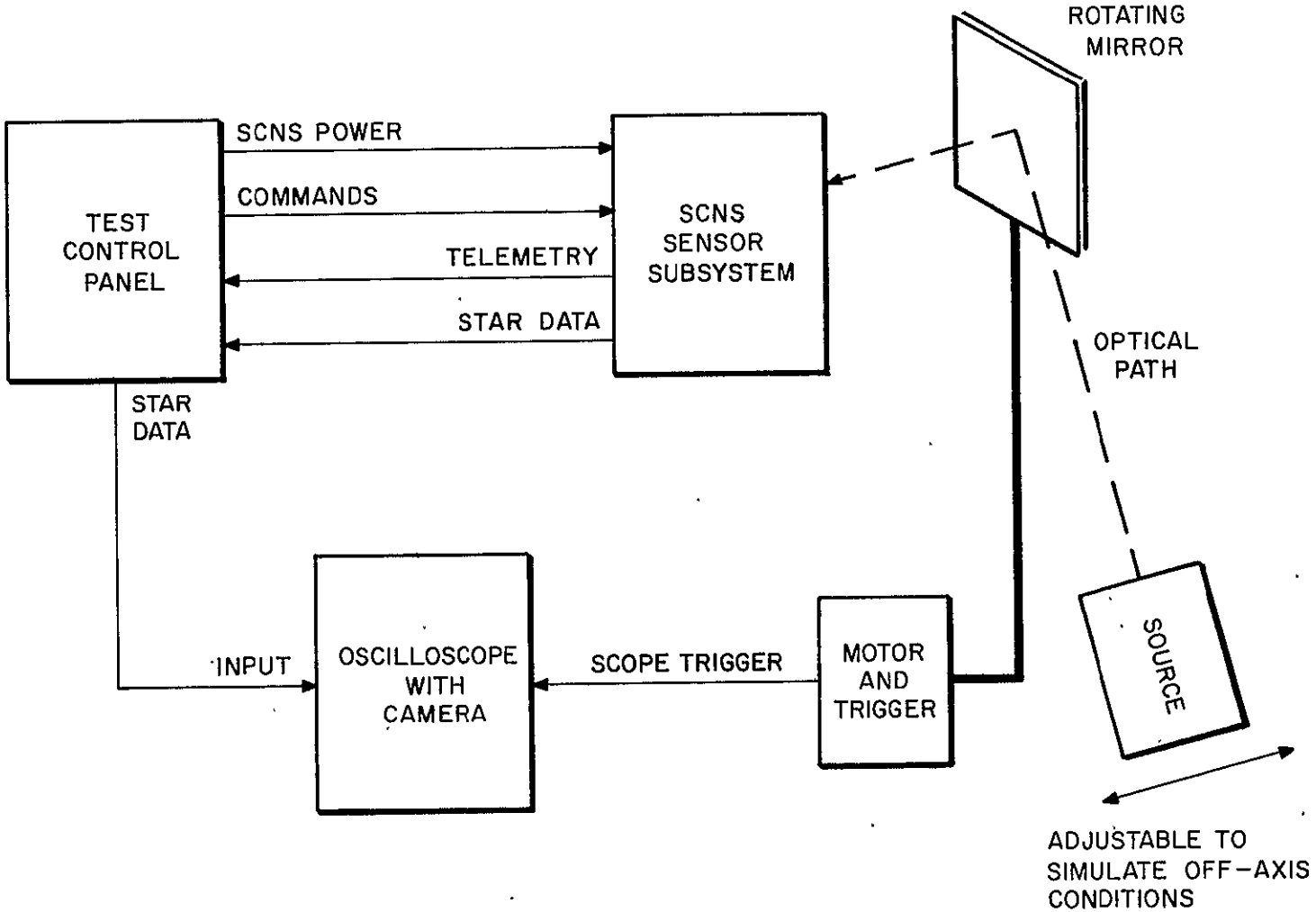

Figure 1-8: Schematic Diagram - Artificial Star Test Configuration

contained as Figure 1-19 of Reference [1]. During flight operation it was noted that actual limit of detectability was slightly degraded over the laboratory determined value. For dark sky conditions the faintest star detected was generally 0.1 to 0.4 magnitudes brigher than the theoretical value derived from the pre-flight calibration tests. A summary of sensor detectability performance for various operational conditions is included as Appendix B.

III. GROUND BASED DATA PROCESSING

Figure I-1 illustrates the procedural steps involved in the acquisition of data from the ATS-III/SCNS equipment. It indicates the dual path available to process the raw data in both analog and digital form. During the experiment operations attitude solutions were obtained utilizing an algorithm named SCAT which provides a solution in four unknowns. A second algorithm evolved during the course of the project. It contained the capability of solving a set of equations containing up to nine unknowns. The program named SCOOT is discussed along with program SCAT in Chapter 3, Section I.

The original Star Data Formatter (SDF) design was governed by the design parameters of the Self-Contained Navigation System, the CTEC/SDS 910 interface and computer, and interface to Ampex FR607 tape recorder. The intention was to process real time data as it occurred and simultaneously record the analog information (System 1 or System 2) on tape. The tape system was considered to be a backup system running on a coarser resolution time base compared to the Star Data Formatter. The Star Data Formatter was designed to process real time data off line (off line being the processing of recorded data from the Ampex FR607).

The SDF analog electronics was designed to accept video from either the SCNS sensor via transmission link or the FR607 data recorder. The SDF contained a level detector which provided a positive going output pulse during the detected star transit. The leading edge of the pulse corresponded to the star-slit ingress time and the trailing edge to the egress time. The SDF digital electronics converted the analog pulse to time encoded leading and trailing edges and also tagged the data. The digital electronics also recorded the time occurrence of the sun pulse generated by the ATS-III sun sensors. Also, the SDF interfaced with the necessary timing signals (1 mc, 1 pps). Operation of the equipment when the satellite was in the earth's shadow permitted an evaluation of sensor performance under dark sky conditions. A photograph of typical analog output taken while the satellite was

in the earth's eclipse is shown in Figure 1-9. The characteristics of this output are a straight baseline, with photomultiplier and background noise superimposed, plus occasional star and dark current pulses.

When bright objects, such as the sun, moon, or sunlit earth is in or near the field of view, the character of the analog output changes markedly. Figure 1-10 shows a typical output for a complete satellite scan with the sun illuminating the shield and/or lens for approximately 180 degrees of the scan. Large overload and recovery transits are present, and photomultiplier noise is increased appreciably in those areas of the scan containing star pulses. The straight baseline has disappeared and it is impossible to detect all of the desired star pulses with a fixed trigger level. The same situation exists when the moon is in the field of view, as shown in Figure 1-11.

A level-follower circuit was designed and added to the SDF that measured the voltage of the baseline and from it provided a component of the bias input to the level-detector. The level-follower had the ability to follow non-linear and variable frequency excursions of the baseline. An indication of the performance of the circuit is shown in Figure 1-12.

It should be noted when comparing Figure 9 with 10, 11, and 12 that Figure 9 has an expanded time scale. The three star pulses shown emerging from the straight baseline noise correspond to those appearing near the extreme right portion of Figure 10.

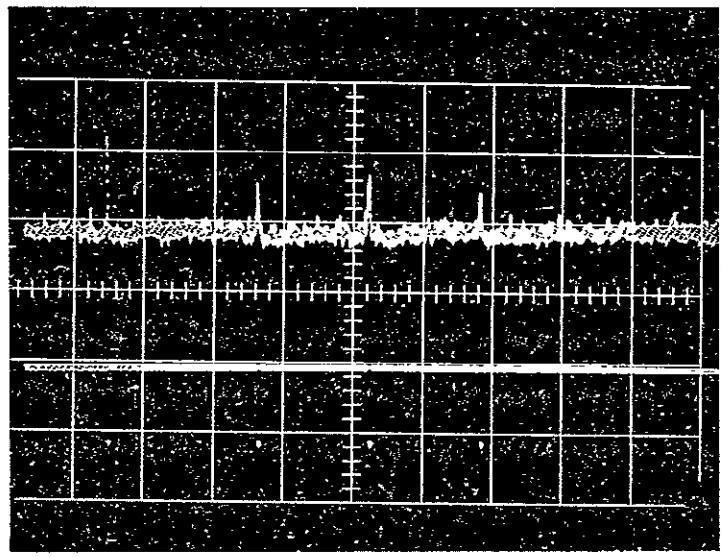

Figure 1-9: Typical Dark Sky Conditions Occurring Within Earth's Eclipse Showing Straight Baseline

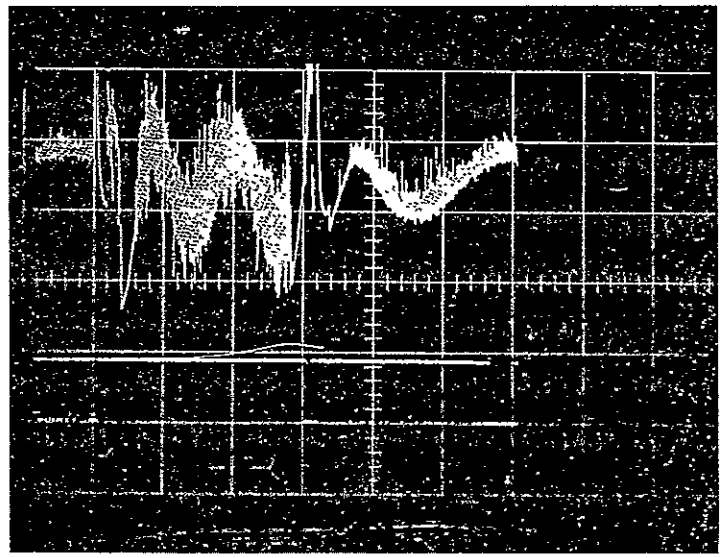

Figure 1-10: Bright Object Interference Showing Varying Baseline

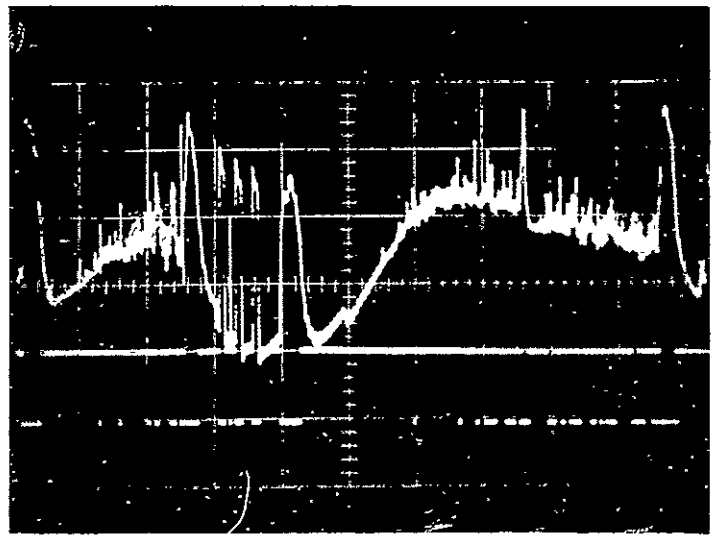

Figure 1-11: Lunar Transits Superimposed on Varying Baseline

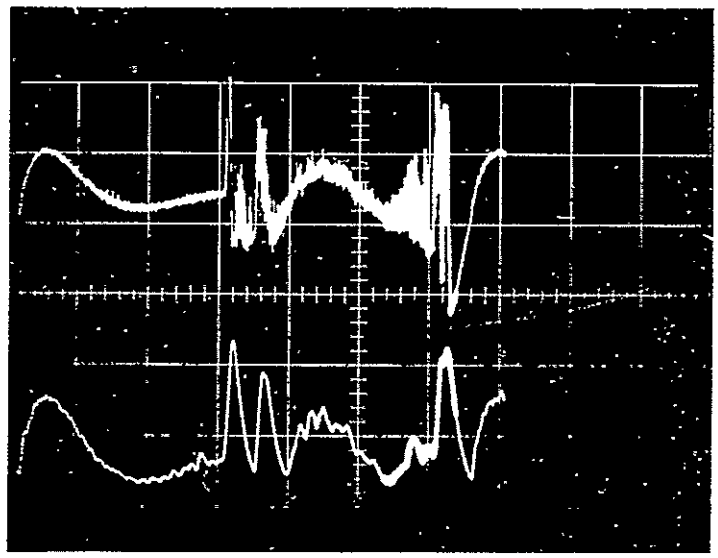

Figure 1-12: Output Characteristic of Baseline Following Circuit

CHAPTER 2
FLIGHT EQUIPMENT PERFORMANCE

INTRODUCTION

For approximately sixty minutes each day during both spring and fall eclipses, the ATS-III satellite was in the earth's shadow. Under those conditions, with the exception of an illuminated crescent at the earth's south polar region[1], the star sensor viewed the nighttime sky. Typical sensor output is reproduced in Figure 2-1.

The data of Figure 2-1 are reproduced portions of a single scan analog output at a specific value of sensor gain. A higher gain would produce stronger star pulses at the expense of an increased noise level. As expected, the brighter stars produce stronger pulses. Sirius, the brightest star in the sky, has a visual magnitude of -1.58. Antares, the sixteenth brightest[2] and Fomalhaut, the seventeenth brightest, have visual magnitudes of +1.22 and +1.29 respectively. Both possess comparable pulse heights and both possess weaker pulses relative to Sirius. However, it is also observed that a given star does not appear to regularly produce an equally strong output pulse as it crosses each of the three reticle slits. This can be explained with the aid of Figure 2-2. Due to the off-axis attenuation or vignetting of the optical system when a star crosses the outer two slits, its radiation is reduced by a factor greater than the center slit. The center pulse should, therefore, possess a greater height and this is illustrated in Figure 2-2B. However,

---

1. The upper edge of the SCNS field of view scanned within 1.5 degrees of the earth's limb. A marked rise in background noise level was noted as the field scanned past the earth. The halo effect is produced by atmospheric scattering of the sun's rays.

2. The number designation given a star is predicated upon its visual magnitude, and is ranked higher according to decreasing brightness for all stars over the entire celestial sphere. Star number 16 (Antares) is the sixteenth brightest star (visual) in the sky.

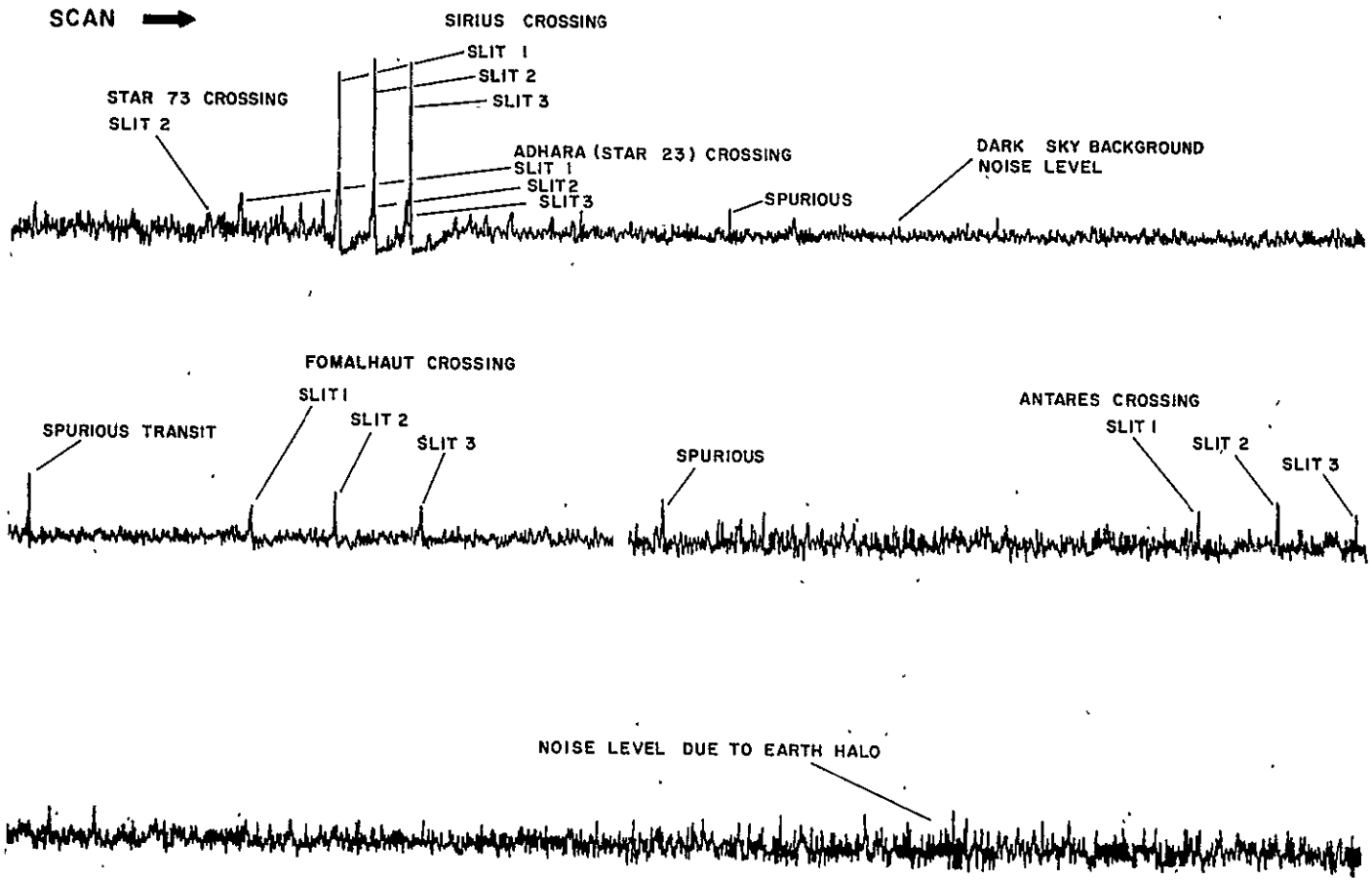

Figure 2-1: Reproduced Portions of Typical Analog Output for Dark Sky Conditions.

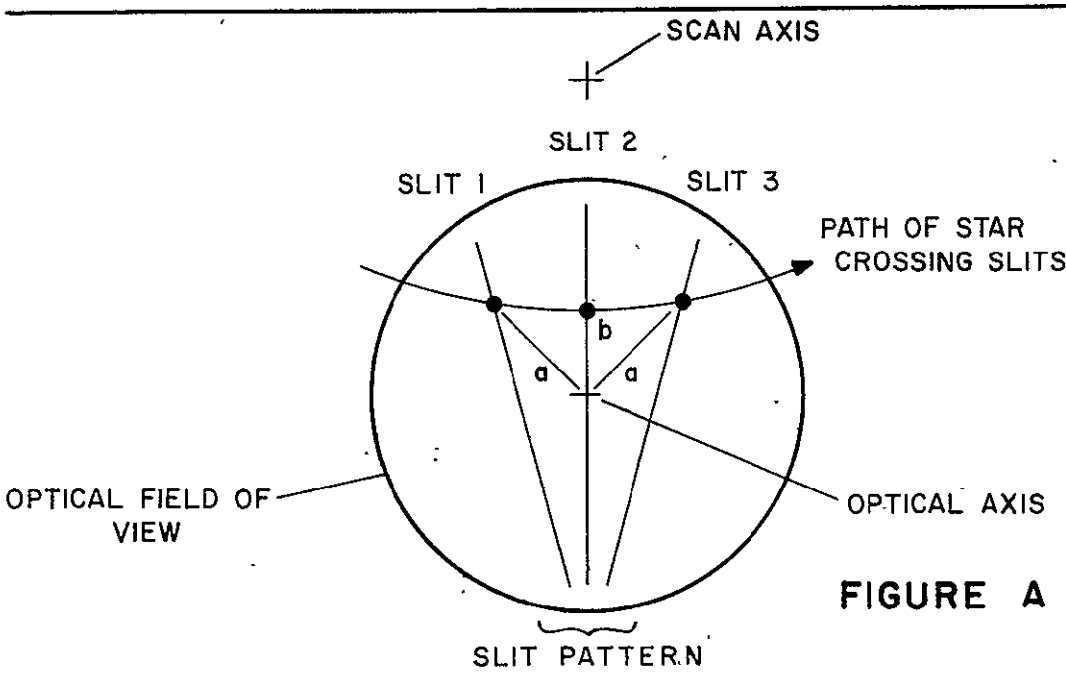

FIGURE A

Stars crossing the outer slits (1, 3) do so at a greater distance from the optical axis (a > b). Pulse heights are less than center slit (2) pulse due to off-axis attenuation of starlight within the optical system (vignetting).

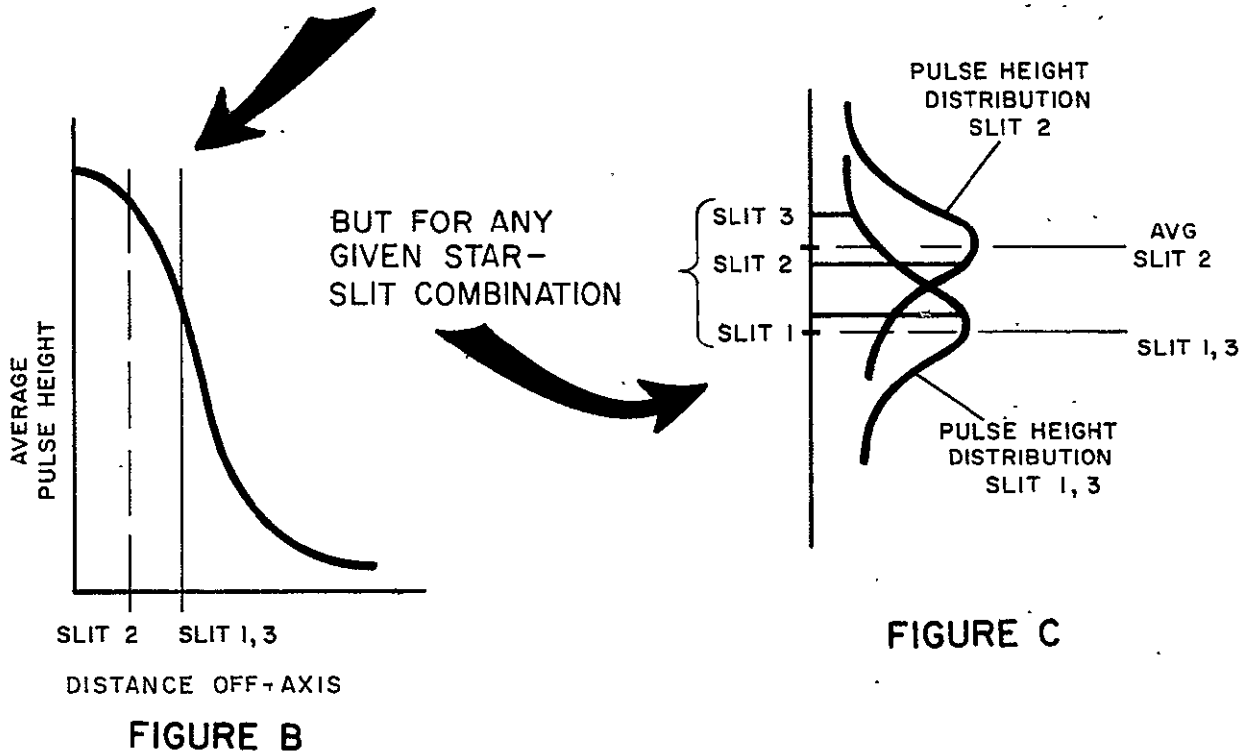

FIGURE B

FIGURE C

Figure 2-2: Statistical Nature of a Star Pulse

due to the statistical behavior of photon arrival rate the outer slit pulse heights could be unequal, as shown in Figure 2-2C.

The analog data illustrated in Figure 2-1 shows clearly only the brighter stars contained within the region of sky swept out by the optical field of view. Although not easily discernable, pulses from fainter stars are contained within the noise spectrum. Digital filtering techniques implemented as routines of the ground based computer automated data processing program successfully extracted and identified stellar targets as faint as visual magnitude 3.8[3].

Figure 2-3 graphically locates those stellar targets which were both regularly detected[4] and occasionally detected. The grid represents that portion of the southern sky swept out as an annulus by the field of view and corresponds to a dark sky condition occurring when the satellite was in the earth's shadow during the fall eclipse.

The stellar limiting magnitude (or faintest star detectable) based upon detectability alone was, therefore, 3.8. The theoretical limiting magnitude is 4.5. However, determination of vehicle attitude was obtained using only the eight stellar targets which were regularly detected. Figure 2-3 identifies these stars and also indicates the excellent geometric spacing of the stars over the entire scan - a condition which generally leads to a more accurate attitude solution. The limiting magnitude, then, based upon useful star information corresponds to the faintest regularly detected star, Dschubba, having a visual magnitude of 2.54.

---

3. Criterion was that the star be detected in at least one of the three slits 10% of the time.

4. Criterion was that the star to be detected in all three slits (as triplets) at least 25% of the time.

NO.	STAR NAME	MAG	NO.	STAR NAME	MAG.
1	SIRIUS	−1 58	38	WEZEN	1.98
16	ANTARES	1 22	39	MIRZAM	1.99
17	FOMALHAUT	1 29	48	NUNK I	2.14
23	ADHARA	1 63	81	DSCHUBBA	2.54

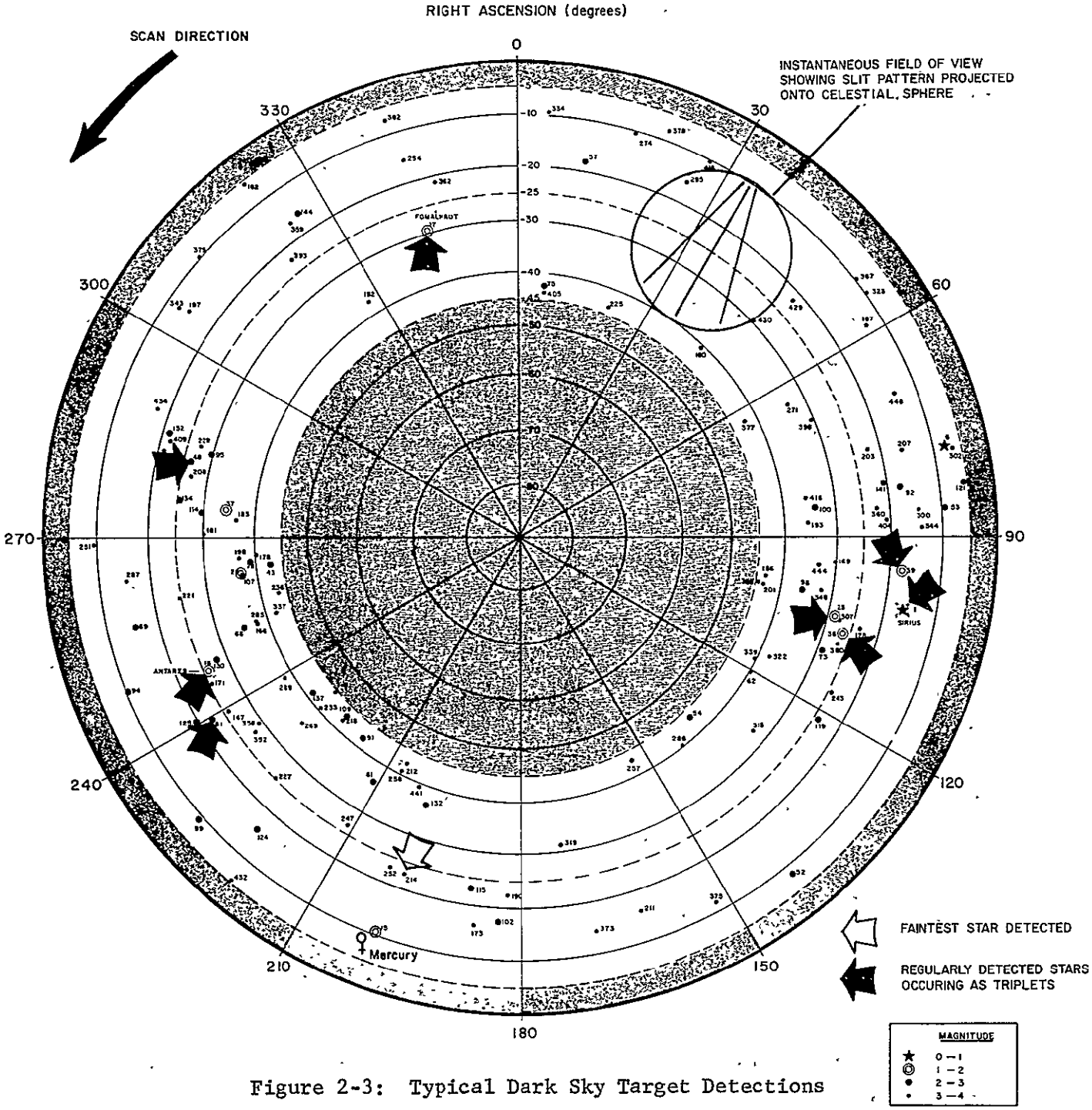

Figure 2-3: Typical Dark Sky Target Detections

When other than dark sky conditions prevailed, stellar target detection was degraded. These conditions occurred whenever the satellite came out of the earth's shadow into full sunlight and also, but to a lesser extent, whenever the full or nearly full moon entered the field of view. When the satellite was in full sunlight, 180 to 200 degrees of the scanned star field was blanked out by the sun's interference, even though the sun was never closer than 28 degrees to the edge of the field of view. When the full moon entered the field of view an additional 50 to 70 degrees of scanned star field was wiped out. When both conditions occurred, a reduced number of stars were regularly detectable. A less accurate attitude solution resulted and in certain instances, due to the geometric spacing of detected targets, no solution was possible. Figure 2-4 illustrates the effect produced by the combined sun and moon interference. In this instance, due to the fact that Fomalhaut was regularly detected, attitude solution was possible. The limiting magnitude, based upon daylight detectability and using the criterion that the target is detected occasionally (less than ten percent of time in any one slit), is 2.91 visual. If only "usable targets" is assumed as the criterion, the limiting magnitude again becomes 2.54.

During daylight operation of the star sensor a significant rise in the noise level was observed. Reproduced portions of the analog output for typical sunlit conditions are included in Figure 2-5. In addition to the obvious increase in noise due to sun and moon interference, the baseline assumes a varying characteristic, and contains large overload and recovery transients. The straight baseline, typical of dark sky viewing, shown in Figure 2-1 has disappeared. It was for this reason that the ground based data processing equipment was modified to provide a baseline following circuit described earlier which permitted detection of stellar targets not possible with a fixed threshold level.

An additional observation from Figure 2-5 is the characteristic behavior of the electronics in recovering from saturation following an incidence of high energy radiation.

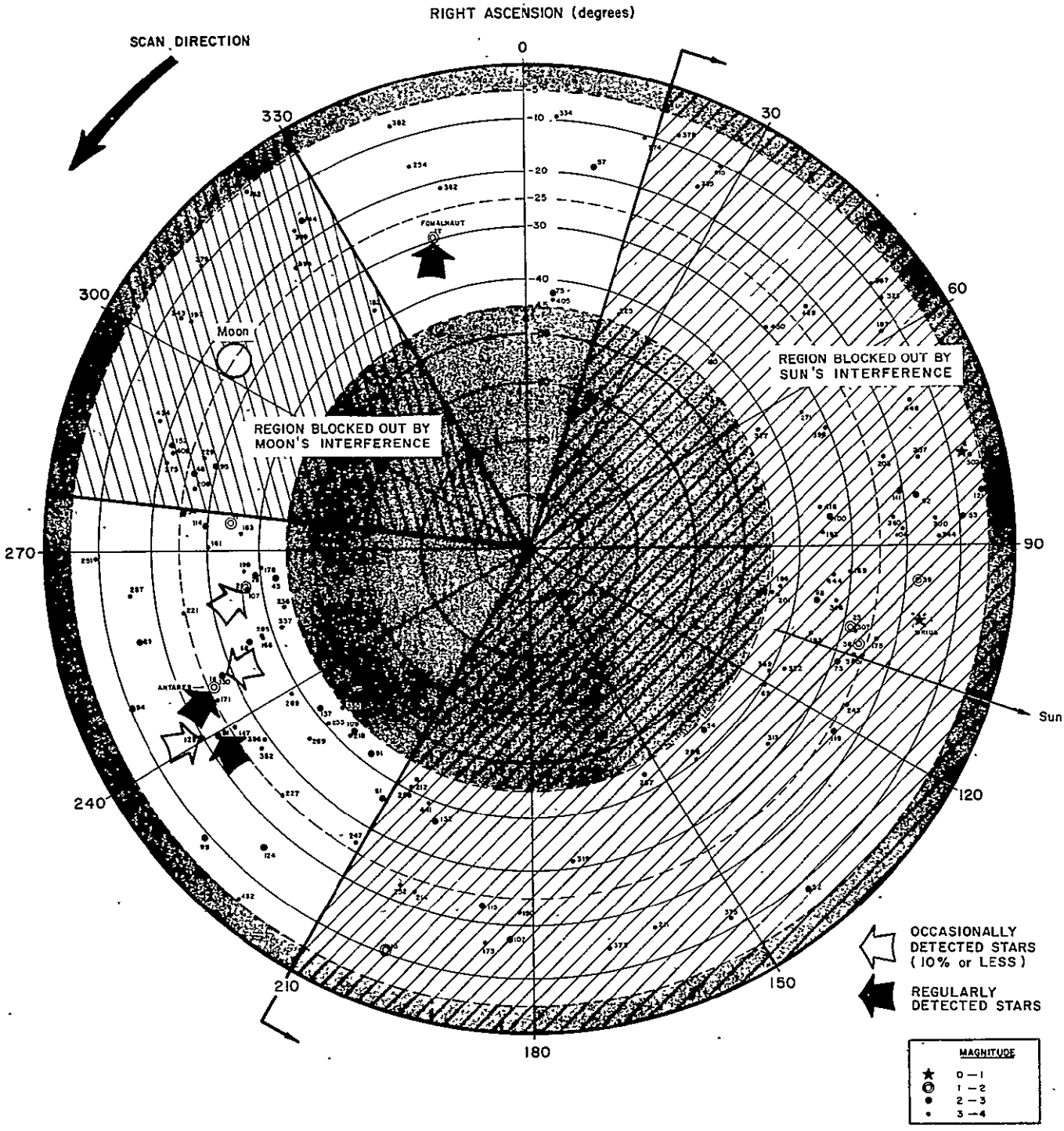

Figure 2-4: Typical Daylight Sky Target Detections

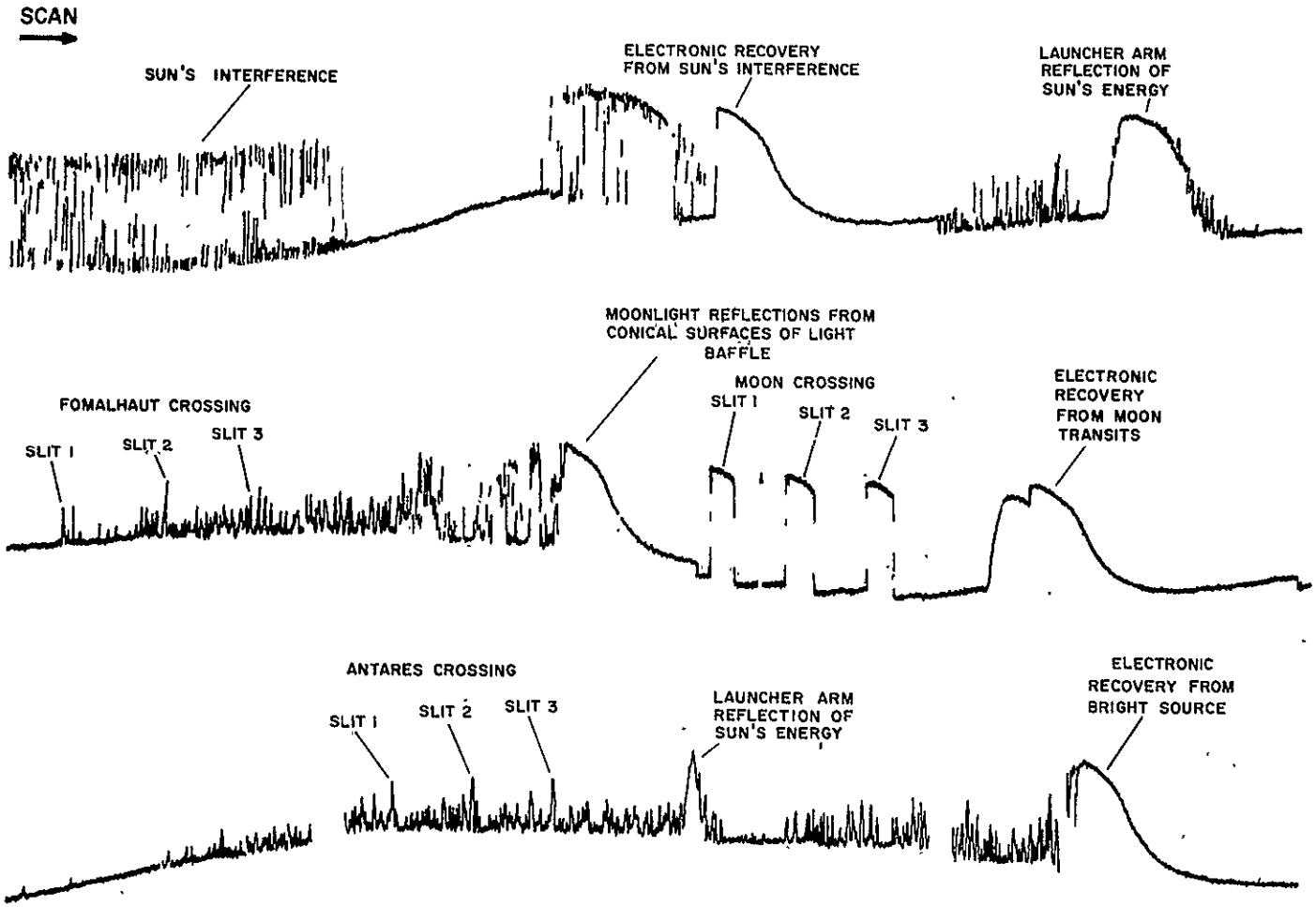

Figure 2-5: Reproduced Portions of Analog Output for Typical Sunlit Operation Showing Varying Baseline Characteristic

I. STAR SENSOR PERFORMANCE

A. Detectability

The primary method of evaluating the detectability of the SCNS sensor is to plot the detection frequency (the ratio of the number of times a particular star/slit was detected to the number of maximum possible detections) against the instrument magnitude[5] for a given sensor configuration. Data required for the preparation of detection frequency versus instrument magnitude curves are obtained from an analysis of the raw digital data tapes in conjunction with the computed satellite attitude. Each star/slit in the listing of available stars ordered by visual magnitude to 4.0 is considered as a potential candidate able to provide a detectable pulse. Each computed star/slit transit time is compared with all of the measured transit times for each scan. Whenever a comparison produces agreement to within $\pm$ 200 microseconds[6], the measured time is associated with the known star/slit. This is done for all stars in the field of view. The instrument magnitude which depends upon the star color-temperature and its off-axis angle is identified with each star candidate. The number of times a star/slit combination is theoretically scanned is determined by counting the number of times each degree of right ascension is scanned, deducting from the total those scans missed during the computer input/output (tape write) processing time for each data set. In general, the brighter on-axis stars are detected with higher frequencies than dimmer off-axis stars. Some noteable exceptions are apparent but in most cases any apparent detection anomally can be explained.

---

5. The instrument magnitude relates stellar magnitudes to the spectral response of the SCNS sensor. A discussion of the significance of instrument magnitude and a listing of star corrections is included as Appendix C.

6. At a nominal satellite spin rate of 600 degrees per second, the sensor rotational slit width of 7.6 arc minutes is equivalent to a slit transit time of 211 microseconds.

Figure 2-6 is typical of the detection frequency versus instrument magnitude characteristic. The curve was drawn from data taken when the satellite was within the earth's shadow. Figure 2-7 was also compiled from data taken during dark sky conditions but separated from the data of Figure 2-6 by approximately six months. Three observations are made:

1. There is a great deal of scatter in the data as seen in the two figures, a condition which one would expect even under the best of detection conditions. However, some bright star/slit combinations, noteably star number 1 (Sirius), in slit 3 appears to be less detectable than its predicted frequency. This can be explained, with the aid of Figure 2-8, by the fact that the target is so bright that a systematic shift in the actual detection transit time occurs. The cause is fundamental to the electronics. This shift makes the measured and computed transit times disagree enough so that occasionally this star/slit crossing will fall outside the acceptable tolerance about the computed transit time, thereby affecting a reduced detectability.

2. In many cases, a dimmer star has a higher detection frequency than its magnitude might predict. This is generally caused by a conflict with one or more additional stars. A conflict exists whenever more than one star appears in a given slit within a transit time interval. For the sake of clarity, most of the points below a detection frequency of about .2 have been deleted.

3. A comparison of the results obtained during spring and autumn eclipses reveals an apparent loss of sensitivity over the six month time interval involved. This becomes apparent when noting the shift to a higher gain setting (from 5 to 6) required to detect a given magnitude star. Some portion of the apparent loss of sensitivity can be accounted for by ground based equipment modifications and by some minor variations in the operational methods employed at each of the data acquisition intervals. However, it is apparent that a deterioration of approximately one magnitude equivalent sensitivity did occur over six months of operational usage.

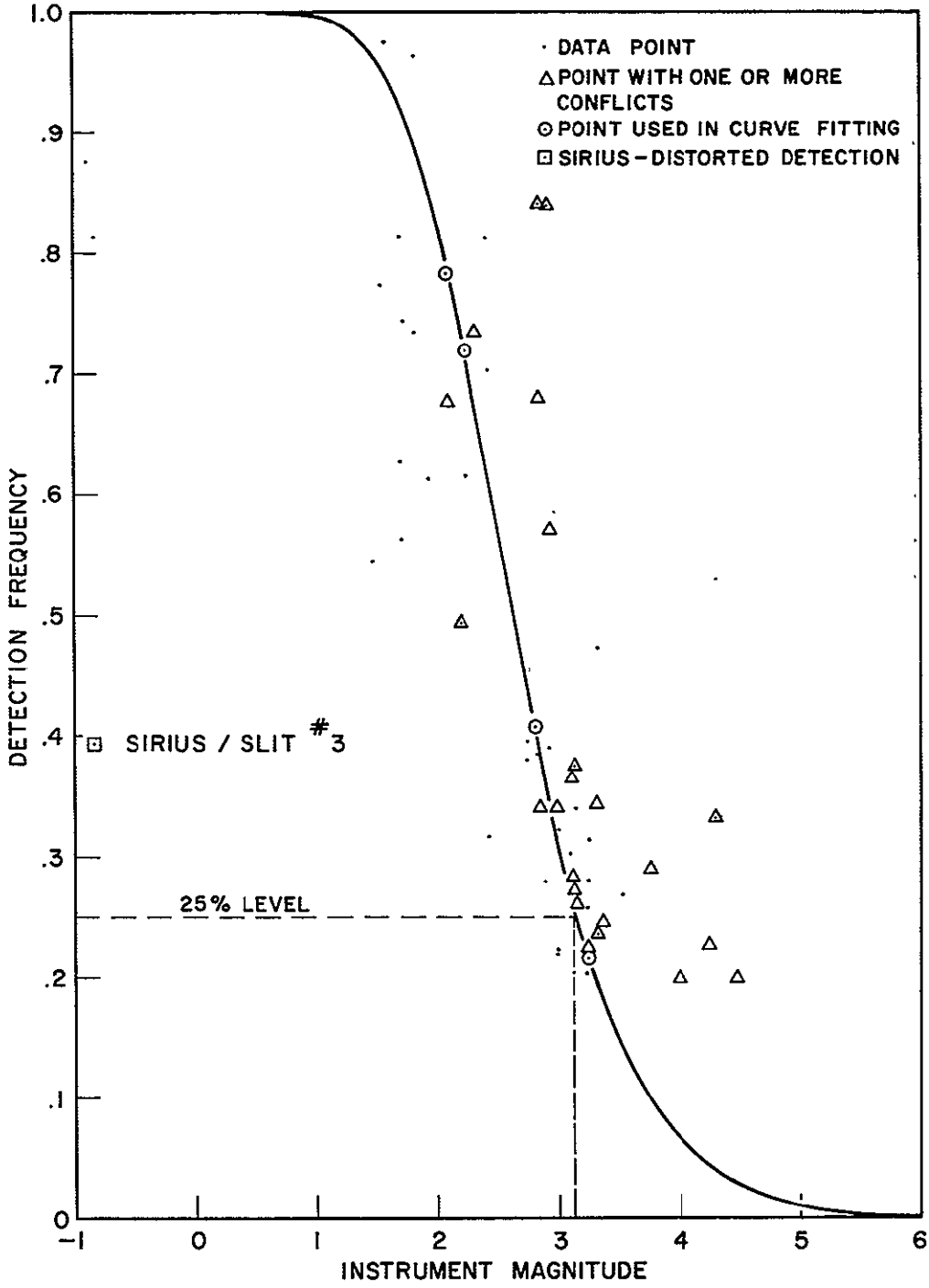

Figure 2-6: Typical Star Detection Frequency Under Dark Sky Conditions (Spring Eclipse) Gain Setting of 5.

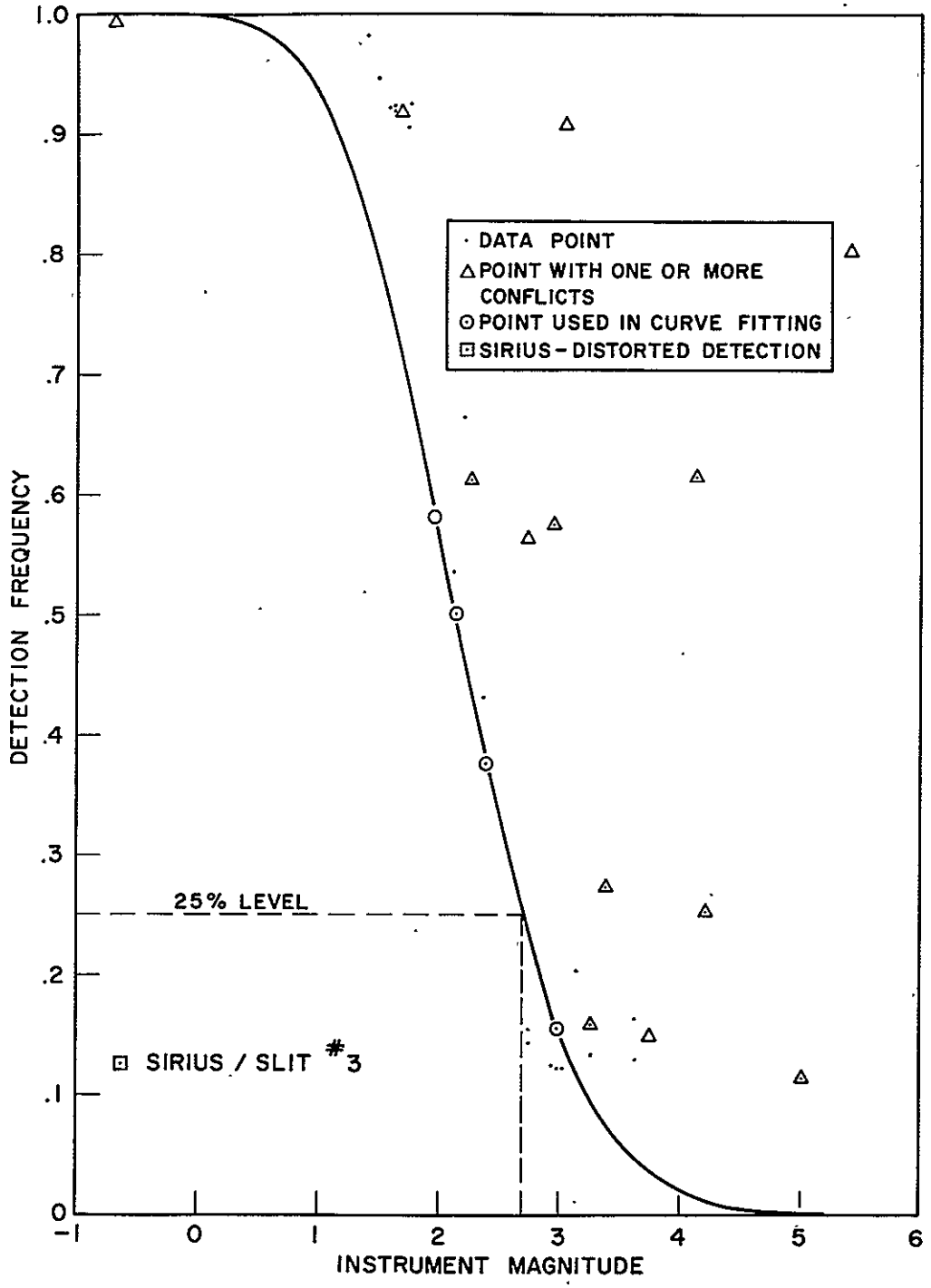

Figure 2-7: Typical Star Detection Frequency Under Dark Sky Conditions (Autumn Eclipse) Gain Setting of 6

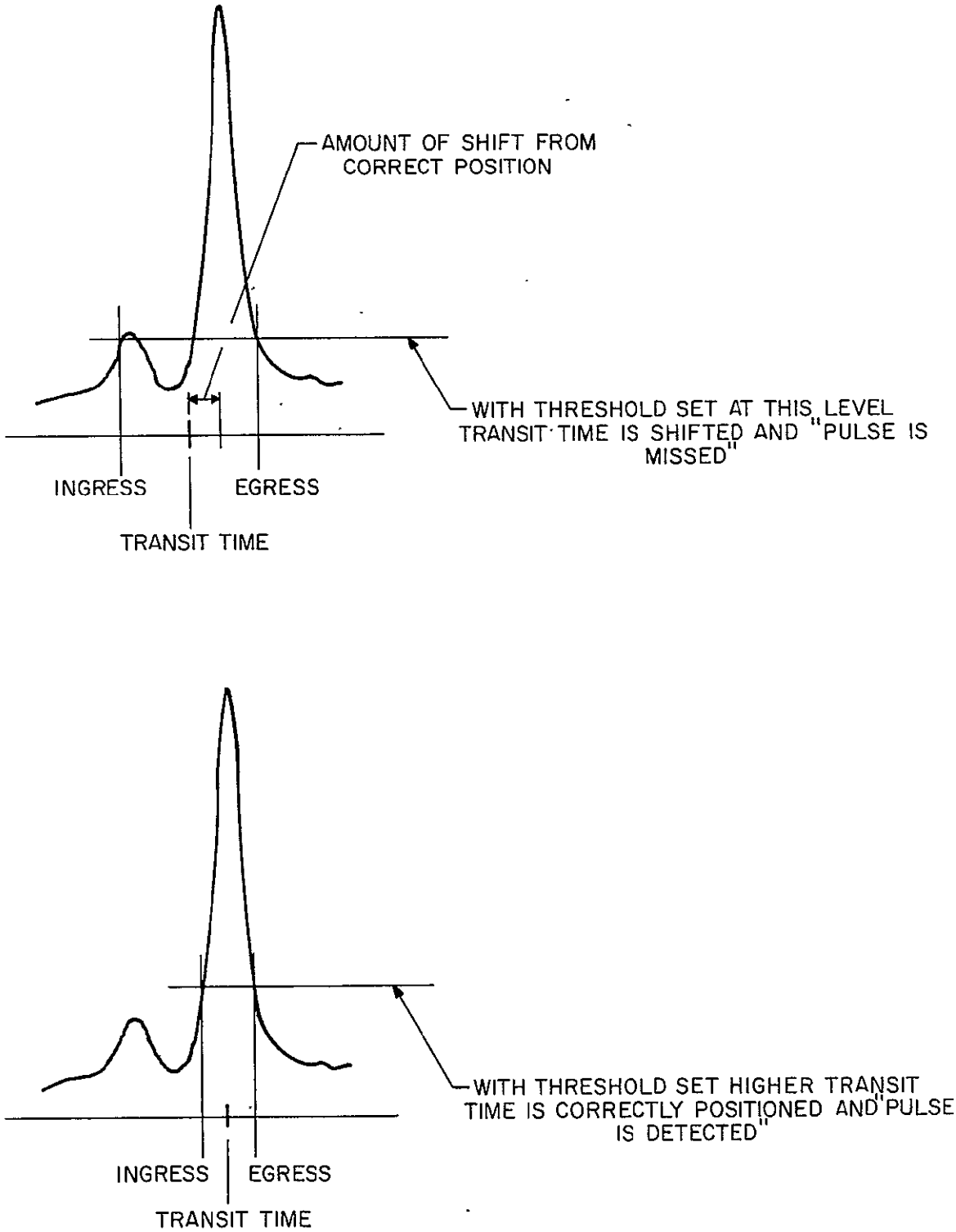

Figure 2-8: Missed Detections of Sirius by Trailing Slit

B. Bright Source Recovery

The recovery characteristic of the star sensor after an encounter with very bright sources was a particularly important and unanswered question before the ATS-III satellite was launched. Prior to satellite launch, tests were conducted relative to photomultiplier response to bright object interference. The tests were conducted by exposing the photocathode surface to bright objects placed in close proximity. Unfortunately, it was not possible to predict performance with any degree of certainty and, in particular, be able to describe the recovery characteristics of the photomultiplier or its behavior when scanning near the sun or moon.

Discussion of the recovery characteristics of the detector is based upon operational data obtained when the satellite was in full sunlight and when a nearly full moon was in the sensor field of view. In addition, the brightly illuminated halo about the south polar region of the earth was only confined to the time period centered about local satellite midnight so that the spacecraft, earth, and sun were approximately in line. The relative positions of the sun and moon for this operating condition are shown in Figure 2-9 along with a representation of the background noise conditions expressed as a function of right ascension. The noise pulse frequency results were obtained from the original digital data by deleting all of the identified stellar detections to visual magnitude 4.0, and subsequently concluding that the remaining "detections" are included within the background noise distribution. The unit of the ordinate scale is expressed as a frequency but can be interpreted to mean the number of noise pulses contained within each degree of the total scan per scan. For example, a value of 0.1 (on the frequency scale) means one noise pulse per degree for every 10 scans.

The moon's position has been corrected by approximately two degrees for parallax to represent apparent right ascension as viewed from the satellite. A sun gate data lock-out[7] was operative and was positioned from approximately

7. Lock-out is defined as the disabling of the ground based data processing equipment when energized by pulses from the on-board sun sensor.

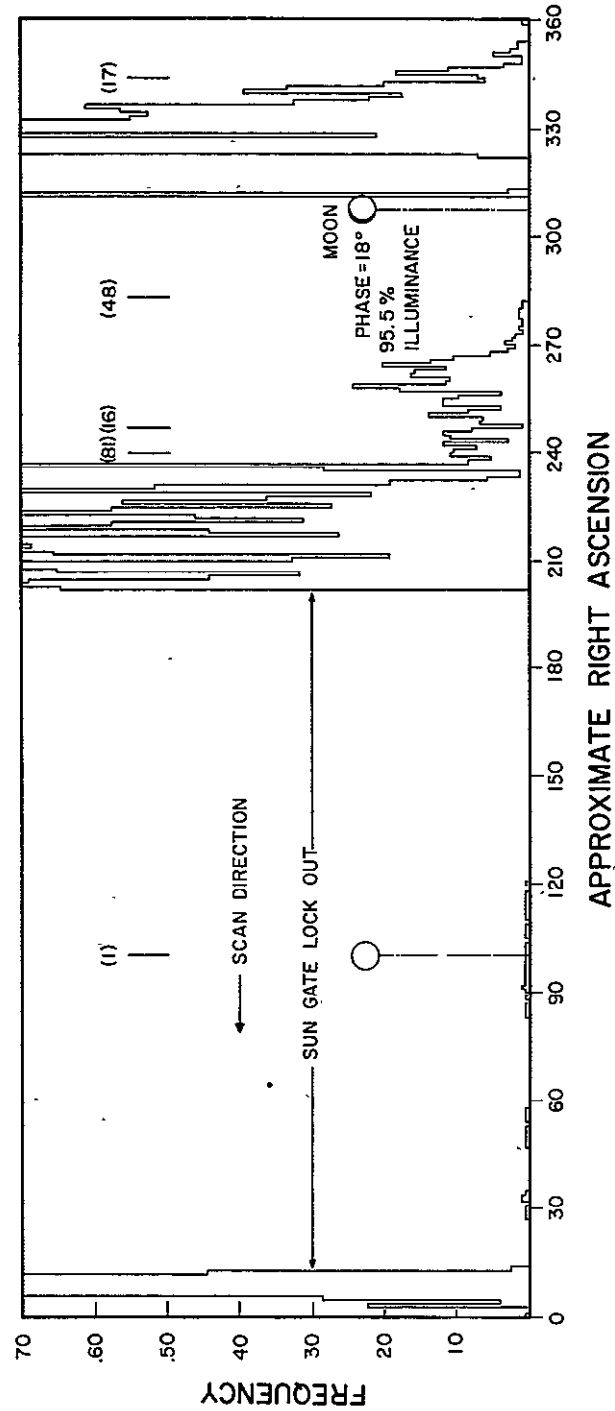

Figure 2-9: Typical Noise Pulse Frequency for Daylight Conditions

202 degrees to 23 degrees[8] with the sun at 110 degrees. Under the operating condition, the gate had been fully extended to prevent digitizing of the noise pulses with subsequent overloading of the computer memory and digital tape. It is apparent from the data that bright source pulses were processed at the extremities of the lock-out gate. At a later date the sun gate was modified to increase the extent of lock-out to include even greater portions of any noise dominated scan.

The region from 236 to 202 degrees is sun associated noise and could be locked out. The large spike at 236 degrees is the sun reflecting off the fully extended ejector arm. The burst of noise in the region about 345 to 324 degrees is noise generated by the moon's illumination reflecting off the side of the sunshield just prior to its entrance into the center of the field of view. The large spike at 312 degrees is a very repeatable pulse which shows up regularly between the three moon transits. It has not been adequately explained, although it is conjectured to be a phenomenon related to the sensor electronics caused by the high intensity surge of energy from the moon[9]. It is also noteworthy to point out that the scan area immediately following the moon in right ascension (310 to 280 degrees) is noise free, indicating that the photomultiplier tube and electronics are in a recovery phase. In fact, this recovery interval seems to extend approximately 42 degrees beyond the moon's center as evidenced by the slow rise in background noise up to approximately 266 degrees.

The positions of five regularly detected stars are also shown in Figure 2-9 to provide indication of the difficulty in making positive identifications of targets buried within background noise caused by the sun

---

8. Since the scan direction was counterclockwise around the North Pole, it is shown going right to left on the right ascension scale.

9. This unexplained spike can be seen lying between the moon/slit 1 and moon/slit 2 crossings of Figure 2-5.

and moon. No detections of Sirius were made due to the sun gate lock-out but other star/slit combinations were detected with the detection frequencies indicated in Table 2-I. The detection frequency is the ratio of the number of times a star was detected in the slit to the maximum number possible.

Star 48 (Nunki) appears in Table 2-I in slit 3 only and at an extremely low detection frequency. This is due to the proximity of Star 48 to the moon. Slit 3 is slightly farther ($-28^{\circ}.9$) from the moon than slits 2 and 1 ($-24^{\circ}.5$ and $-20^{\circ}.1$ respectively) which, of course, would be obliterated by the moon's illuminance.

The only star/slit combination that appears out of place in Table 2-I is 16/2; however, there is some rationale for its low position. For the particular set of operating conditions at that time, the spacecraft sun pulse which takes priority over star transits[10], occurred somewhere between 16/1 and 16/3 transits. This occasionally caused the loss of slit 2 transits.

A further illustration of the effect of the moon on star detection frequency is shown in Figure 2-10 in which a detection frequency paramater *S is identified as a function of moon separation angle. In an attempt to remove some of the minor detection frequency variations caused by changes in the threshold level from one data set to the next and to account for the influence of instrument magnitude on detection frequency, a normalized parameter *S was chosen where

$$*S_n^{(m)} = \frac{S_n^{(m)}}{S_{23}^{(m)}} \times \frac{S_{23}^{(m)}}{S_n^{(263)}} \quad , \text{ and}$$

$S_n^{(m)}$ is the detection frequency of the nth star on day m.

---

10. A condition established within the ground based data processing equipment.

TABLE 2-I

TYPICAL STAR/SLIT DETECTION FREQUENCIES

FOR DAYLIGHT CONDITIONS

Scan Separation From Moon[11]	Star/Slit	Detection Frequency	Instrument Magnitude
-56.4	16/1	.884	1.72
36.2	17/2	.873	1.39
-65.4	16/3	.784	1.72
30.9	17/3	.747	1.60
41.5	17/1	.646	1.60
-68.2	81/2	.571	2.30
-71.7	81/3	.398	2.41
-60.9	16/2	.313	1.56
-64.7	81/1	.064	2.41
-28.9	48/3	.013	2.09

Normalized data is presented in Figure 2-10 using a particular day (Day 263) and the star/slit combination 23/2 as the basis for normalization.

Day 263 was used as a basis for normalization to account for variations in detectability due to the moon's presence because on that day the moon was well outside the field of view. The curves give indication that for stars well away from the moon, the detection frequency of most stars is increased by the moon's presence in the field of view. This is not intuitive and may be related to the characteristic nature of the baseline following circuits.

The detection frequency of star 23 was used for normalization to minimize threshold variations because it has an instrument magnitude comparable to that for stars 16 and 17 (and thus the sensor should respond to these stars in much the same manner). More importantly, it was well removed from the moon's

11. Scan separation in degrees is positive when the star appears in front of the moon (in the direction of the scan), negative when the star occurs after the moon.

Figure 2-10: Detectability with Moon in the Field of View

influence for each of the data acquisition periods employed. Three of the stars, 16, 48 and 81, were observed on several nights when the moon was both behind (negative scan separations) and ahead (positive scan separations) of the stars. Using these and their ranges of separations from the moon just prior to and shortly after encountering the moon, it is shown that the detection cutoff point is in the range of from 0 to 16 degrees in front of the center of the moon's position. The detection turn-on point is located from 20 to 45 degrees behind the moon's center. As would be expected, the recovery period extends over a broader range than the more abrupt turn-off region. By deleting the moon-no moon normalization factor $S_{23}^{(263)}/S_{n}^{(263)}$, a slower recovery (after lunar encounter) to normal detectability for the two fainter stars 48 and 81 is evident. This is shown for the data normalized using 23/2 only.

C. Spatial Noise

A measure of SCNS instrument performance as a star detection device is obtainable by comparing the star detection frequencies described in Section A with the noise background from which such detections are determined. Figure 2-11 shows the noise pulse frequency under typical dark sky conditions just as Figure 2-9 did for daylight conditions. The noise pulse frequency histograms indicates the position of the sun as observed from the satellite. Because the results shown were obtained from the eclipse data, the sensor field of view does not scan past the sun but sees only the halo about the earth. The earth directly blocks any incident sunlight from illuminating the satellite. The geometry of the sun-earth-satellite relationship is given in Figure 2-12. It is apparent, since no direct sunlight illuminates the satellite, that the high noise pulse frequencies observed in Figure 2-11 attributed to solar illumination of the earth's atmosphere which appears as a halo around the earth in the region of the poles.

A second observation which may be made from a study of the background noise is the increase in noise pulses per scan in the region of the Milky Way. Notice that except for star 17 (Fomalhaut) other regularly detectable stars, 1, 16, 48 and 81, all fall within the Milky Way.

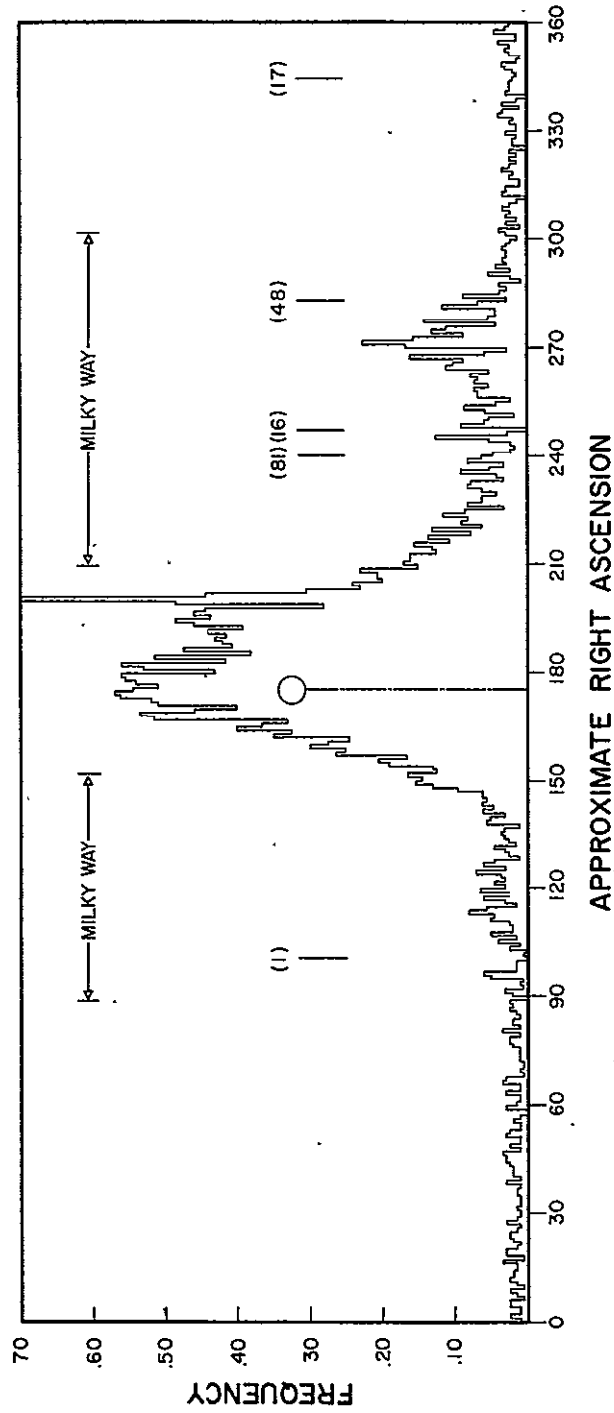

Figure 2-11: Typical Noise Pulse Frequency for Dark Sky Conditions

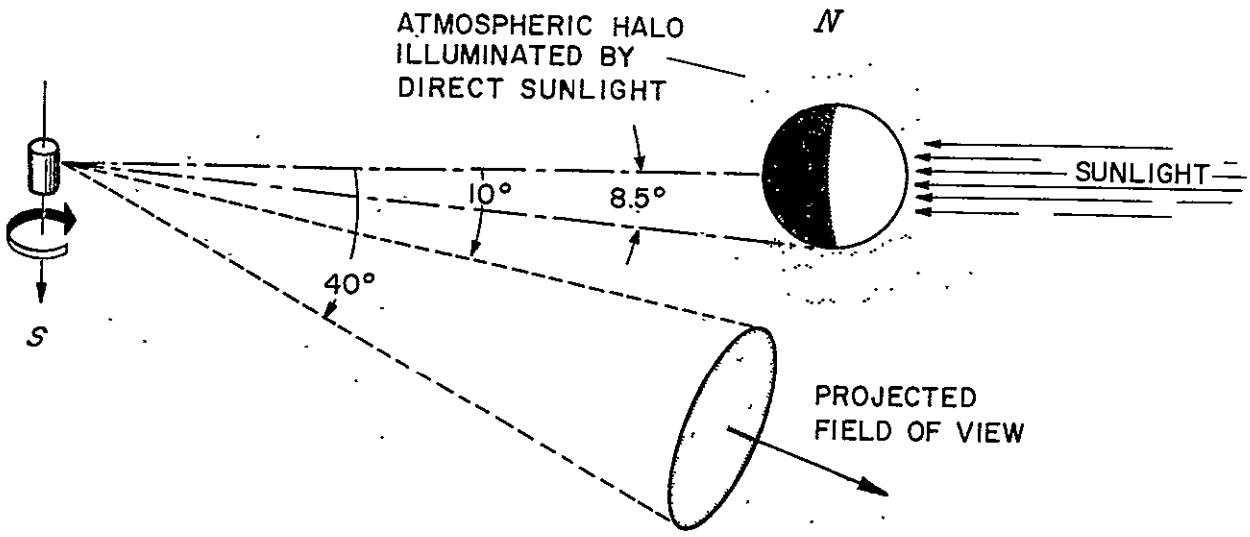

Figure 2-12: Geometric Relationship Occurring During Eclipse Operations

D. Measurement Accurracy

Transit time accuracy of star detections for the SCNS sensor have been analyzed, utilizing three stars having widely separated magnitudes. The selected stars and their characteristics are listed in Table 2-II. Each was regularly detected in slit 2.

TABLE 2-II

SELECTED STARS USED IN DETECTION ACCURACY ANALYSIS

Star Number	Star Name	Visual Magnitude	Instrument Magnitude
1	Sirius	-1.58	-0.8
16	Antares	1.22	1.6
48	Nunki	2.14	2.0

Figure 2-13 indicates the transit time position within a particular scan for each of the stars listed in Table 2-II for dark sky conditions occurring in both spring and autumn eclipses and for similar sensor operating conditions. Broken lines are used to connect points where detections from intermediate scans are missing. The solid vertical line for each star/slit combination represents the averaged transit time (mean). Also indicated for each graph is the standard deviation (σ) of the transits around the mean. Transit times were obtained by averaging the leading and trailing edges of each pulse (in effect adding one-half the pulse width to the leading edge threshold crossing time).

One technique developed in conjunction with the project activity was a method of filtering star transits on the basis of both position within the scan and its pulse width. Transits were discarded which deviated by more than one standard deviation from a mean transit time and which had pulse widths exceeding a predetermined narrow band-width. Filtering was done for all the regularly detectable stars in order to produce a set of highly selective filtered transit times. When these times are used as input data to the attitude algorithm, a reliable and accurate solution with small functional residuals results.

E. Lunar Detectability

When the full moon which subtends slightly over 0.5° is centered on one of the slits (each having a 7.6 arc minute projected width) the light input to the photomultiplier is approximately 10^4 times that from Sirius, the brightest star in the sky. When the moon is detected the photomultiplier output electronics are severely overdriven. Recovery of the electronics from this condition exhibits a complex pattern. This is observable in Figure 2-5. The net effect of this behavior, as it relates to the interpretation of the lunar transit data, is that the leading edges of the apparent moon pulses are actually recovery transits from the preceding pulses. The pulses result from moon crossings of a preceding slit and/or moon reflections off the cone.

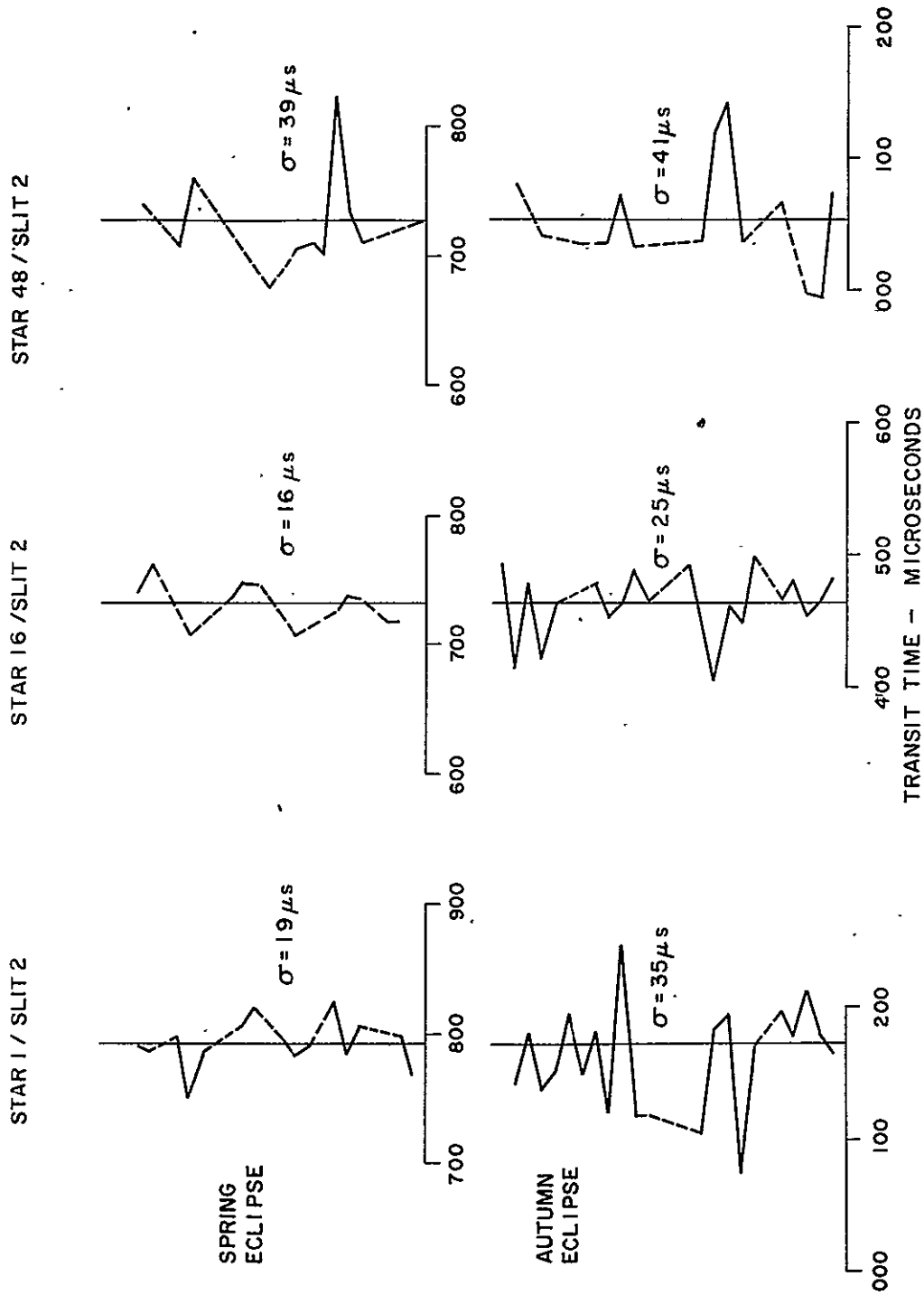

Figure 2-13: Star Measurement Accuracies for Spring and Autumn Eclipse Conditions

Moon simulated laboratory tests were performed using the spare flight SCNS model. The results led to the conclusion that the trailing edges of the lunar pulses correspond to the optical event associated with the instant of moon/slit egress. This was corroborated by analyzing over thirty separate data sets containing moon transits. The expected average lunar trailing edge detection was calculated for each data set and for each slit, taking into account the parallax in the moon's apparent direction and extent, as seen from the spacecraft. Because the moon is an extended source and the slit crossings occur at various angles, each slit exits from different points on the moon's illuminated surface. This will give rise to a small differential in the slit-to-slit separation times. For the days under consideration, the slits exited from the moon's limb, not the terminator. Thus, lunar phase does not affect the lunar detection problem.

Accurate ephemerids for the position of the sun[4], the moon[4], and the spacecraft[5], and geocentric semi-diameter of the moon[6] were fitted to polynominal interpolation expressions covering the time of the SCNS data acquisition. Then, for the time of each data set, the apparent celestial direction of the center of the moon as seen from the spacecraft was determined. The precise spacecraft attitude solution (including values for the second and third time derivative of the azimuth angle $\ddot{s}$ and $\dddot{s}$ for the group of data sets under consideration was then used to calculate the time when the trailing edge of each slit would cross the moon's limb.

If $\hat{n}_i$ denotes the time varying normal to the ith slit plane; $\hat{m}$ the apparent celestial direction of the moon as seen from the spacecraft; φ the apparent lunar radius as seen from the spacecraft; and ζ the half-width of the slit, the condition that the moon begins its egress from the trailing edge of slit i is describable by the equation:

$$\hat{m} \cdot \hat{n}_i = \cos\left[90^\circ + (\varphi + \zeta)\right]. \qquad (1)$$

Since this equation is a single condition in t_i, the time of the trailing

edge crossing, it may be solved to determine t_i.

For each data set, each of the 15 seconds duration, the average lunar trailing edge transit times were computed for the measured data. These measured detection times were then compared with the predicted detection times. If, for each slit, these differences were constant from set-to-set and from day-to-day, they could be used as correction factors to be added to the measured detection times to obtain the actual trailing edge detection times.

The results of this analysis are shown in Figure 2-14 where, for each day, the average of the difference between the predicted and measured detection times is plotted against the phase of the moon as seen from the spacecraft. The standard deviations of the points range from one to seven microseconds with an average of four microseconds. The electronics of the spacecraft are overloaded in such a way that the trailing edge detection by the first slit is not as consistent as the trailing edge detection by slits 2 and 3. For five data sets the correction factors for slit 1 turned out to be very large (i.e., over 500 msec). These results were not included in the data presented.

There appears to be a strong correlation between the correction factor and the phase of the moon. The correction is larger at full moon (0 degrees phase) than at new moon (180° phase). This effect may be qualitatively explained as follows: The output of the photomultiplier tube is accumulated in energy storing elements within the electronics. When the input voltage falls below a given level, the energy balance in the first stages can no longer be maintained, and the relative input polarity to the last stage reverses. When this occurs, the output state changes almost discontinuously from the saturation state of maximum illumination to the opposite saturation state which results in zero output. The trailing edge of the pulse is then recorded. When the moon is crescent, the integrated input from the

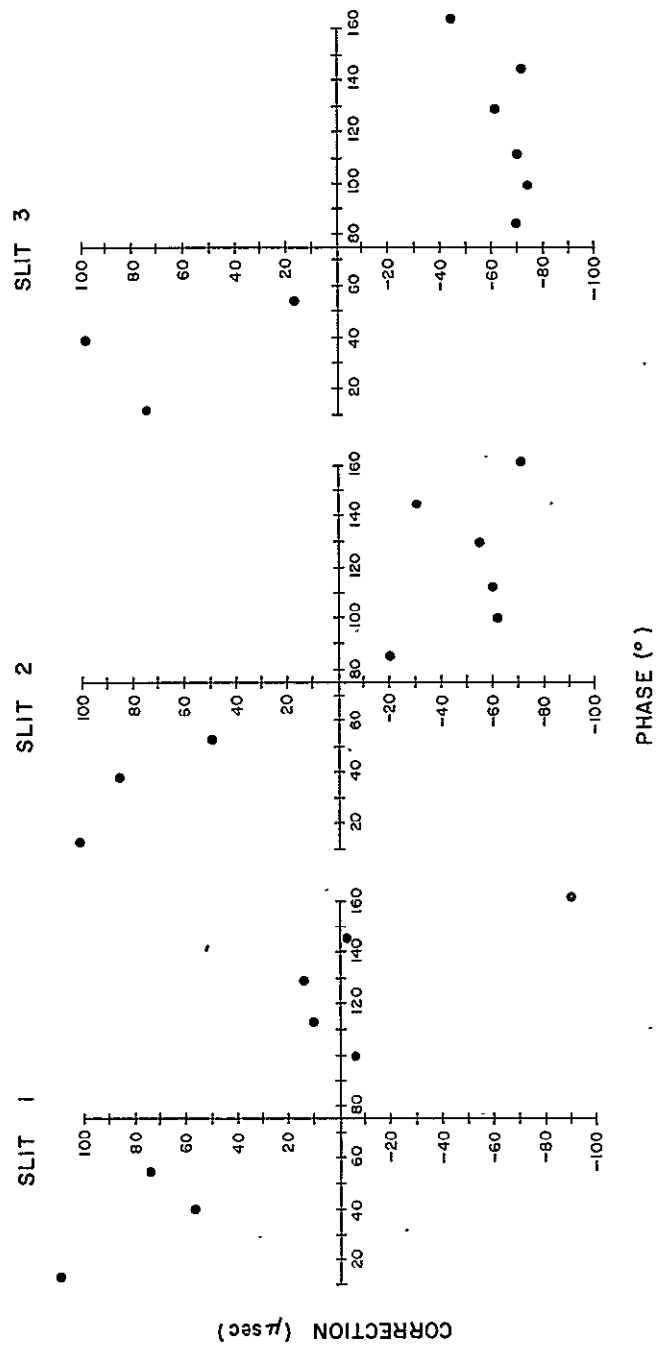

Figure 2-14: Slit Correction Factors as a Function of Lunar Phase

photomultiplier saturates the electronics for a shorter time than when the moon is full and the input continues to be integrated by the energy storage elements while the pulse goes through its peak and starts down its trailing edge. Only when the input voltage falls below the level needed to maintain the energy balance do the polarity reversal and output state changes occur. However, when the moon is full, the energy storage elements are in equilibrium, so that at the instant the early stages come out of saturation, the polarity reversal occurs. Hence, the trailing edge detections at full moon should occur earlier than the trailing edge detections when the moon is crescent. Thus, the correction factor, which is the difference between the predicted and measured detection times, should be larger at full moon than when the moon is crescent. Such behavior is, indeed, observed.

The simplest relationship between the phase and the correction factor is a linear relation between the two. The effect on the solution of the navigation problem of applying such a correction factor to each measurement of the trailing edge of the moon is described in Chapter 4.

F. Ejected Probe Detectability

Two probe ejections were conducted with neither providing adequate data to solve the navigation problem. It was concluded that the first launch exhibited an error in timing but near nominal mechanical performance; in the second launch, timing was correct but the ejection mechanism malfunctioned.

Even though the malfunction prevented probe sightings from being successfully utilized[12] to determine satellite orbital position, a measure of the detectability of the sensor-probe combination was obtained. The second probe was tracked by the sensor to a limit of 8.6 miles, equivalent to a star of 1.92, visual, and 2.88, instrument magnitude.

12. Launch error for the second probe prevented the probe from re-entering the sensor field of view on its return orbit 24 hours after launch. Sightings were only possible up to 2.5 hours after launch.

The parallax in the SCNS sightings of the probe on the first few scans after ejection was used to determine the initial conditions of launch. The specific conditions are the time of release, t_o, the azimuth of release λ relative to a radial line through the spin axis and the release point, the elevation of release E relative to the azimuth plane, and the speed of ejection Δv relative to the spacecraft.

For the second probe, the parallax analysis has been carried through and the results are summarized in Table 2-III.

TABLE 2-III

INITIAL CONDITIONS FOR SECOND PROBE EJECTION -
RESULTS FROM PARALLAX ANALYSIS

Time of release (20 July 1968):	t_o	= 0h 0m 0.7626 seconds
Relative azimuth of release:	λ	= $-12^{\circ}.89$
Elevation of release:	E	= $23^{\circ}.02$
Release speed:	Δv	= 4.54 feet/second

It should be noted here that the navigation equations described in Chapter 4 could not be solved for a precise value of the release speed, particularly for the short time base - two and one-half hours - over which probe data was acquired. Thus, the parallax analysis was the only method which yielded a direct determination of Δv.

Once the release speed was determined, it was used in connection with the navigation equations to describe the apparent direction and separation distance from the satellite to the probe as a function of time. The results of this characterization are summarized in Table 2-IV for three times at which probe detections were acquired on 20 July (Day 202).

TABLE 2-IV

SECOND EJECTED PROBE - DIRECTION AND SEPARATION FROM THE SATELLITE

Time	Right Ascension	Declination	Separation
1:48	$261^{\circ}.85$	$-20^{\circ}.51$	5.9 miles
2:15	$262^{\circ}.65$	$-19^{\circ}.44$	7.6 miles
2:30	$263^{\circ}.29$	$-18^{\circ}.79$	8.6 miles

The data in the last column of Table 2-IV represent one of the factors in a separation - apparent magnitude relation for the probe; such a relation provides the basic measure of probe detectability.

To complete the detectability characterization, the apparent magnitudes corresponding to the separations were found. Actually, since the probe brightness follows an inverse square relationship with distance, it is sufficient to determine the apparent magnitude corresponding to one known separation. At 1:48, the detection frequency of the probe in each slit was slightl below the detection frequencies of the two brightest accessible stars in the field (Fomalhaut and Antares) but still well above the noise level. At 1:48 the instrument magnitude of the probe, corrected to the optical axis, was found to be 1.73 with a spread of only 0.09 magnitude among the three slits.

The instrument magnitude corrected to the optical axis takes the particular spectral response characteristics of the SCNS instrument into account If it is assumed that the probe reflectivity is essentially constant with wavelength, then the color index of the probe was essentially that of the sun. Since the sun is a rather red star, as seen by SCNS, the instrument magnitude for a star of this color (B-V = 0.62) is 0.38 units fainter than it visual magnitude. Thus, at 1:48 the visual magnitude of the probe is 1.35.

As was noted above, the probe brightness can be predicted for other separation values by employing the inverse square law. Table 2-V presents

this information in equivalent form in terms of time. In the righthand column, the magnitude has been corrected for both spectral response and location of the probe in the field of view; this is the instrument magnitude of the probe as it appears in the center one of the three slits.

TABLE 2-V

MAGNITUDES OF SECOND EJECTED PROBE

Time (20 July 1968)	Visual Magnitude	Instrument Magnitude (on the optical axis)	Apparent Instrument Magnitude (at the actual off-axis crossing for slit 2)
1:48	1.35	1.73	1.89
2:15	1.90	2.28	2.54
2:30	2.17	2.55	2.88

In Table 2-VI the observed magnitude, as indicated in the last column of Table 2-V is compared with the predicted magnitude. The predicted magnitude was obtained before conducting the experiment.

TABLE 2-VI

COMPARISON OF OBSERVED AND PREDICTED MAGNITUDES

Time	Observed Magnitude	Predicted Magnitude	Difference
1:48	1.89	.99	
2:15	2.54	1.64	0.90
2:30	2.88	1.98	

Thus, the predicted magnitude was determined to be less than one magnitude difference from the observed magnitude.

CHAPTER 3
DETERMINATION OF SATELLITE ATTITUDE

INTRODUCTION

The processing of star data makes use of computer programs designed to solve a set of equations which describe satellite motion. The development of the attitude method presented here, includes a description of the coordinate system used and defines the basic constraint equation in the unknowns of the problem. Several computer programs to obtain attitude solutions were written during the performance of the experiment. An early program designated BOOTS was designed to accept hand identified star transits. A fully automatic program designated SCAT, needing no hand identification, was subsequently written which solves for four parametric unknowns. A later program was designed to accommodate an increased number of unknowns. Each of these programs is discussed in some detail within the chapter. The SCAT program which served as the basic program in determining satellite attitudes has each of its routines fully described in Section I B. This description has been presented in sufficient detail to serve as a users manual. Section II documents the numerical results and for the most part tabulates the values of each of the solved for unknowns according to the environmental conditions of each experiment. A measure of instrument accuracy is expressed in the tabulation of the residuals for each of the unknowns, and are also included in the section.

CONCLUSIONS

Chapter 3 relates the results of the data processing methods and the accuracy of the attitude solutions. The most significant observations from the results are included here as conclusions.

1. Attitude solutions obtained from data taken when the satellite was in the earth's eclipse, contained residuals which were typically 60 arc seconds. The standard deviations of the computed spin axis directions were generally less than 10 arc seconds and for the azimuthal rotation about the spin axis less than 15 arc seconds.

2. Attitude solutions were obtained through the use of a completely automatic computer program, requiring no hand identification of stellar targets. Two programs were written. The basic program (SCAT) solved for four unknowns (two pointing angles, azimuthal position and spin velocity). A more complete program, based upon SCAT, was used to solve the eight unknown problem.

3. Attitude solutions obtained from data taken when the satellite was in full sunlight contained residuals which were typically 90 arc seconds. The standard deviation of the computed spin axis directions were generally 100 arc seconds and for the azimuthal rotation about the spin axis 40 arc seconds. Degraded accuracy was due to the reduction in the number of regularly detected targets and the resultant poorer geometry.

4. The parameters which define the location of the slit intersection with respect to the satellite figure axis were observed to change with time and particularly with each maneuver. Slight changes in spin axis position, most probably due to loss of mass, was concluded as the cause.

5. The degree of satellite nutation (and precession) was observed to be negligible in comparison to the ability of the star sensor to detect the motion. The coning angle was found to be less than one minute of arc which permitted the utilization of a mathematical model which assumed rotational motion about a fixed axis.

6. It was observed that the satellite in passing from full sunlight into the earth's shadow increased in spin velocity, necessitating the inclusion of the spin acceleration term as an additional unknown.

7. Over the 28 days when the satellite was in the earth's fall eclipse the direction of the spin axis changed by a negligible but constant rate. The total angular changes for each of the two parameters over the interval were less than 12 arc minutes. The most probable cause was due to magnetic, gravitational, and gas leakage torques.

I. STAR DATA PROCESSING

A. Development of the Attitude Determination Method

The general problem is to find the orientation as a function of time, t, of a coordinate system fixed in a spinning body as measured in a stationary coordinate system. The basic input measurements which yield this orientation, or attitude, are the times of transit of known stars across a slit.

A slit is etched on the focal plane of an optical system as shown in Figure 3-1. If the slit is a straight line segment and the optical system

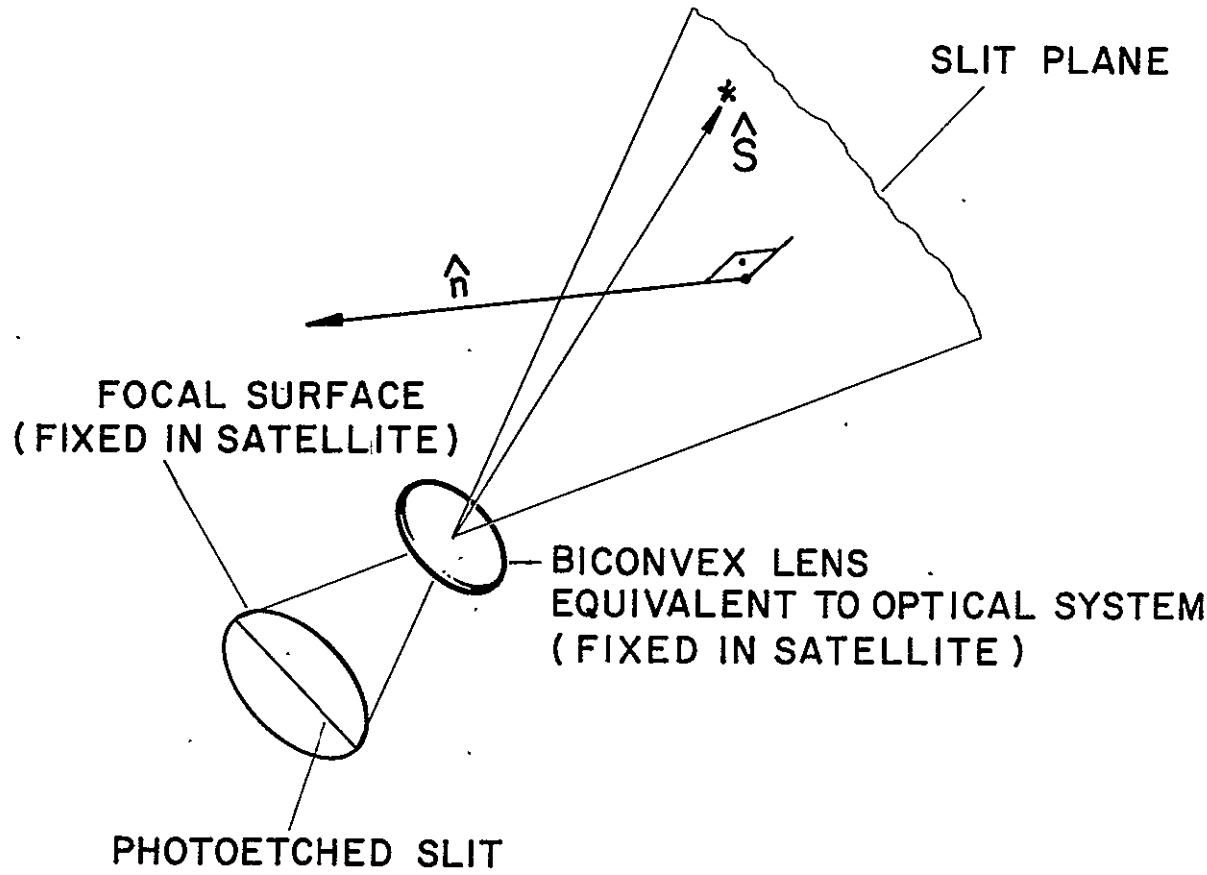

Figure 3-1: The Slit Plane and Its Normal $\hat{n}$

is distortionless, then a portion of a plane will be defined which contains the slit, and the nodal point of lens system. Given a distant bright point source, this source will be sensed by a detector behind the slit if, and only if, it lies on the plane defined by the slit and optical system. If a point source crosses the plane, the source transits the slit. The instant the point source lies in the plane is called the transit time.

For any transit time of a star, the following equation may be written:

$$\hat{n} \cdot \hat{S} = 0 \qquad (1)$$

where

$\hat{n}$ = unit vector normal to the plane defined by the optical system
$\hat{S}$ = unit vector in the star's direction.

Since the optical system is fixed within the satellite, $\hat{n}$ is also fixed within the satellite. Its components are therefore most easily written in a coordinate system fixed in the satellite. On the other hand, $\hat{S}$ is most easily written in a celestial coordinate system (a system in which the star directions are cataloged)[1]. In order that these vectors may be written in the same coordinate system, parameters which specify the orientation of the coordinate system fixed in the satellite with respect to the celestial system must be introduced. However, these are the very parameters which are to be determined.

In order to define parameters which allows $\hat{n}$ and $\hat{S}$ to be written in the same coordinate system, the physics which govern the motion of the satellite

(1) At this point it is assumed that the star has been identified although such identification is not a trivial problem. Target identification is treated in Section I B.

must be considered. Two models were applied to the ATS-III satellite attitude dynamics as follows:

(1) Spinning, rigid, nearly symmetric, untorqued body

(2) Body spinning about a fixed axis.

The first assumption permits a precessional motion of the spacecraft. It was discovered during data processing that the angle between the satellite's angular momentum vector and the principal axis of its largest moment of inertia was extremely small (i.e. less than a minute of arc). This observation was also made independently through the use of an on-board accelerometer. It was apparent that the motion of the spacecraft principal axis was too small to be reliably detected by the star sensor. Consequently, the precessional model was abandoned and the simpler fixed axis model was used to obtain the majority of the results which follow. A discussion of the analysis of the precessional motion model may be found in reference[2].

An analysis of the model assuming a body spinning about a fixed axis is included below. A six coordinate frame system is used to define satellite attitude. The development of the coordinate system is presented.

1. Coordinate Systems and Transformations

Figure 3-2 defines the coordinate systems S_1, S_2, and S_3. The system S_1, is the celestial system. $\hat{i}_1$ is in the direction of the First Point of Aries, $\hat{k}_1$ is in the direction of the North Pole. The system S_3, is such that $\hat{k}_3$ is in the direction of the spin axis of the spacecraft. Hence, for ATS-III satellite $\hat{k}_3$ has approximately the direction of the South Pole. The figure, however, is drawn with $\hat{k}_3$ closer to the North Pole for ease of illustration.

For the general case, two angles are required to define the direction

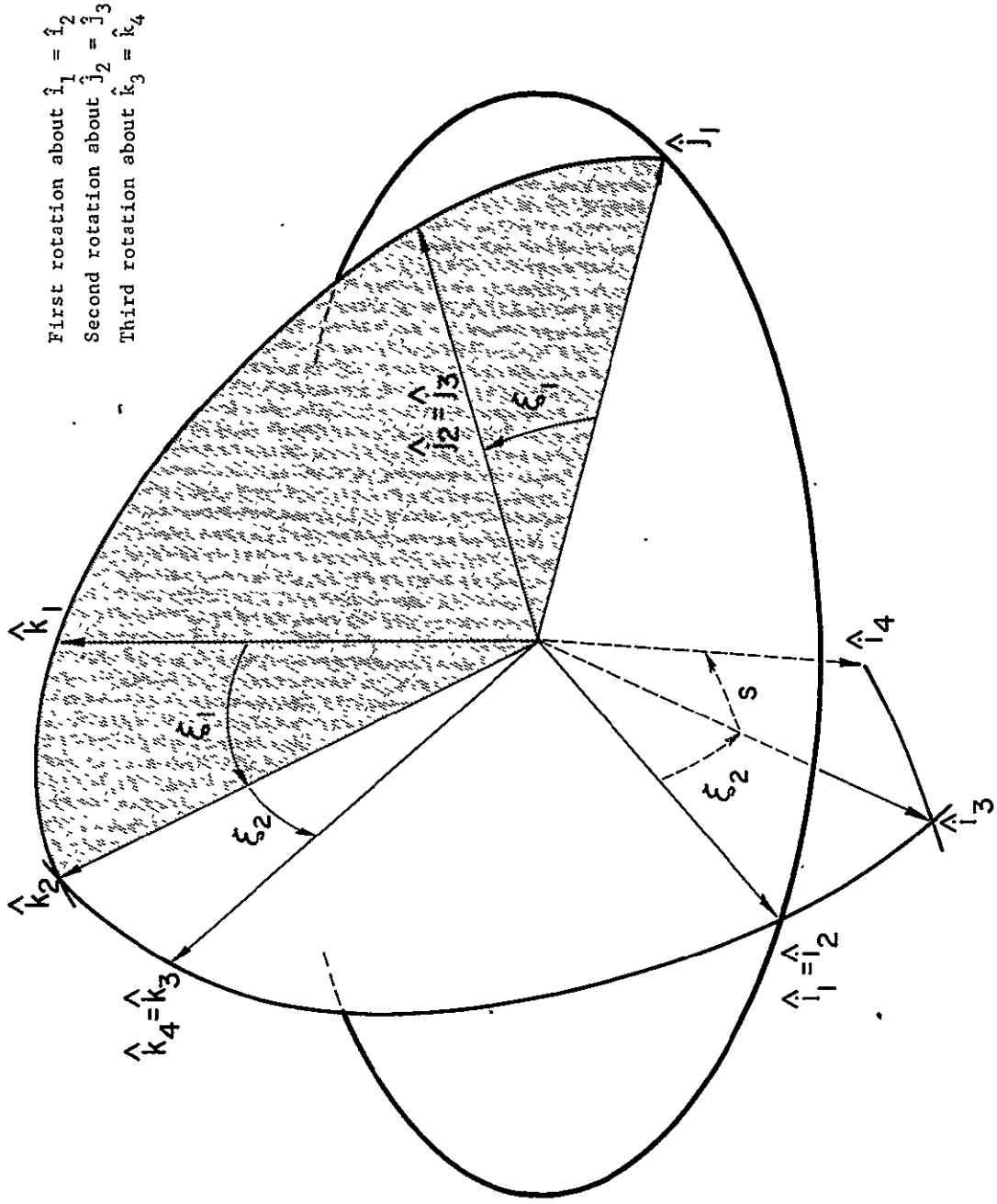

Figure 3-2: The Orientation of S_3 with Respect to S_1 Defined by ξ_1 and ξ_2

of the spin axis, $\hat{k}_3$, with respect to the coordinate system S_1. These angles are chosen to be called ξ_1 and ξ_2, and are defined as follows:

$\hat{k}_1 \rightarrow \hat{k}_2$ rotation ξ_1 about $\hat{i}_1 = \hat{i}_2$
$\hat{k}_2 \rightarrow \hat{k}_3$ rotation ξ_2 about $\hat{j}_2 \quad \hat{j}_3$.

It is more conventional to locate the direction of an axis with respect to S_1 by its right ascension and declination rather than by ξ_1 and ξ_2. However, if the axis is close to the North or South Pole, its right ascension is poorly defined and undefined if the axis has the direction of the North or South Pole. Since the satellite spin axis always lies close to the South Pole, its direction is chosen to be defined by ξ_1 and ξ_2. This is done to eliminate a near singularity which would be present in the conventional formulation. However, the choice of ξ_1 and ξ_2 introduces a signularity if the spin axis, $\hat{k}_3$, were at $\pm \hat{i}_1$.

The system S_3 has one axis fixed in the satellite, $\hat{k}_3$. However, S_3 is an inertial system if the satellite is spinning about a fixed axis. Another system, S_4, is fixed in the satellite such that

$\hat{i}_3 \rightarrow \hat{i}_4$ a rotation s about $\hat{k}_3 = \hat{k}_4$.

The choice of the position of $\hat{i}_4$ is not arbitrary but will be defined by the position of the slits.

Three slits were designed and fabricated to intersect at a point so the center slit bisects the angle formed by the outer two slits as shown in Figure 3-3. The point of intersection, of course, rotates with the satellite. The $\hat{i}_4$ direction is chosen such that the ($\hat{i}_4$, $\hat{k}_4$) plane contains this common point.

Let the angle from $\hat{k}_4$ to the intersection of the slits be σ, and let $\hat{k}_5$ be the unit vector to this point. The nominal position of the center slit is in th

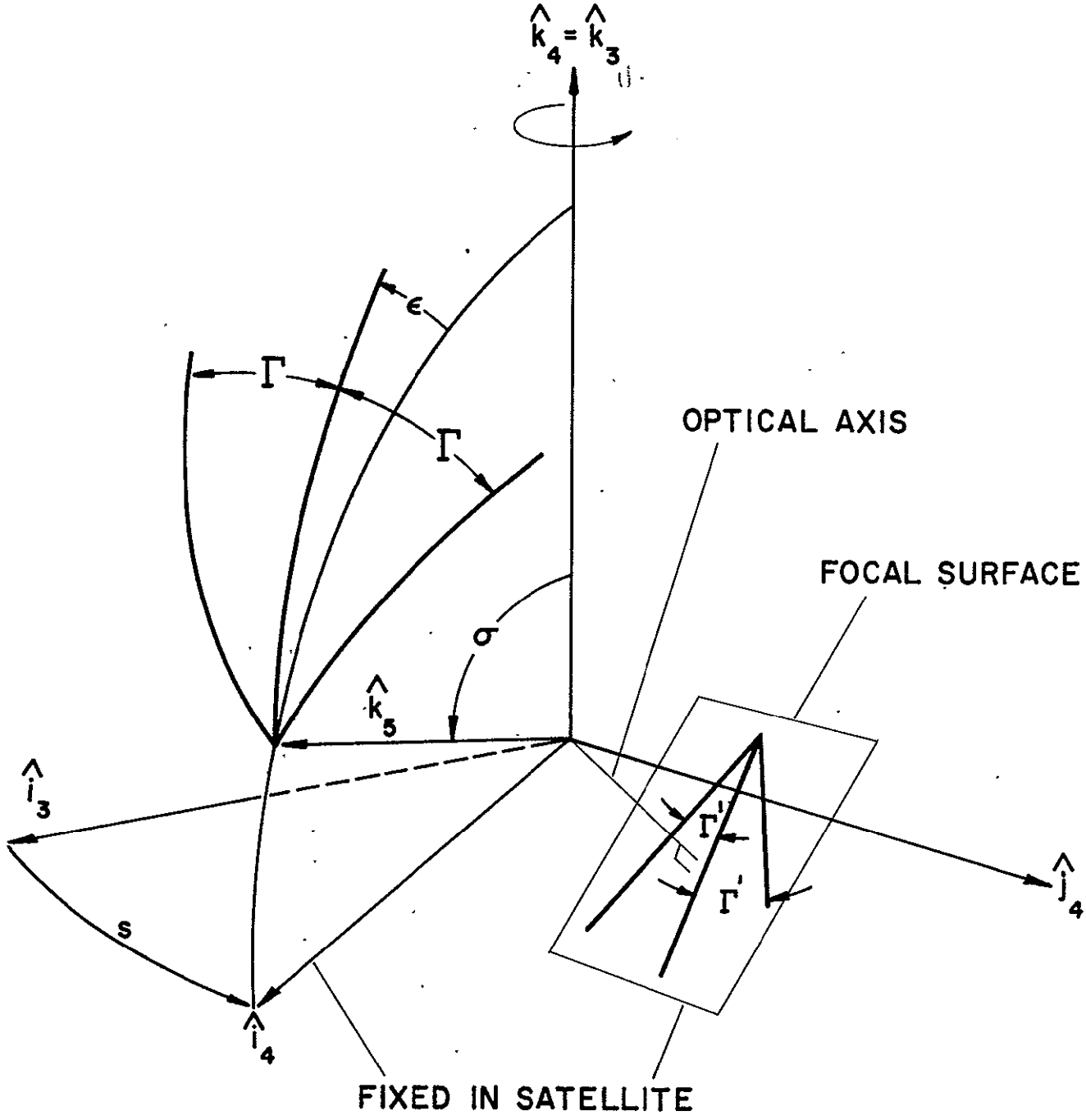

Figure 3-3: The Orientation of the Slits as Defined by ϵ, Γ, σ

$(\hat{i}_4, \hat{k}_4)$ plane. Its actual position may then be defined by a rotation of ϵ about $\hat{k}_5$. Finally, the two outer slits each make an angle Γ with the center slit. The angles σ, ϵ, Γ, ξ_1, and ξ_2 are usually treated as constants independent of time. The angle s however is time dependent and is assumed to be of the form

$$s = s_o + \dot{s}t = \tfrac{1}{2}\ddot{s}t^2 + \frac{1}{6}\dddot{s}t^3 \quad . \tag{2}$$

This form is essential if the spacecraft is shaded from the sun[2], otherwise we may usually set $\ddot{s} = \dddot{s} = 0$.

Now, the system S_5 is defined so that

$\hat{k}_4 \rightarrow \hat{k}_5$ a rotation σ about $\hat{j}_4 = \hat{j}_5$.

System S_{6j}, j = 1, 2, 3 are defined by each of the three slits so that

$\hat{i}_5 \rightarrow \hat{i}_{6j}$ a rotation ρ_j about $\hat{k}_5 = \hat{k}_{6j}$

here $\rho_1 = \epsilon + \Gamma$
$\rho_2 = \epsilon$
$\rho_3 = \epsilon - \Gamma$

Thus, the plane defined by the jth slit is the $(\hat{i}_{6j}, \hat{k}_{6j})$ plane.

The transformations between the various systems may now be given as:

$$\begin{pmatrix} \hat{i}_3 \\ \hat{j}_3 \\ \hat{k}_3 \end{pmatrix} = H(\xi_1, \xi_2) \begin{pmatrix} \hat{i}_1 \\ \hat{j}_1 \\ \hat{k}_1 \end{pmatrix} \quad \text{(celestial to spin)}$$

(2) For reasons to be explained in Section I-B.

$$\begin{pmatrix} \hat{i}_4 \\ \hat{j}_4 \\ \hat{k}_4 \end{pmatrix} = R\,(s) \begin{pmatrix} \hat{i}_3 \\ \hat{j}_3 \\ \hat{k}_3 \end{pmatrix} \quad \text{(Spin to satellite fixed)}$$

$$\begin{pmatrix} \hat{i}_{6j} \\ \hat{j}_{6j} \\ \hat{k}_{6j} \end{pmatrix} = B\,(\sigma, \rho_j) \begin{pmatrix} \hat{i}_4 \\ \hat{j}_4 \\ \hat{k}_4 \end{pmatrix} \text{(satellite fixed to slit)}$$

where

$$H = \begin{pmatrix} \cos \xi_2 & \sin \xi_1 \sin \xi_2 & -\cos \xi_1 \sin \xi_2 \\ 0 & \cos \xi_1 & \sin \xi_1 \\ \sin \xi_2 & -\sin \xi_1 \cos \xi_2 & \cos \xi_1 \cos \xi_2 \end{pmatrix}$$

$$R = \begin{pmatrix} \cos s & \sin s & 0 \\ -\sin s & \cos s & 0 \\ 0 & 0 & 1 \end{pmatrix}$$

$$B_j = \begin{pmatrix} \cos \rho_j \cos \sigma & \sin \rho_j & -\cos \rho_j \sin \sigma \\ -\sin \rho_j \cos \sigma & \cos \rho_j & \sin \rho_j \sin \sigma \\ \sin \sigma & 0 & \cos \sigma \end{pmatrix}$$

2. The Constraint Equation

It is now possible to write Equation (1) in a usable form, and when so written, becomes the constraint equation because it offers a constraint on the attitude at the instant of transit of any known star.

The components of $\hat{S}$ are simply:

$$\hat{S} = \cos\delta \cos\alpha \, \hat{i}_1 + \cos\delta \sin\alpha \, \hat{j} + \sin\delta \, \hat{k}_1 \qquad (3)$$

where α = star's right ascension (known)

δ = star's declination (known)

while those of $\hat{n}_j$, the unit normal pertinent to the jth slit is simply

$$\hat{n}_j = \hat{j}_{6j} .$$

But,

$$\hat{j}_{6j} = B_{2j} \; R \; H \begin{pmatrix} \hat{i}_1 \\ \hat{j}_1 \\ \hat{k}_1 \end{pmatrix}$$

where B_{2j} is the second row of B_j. Thus, the constraint equation becomes:

$$0 = B_{2j} \; R \; H \; \hat{S} \qquad (4)$$

where $\hat{S}$ is a column vector whose components are given by (3).

If the following are assumed:

(1) The satellite is spinning about a fixed axis so that ξ_1 and ξ_2 are constant.

(2) $s = s_o + \dot{s}\, t + \frac{1}{2} \ddot{s}\, t^2 + 1/6 \dddot{s}\, t^3$, where s_o, $\dot{s}$, $\ddot{s}$, and $\dddot{s}$ are constant.

(3) The optical system is fixed in the satellite and is distortion free.

(4) The three slits intersect in a common point, and the angle between the center slit bisects the angle formed by the outer slits;

then (4) represents the implications of this model and is one equation in the 9 unknowns ξ_1, ξ_2, $\dot{s}_o$, $\ddot{s}$, $\dddot{s}$, s, ϵ, Γ, σ.

The components of $\hat{S}$ and the transit time, t, are measured. If a large number of measurements are taken, an overdetermined system is defined and a "least squares" solution may be sought.

Obtaining a solution is a non-trivial although standard problem and need not be discussed here. Finally, it is noted that ξ_1, ξ_2, s_o, $\dot{s}$, $\ddot{s}$, and $\dddot{s}$ define the attitude of the satellite, and ϵ, Γ, and σ are parasitic parameters which define the orientation of the slits within the satellite.

B. Computer Program

With the absence of both spatial noise and a high incidence of spurious transits, the stellar target identification process would be relatively simple and straight forward. Almost every star detected would appear as a unique triplet of star signals. Time separations of triplet pulses for a given star could be compared unambiguously to known separations of candidate stars, and a matching of triplets to corresponding stars accomplished.

Section C of Chapter 2 describes the nature of spatial noise observed in the SCNS output data. The high incidence of noise necessitated the use of digital filtering techniques which were accomplished with the computer as a part of the ground based data processing.

A program was written to perform the necessary digital filtering and to calculate the attitude parameters. The program utilizes signals from stars which have been identified by the digital filtering process through star transits across known slits.

A program called SCAT[3] determines the three axis attitude of a spinning spacecraft from star transit times obtained from an on-board electro-optical star sensor.

SCAT reads a central crossing time and a measure of the transit width

of transit events obtained from the star sensor and written on tape in FORTRAN-compatible Binary Coded Decimal (BCD) format. It then identifies as many of these transits as possible which originate from a known star and a known instrument slit. The program then uses these identified transits to calculate the four most important attitude parameters, other attitude parameters being set equal to their nominal values.

An earlier program designated BOOTS was designed to accept hand identified star transits in a single data set and obtain an attitude solution on the basis of the identifications. The program then would "bootstrap" through all subsequent sets, identifying stars and computing attitudes. Use of this approach was required whenever there were fewer than three solidly detected star triplets - the minimum number required for automatic identification.

SCAT requires no such hand identification. SCAT solves for the two angles - ξ_1 and ξ_2, which define satellite pointing direction, the initial azimuth position s_o and the spin rate $\dot{s}$. These parameters constitute the four unknowns.

A second fully automatic program, called SCOOT, was designed to accommodate additional unknowns, including the slit parameters ϵ, Γ, and σ and the terms $\ddot{s}$ and $\dddot{s}$, and is essentially an expansion of the program SCAT. SCAT,

---

(3) The acronym SCAT was given to the automatic computer program written to process star data which leads to the solution of the four attitude parameters ξ_1, ξ_2, s_o and $\dot{s}$. The letters used stem from scanning attitude and the fact that the solution is obtained quickly, and is necessary for purposes of program identification.

therefore, is the basic program utilized in the processing of star data.

The sequence from raw data to final attitude consists of the following broad substeps:

1. From the raw data, determine the scan period to within approximately one part in 10^5.

2. Modulo all transit data within a data set consisting of approximately 25 scans with respect to this scan period. In effect, this operation performs a multi-scan correlation on the data.

3. Detect clusters of repeated pulses in the moduloed data. This picks out events which are highly correlated with the scan azimuth and rejects the transits from spurious noise events or from very weakly detectable stars.

4. Search through the detected pulse clusters for triplets of clusters which represent possible transits of a star across the three slits.

5. Compute the separation angles between triplets as these angles are projected on the celestial sphere; match these separations with the separations on known pairs of stars.

6. Link the separation star pairs into a closed spherical polygon, a star pattern as seen on the celestial sphere. If the process is successful to this point, each pulse cluster used in a linked triplet may be identified with the corresponding star and instrument slit.

7. Return to the original data and match these identified stars to the individual transit times in each scan.

8. Perform a least squares attitude solution using these identified transits.

9. Using the period calculated in the attitude solution, remodulo the transit data.

10. Given the above attitude solution, generate transit times for all stars in the field of view for all three slits.

11. Retain moduloed peaks that correspond to generated transit times. This picks up peaks of only one or two slits. Each peak may be identified with the corresponding star and instrument slit.

12. Return to original transit data and keep only measured transits that can be matched within a specified tolerance to one of the identified, remoduloed peaks.

13. Recalculate the four attitude parameters using these identified, measured transits.

These substeps are executed by the main program and various subroutines as shown in the flow chart of Figure 3-4. A description of each of the routines is included below:

SCAT

The program SCAT begins by reading in a star catalog containing a maximum of 460 stars ordered by visual magnitude. For each star the serial number, the general catalog number, right ascension, declination, and magnitude are read in. The direction cosines of each star are calculated and put in the array SDC. The limits on the field of view are calculated from the estimated pointing direction (RA, DE) and only stars brighter than a specified magnitude (XLM) and within the field of view are considered throughout the remainder of the program. The index numbers of these NLS stars in the star catalog are put in the list IAS. The angular separations between these stars are then calculated and put in the array SEP.

A header card for a data set is now read in and the input tape is searched for this data set. The centers and widths of the NTT transits are put in the arrays TTQ and IWD, respectively. A maximum of 4,000 transits is read in.

Pulses from the sun sensor have been written on the tape as having a width of -100. These are now detected and eliminated.

The subrouting PERIOD is now called to determine an estimate of the scan period given estimates of the upper and lower limits of the period and the measured transit times.

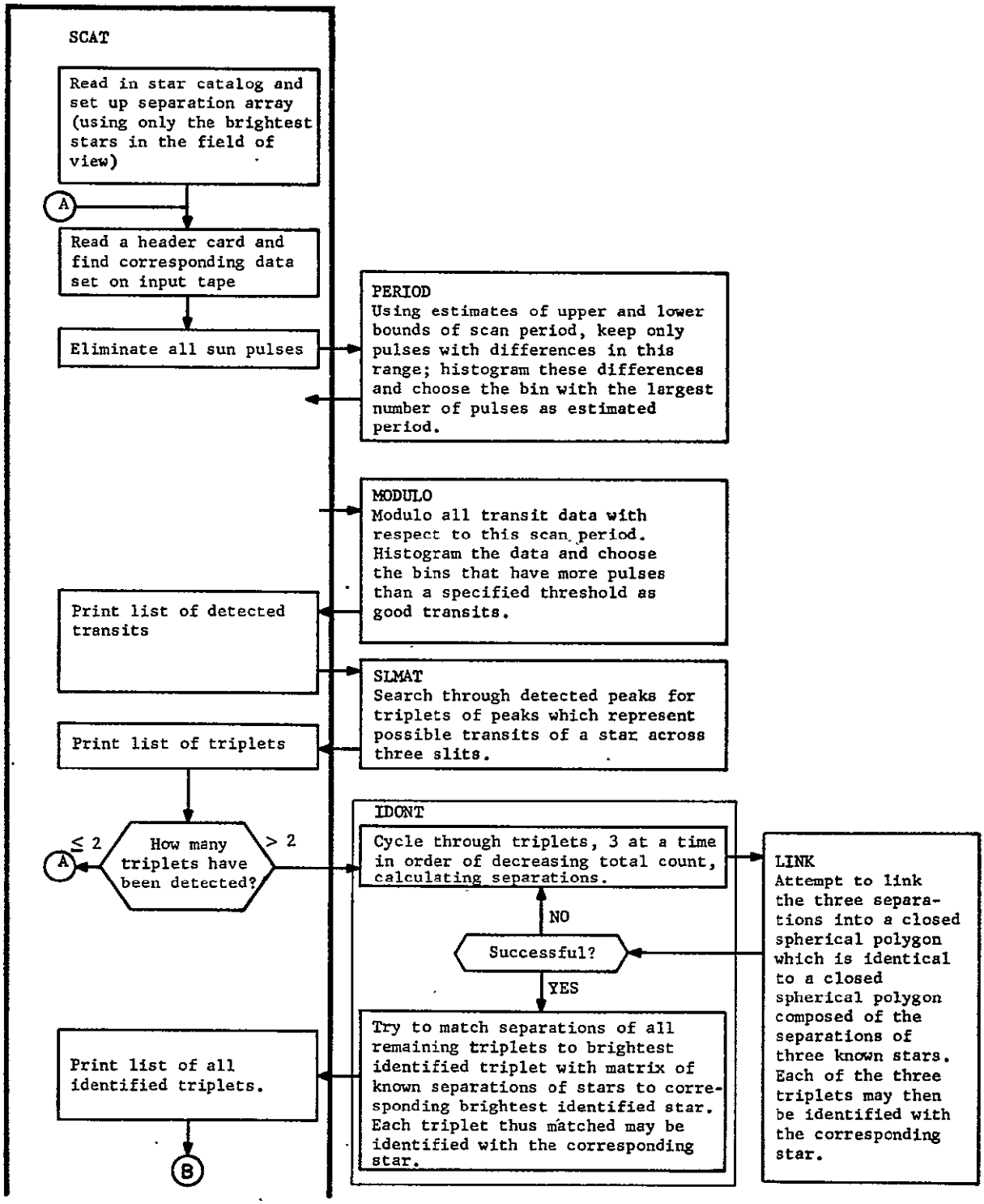

Figure 3-4: Computer Program, SCAT-Flow Chart

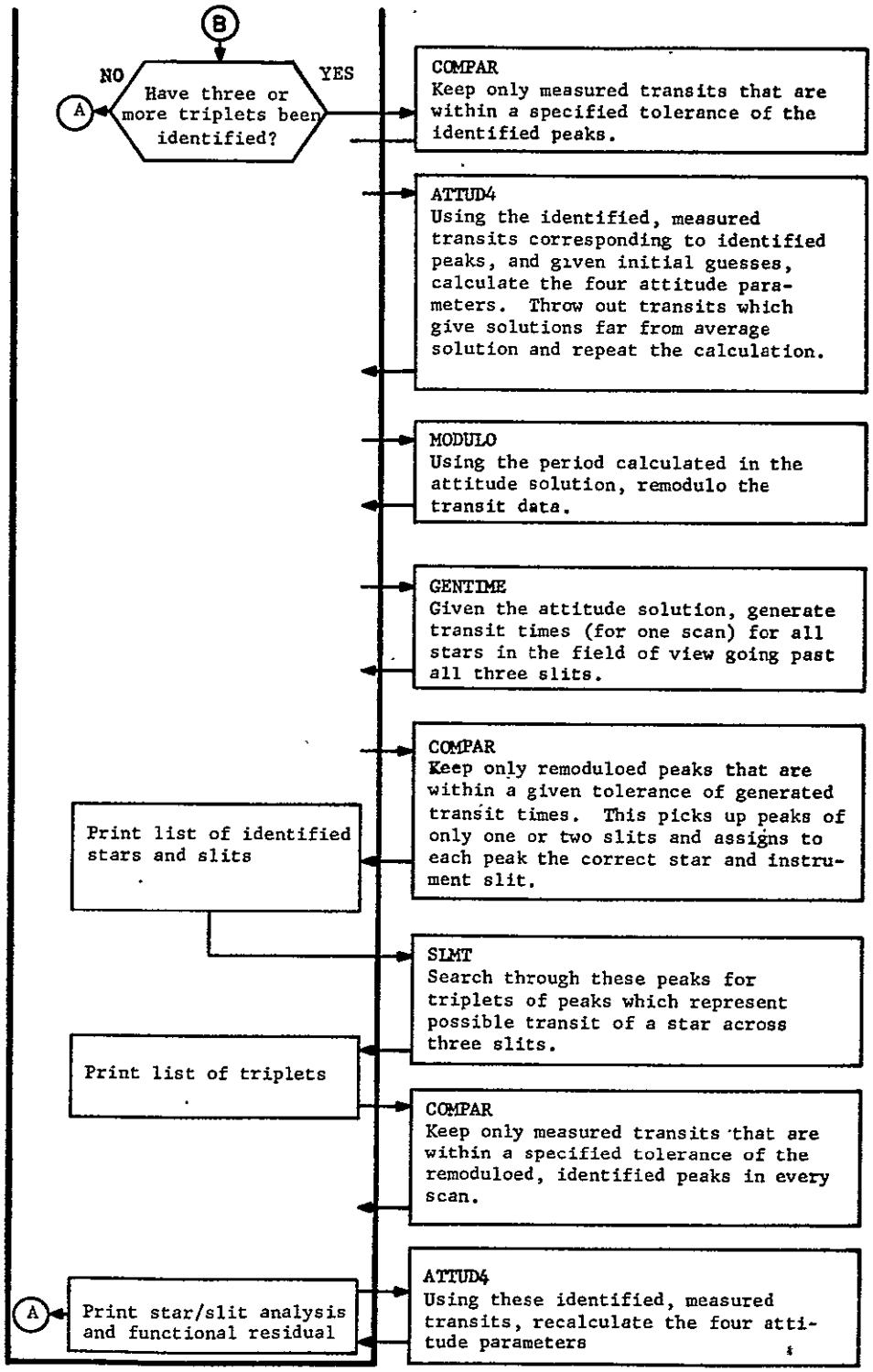

Figure 3-4: (Continued)

All transit data are moduloed with respect to this scan period by subrouting MODULO. The centers of the ITT detected peaks are returned in the array AVTT and the number of transits in each peak in the array NAV.

The subroutine SIMAT is now called to search through the detected peaks and attempt to identify as many as possible as members of triplets of peaks having equal spacing. The centers of the three peaks belonging to each of the NGT identified triplets are returned in the array GT.

If less than three triplets have been detected, the program quits this data set and reads in a new data set.

If at least three triplets have been detected, the subroutine IDONT identifies as many as possible of these triplets with known stars from the catalog. The triplets that have been identified are tagged by setting ID(n) equal to the index of the corresponding catalog star.

The identified triplets are printed with the corresponding star and the unidentified triplets are printed with the comment: "Unidentified triplet". The identified peaks are put in the array TTI and the corresponding star and instrument slit in the arrays MST and MSL, respectively. If no triplets have been identified, the program quits this data set and reads in a new data set.

An estimate of the origin, SO, of the azimuth angle is made using the first identified star crossing the counter slit. The subroutine COMPAR returns to the original transit data, matches the measured transit times to the identified peaks, and retains

only those transit times that are within a specified tolerance of an identified peak. These matched transit times are put in the array TTI and are used by the subroutine ATTUD4 to solve the four unknown problem and calculate the four attitude parameters.

The subroutine MODULO is again called to remodulo the transit data using the period determined by the attitude solution. The ITT detected peaks are put in the array AVTT.

Using the calculated attitude parameters, the subroutine GENTIME generates a transit time for each star in the field of view going past all three slits. These generated transit times are put in the array TTI and are compared with the remoduloed peaks by the subroutine COMPAR. Only those peaks that are within a specified tolerance of the generated transit times are retained. They are stored in the array TTI. This procedure picks up peaks that are not in triplets but originate as the transit of only one or two slits by a star. The corresponding known star and slit are stored in the arrays MST and MSL, respectively.

The subroutine SLMAT again detects as many triplets as possible and these triplets are printed out.

The origin of the azimuth angle is again estimated from the first identified star.

The subroutine COMPAR returns to the original transit times and matches the measured transit times to the identified, remoduloed peaks. Only those transits that are within a specified tolerance of the identified peaks are kept. These are returned in the array TTI and the corresponding stars and slits in the

arrays MSTT and MSLT. These matched transit times are then used by the subroutine ATTUD4 to recalculate the four attitude parameters.

PERIOD

The routine PERIOD uses the raw transit data and estimates of the lower and upper bounds (TMIN, TMAX) of the spin period to determine a reasonable approximation of the period.

The routine cycles through all of the transit times, forming the difference between the transit time and all succeeding transit times. The differences which lie between TMIN and TMAX are stored in the array DT. These differences are sorted into order by the subroutine SORT. The program then cycles through the differences, counting how many fall into each bin of a histogram whose bin width is specified (TP), and lower and upper bounds are TMIN - TP and TMAX + TP.

The mean of the differences in the bin containing the largest number of differences is chosen as the period and the variance is calculated.

MODULO

This routine moduloes all transit times to within one scan period.

The transit data (TT) is cycled through, each transit being moduloed with respect to the period (PER). The moduloed transits are then sorted into order and put into a histogram whose bin width is twice a specified quantity, SW. The lower edges of the overlapping bins begin at intervals of SW and the range of the histogram is from 0 to PER.

The bins that contain more transits than a given threshold are considered to be solidly detectable peaks. The threshold is equal to a specified percentage (THRESH) times the number of effective scans. If more than one acceptable bin are adjacent, only the bin with the largest number of transits is chosen. The mean positions of the transit times in the detected bins are stored in the array AVTT and the number of transits in the corresponding bin is stored in NAV.

SIMAT

The routine SIMAT searches through the detected peaks for triplets of peaks separated by equal spacing. The lower and upper limits of the allowed spacing (HDTMIN and MDTMAX) are equal to the minimum and maximum possible differences of transit times of one star across two slits. Each detected triplet represents a possible transit of a star across the three slits.

The routine overlaps the first few peaks onto the end to make a continuous band in order to detect triplets which overlap the zero mark. The routine then cycles through these peaks (WT), attempting with each peak to find two other peaks which are equally spaced (i.e., equal within the tolerance DT). These spacings must be between HDTMIN and HDTMAX. The positions of the three peaks of the detected triplets are stored in the array GT(N, 3). The number of transits in the detected peaks are stored in NE(N, I, 1), the corresponding identified star in NE(N, I, 2) and the corresponding slit in NE(N, I, 3).

IDONT

The routine IDONT identifies as many triplets as possible with known stars.

The routine assumes that each triplet is the result of

transits of a target star across all three slits. Using the slit parameters (SIG, GAM, EPS), the spin rate (W), and the transit times across the first and third slits (TT(N, 1), TT(N, 3) for each triplet, the direction cosines of the line from the center of the celestial sphere to the target star with respect to the spin axis is calculated for each triplet. These direction cosines are stored in the array U(N, 3).

All of the triplets are now cycled through, three at a time, each time taking the three triplets having the largest total count of transits and not yet used together. For each set the separations (TRIP) of the projections on the celestial sphere of each of the three triplets from each other are calculated from the previously calculated direction cosines of each triplet. The subroutine LINK is now called to attempt to link the separation star pairs into a closed spherical polygon which is identical to a closed spherical polygon composed of the separations of three known stars. If this linkage is successful, the triplets may be identified with the corresponding stars.

If no such linkage is possible for any set of three triplets, the routine returns to the main program.

If a linkage has been established, the remaining triplets are cycled through. For each triplet the separations (Z) between the projection of this triplet and the projections of the first three identified triplets on the celestial sphere are calculated. These are compared to the matrix (SEP) of separations of the known stars with the first three identified stars. If, for a given known star, these separations match within a specified tolerance (ES), the triplet is identified with the corresponding known star.

The indices of the IKK identified triplets are stored in the

array ND and the indices of the corresponding known stars are stored in the array ID.

LINK

The routine LINK attempts to link the three separations of the projections on the celestial sphere of three triplets into a closed spherical polygon which is identical to a closed spherical polygon composed of the separations of three known stars. If this procedure is successful, each of the three triplets may be identified with the corresponding known star.

The matrix (SEP) of the separations of the known stars is searched for all star pairs whose separation is similar to any of the separations (TRIP) of the three triplet pairs. The indices of all star pairs whose separations are within a specified tolerance (E1) of one of the separations of the three triplet pairs are placed in a table ITT, each of whose three columns is headed by one of the triplet pairs. The difference between the separations of the known star and triplet pairs is placed in the table ETT. NIS(J) is the number of entries placed in each column of the table.

The entries of the table are then cycled through and a continuous chain of indices from column one to column two, from column two to column three, and from column three to column one is searched for. If only one such linkage is found, the known star indices can be identified with the corresponding triplets heading the table. If more than one linkage is found, the linkage having the smallest root mean square error is accepted. The indices of the identified stars are stored in the array ID.

COMPAR

The routine COMPAR compares an ordered list (TTC) of transits

or peaks having NC elements with an ordered list (TTM) of transits or peaks having NM elements. Only the elements of TTC which are within a specified tolerance (TOL) of any element of TTM are retained. The NCP retained elements are stored in the array TTM. The subscripts of the star index number (MST) and slit number (MSL) corresponding to a retained element of TTC are adjusted to correspond to the new position of the element in the list TTM.

ATTUD4

The routine ATTUD4 uses the identified, measured transits and initial guesses of the attitude parameters to calculate the attitude parameters. The unknown attitude parameters are: XI1 XI2 which are the pointing angles, S^{o} which is the origin of the $\hat{i}_4$ axis at time t = 0, and SD which is the angular spin rate. The routine solves the basic constraint equation by an iterative scheme. In each iteration the best solution is found by a least square fit of all of the identified transits. The procedure is described in detail in the Feasibility Study Report for Self-Contained Navigation System, pp. 255-257[3].

The routine first calls HMAT to calculate the matrix H which transforms coordinates from the astronomic coordinate system S_1 to the inertial system S_3 whose $\hat{k}_3$ unit vector is parallel to the angular momentum vector.

For each transit the following steps are carried out. The Euler matrix R is calculated by the subroutine RMAT. The matrix R transforms coordinates from the S_3 system to the coordinate system S_4 which is fixed to the spinning body and whose $\hat{k}_4$ unit vector lies parallel to the principal axis of the body. The B matrix which transforms coordinates from the S_4 system to the coordinate system S_{6j} whose $\hat{j}_{6j}$ unit

vector lies perpendicular to the jth slit plane has already been calculated for each slit. The products of the second row of B with the matrix R and with the derivative of R are calculated and stored in B2R and B2RS. The products of the direction cosines (SDC) of the star corresponding to the transit under consideration with the H matrix and its partial derivatives are calculated and stored in HS, H1S, and H2S. These quantities are then used to calculate the various coefficients which are normalized and converted into time units before being stored in the matrix V.

The matrix $\left[(V^TV)^{-1}V^T\right]^T$ is calculated by the subroutine GENINV and the corrections (DX) to the attitude parameters are calculated. After the attitude parameters are updated, the correction terms are compared with the error tolerances (EPS). If any of the correction terms are larger than its corresponding error tolerance, the new attitude parameters are used as input and the calculation is repeated. Up to 50 such iterations are allowed in searching for a converging solution.

After a converging solution has been achieved, the transits with residuals (ATK) greater than twice the RMS residual (SIG) are eliminated and the entire calculation is repeated.

Finally, the standard deviations of the four unknowns are calculated.

GENTIME

Given the spin axis direction (included in the H matrix), the initial azimuth (SO) and the azimuth rate (SD) from the attitude solution, GENTIME generates expected transit times for all of the stars in the field of view (LS) going past all three

slits.

The direction cosines of each star are transformed from the S_1 coordinate system to the S_3 coordinate system. These are stored in the array HS. For each star, the azimuth (S) corresponding to the transit time for each slit is calculated and the transit time corresponding to the azimuth is stored in TTC. The corresponding star index and slit number are stored in the arrays MTX and MLX, respectively.

These generated transits are sorted in order of occurence. All transit pairs which are closer together than the rotational slit width (ROTSW) may lead to ambiguous transits since the transits would overlap. The generated transits are searched for such pairs. They are then printed out as having possible transit time conflicts.

GENINV

The routine GENINV takes the matrix A, which has NR rows and NC columns and calculates the matrix A', the generalized inverse of A. The transpose of A' is stored in A and is returned to the calling program.

B2VEC

The B matrix transforms coordinates from the S_4 system, in which the $\hat{k}_4$ unit vector is parallel to the spin axis, to the S_{6j} system in which the $\hat{j}_{6j}$ unit vector is normal to the slit plane. For each slit there will be a separate B matrix. Since the component of a detected star's direction along the $\hat{j}_{6j}$ axis will

always equal to zero, the easiest set of equations to solve will involve only the second row of the B matrix. These equations will be

$$0 = B_2 \hat{S}_6 ,$$

where B_2 is the second row of B. For each slit the elements of the second row are

$$- \sin \rho \cos \sigma, \cos \rho, \sin \rho \sin \sigma,$$

where ρ and σ are the slit parameters.

The routine B2VEC calculates the second row of the B matrix for each slit and stores the results in the array B2(3, 3).

HMAT

Given the angles XI1 and XI2, the routine HMAT calculates the elements of the matrix H and the partial derivatives (HP(1, N, N), HP(2, N, N)) of these elements. The matrix H transforms coordinates from the astronomic coordinate system $\hat{S}_1$ to the inertial system $\hat{S}_3$ whose $\hat{k}_3$ unit vector is parallel to the angular momentum vector. The elements of the matrix are

$$H = \begin{pmatrix} \cos \xi_2 & \sin \xi_1 \sin \xi_2 & -\cos \xi_1 \sin \xi_2 \\ 0 & \cos \xi_1 & \sin \xi_1 \\ \sin \xi_2 & -\sin \xi_1 \cos \xi_2 & \cos \xi_1 \cos \xi_2 \end{pmatrix} .$$

RMAT

Given the angle SPF, the routine RMAT calculates the elements of the Euler matrix R and the partial derivatives (RP0) of these elements. The matrix R transforms coordinates from the inertial

system $\hat{S}_3$, whose $\hat{k}_3$ unit vector is parallel to the angular momentum vector, to the coordinate system $\hat{S}_6$, which is fixed in the spinning body and whose $\hat{k}_4$ unit vector lies parallel to the principal axis of the body. The elements of $\bar{R}$ are

$$R = \begin{pmatrix} \cos\beta & \sin\beta & 0 \\ -\sin\beta & \cos\beta & 0 \\ 0 & 0 & 1 \end{pmatrix}$$

where β is the azimuth angle SPF.

SORT

The routine SORT (or MORT) sorts the N elements of the list $\bar{X}$ from the smallest to largest (algebraically) and returns the list in the array X to the calling routine. The list KEY, which is also returned, contains the position in the original list of each element in the new list.

A dictionary of selected variables used in SCAT is included as Table I. A listing of parameters which must be specified at the beginning of the program along with typical values for each (shown in parentheses) is included as Table II.

The first input to the program is a star catalog containing a maximum of 460 stars -- one card for each star. The cards are read in with the format (I3, I7, 2F20.13, F10.2). Each card contains the following information for one star: serial number of the star, general catalog number, right ascension in radians, declination in radians and magnitude.

For each data set on the input tape for which an attitude determination is desired, a header card is read in. The header card contains the data set number and a comment. The header cards are read in with the format (I5, 1X, I3, 31X, 5A8). The last such card should be a blank card.

TABLE 3-I

DICTIONARY OF SELECTED VARIABLES IN SCAT

SDC(N, 3)	direction cosines of catalog stars
SEP(N, N)	separation matrix of catalog stars
IAS(N)	list of indices of stars in catalog that are in field of view
NLS	number of stars in catalog that are in field of view
TTQ(N)	center of measured transit
IWD(N)	width of measured transit
NTT	number of measured transits
AVTT(N)	average of transit times in N^{th} good moduloed peak
NAV(N)	number of transits in N^{th} good peak
ITT	number of good peaks
GT(N, 3)	positions of peaks of N^{th} triplet
NGT	number of triplets
ID(N)	index of corresponding catalog star for N^{th} identified triplet
TTI(N)	position of N^{th} identified peak or transit
MST(N)	star corresponding to N^{th} identified peak or transit
NSL(N)	slit corresponding to N^{th} identified peak or transit
NLP	number of matched peaks or transits
PER	period
SD	spin rate
SO	origin of $\hat{i}_4$ axis at time t = 0
XI1	pointing angle of angular momentum vector
XI2	pointing angle of angular momentum vector

TABLE 3-II

LISTING OF SCAT PARAMETERS

TO BE SPECIFIED

NS	number of last catalog star to be read in (460)
XLM	magnitude of faintest catalog star desired in list IAS (4)
MAXWD	maximum allowed width for acceptance of transit (1000)
TOL2	tolerance for comparing identified with measured transit times (0.000110)
TOL3	final tolerance in slit matching to obtain triplets (0.000220)
GAP	if difference between two consecutive transit times are greater than this quantity, a writing gap is assumed to have occurred (1.200)
TGAP	actual length of writing gap (1.260)
PERSLT	bin size for determination of scan period (0.000050)
HDTMIN	minimum peak-to-peak separation for triplet search (0.012000)
HDTMAX	maximum peak-to-peak separation for triplet search (0.012000)
THRESH	threshold of relative count frequency for detection of repeatable triplets (0.30)
EID	tolerance in degrees for comparing the separation of measured triplets with star separations (0.20)
TMIN	minimum limit on the scan period (0.564800)
TMAX	maximum limit on the scan period (0.565800)
SW	bin width for selection of repeatable transits (0.000110)
XLD XHD	limits (in degrees) of field of view (50.0 and 80.0)
XI1D XI2D	initial angles of rotation involved in transformation from S_1 system to S_3 system (180.0 and 0.0)
RAD	right ascension (in degrees) of initial pointing direction of angular momentum vector (135.0)
DED	declination (in degrees) of initial pointing direction of angular momentum vector (-89.5)
SIGMAD CGAMD EPSD	slit parameters in degrees (84.43651, -11.08676, 0.91898)
ROTSW	rotational slit width in arc minutes (7.6)

The data is written on the input tape in data sets consisting of all the transits in approximately 25 scans. For each data set, the first record contains the data set number, the number of transits in the set, and the starting time of the set in hours, minutes, and seconds in the format (6X, I3, I6, 2I5, F12.6). The next records contain the list of transit times and transit widths -- eight transits per record. The records are written on the tape with the format (8(F10.6, I5). The widths of the transits corresponding to sun pulses have been written on the tape as -100.

II. ATTITUDE DETERMINATION

The numerical results of satellite attitudes are documented within this section. The results were obtained from data acquired at various times between 13 March and 4 October 1968.

Figure 3-5 illustrates the geometric relationship between the SCNS field of view and sources of bright object interference. The effectiveness of the instrument field of view was influenced by bright object constraints when, under certain conditions, the number of solidly detected targets was reduced thereby affecting the accuracy of the attitude solution. The field of view was further affected by the loss of sensitivity for off-axis sources -- a condition brought about by the nature of the optical system. This was discussed in Section I of Chapter 1.

A. Precessional Motion Model

On Day 73 (13 March 1968) the satellite was in the earth's eclipse for approximately one hour. During that interval star sensor measurements were acquired which utilized a mathematical model based upon the following assumptions:

(1) The satellite is torque free, rigid, and nearly symmetric.

(2) The angular momentum of the satellite is nearly parallel to the principal axis of largest moment of inertia.

For reasons to be explained later, this model was applied to Day 73 data only. The model, termed the Precessional Motion Model, considers precession of the satellite principal axis about the angular momentum vector.

The results from measurements taken over an interval of approximately 13 seconds are shown in Table 3-III. All angles listed in the table are measured in degrees and all rates are in degrees/seconds. Figure 3-6 is included as an aid in understanding the notations used in Table 3-III. In each of the distinct cases shown in Table 3-III no star dimmer than magnitude 2.2 was utilized. If all measurements were perfect, these cases would yield

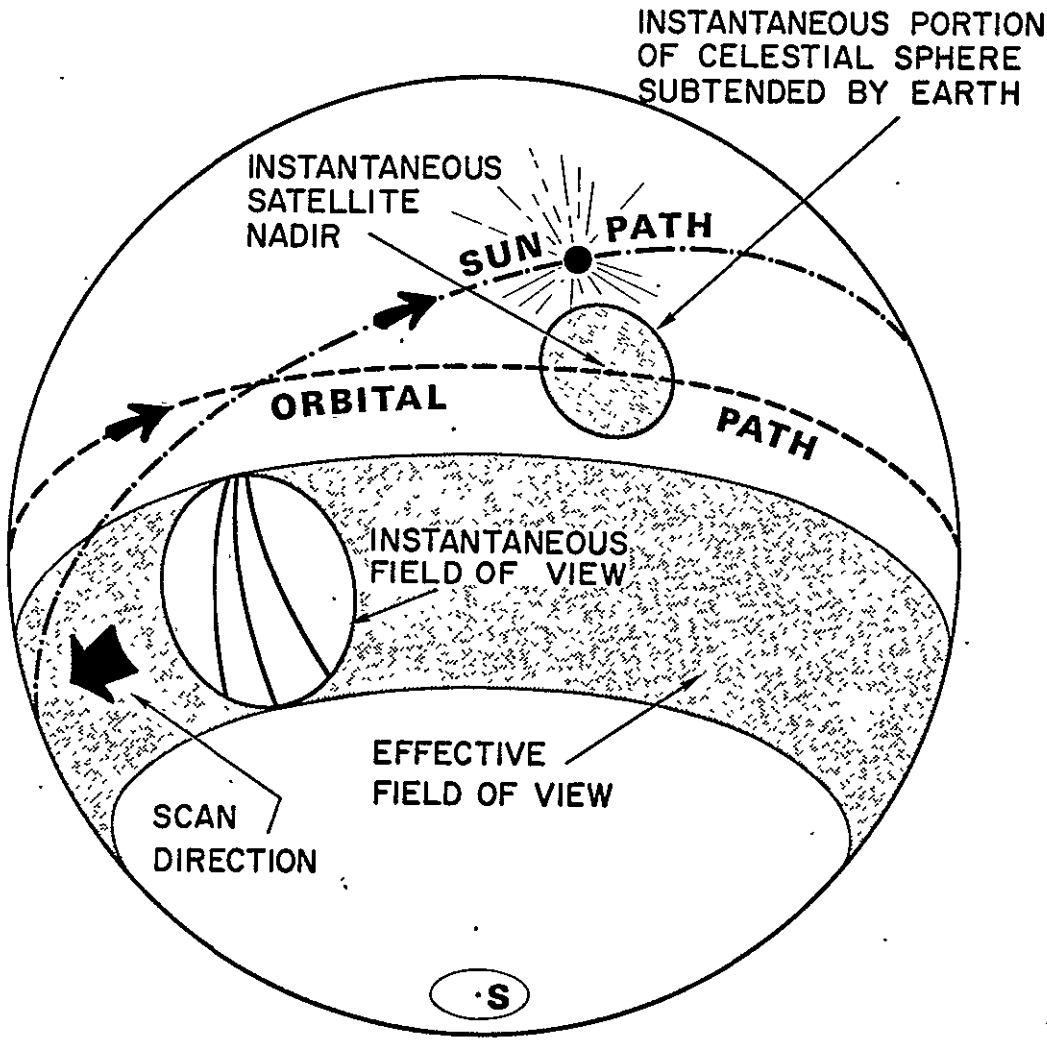

Figure 3-5: Geometric Relationship of the SCNS Field of View

TABLE 3-III

SOLUTION FOR PRECESSION MODEL (DAY 73 DATA, 10 UNKNOWNS)

Half Cone (Nutation) Angle; Initial Spin Angle; Spin Rate; Initial Precession; Precession Rate; Angles Which Define Direction of Angular Momentum; Angles Which Define Location of Slits; Right Ascension and Declination of Angular Momentum Vector

Case No.	θ	ψ_o	$\dot{\psi}$	ϕ_o	$\dot{\phi}$	ξ_1	ξ_2	σ	Γ	ϵ	α	δ
1	.040	-15.656	-11.222	252.672	587.328	180.224	.094	84.264	-11.155	.185	67.36	-89.757
2	.008	-68.720	-21.935	-54.255	598.042	180.197	.093	84.272	-11.057	.192	64.81	-89.782
3**	.005	106.187	-22.589	117.065	598.595	180.202	.105	84.373	-11.122	.186	62.42	-89.772
4*	.003	51.419	-18.211	185.589	594.318	180.213	.093	84.294	-11.170	.186	66.53	-89.768
5**	.003	104.132	-22.445	119.117	594.451	180.197	.119	84.391	-11.114	.184	60.43	-89.773
6	.017	-186.766	-13.423	48.939	589.435	180.200	.111	84.401	-11.105	.184	61.07	-89.771

*, ** Indicate cases which had common initial times

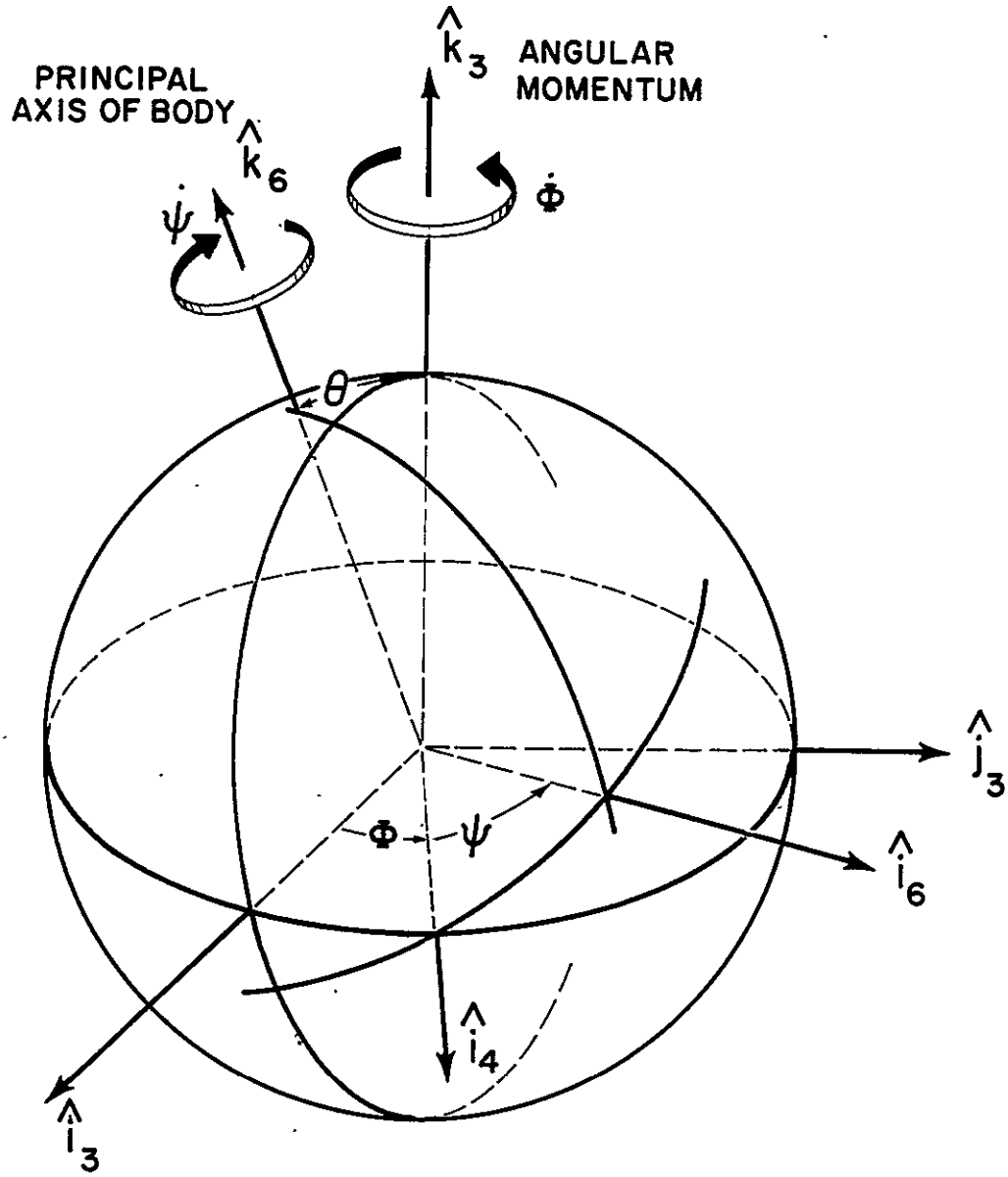

$\hat{i}_3, \hat{j}_3, \hat{k}_3$ — INERTIA SYSTEM WITH $\hat{k}_3$ IN DIRECTION OF ANGULAR MOMENTUM OF SATELLITE.

$\hat{i}_6, \hat{j}_6, \hat{k}_6$ — BODY FIXED SYSTEM WITH $\hat{k}_6$ IN DIRECTION OF PRINCIPAL AXIS OF GREATEST MOMENT.

Figure 3-6: Relationship of Body-Fixed Reference System to Angular Momentum Frame

the same values for 8 of the unknowns. The values of ψ_o and Φ_o, however, would vary because not all cases shared a common initial time. The initial time was the same for Cases 2, 4 and 3, 5. Thus, except for the effect of errors, Cases 2 and 4 would process a common ψ_o and a common Φ_o. This is also true for Cases 3 and 5. In Table 3-IV the six cases are briefly described.

TABLE 3-IV

DESCRIPTION OF CASES LISTED IN TABLE 3-III

Case No.	Number of Stellar Targets Used[4]	Time Interval (sec)		Comments
		Begin	End	
1	3	.888455	13.989168	Cases 1 and 2 utilize the same stars, but no common transit times.
2	3	.263583	13.364247	
3	6	.265618	13.421220	Uses all point sources reliabily detected.
4	4	.263583	13.989168	Same as Case 2 except Mercury used.
5	5	.265618	13.417741	Same as Case 3 except Mercury not used.
6	6	.267434	14.044438	Cases 3 and 6 utilize same stars, but no common transits

Table 3-III indicates an extremely small cone angle. Also the angular momentum vector of the satellite points very close to the celestial South Pole. In addition, the variation of the angles θ, ξ_1, ξ_2, σ, Γ, and ϵ is about one minute of arc.

For small θ, the angles Φ and ψ are poorly defined, and only their sum is important. The variations of ψ_o in Cases 2 and 4 implies that the measurement of θ is in the noise, (i.e. the error in the determination of θ is about the size of θ itself).

(4) Venus and Mercury are included as potential targets.

From $\dot{\psi}$, $\dot{\Phi}$, and θ it is possible to determine the ratio of the largest to the smallest moment of inertia

$$\frac{A}{C} = \frac{\dot{\Phi} \cos \theta}{\dot{\psi} + \dot{\Phi} \cos \theta} \tag{5}$$

For each of the six cases, $1.023 \leq A/C \leq 1.040$.

Since the angle θ is extremely small, the precession model was abandoned in favor of a model which assumes $\theta \equiv 0$ (i.e. the satellite is assumed to rotate about a fixed axis). However, if θ were about two minutes of arc or larger, the instrument accuracy is sufficient to justify the use of the precession model.

This assumption of a fixed axis of spin is valid because the spacecraft contains a precession and nutation damper which apparently restricts the angle between the satellite principal axis and angular momentum vector to less than one minute of arc.

B. Fixed Spin Axis Model

The assumption of a fixed spin axis formulates the mathematical model in terms of eight unknowns. The eight unknown problem includes a spin acceleration term, $\ddot{s}$, introduced by the fact that the satellite, in passing from full sunlight into earth's shadow cools. This cooling causes physical shrinkage of the satellite with the consequence that the spin velocity increases to conserve momentum. Therefore the velocity term is not a constant.

The following terms define the eight unknowns of the model:

s_o - initial position of $\hat{i}_3$ body axis
$\dot{s}$ - spin rate
$\ddot{s}$ - spin acceleration

ξ_1, ξ_2 } angles which define direction of spin axis with respect to celestial sphere

σ, Γ, ϵ } angles which define location of slits with respect to body axis

Attitude solutions obtained from data taken on Days 73, 95, 96 and 97 is presented in Table 3-V which lists the derived values of the eight unknowns: $\dot{s}$ is in degrees/second, $\ddot{s}$ is in degrees/second^2, and all other angles are expressed in degrees. α and δ the right ascension and declination, respectively, of the spin axis are listed as are the number of transits used; Σ, the RMS value of the residuals (in seconds x 10^{-6}); and the duration of time over which the transits were gathered (in seconds). The three solutions obtained for Day 97 result from three distinct sets of transit times with a common interval of time. A spacecraft maneuver was performed on 22 March, thereby explaining the relatively large change in attitude observed between Days 73 and 95. Also shown in Table 3-V are estimates of the standard deviation of the eight unknowns which were obtained from the residuals of the final solution.

Let $\overline{\xi_1}$ = maximum value of ξ_1 from the three values of ξ_1 obtained from Day 97

$\underline{\xi_1}$ = minimum value

$\tilde{\xi}_1 = \overline{\xi_1} - \underline{\xi_1}$

Using similar definitions for other variables, we obtain

$\tilde{\xi}_1$ = 21.6 sec = $\tilde{\delta}$

$\tilde{\xi}$ = 14.4 sec

$\tilde{\ddot{s}}$ = .03 sec/sec^2

$\tilde{\Gamma}$ = 95.4 sec

$\tilde{\epsilon}$ = 36 sec

$\tilde{\sigma}$ = 1,584 sec

$\tilde{\alpha}$ = 11,736 sec

TABLE 3-V

SUMMARY OF ATTITUDE RESULTS FROM DATA TAKEN ON DAYS 73, 95, 96 AND 97

Day	ξ_1	ξ_2	s_o	$\dot{s}$	$\ddot{s}$	Γ	ϵ	σ	α	δ	No. of Transit	Σ	Duration
73	180.221	.121	256.694	575.9005	.00012	-11.1688	.193	84.280	61.277	-89.748	444	31.8	104
95	180.443	.090	126.143	576.1102	.00018	-11.0943	.196	84.410	78.508	-89.548	1101	27.9	73
96	180.441	.089	47.497	576.3982	.00010	-11.0834	.220	84.436	78.548	-89.550	867	34.9	84
97	180.457	.090	126.640	576.2715	.00013	-11.1117	.227	84.368	78.899	-89.534	565	29.0	100
97	180.463	.086	197.649	576.2735	.00014	-11.1241	.219	84.348	79.424	-89.529	611	29.2	74
97	180.457	.087	-233.360	576.2715	.00013	-11.0976	.229	84.392	79.225	-89.535	744	28.8	99

Day	$\sigma(\xi_1)$	$\sigma(\xi_2)$	$\sigma(s_o)$	$\sigma(\dot{s})$	$\sigma(\ddot{s})$	$\sigma(\Gamma)$	$\sigma(\epsilon)$	$\sigma(\sigma)$
73	13.08	8.63	9.44	.446	.0078	32.26	29.33	54.17
95	5.90	4.67	8.76	.328	.0086	22.85	18.70	44.63
96	10.78	5.68	11.92	.391	.0089	35.15	26.65	67.26
97	8.62	6.38	12.00	.274	.0054	34.12	27.88	69.45
97	8.31	6.17	11.93	.400	.0105	32.36	26.48	66.09
97	7.52	5.53	10.53	.257	.0051	28.94	23.79	58.92

Σ -- measured in microseconds

Duration -- in seconds

Standard deviations -- in seconds of arc

Note that all parameters are quite accurately determined except for σ (angle which determines the position of the slit concurrence) and α (right ascension of the spin direction). The right ascension, α, is poorly determined because the spin axis lies close to the South Pole, and σ is poorly determined because the angle between the center slit and the outer slit is a relatively small angle ($11^{\circ}.1020$).

In Figure 3-7, the computed direction of the satellite spin axis is plotted as a function of time for Day 201 (19 July), (the day on which the second probe was ejected). The satellite on that day was in full sunlight over its entire orbit. The results shown in Figure 3-7 were derived using much poorer stellar geometry than that used to derive the results of Days 73, 95, 96 and 97. Poor geometry has a dual cause: (1) Direct blocking due to the sun's interference and (2) blocking due to sun's reflections off the launch mechanism arm used to eject the first and second probes. Only three stars were regularly detected. This fact led to solutions having a standard deviation of about 1.5 minutes of arc for the direction. Therefore, it is probably not permissible to interpret the variations of the spin direction given in Figure 3-7 as real. These variations are almost entirely due to errors in the transit times.

In obtaining the results shown it is assumed that the satellite spins uniformly about a fixed axis, and that the parameters which characterize the slits are fixed so that $\Gamma = -11.087^{\circ}$, $\epsilon = .199^{\circ}$, $\sigma = 84.437^{\circ}$.

Figure 3-8 is similar to Figure 3-7 except that the time interval is extended over 28 days. Note, however, that α and θ are much smoother in Figure 3-8 due to the improved stellar geometry on Days 249 to 277. On Day 201 only three stars were regularly detected. On Days 249 - 277 when the satellite was in the earth's shadow, eight stars were regularly detected.

The results of Figure 3-8 indicate a systematic increase with time for both the right ascension and declination of the spin axis. This increase

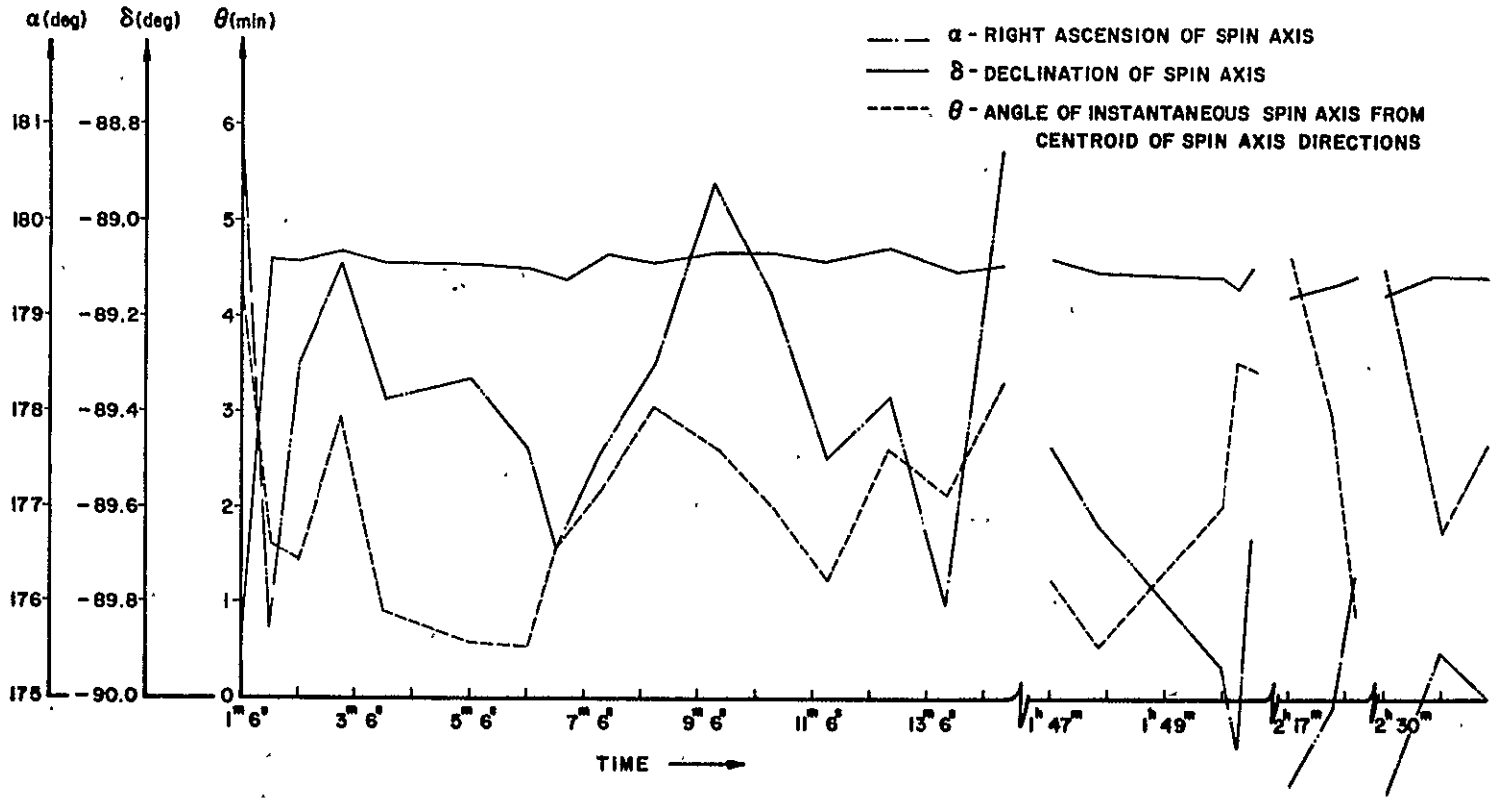

Figure 3-7: Direction of Satellite Spin Axis as a Function of Time on Day 201

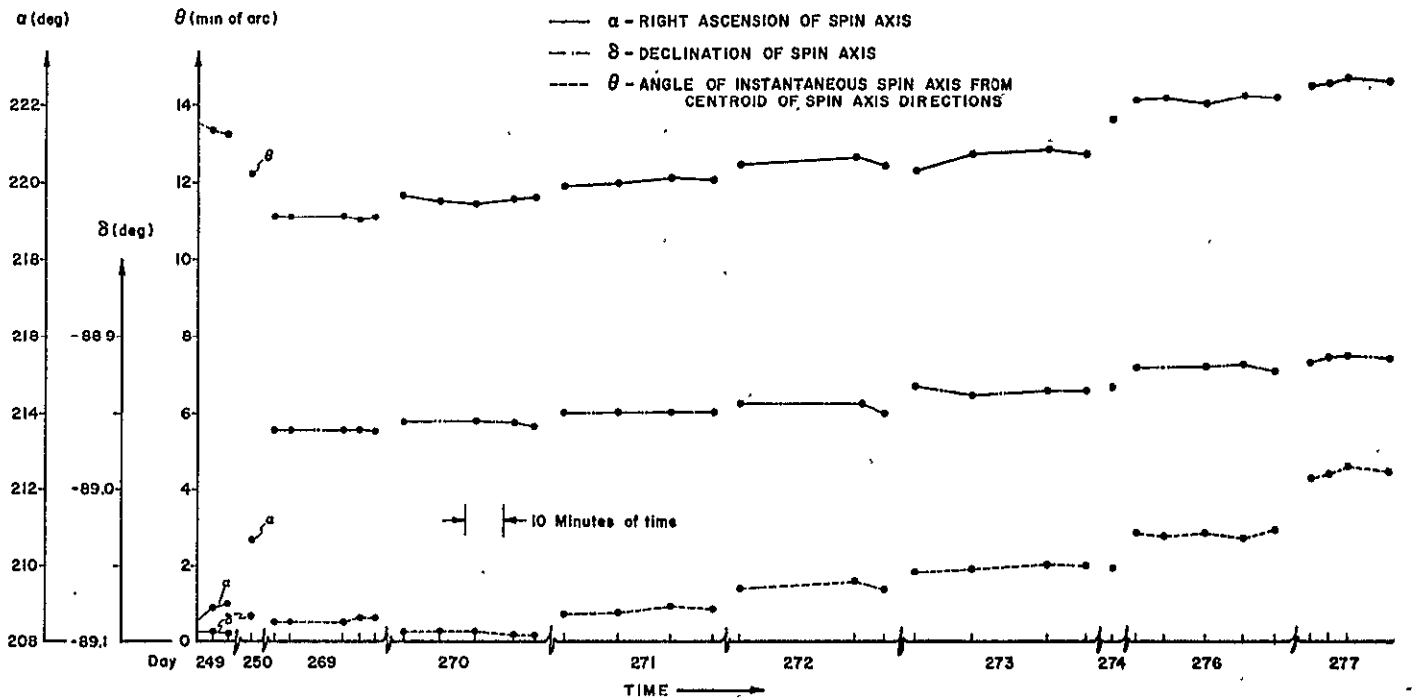

Figure 3-8: Direction of Satellite Spin Axis as a Function of Time on Days 249 to 277

is small but real. Note that the direction of the spin axis varies by less than 14 minutes of arc from its centroid in the 28 day interval. These small changes are the effect of torques acting on the satellite, due most probably to magnetic and gravitational effects.

Table 3-VI provides a detailed tabulation of the computed spacecraft attitudes from Day 249 to 277.

C. Slit Parameters

The slit parameters σ, ϵ, and Γ defined in Figure 3-3 represent parasitic unknowns in the attitude problem. A shift in the spin axis relative to the star sensor will change either ϵ, σ, or both; but such a shift will not affect Γ. This is because ϵ and σ define the orientation of the sensor with respect to the satellite spin axis, but Γ does not. The slit separation, Γ, depends only on the mask on which the slits were etched and the location of this mask with respect to the instrument's optical axis. Unless the SCNS instrument undergoes significant internal displacements, Γ will be independent of time. However, ϵ and σ may very well be time dependent for the spacecraft is not a rigid body.

A means of measuring Γ independently (from that of treating it as an unknown in the attitude problem) exits. Γ was therefore obtained by measuring the angle between the slits on the mask and the location of the mask with respect to the optical system of the instrument. The resultant value for Γ was $-11.^{\circ}102 \pm .02^{\circ}$ which is in good agreement with values obtained from the stellar transits.

It should be recognized that ϵ and σ were not measured by an independent means, due to the difficulty of accurately measuring the orientation of the SCNS instrument with respect to the satellite spin axis. A further discussion relative to slit characterization is included as Appendix D.

All results after Day 201, except for Day 263, were obtained by assuming

TABLE 3-VI

ATTITUDE AND SLIT PARAMETERS OBTAINED FROM DAY 249 to 277

DAY	h	m	s	ξ_1	ξ_2	s_o	$\dot{s}$	$\ddot{s} \times 10^3$	$\dddot{s} \times 10^8$	ϵ	σ
249	3	1	52.	179.55261	-.78828	-258.37690	636.76887	.201162	-7.28640	.35356	84.21268
	3	5	46.	179.54909	-.78427	-289.09922	636.81403	.183327	-5.42379	.37506	84.20182
	3	9	39.	179.54789	-.78369	-226.55999	636.85543	.167515	-2.99884	.39733	84.20899
250	2	56	52.	179.53187	-.78772	-152.86261	636.72988	.210150	-6.44431	.40470	84.19895
269	2	55	26.	179.34523	-.80512	-96.22028	636.94307	.136820	.223200	.38259	84.20411
	2	59	59.	179.34562	-.80565	-85.69124	636.97998	.128174	-.855446	.38844	84.20344
	3	13	57.	179.34508	-.80512	-133.11407	637.08027	.109005	-.828800	.36724	84.20235
	3	18	9.	179.34644	-.80588	-145.44161	637.10730	.107780	-3.57838	.37354	84.20657
	3	22	14.	179.34659	-.80503	-290.99994	637.13277	.101684	-1.22416	.37648	84.20403
270	2	46	17.	179.33416	-.80336	-350.14623	636.86344	.153739	11.7902	.39458	84.18103
	2	56	1.	179.33638	-.80491	-275.72152	636.95077	.142589	-8.02144	.38864	84.18266
	3	6	0.	179.33779	-.80517	-318.43541	637.02830	.118495	-1.38603	.39836	84.17786
	3	16	0.	179.33597	-.80331	-40.52580	637.09696	.104282	.244014	.39144	84.17348
	3	21	0.	179.33620	-.80239	-66.69590	637.12852	.102382	-1.17487	.38537	84.17294
271	2	39	2.	179.32657	-.80536	-322.55184	636.77110	.193076	-10.3370	.41091	84.18262
	2	53	10.	179.32573	-.80398	-278.37814	636.91178	.143635	-2.36739	.41751	84.18034
	3	7	0.	179.32328	-.80266	-74.80117	637.02107	.122294	-4.03589	.41989	84.18037
	3	18	0.	179.32422	-.80366	-95.73663	637.09574	.106830	-1.75402	.40270	84.18009
272	2	40	2.	179.31560	-.80302	-274.08844	636.79835	.184237	-6.80615	.42820	84.17452
	3	10	38.	179.31256	-.79986	-135.73530	637.05952	.113796	-2.20786	.42118	84.17376
	3	18	2.	179.31566	-.80294	-230.36006	637.10804	.106853	-2.39279	.44390	84.17316
273	2	31	2.	179.31157	-.81410	-356.79356	636.67081	.233408	-11.0348	.47958	84.18827
	2	45	59.	179.30732	-.80427	-140.35696	636.84500	.166588	-8.41468	.44847	84.17956
	3	6	0.	179.30527	-.80423	-183.38722	637.01312	.121298	-2.98056	.44243	84.17376
	3	16	0.	179.30711	-.80546	-274.54730	637.08176	.108437	-1.87672	.43239	84.17511
274	3	14	47.	179.29267	-.79744	-134.57631	637.07120	.104404	4.70085	.43263	84.16640
276	2	37	47.	179.27728	-.80025	-8.33732	636.72993	.200037	-8.15586	.38674	84.18593
	2	45	0.	179.27690	-.79926	-46.58335	636.80956	.170455	-5.70767	.35590	84.17783
	2	56	0.	179.27918	-.80086	-197.61615	636.91136	.140322	-2.70504	.35141	84.18361
	3	7	0.	179.27557	-.79927	-286.99748	636.99751	.119918	-1.67184	.36614	84.17696
	3	14	45.	179.27959	-.79721	-350.48496	637.05142	.105532	3.86296	.35768	84.17520
277	2	55	2.	179.27051	-.79829	-23.76617	636.88593	.145909	-3.44978	.41227	84.21091
	3	0	2.	179.26881	-.79821	-111.58610	636.92806	.136487	-3.76851	.38781	84.21330
	3	10	0.	179.26610	-.79719	-85.40157	637.00392	.119686	-2.46531	.41452	84.20792
	3	15	31.	179.26769	-.79795	-190.69802	637.04229	.111618	-1.39404	.41346	84.21500

$\Gamma = -11.102^{\circ}$. Day 263 data was reduced by assuming Γ to be unknown, and a result of $\Gamma = -11.092^{\circ}$ was obtained.

D. Attitude as a Function of Time

Table 3-VII presents a summary of the attitude parameters for each day in which measurements were taken. Except for Days 132, 133, 134, and 135 a solution was obtained for each day on which measurements were made. No solutions were possible on these days because of the unfavorable position of the sun. For these four days, a computer program could not obtain a star identification.

The values shown in Table 3-VII represent average values of parameters for each day shown. Horizontal lines are used to separate groups of days over which no spacecraft maneuvers were performed. Thus, no maneuvers were present from Day 95 to Day 97, resulting in a relatively fixed direction for the spin axis.

Note that ϵ shows a strong tendency to increase with each maneuver. An explanation for that behavior is as follows: The sensor is fixed with respect to the figure axis of the satellite, but the spin axis of the satellite will very nearly coincide with the principal axis of greater moment of inertia. Hence, as the satellite looses mass, the spin axis may change slightly with respect to the satellite's figure axis. This change will affect ϵ and/or σ. No systematic change in σ with time is noted. However, the error in σ is probably two or three times greater than the error in ϵ (listed in Table VIII). This results because σ defines the position of the common intersection of the three slits, and this intersection is somewhat poorly defined because $|\Gamma|$ is small compared to 90°.

From Day 249 to Day 277 a non zero $\ddot{s}$ and $\dddot{s}$ were assumed because the satellite was in the earth's eclipse when the measurements were taken. Table 3-VII lists the computed $\ddot{s}$ as always being positive and the computed $\dddot{s}$

TABLE 3-VII

ATTITUDE PARAMETERS AS A FUNCTION OF TIME

Day	ξ_1	ξ_2	$\dot{s}$	$\ddot{s} \times 10^4$	$\dddot{s} \times 10^{-8}$	Γ	ϵ	σ	α	δ
73e	180.221	.121	575.9005	1.2	0*	-11.1688	.193	84.280	61.277	-89.748
95e	180.443	.090	576.1102	1.8	0*	-11.0943	.196	84.410	78.508	-89.548
96e	180.441	.089	576.3982	1.0	0*	-11.0834	.220	84.436	78.548	-89.550
97e	180.460	.088	576.2735	1.3	0*	-11.1111	.223	84.369	79.283	-89.533
131	180.180	-.070	576.8571	0*	0*	-11.087*	.199*	84.437*		
132	No solution was obtained for these four days because of the unfavorable position of the sun.									
133										
134										
135										
151	180.829	-.217	558.765	0*	0*	-11.101	.230	84.453	104.67	-89.142
171	180.708	-.731	597.150	0*	0*	-11.087*	.199*	84.437*	135.92	-88.981
193	180.686	-.617	597.891	0*	0*	-11.087*	.199*	84.437*	131.97	-89.076
201	180.051	-.878	598.923	0*	0*	-11.087*	.199*	84.437*	176.68	-89.119
249e	179.550	-.785	636.8128	1.8	-5.2	-11.102*	.375	84.208	209.82	-89.094
250e	179.532	-.788	636.7299	2.1	-6.4	-11.102*	.405	84.199	210.70	-89.082
263e	179.403	-.805	637.0817	1.1	0*	-11.092	.458	84.213	216.56	-88.997
269e	179.346	-.805	637.0487	1.0	-1.2	-11.102*	.378	84.204	219.09	-88.962
270e	179.336	-.804	637.0136	1.2	1.6	-11.102*	.392	84.178	219.45	-88.956
271e	179.324	-.804	637.7599	1.1	-3.7	-11.102*	.410	84.181	220.06	-88.948
272e	179.315	-.802	636.9886	1.3	-3.8	-11.102*	.431	84.173	220.50	-88.944
273e	179.306	-.806	636.9027	1.6	-6.1	-11.102*	.451	84.179	220.73	-88.935
274e	179.293	-.797	637.0712	1.0	4.7	-11.102*	.433	84.166	221.57	-88.934
276e	179.278	-.799	636.9226	1.1	-4.4	-11.102*	.364	84.178	222.10	-88.922
277e	179.268	-.798	636.9651	1.2	-2.8	-11.102*	.407	84.212	222.53	-88.916
278e	179.263	-.770	636.9112	0*	0*	-11.094*	.460*	84.212*	223.73	-88.933

* Fixed value. e Indicates the satellite was eclipsed when the measurements were taken.

as usually negative. This result is theoretically possible as may be seen from the following simple argument: Assume the satellite is spinning about a fixed axis, then

$$L_o = C\,\dot{s},\ \dot{s} > 0$$

where L_o = the satellite angular momentum

C = the moment of inertia about the spin axis

but, $0 = \dot{C}\,\dot{s} + C\,\ddot{s}$

$$0 = \ddot{C}\,\dot{s} + 2\,\dot{C}\,\ddot{s} + C\,\dddot{s}$$

since $\dot{d} = 0$.

So,

$$\ddot{s} = -\frac{\dot{C}\,\dot{s}}{C}$$

$$\dddot{s} = \frac{\dot{s}}{C^2}\left(2\,\dot{C}^2 - C\,\ddot{C}\right)$$

Now, if the satellite is losing heat due to radiation, $\dot{C} < 0$, $\ddot{C} > 0$, Hence $\ddot{s} > 0$.

But

$\dddot{s} > 0$, for $2\,\dot{C}^2 > C\,\ddot{C} > 0$

$\dddot{s} < 0$, for $\ddot{C}\,C > 2\,\dot{C}^2 > 0$.

The above argument is further discussed as Appendix B.

Figure 3-9 plots, in polar coordinates, the declination and right ascension of the spin axis for each day on which results were obtained. Note that this axis was always less than 1.05° from the South Pole, but its right ascension varied by almost 180° in the time interval from Day 73 to Day 278. No spacecraft maneuvers were performed from Day 95 to 97, nor from Day 171 to 278.

E. Accuracy of Attitude Determination

A primary reference of higher precision than the star sensor used to obtain attitude solutions is, of course, not available. The accuracy of the computed attitudes are therefore only estimates. Two methods for estimating

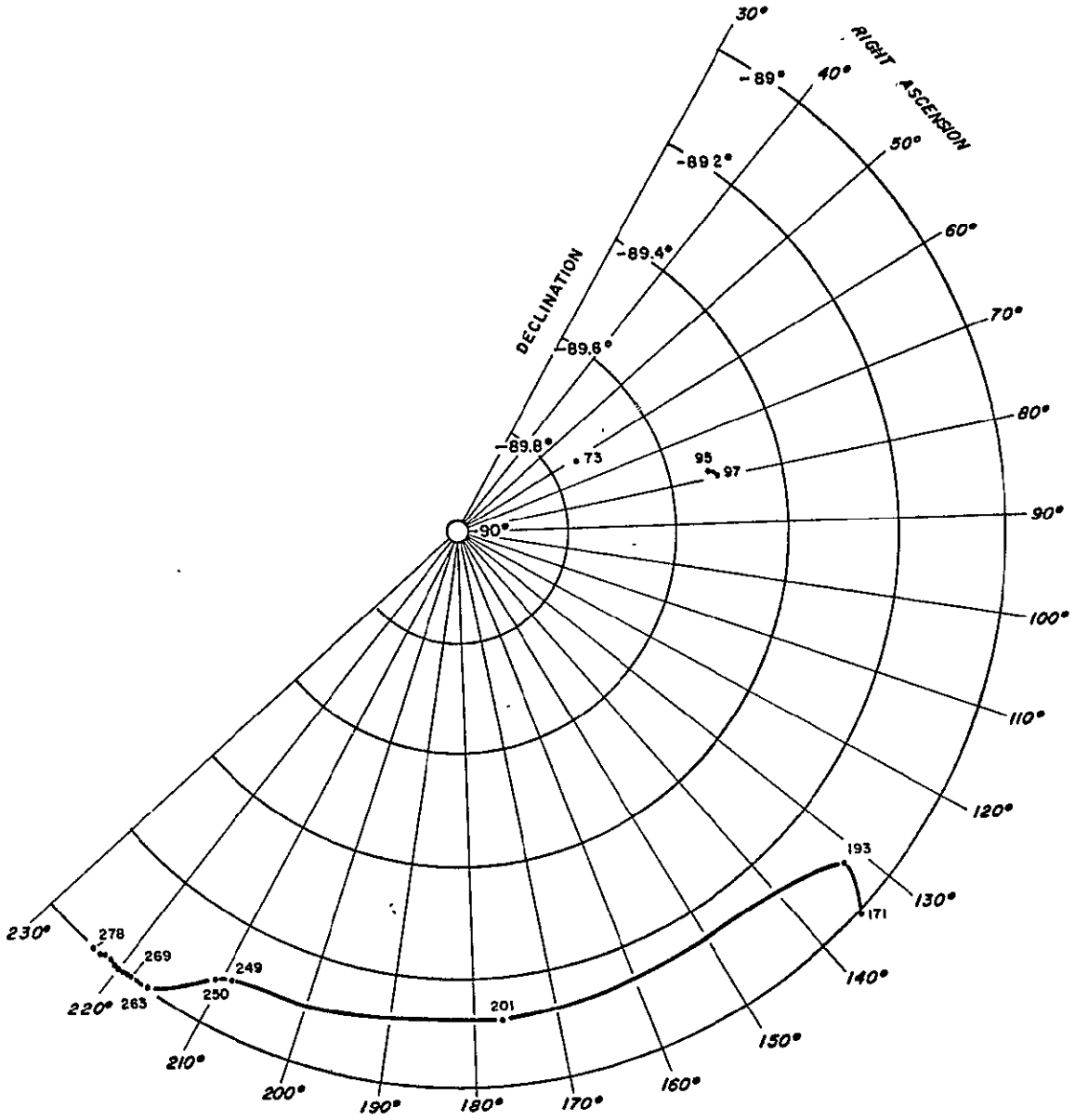

Figure 3-9: Direction of Spin Axis for Various Days

accuracy are utilized. The first requires two or more sets of independent transit times to compute the attitude. The accuracy is then estimated from the degree of consistency in the results. The second method makes use of the residuals in the least squares solution of the attitude parameters to estimate the accuracy of those parameters. Both methods yield about the same estimates.

Table 3-VII lists the estimated standard deviation of the attitude parameters for both good and bad geometry obtained on Days 201 and 273 respectively.

TABLE 3-VIII

STANDARD DEVIATION OF ATTITUDE PARAMETERS

GOOD AND POOR GEOMETRIES

Parameter	Good Geometry (Day 269)	Poor Geometry (Day 201)
$\sigma(\xi_1)$	5.5	36.7
$\sigma(\xi_2)$	4.8	74.4
$\sigma(s_o)$	16.	37.8
$\sigma(\dot{s})$	.29	2.1
$\sigma(\ddot{s})$	.008	--
$\sigma(\dddot{s})$	.0001	--
$\sigma(\Gamma)$	35.7	--
$\sigma(\epsilon)$	12.0	--

In Table 3-VIII the standard deviation of the angles are indicated in seconds of arc, and time is measured in seconds.

Generally speaking, for all data the standard deviation of the mean direction of the spin axis is between 6 arc seconds for good geometry and 100 arc seconds for poor geometry. For the azimuthal direction (rotation about the spin axis) the standard deviation is between 15 arc seconds and 40 arc seconds.

CHAPTER 4
DETERMINATION OF SATELLITE ORBIT

I. NAVIGATION DATA PROCESSING

A method of obtaining the orbit of a satellite by sightings of a second satellite is described herein. Also included in the following section is a description of a computer program which may be used to calculate the orbit.

A. Analysis of Navigation Problem

The general problem is to obtain the time-path of a satellite by sightings of a second satellite. In practice, two secondary satellites were used as targets; a 3 inch diameter probe ejected from the satellite itself, and the moon. However, these targets were never used together during a common time interval. Sightings from the satellite to the secondary satellite are supplied by three slits fixed in the ATS-III satellite. These same slits were used to obtain the attitude of the satellite as discussed in Chapter 3.

Generally speaking, the time-path of the satellite is obtained from observing parallax in the direction to the secondary satellite as reviewed from the primary satellite. This direction is a function of time and is defined with respect to a fixed star field. However, it was not measured directly by the SCNS instrument on-board the ATS-III satellite. In the following paragraphs consideration is given to defining the specific nature of the measurements.

1. Constraint Implied by Slit Transits

A discussion of geometric properties of the SCNS optical instrument pertinent to the determination of attitude was presented in Chapter 3. For the ATS-III/SCNS experiment three slits were etched on the focal plane of the optical system. If each slit is a straight line segment and the optical system is distortionless, then a portion of a plane will be defined by each slit and the optical system which is illustrated in Figure 3-1. Each such plane contains the slit and the nodal point of the lens system. Given a

distant bright source, this source will be sensed by a detector behind the focal plane if, and only if, it lies on one of the planes defined by a slit and the optical system. Since the optical system is fixed with respect to the satellite, the slit-planes rotate with respect to the stars, moon, and ejected probe. These targets thus intermittently cross the slit-planes. With each crossing, a time is sensed and recorded. This time is called the transit time of the target.

Let, $\bar{R}_1$ (t) = position vector of the satellite at time t.

$\bar{R}_2$ (t) = position vector of the secondary satellite's center at time t. The secondary being the moon or an ejected probe.

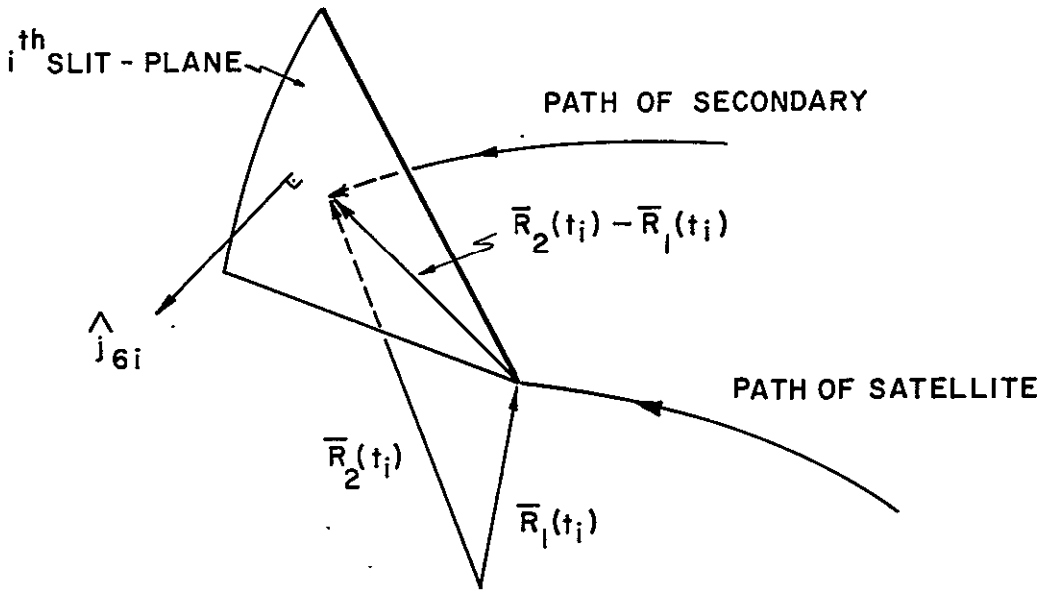

Figure 4-1: Position of Satellite, Secondary, and Slit Normal at Transit Time

For the moment, assume that the secondary satellite is a point target. This assumption is valid for the case of an ejected probe if the time of transit is greater than about 5 minutes after ejection. However, it is not valid if the secondary is the moon.

Now, when the secondary transits the slit at time t_i, the vector from the satellite to the secondary must lie in the slit-plane. Thus,

$$\hat{j}_{6j}\ (t_i) \cdot \left(\overline{R}_2\ (t_i) - \overline{R}_1\ (t_i)\right) = 0 \qquad (1)$$

where $\hat{j}_{6j}\ (t_i)$ = unit vector normal to the jth slit-plane at t_i (notation used in Chapter 3).

To calculate the dot product in (1), the vectors $\hat{j}_{6j}$ and $\overline{R}_2 - \overline{R}_1$ must be expressed in the same coordinate system. This system is chosen to be S_1 with $\hat{i}_1$ in the direction of the First Point of Aries, $\hat{k}_1$ in the direction of the North Pole, and $\hat{j}_1 = \hat{k}_1 \times \hat{i}_1$. Since the attitude of the satellite at any time is computable by use of star transits, $\hat{j}_{6j}\ (t_i)$ has known components in S_1. The earlier notation of Chapter 3 yields

$$\hat{j}_{6j}\ (t_i) = B_{2j}\ R\ (t_i)\ H \begin{pmatrix} \hat{i}_1 \\ \hat{j}_1 \\ \hat{k}_1 \end{pmatrix}$$

where

B_{2j} is a 1 x 3 matrix (row matrix)

$R(t_i)$ is a 3 x 3 matrix

H is a 3 x 3 matrix.

Let $B_{2j} R(t_i) H = N_j(t_i)$ where $N_j(t_i)$ is 1 x 3 matrix and is computable from the transit times of known stars. Thus (1) may be rewritten in matrix notation as

$$N_j(t_i)\left(\bar{R}_2(t_i) - \bar{R}_1(t_i)\right) = 0 \tag{2}$$

where $\bar{R}_2(t_i)$ and $\bar{R}_1(t_i)$ are 3 x 1 column vectors.

Equation (2) is a constraint equation, for it constrains the position of the satellite and the secondary which may occur at the measured transit of the secondary satellite. This equation is used if the secondary is an ejected probe since the probe may be considered to be a point target at times greater than 5 minutes after ejection.

To derive the constraint equation for the case in which the secondary is the moon, two new complications must be considered in the analysis; viz., the moon is an extended body, and the slit is not an ideal line, but has a non-zero width. A typical sensor output, as the slit crosses the moon, is shown in Figure 2-5. It was determined that the most clearly identifiable feature in the sensor output from moon crossings occurs as the slit's trailing edge leaves the moon's limb.

The constraint equation obtained if the moon is used as the secondary satellite thus becomes

$$-R_m = N_j(t_i - \Delta t)\left[\bar{R}_2(t_i - \Delta t) - \bar{R}_1(t_i - \Delta t)\right] \tag{3}$$

where $2\Delta t$ = duration of time a star is within the slit

R_m = radius of the moon ($-R_m$ appears in the equation because of the convention used to define the direction of the positive slit-plane normal).

The slits were constructed so that Δt is the same for each slit. It is computable since the angular extent of the slits and their rate of rotation is known. Equation (3) holds only when a slit leaves any portion of an illuminated limb (as opposed to a day-night line). This was always the case when the measurements were taken.

In summary, Equations (2) and (3) are relations which constrain the motion of the secondary satellite and the primary satellite. Equation (2) holds if the secondary is an ejected probe, while (3) holds if the secondary is the moon. The row vector N_j in these equations is computable from the attitude which in turn is found from star transits. These equations, in themselves, are not sufficient to determine the orbit for the positions change with each measurement. However, the equations of motions of the primary and secondary satellite offer added information which is sufficient for a solution.

2. Analytical Statement of the Problem

The analytical problem to be solved so that the time-path of the primary may be determined from transits of the secondary may now be stated. First assume the secondary is an ejected probe. Then, the equations of motion yield

$$\ddot{\bar{R}}_k (t) = \bar{G} (\bar{R}_k (t), t), \quad k = 1, 2 \tag{4}$$

for all t.

$$\begin{aligned} \bar{R}_2 (t_0) &= \bar{R}_1 (t_0) \\ \dot{\bar{R}}_2 (t_0) &= \dot{\bar{R}}_1 + \overline{\Delta v} \end{aligned} \tag{5}$$

where

t_0 = time of ejection

$\overline{\Delta v}$ = ejection velocity

$$0 = N_j\ (t_i)\ \left(\bar{R}_2\ (t_i) - \bar{R}_1\ (t_i)\right),\ j = 1, 2, 3 \tag{6}$$

where t_i = a measured transit time of the probe across the jth slit.

The 1 x 3 row vector N_j in (6) is computable from the attitude solution.

The problem is to find vectors $\bar{R}_1\ (t)$ and $\bar{R}_2\ (t)$ which satisfy the following conditions:

(a) the given differential equations (4) for all t,

(b) the incomplete initial condition (5), and

(c) the constraint equations, (6), at discrete times t_i, i = 1, 2, ..., n.

If the moon is used as the secondary, then its time-path may be considered as known. Hence, for this case the problem takes the form

$$\ddot{\bar{R}}_1 = \bar{G}\ (\bar{R}_1\ (t),\ t) \tag{7}$$

for all t.

$$0 = N_j\ (t_i - \Delta t)\ \left(\bar{R}_2\ (t_i - \Delta t) - \bar{R}_1\ (t_i - \Delta t)\right) \tag{8}$$

$j = 1, 2, 3$

$i = 1, 2, \ldots, n.$

3. Method of Solution

First, assume the secondary satellite is an ejected probe. Also, suppose $\bar{R}_{10}\ (t_0)$ and $\dot{\bar{R}}_{10}\ (t_0)$ are chosen such that they are "close to" their true values, $\bar{R}_1\ (t_0)$ and $\dot{\bar{R}}_1\ (t_0)$. Moreover, assume the ejection velocity $\overline{\Delta v}$ is given.

This information is sufficient to yield $\bar{R}_{k0}(t)$ for all t as the solution of the differential equations (4). Now, the position vectors so obtained will undoubtedly not satisfy the constraint equation (6) at each measured transit time t_i. Instead, define t_{ci} such that

$$0 = N_j(t_{ci})\left(\bar{R}_{20}(t_{ci}) - \bar{R}_{10}(t_{ci})\right)$$

and

$|t_{ci} - t_i| \leq .5\,P$ where P is the rotational period of the satellite ($P \doteq .6$ seconds). Also, let $t_{ci} - t_i = \delta t_i$. Now, the δt_i's are a measure of the error in the original guesses $\bar{R}_{10}(t_0)$ and $\dot{\bar{R}}_{10}(t_0)$ and $\dot{\bar{R}}_{20}(t_0)$. If each of these time deviations is small, then a solution of the problem has been obtained. If not, then these time deviations may be used to correct the guessed initial conditions by use of a linearization method. This point will now be considered.

Let,

$$\bar{X}_k(t) = \begin{pmatrix} R_k(t) \\ \dot{R}_k(t) \end{pmatrix}, \quad k = 1, 2.$$

By use of this substitution, (4) may be written as a first order system of differential equations of the form

$$\dot{\bar{X}}_k = \bar{F}(\bar{X}_k, t), \quad k = 1, 2 \tag{9}$$

Given $\bar{X}_{10}(t_0)$, the initial position and velocity of the probe is determined by

$$\bar{X}_{20}(t_0) = \bar{X}_{10}(t_0) + \begin{pmatrix} 0 \\ \Delta\bar{v}_0 \end{pmatrix}$$

where $\overline{\Delta v_0}$ = nominal velocity of probe ejection. Now, for all t, X_{k0} (t) can be found as a solution to the system of differential equations

$$\dot{\overline{X}}_{k0} = \overline{F} \left(\overline{X}_{k0}, t\right) , \; k = 1, 2 \tag{10}$$

The solution vectors, $\overline{X}_{k0}$ (t), constitute the "nominal trajectories" of the satellite and probe.

Now let $\overline{X}_k$ (t) = $\overline{X}_{k0}$ (t) + $\delta \overline{X}_k$ (t) .

Substituting this expression into (9) and taking advantage of the fact that $\overline{X}_{k0}$ (t) must satisfy (10), one obtains an approximation equation which $\delta\overline{X}_k$ (t) must satisfy. Thus,

$$\delta\dot{\overline{X}}_k = \nabla\overline{F} \left(\overline{X}_{k0}, t\right) \delta\overline{X}_k + \ldots \tag{11}$$

where

$$\nabla\overline{F} \left(\overline{X}_{k0}, t\right) = \begin{pmatrix} \frac{\partial F_1}{\partial x} & \frac{\partial F_1}{\partial y} & \cdots & \frac{\partial F_1}{\partial \dot{z}} \\ \frac{\partial F_2}{\partial x} & \frac{\partial F_2}{\partial y} & \cdots & \frac{\partial F_2}{\partial \dot{z}} \\ & & \vdots & \\ \frac{\partial F_6}{\partial x} & & \cdots & \frac{\partial F_6}{\partial \dot{z}} \end{pmatrix}$$

evaluated at $\dot{X}_{k0}$,(t). Here F_1, F_2, ... F_6 are the components of $\overline{F}$.

So, to a first order approximation, $\delta\overline{X}_k$ satisfies a linear homogeneous differential equation. The coefficients of $\delta\overline{X}_k$ are non-constants, being functions of the nominal trajectory. The solution of this system may be written as

$$\delta\bar{X}_k\ (t) = \Phi_k\ (t,\ t_0)\ \delta\bar{X}_k\ (t_0) \tag{12}$$

where

$$\dot{\Phi}_k\ (t,\ t_0) = \nabla\bar{F}\ (\bar{X}_{k0},\ t)\ \Phi_k\ (t,\ t_0)$$

$$\Phi_k\ (t_0,\ t_0) = I,\ (6 \times 6 \text{ identity}).$$

Equation (12) relates position and velocity deviations from the nominal trajectory at one time to position and velocity deviations at another time. The matrix Φ in this equation is called the transition matrix in the language of orbital theory, it is called a fundamental solution matrix in the language of differential equation theory.

Equation (6) must also be linearized. To do so, define t_{ci} such that

$$0 = N_j\ (t_{ci})\ \left(\bar{R}_{20}\ (t_{ci}) - \bar{R}_{10}\ (t_{ci})\right).$$

$|t_{ci} - t_i| \leq .5\ P$, where $P \doteq .6$ seconds is the rotation period of the satellite.

Since N, $\bar{R}_{20}$, and $\bar{R}_{10}$ are known functions of time, t_{ci} is computable for each i. Now set

$$t_{ci} + \delta t_i = t_i$$

and rewrite (6) in the form

$$0 = N_j\ (t_{ci} + \delta t_i)\ \left(\bar{R}_{20}\ (t_{ci} + \delta t_i) - \bar{R}_{10}\ (t_{ci} + \delta t_i) + \right.$$

$$\left. \delta\bar{R}_2\ (t_{ci} + \delta t_i) - \delta\bar{R}_1\ (t_{ci} + \delta t_i)\right).$$

If higher powers of δt_i are neglected, one obtains $U_j\ (t_{ci})\ \delta_{ti} =$ (13)

$N_j\ (t_{ci})\left(\delta\bar{R}_2\ (t_{ci}) - \delta\bar{R}_1\ (t_{ci})\right)$

where $U_j = \dot{N}_j\ (\bar{R}_{20} - \bar{R}_{10}) + N\ (\dot{\bar{R}}_{20} - \dot{\bar{R}}_{10})$.

Equation (13) relates deviations of the position of the primary and ejected probe from their respective nominal positions to a change in the transit time of the probe. In this equation all quantities are known except $\delta\dot{\bar{R}}_2\ (t_{ci})$ and $\delta\dot{\bar{R}}_1\ (t_{ci})$.

Substituting (12) into (13) one finds

$$U_j\ \delta t_i = N_j K\left(\bar{\Phi}_2\ (t_{ci}, t_0)\ \delta\bar{X}_2\ (t_0) - \bar{\Phi}_1\ (t_{ci}, t_0)\ \delta\bar{X}_1(t_0)\right) \tag{14}$$

where K = (I, 0), I being the 3 x 3 identity
0 being the 3 x 3 zero number.

Thus far, no use of the incomplete initial conditions (5) has been made. These conditions imply

$$\delta\bar{X}_2\ (t_0) = \delta X_1\ (t_0) + \begin{pmatrix} 0 \\ \delta\Delta\bar{v} \end{pmatrix}$$

where $\delta\Delta\bar{v} = \overline{\Delta v} - \overline{\Delta v_0}$ = deviation of ejection velocity from its nominal value. Hence, (14) becomes

$$U_j\ \delta t_i = N_j\ (\alpha_2 - \alpha_1, \beta_2 - \beta_1, \beta_2) \begin{pmatrix} \delta\bar{X}_1\ (t_0) \\ \delta\Delta\bar{v} \end{pmatrix} , \tag{15}$$

where, $K\bar{\Phi}_k\ (t, t_0) = (\alpha_k, \beta_k)$. α_k and β_k are 3 x 3 submatrices of $\bar{\Phi}_k$.

U_j, N_j, α's and β's are evaluated at t_{ci}.

Equation (15) represents one equation in nine unknowns. If a sufficient number of independent measurements are made, these nine unknowns may be

computed. After finding $\delta\overline{X}_1\ (t_0)$ and $\delta\overline{\Delta v}$, better reference trajectories may be obtained, and the entire process may be repeated.

For reasons which will be considered later, the ejection speed $|\overline{\Delta v}|$, cannot be treated as an unknown in the total problem. However, the direction of $\overline{\Delta v}$ must be considered unknown, for the ejection mechanism is not to be relied upon to furnish a known direction.

In order to rewrite (15) so that $|\overline{\Delta v}|$ is considered as known, let

$$\overline{\Delta v} = \Delta v\ \hat{u}$$
$$= \Delta v\ (\cos e \cos a\ \hat{i} + \cos e \sin a\ \hat{j}_1 + \sin e\ k)$$

where

Δv = ejection speed = $|\overline{\Delta v}|$
a = right ascension of ejection velocity
e = declination of ejection velocity.

Also let,

$\hat{u} = \hat{u}_0 + \delta\ \hat{u}$, $\hat{u}_0$ the nominal value of $\hat{u}$.

The reference orbits are chosen to satisfy

$$\overline{X}_2\ (t_0) = \overline{X}_1\ (t_0) + \Delta v \begin{pmatrix} 0 \\ \hat{u}_0 \end{pmatrix}.$$

Hence

$$\delta\overline{X}_2\ (t_0) = \delta\overline{X}_1\ (t_0) + \Delta v \begin{pmatrix} 0 \\ \delta\hat{u} \end{pmatrix}.$$

Now

$$\delta\hat{u} = \begin{pmatrix} -\sin a_o & -\sin e_o \cos a_o \\ \cos a_o & -\sin e_o \sin a_o \\ 0 & \cos e_o \end{pmatrix} \begin{pmatrix} \cos e_o \, \delta a_o \\ \delta e_o \end{pmatrix}$$

$$= M \begin{pmatrix} \cos e_o \, \delta a_o \\ \delta e_o \end{pmatrix} \quad , M \text{ a } 3 \times 2 \text{ matrix.}$$

Hence, (15) becomes

$$U_j(t_{ci})\,\delta_{ti} = N_j(\alpha_2 - \alpha_1, \beta_2 - \beta_1, \Delta v\, \beta_2\, M) \begin{pmatrix} \delta\bar{X}_1(t_0) \\ \cos e_o \, \delta a_o \\ \delta e_o \end{pmatrix}. \qquad (16)$$

The problem now contains the eight unknowns $\delta\bar{X}_1(t_0)$, $\cos e_o\, \delta a_o$, and δe_o. This is the recommended form to be used with transits of an ejected probe. The ejection speed Δv must be given.

Now, consider the secondary to be the moon. For this case t_{ci} will be defined such that

$$-R_m = N_j(t_{ci})\left(\bar{R}_{20}(t_{ci}) - \bar{R}_{10}(t_{ci})\right)$$

$|t_{ci} - t_i| \leq .5\ P$. Define δt_i as $\delta t_i = t_{ci} - t_i + \Delta t$.

Assume the orbit of the moon is known, then (13) becomes

$$U_j(t_{ci})\,\delta t_i = -N_j(t_{ci})\,\delta R_1(t_{ci}) \qquad (17)$$

and (16) becomes

$$U_j(t_{ci})\,\delta t_i = -N_j(t_{ci})(\alpha_1, \beta_1)\,\delta\bar{X}_1(t_0). \qquad (18)$$

Hence, for the case in which the secondary is an ejected probe (16) is one member of a linear system of equations whose solution yields corrections to the initial guess of the spacecraft position and velocity and direction of ejection. If the moon is the secondary, (18) represents the correction equation. For this case the moon's orbit is assumed given.

B. Data Processing Program

The steps required to prepare and run the computer program to solve the navigation problem using both the moon and satellite particle are outlined below in which preparation of satellite attitude, selection and identification of particle and moon transits and the filtering and adjusting of the data are described. A description of the operation of the actual navigation program is included later. The block diagram in Figure 4-2 shows the data processing tasks required to determine the satellite orbit from observations of the particle. Figure 4-3 shows the tasks required when using moon transits.

1. Probe Navigation Data

Ejection of the second of three particles[1] took place on Day 202 at 0000 GMT (July 20, 1968). Attitude data had been collected for several minutes prior to ejection and continued for some 15 minutes afterwards. Transit data was digitized live from one minute before to approximately three minutes after ejection and at various times thereafter for six hours. Star data was also gathered on the second and third nights of the navigation experiment but sighting of the probe could not be made from the first night

The process of isolating probe and transits from the noise and from star transits can be described by the following operations outlined in Figure 4-2:

1. The first particle was ejected prematurely, preventing useful navigation sightings. The third particle is contained within the satellite as of the publication date of this document.

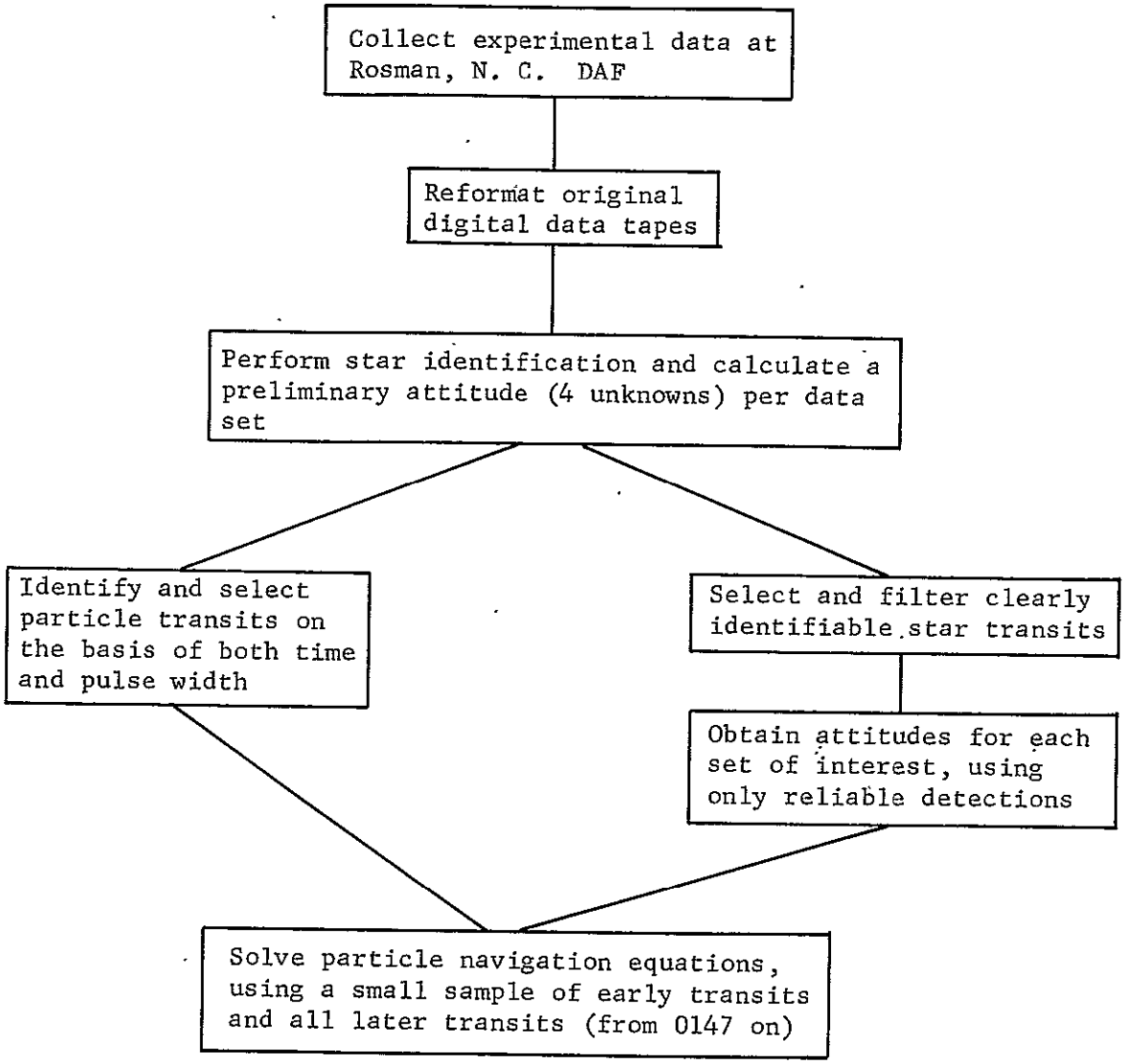

Figure 4-2: Data Processing Tasks for Particle Navigation

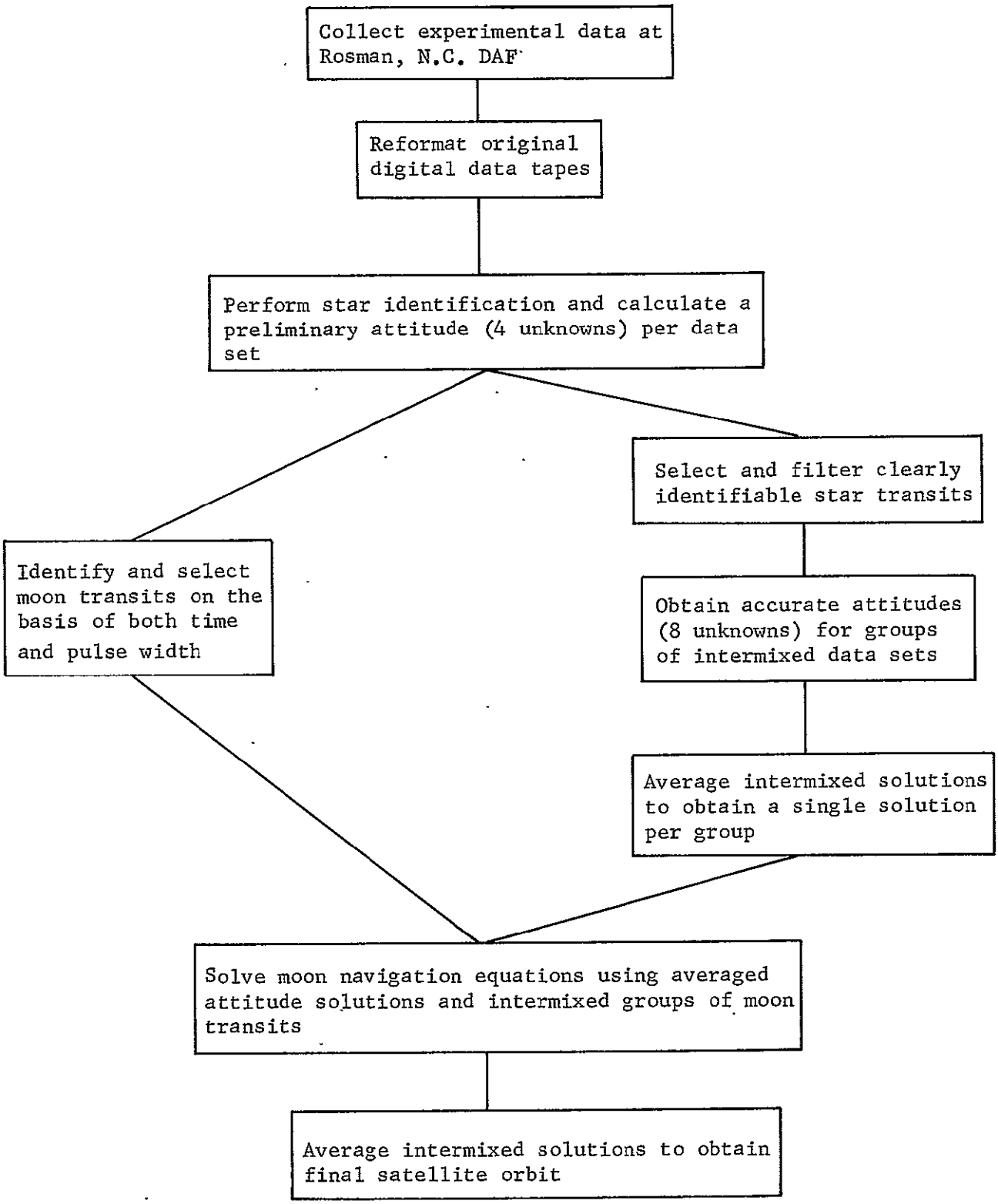

Figure 4-3: Data Processing Tasks for Moon Navigation

3

1. Obtain satellite attitude for each data set.
2. Plot a histogram of all pulses resolved to the first can.
3. Eliminate all identifiable star pulses
4. Find three repeatable, properly spaced transits from the particle.
5. Search all scans in each set for transits close to the manually determined particle transits.
6. Filter all candidate transits on the basis of both pulse width and position within the scan.

The steps outlined above were repeated for each set of data from shortly after particle ejection to the time where the particle could no longer be observed. Identification of the particle transits became more difficult as it moved farther from the satellite, not only because of the lower detectability with distance as one would expect, but also because the particle was very nearly coincident with a transit from a faint star.

Preliminary attitudes were obtained for many of the data sets. Based on these attitudes, a selection was made manually of the bright stars thought to be most reliably detectable. Then, attitudes were recalculated using only these stars which reduced random errors introduced by misidentifications. Slit parameters determined with data obtained from earlier experiments were used. The attitudes so obtained are given in Table 4-I.

2. Moon Navigation Data

Collection of experimental data for the moon navigation phase of this project was completed during September and early October. Two groups of days were favorable for observing the moon while the ATS-III spacecraft passed through the earth's shadow each day during the fall eclipse. Data was obtained on September 5 and 6 and from September 25 through October 4. The time base (29 days) over which observations were made was an important consideration. During any given night, the spacecraft moved through as much as 1/30 of an orbit during the observations and from September 25 through

TABLE 4-I

ATTITUDES FOR SECOND PARTICLE NAVIGATION (DAY 202)

Time	ξ_2	$\dot{\xi}_2$	s_o	$\dot{s}$
0001:06	179.98510	-0.94688	103.92234	598.92117
0005:07	180.03736	-0.90411	104.01863	598.92306
0008:06	180.01195	-0.92162	103.98668	598.92328
0013:36	180.06158	-0.89467	103.95315	598.92403
0014:37	179.98780	-0.91140	104.00222	598.92292
0147:00	180.03745	-0.92439	103.77701	598.92436
0148:20	180.07191	-0.88667	103.80030	598.92288
0148:52	180.05138	-0.90771	103.89069	598.92580
0217:01	180.08580	-0.83968	103.72557	598.91330
0217:46	180.07667	-0.86864	103.76770	598.91382
0218:01	180.05829	-0.90165	103.66706	598.91282
0230:00	180.08717	-0.84285	103.74656	598.90948
0230:15	180.06163	-0.91177	103.62944	598.90946
0230:30	180.07431	-0.84206	103.57260	598.90930
0231:00	180.06994	-0.89183	103.74505	598.90954
0231:15	180.09868	-0.80564	103.65933	598.90911
0231:44	180.07402	-0.87156	103.74375	598.91048

October 4 the moon travelled through about 9/28 of its orbit. The relative motions of these two objects determine the final accuracy of the navigation results.

Transit data was collected successfuly on ten days during the eclipse with the moon in the field of view. The amount and distribution of moon transits is tabulated in Table 4-II.

Preliminary attitudes for most of the data sets on each of the 10 days indicated in Table 4-II were computed.

The attitude solutions obtained each day are tabulated as Table 4-III. Notice the slow drift in right ascension with time. Clearly the spin rate does not represent the sunlit rate, nor can the rates be compared directly from one day to the next since the eclipse does not begin at precisely the same time each day and the spin rate is directly related to the cool-down experienced while the spacecraft was in the earth's shadow. The column headed "Residual" gives the root mean square of the functional residuals in microseconds for the data set in question (approximately 15 seconds of data).

Figure 4-4 shows the approximate position of the moon with respect to the star field on the observation days. It is important to note the following features:

1. Although both Mercury and Venus appear in the same part of field of view (FOV from about -10^{o} to -40^{o} declination), no evidence of any Mercury detections can be found in the digital data. Since the visual magnitudes of these two planets are +0.70 and -3.40, respectively, and because of the dramatic cutoff with distance from the optical axis, this could have been anticipated.
2. Because of the relative geometry of the Sun-Earth, Moon, and spacecraft, and since the sensor scanned in a backward direction in right ascension, all three slits leave the moon from a point on its limb (in contrast to the day-night line) on each observation day. Since the trailing edge of

TABLE 4-II

MOON TRANSIT TIME DATA

Time				Number of Transits			
Day	From	To	Data Sets	Slit 1	Slit 2	Slit 3	Total
249	0301:53	0313:41	1-47	562	718	698	1978
250	0256:52	0301:53	1-21	108	288	297	693
	0316:16	0317:51*	22-67	227	569	588	1384
269	0255:27	0258:06	1-11	81	141	141	363
	0300:00	0303:58	12-27	123	201	192	516
	0313:58	0326:15	28-76	413	678	661	1752
270	0246:18	0248:08	1- 8	54	107	103	264
	0256:01	0258:56	9-20	78	153	156	387
	0306:01	0308:56	21-32	71	169	160	400
	0316:01	0318:56	33-44	74	167	178	419
	0321:01	0325:50	45-63	97	217	226	540
271	0239:02	0241:47	1-12	105	160	167	432
	0253:11	0255:56	13-24	102	163	180	445
	0307:00	0309:45	25-36	98	164	176	438
	0318:00	0324:47	37-64	229	388	389	1006
272	0240:03	0242:49	1-12	176	182	175	533
	0259:01	0301:50	13-24	0	0	0	0
	0308:31	0313:38	25-45	163	174	174	511
	0318:03	0324:48	46-73	373	395	379	1147
273	0231:02	0233:47	1-12	74	119	127	320
	0246:00	0249:00	13-25	64	141	144	349
	0306:00	0308:45	26-36	84	130	128	342
	0316:01	0323:32	37-64	173	369	380	922
274	0314:47	0321:10	1-15	0	148	147	295
276	0237:48	0241:35	1-16	60	172	164	396
	0245:00	0248:45	17-32	155	236	259	650
	0256:00	0259:55	33-48	113	185	183	481
	0307:01	0310:45	49-63	35	203	195	433
	0314:45	0317:46	64-76	154	186	194	534
277	0255:02	0304:58	1-39	235	524	525	1284
	0310:01	0320:48	40-82	249	605	588	1442
Totals				4303	7483	7486	19272

* Operational filter in place, transits not included in totals.

TABLE 4-III

INITIAL ATTITUDES FOR FALL ECLIPSE MOON NAVIGATION

Day	Time	Rt. Ascension	Declination	Spin Rate	Period	Residual	Stars Used
249	0301:53	207.664	-89.162	636.7697	0.565354	43	1,16,17,73,81
	0313:26	207.427	-89.171	636.8937	0.565243	45	1,16,17,38,81
250	0256:52	211.483	-89.079	636.7308	0.565388	30	1,16,23,38,39,48,73,81
	0301:53	211.359	-89.084	636.7917	0.565334	29	1,16,23,38,48,73,81
269	0255:27	215.599	-88.959	636.9445	0.565198	55	1,16,17,23,38,39,48,73,81
	0325:59	217.058	-88.970	637.1557	0.565011	50	1,16,17,23,38,39,48,73,81
270	0246:18	219.769	-88.960	636.8642	0.565270	27	1,16,17,23,38,39,48,73,81
	0326:44	219.140	-88.975	637.1554	0.565011	26	1,16,17,23,38,39,48,81
271	0239:02	219.361	-88.950	636.7721	0.565351	30	1,16,17,23,38,39,48,73
	0324:47	220.146	-88.952	637.1375	0.565027	28	1,16,17,23,38,48,73
272	0240:02	220.146	-88.944	636.7996	0.565327	26	1,17,23,38,48,73
	0324:48	220.277	-88.948	637.1499	0.565016	28	1,17,23,38,48,73
273	0231:02	220.674	-88.946	636.6723	0.565440	39	1,17,23,48,Venus
	0323:32	217.450	-88.933	637.1291	0.565035	46	1,17,23,38,48,73,Venus
274	0314:47	220.989	-88.933	637.0716	0.565086	45	1,16,17,23,38,Venus
	0321:10	221.408	-88.944	637.1112	0.565050	34	1,16,17,23,Venus
276	0237:48	222.504	-88.924	636.7313	0.565388	27	1,16,17,23,38,73,81,Venus
	0317:46	223.403	-89.027	637.0720	0.565085	47	1,16,17,81,Venus
277	0255:03	222.619	-88.925	636.8874	0.565249	30	1,16,17,23,38,48,81,Venus
	0320:48	222.817	-88.908	637.0764	0.565081	35	1,16,17,23,38,39,48,73,81,Venus

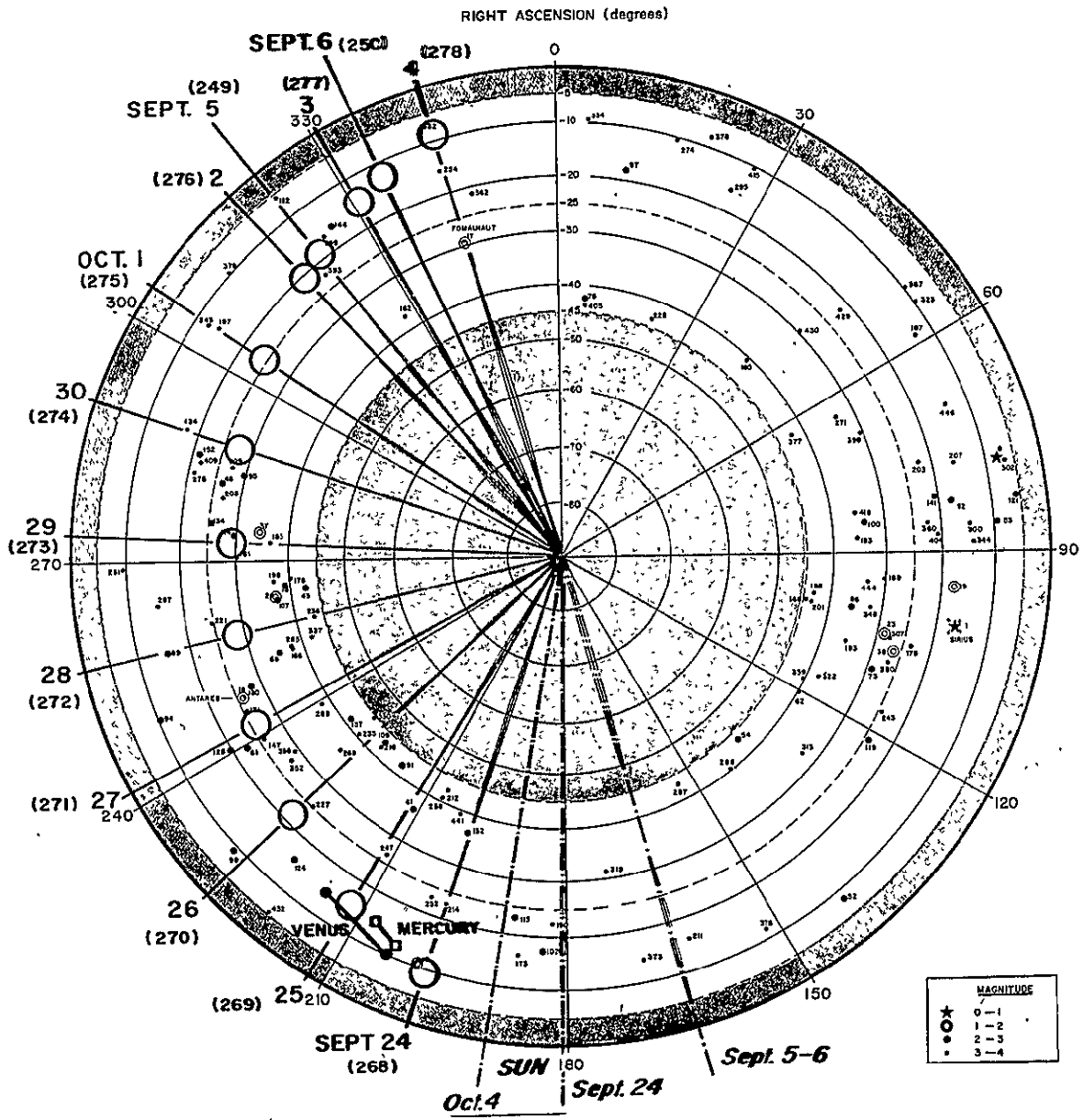

Figure 4-4: Sun, Moon and Venus for Time Period Sept. 5,6, Sept. 24 - Oct. 4 (0000 GMT)

each pulse determines the transit time, determination of the moon's center was simplified.

3. Because the moon is a bright object, it completely obliterates that part of the scan approximately 25 degrees on either side of it. This means that on certain days one or more key stars are lost. Those stars which are regularly detected (when not in the vicinity of the moon) included Stars 1, 16, 17, 23, 38, 39, 48, and 81. From Day 273 on, the updated position of Venus was added to the star catalog and was treated as an additional star.

A great deal of care was used in the process of selecting all possible moon transit times and in deleting those which were felt to be misidentifications or inaccurate detections. The first step in obtaining these times and isolating them from the star transits was to generate an attitude solution for as many data sets as possible on each day through the use of the program SCAT1. Among other information, this program lists all the repeatable pulses not associated with any known star resolved by a multiple of the scan period to the first scan. Comparing these averages with the known position of the moon (from an ephemeris), the relative position within a scan could be estimated and the three transits punched on a tabulating card along with the data set number and spin period. These cards were used as input data along with the original digital tape to a second computer program to search for transits falling within a relatively large tolerance of these averaged times. Transits adjusted to a trailing edge for each scan and their associated pulse widths are tabulated as Figure 4-5 for a typical data set from one particular day (Day 270). The row labeled "Difference" is the slit-to-slit difference in transit times for $\Delta_1 = \text{slit}_2 - \text{slit}_1$ and $\Delta_2 = \text{slit}_3 - \text{slit}_2$. The last entry in this row is the difference of the differences, $\Delta = \Delta_2 - \Delta_1$. Notice that Δ is quite different from zero as would be expected since all three slits leave the moon from slightly different points on the limb. It is clear that slit 1 is not as regularly detectable as either slits 2 or 3 and its pulse width (shown in microseconds) varies considerably more than the other two.

Data Set 270. 35 Period .565060

Scan	Slit One		Slit Two		Slit Three	
	Time	Width	Time	Width	Time	Width
-1	0	0	0	0	0	0
0	0	0	0	0	0	0
1	.025378	2673	.030376	817	.035416	1609
2	.025378	2869	.030374	818	.035413	1610
3	.025377	2616	.030374	820	.035416	1613
4	0	0	.030374	823	.035415	1604
5	0	0	.030374	829	.035413	1610
6	0	0	.030371	820	.035410	1604
7	.025376	2420	.030374	821	.035415	1619
8	0	0	.030372	822	.035412	1610
9	0	0	0	0	0	0
10	0	0	0	0	0	0
11	0	0	0	0	0	0
12	.025370	3049	.030368	823	.035406	1621
13	0	0	.030366	832	.035408	1611
14	0	0	.030366	821	.035406	1609
15	.025368	2310	.030366	832	.035401	1616
16	.025368	3140	.030364	828	.035404	1603
17	.025366	3043	.030363	829	.035403	1616
18	0	0	.030362	821	.035405	1615
19	0	0	.030361	832	.035402	1615
20	0	0	0	0	0	0
21	0	0	0	0	0	0
22	.025358	2785	.030356	824	.035397	1607
23	.025357	2810	.030354	820	.035396	1611
24	.025357	2774	.030354	827	.035396	1608
25	.025355	3010	.030352	822	.035391	1612
26	.025353	2674	.030351	824	.035392	1598
27	0	0	0	0	0	0
28	0	0	0	0	0	0
	13 transits		21 transits		21 transits	
Average	.025366	2782	.030365	824	.035405	1610
Difference		.004999		.005040		.000041
Midpoint	.023975		.029953		.034600	
Smallest	.025353	2310	.030351	817	.035391	1598
Largest	.025378	3140	.030376	832	.035416	1621
Spread	.000024	830	.000025	15	.000024	23

Figure 4-5: Computer Output of Moduloed Moon Transits for Day 270

Each day was scanned visually for data sets which have problems associated with them. These were either corrected if possible by obtaining a better estimate of the location of the moon transits or the set was discarded. Those sets that remain were subjected to a third computer program for further processing. This program used an updated position (as obtained by the average transit from the previous program) about which to search for these same moon transits except for the use of a smaller tolerance. The mean and standard deviation of these moduloed transits were found and only those transits (trailing edges) within plus or minus one standard deviation of the mean were retained which were then written on a separate moon transit tape along with the associated slit number. The result of the processing was a magnetic tape with moon trailing edge transit times and identifying slit number for each of the ten days of observation. The amount of available moon date from each day by slit number is shown in the last four columns of Table 4-II.

3. Computer Program

A FORTRAN computer program has been written and checked out for operation on a Contral Data 6000 series machine to solve the navigation equations as described in Section IIIA. Actually, two separate programs exist for navigation; one for use with particle transits, and one for moon transits. Although the equations to be solved are very similar, the special requirements of the moon navigation problem (such as the availability of an ephemeris for the sun and moon) made it necessary to create two different programs. For the purpose of this report, however, only the moon navigation program will be described here. The particle navigation program can be thought of as a subset of instructions from the moon program.

(a) Input Parameters

Some of the more important parameters to be preset or read in prior to operation of the navigation program are listed below in the order in which they are encountered:

The earth gravitational field constants including fourth order

harmonics as given by Kozai[2].

Gravitational constant in kilometers cubed per second squared.

Earth and moon radii.

Slit corrections for each observation day.

Day and time zero (time of initial conditions).

Hour angle of the first point of Aries at time zero.

Radiation pressure constants.

Convergence criteria for six unknowns.

Moon ephemeris for the first six hours of each observation day and for 0000 hours only on all other days of interest.

Moon horizontal parallax every 12 hours on the observation days and for 0000 hours only on all other days.

Sun ephemeris at 0000 hours of each day.

Sets of attitude parameters (eight unknowns).

Initial estimate of the satellite position and velocity at time zero.

Moon transit times and identifying slit numbers.

(b) Program Operation

The operation of the moon navigation program follows the lines of the flow chart in Figure 4-6. In order to follow the flow of the program, it is suggested that references be made to the equations developed in Section IA. Since the program is essentially one solving a complicated system of non-linear algebraic equations (as contrasted with a program such as SCAT1, the star identification program, which involves a great deal of data manipulation and logical decision making), it is rather straight forward with very little looping and decision making.

---

2. Earth gravity constants were taken from NASA TN D-2103 "The drift of a 24-hour equatorial satellite due to an earth gravity field through 4th order" by C. A. Wagner who cites Kozai's work as a reference.

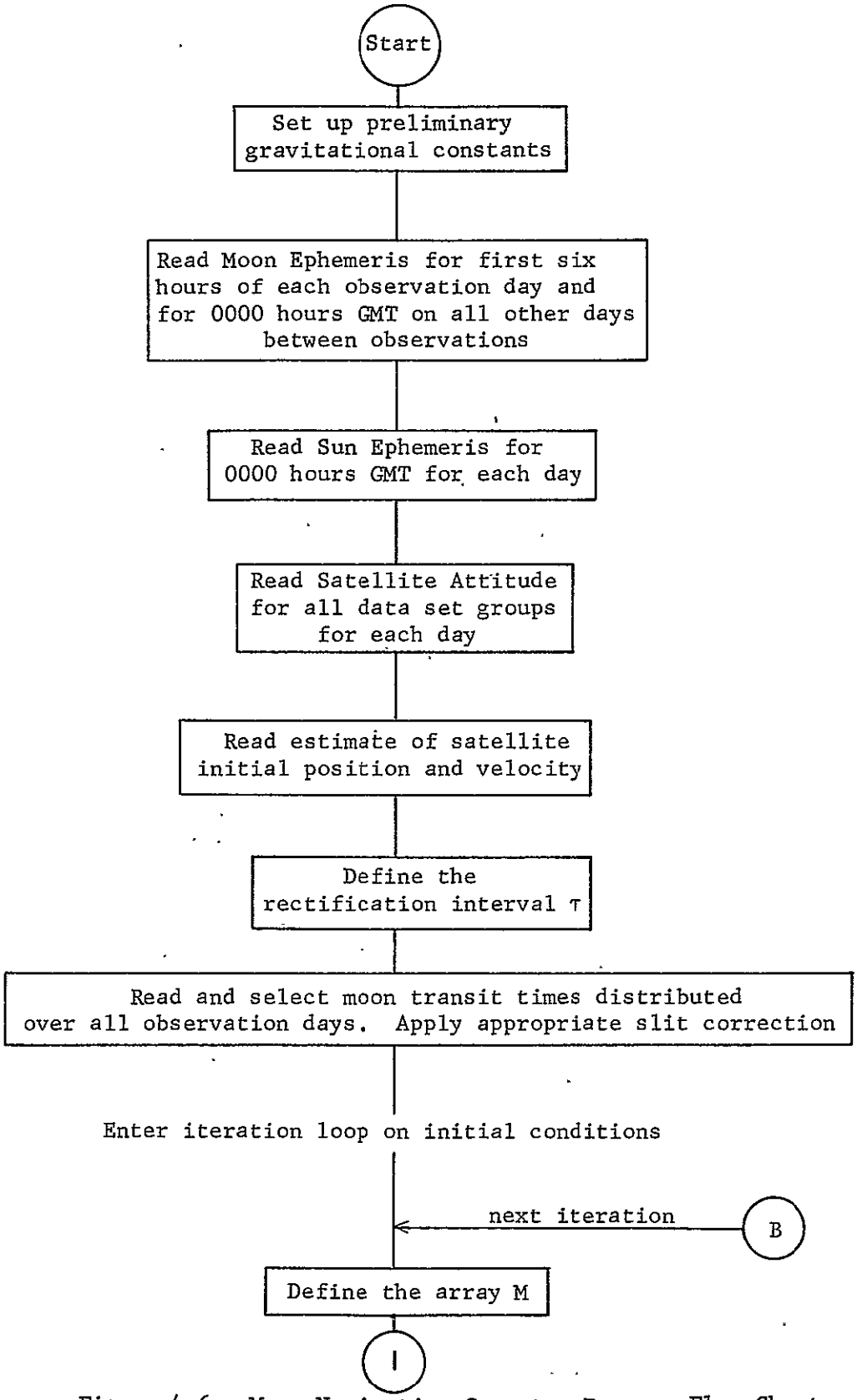

Figure 4-6: Moon Navigation Computer Program Flow Chart

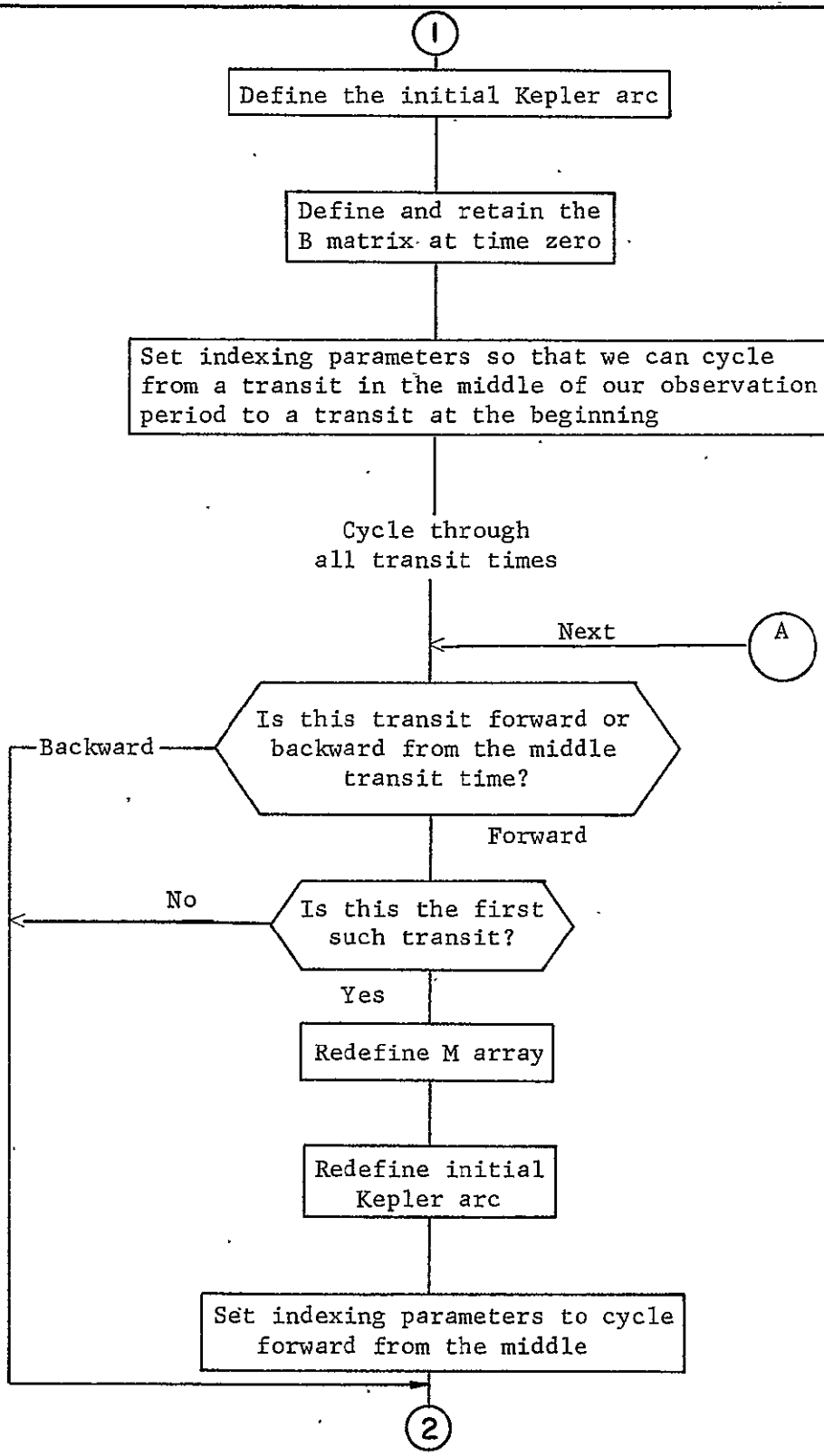

Figure 4-6: (Continued)

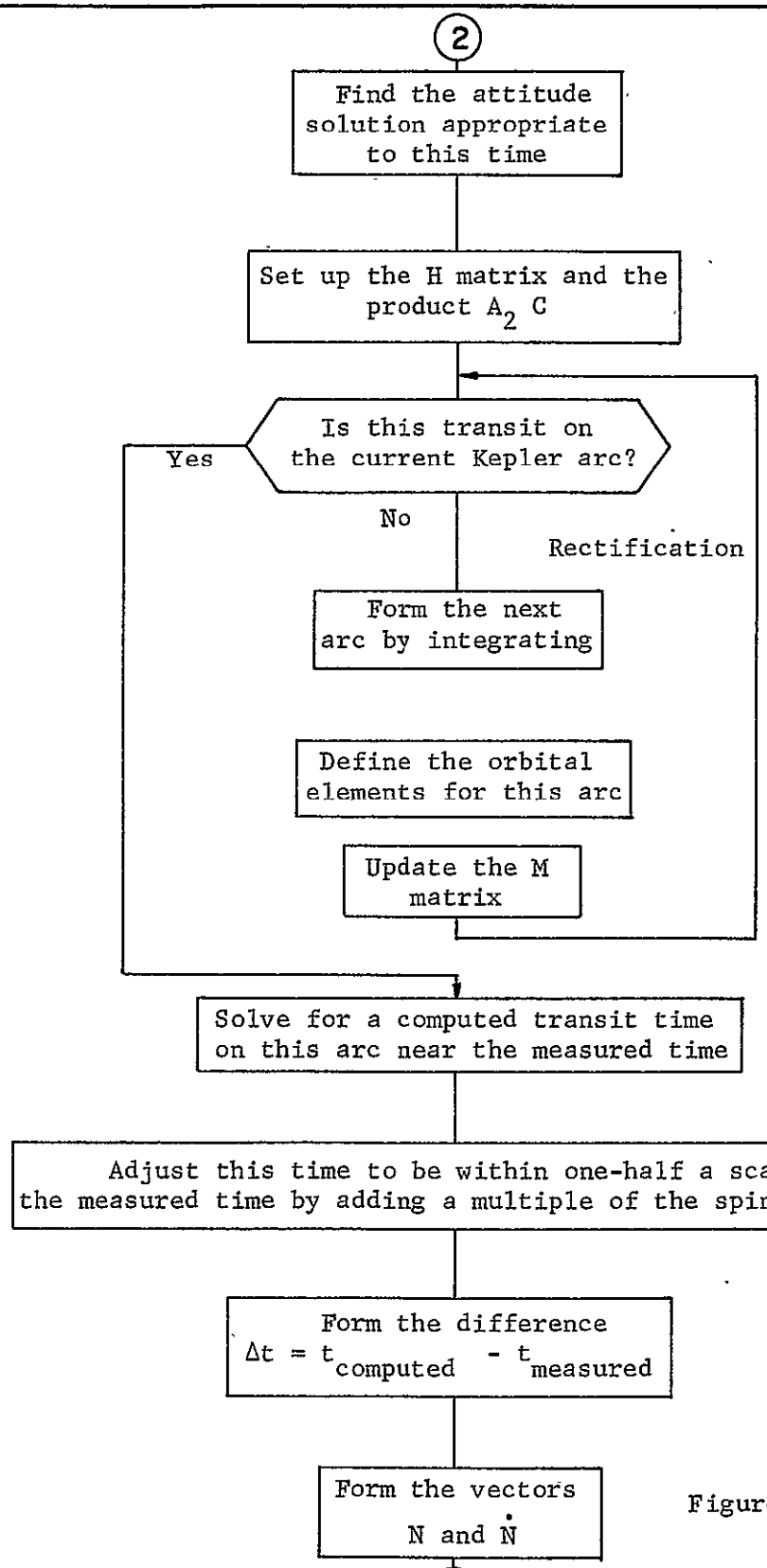

Figure 4-6: (Continued)

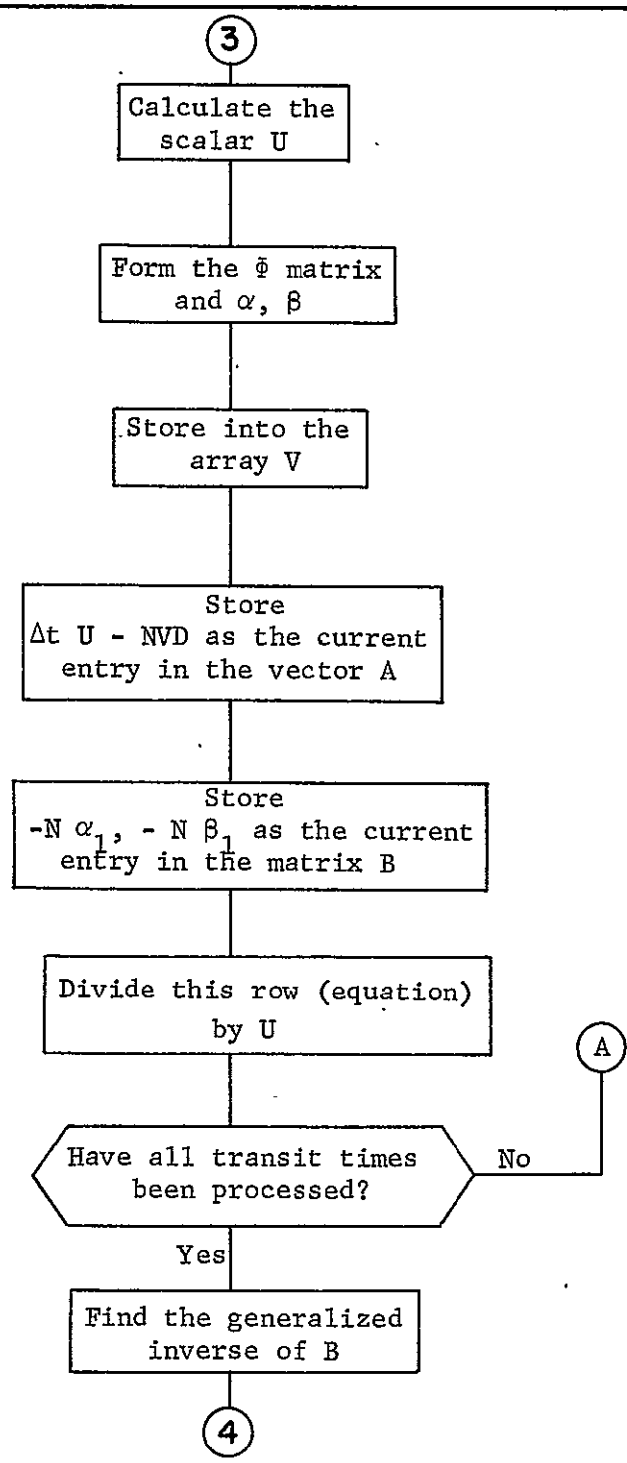

Figure 4-6: (Continued)

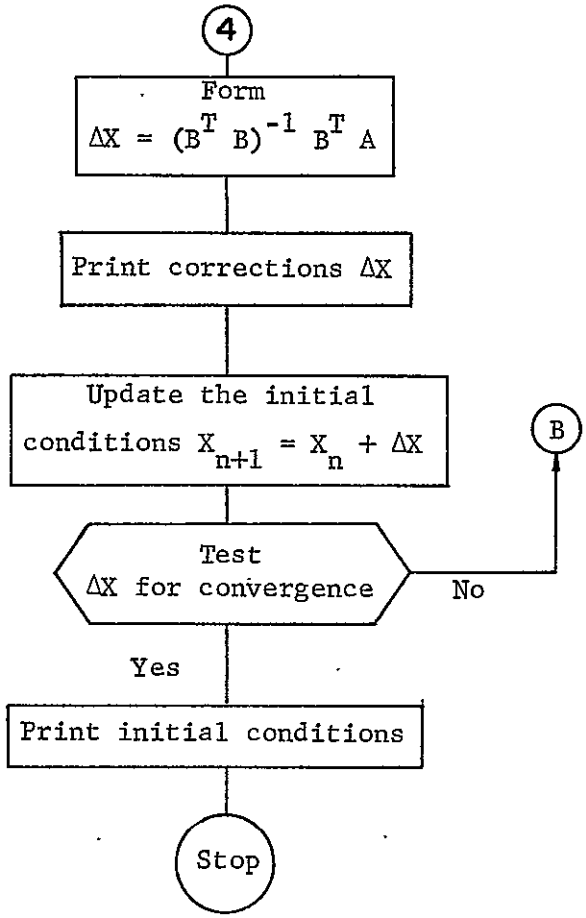

Figure 4-6: (Continued)

The program begins by setting up the array of gravitational constants and the slit corrections for the adjustment to transits from an extended source (for moon data only). Moon ephemeris data is read in from cards for Day 249 through Day 277. Right ascension and declination are read for the first six hours of each observation day and for just 0000 hours on all other days. Similarly, the horizontal parallax of the moon is read in for 0000 hours and 1200 hours on observation days and 0000 hours on all others. Next the right ascension and declination of the sun at the beginning of all the above days is read in.

A set of satellite attitudes (eight unknowns for the moon, four unknowns for the particle) is read in for each of the observation days. Finally, an estimate of the initial conditions of the satellite (position and velocity in kilometers and kilometers per second) at an arbitrary time zero (ejection time for the particle, a time preferably midway between Days 249 and 277 for the moon) are read in.

Next, moon transits are read in from magnetic tape and a subset of these is selected for use in the program. Transits are selected on the following basis:

> Choose the first triplet (three consecutive transits for any one scan) encountered, provided the slit-to-slit transit separation is nearly the same for slits 1-2 as it is for slits 2-3. This test is required because slit one transits were questionable on two of the observation days and cannot always be trusted.
>
> Choose triplets from every third data set unless no such triplet exists, in which case choose the first pair of transits from slits 2 and 3. After finding these transits, the appropriate slit correction is applied.
>
> Next, the initial Kepler arc is set up and the appropriate arrays are initialized. Indexing parameters are set so that we may cycle from time zero to the earliest time, then from time zero to the latest transit time. Indexing through the transits then begins. As each transit is considered, a check is made to see which side of time zero it is on. When the first transit forward of time zero is

encountered, some of the basic arrays are reinitialized so that the required integrations are performed in a positive sense.

The first step after any given transit is chosen is to find the appropriate satellite attitude solution (i.e., the attitude prior to or equal to the current time). Then the H matrix and the product A_2 C are defined.

A test is made to see if this transit falls on the current Kepler arc. If not, a rectification takes place which involves forming the initial conditions for the next arc by integrating over the rectification interval (taken to be one hour) along the current Kepler arc. This integration is accomplished by dividing the time interval into nine steps and applying Simpson's rule to each subinterval. This process requires the use of the forces on the satellite which are obtained through the use of the subroutine FORCES.

If the transit under consideration is on the current Kepler arc, the program will solve for a computed transit time within one-half a satellite rotational period of the measured time and will use the difference between these two times (computed - measured) to form the equations which adjust the present initial conditions to the next best set. A vector D is found by integrating from the time at the beginning of the Kepler arc to the computed time. The vectors N and $\dot{N}$ are defined and the scalar U is computed. Next the transformation matrix Φ is defined and appropriately stored in the array V. The current row of the array B and vector A is then set up where A and B are defined as $A = B\,\Delta X$ with ΔX the correction vector to the current set of satellite initial position and velocity. This row in both A and B is then normalized by dividing by the scalar U. This completes the processing for one transit time.

When all n times have been considered, the generalized inverse of B (with dimensions n rows and 8 columns) is found and the correction vector ΔX

is formed as

$$\Delta X = (B^T B)^{-1} B^T A \ .$$

These corrections are then added to the present values of the initial conditions to form the next estimates

$$X_{n+1} = X_m + \Delta X \ .$$

A test of the magnitude of the corrections is made and when all are smaller than some predetermined values, the iterative process is terminated and the final result printed.

In addition to the main program, several subroutines are required. In general, each subroutine serves a single, straight forward purpose suggested by its name. They are:

GENINV	calculates the generalized inverse of an N by M matrix
ORBIT	determines the orbital elements given a position and velocity vector
PHIMAT	sets up the 6 x 6 matrix $\bar{\Phi}$
FORCES	forms the forces for the satellite at a given time due to the earth's gravitational field, radiation pressure, and perturbations due to the sun and moon
CVEC	forms the integral $\int \bar{\Phi}^{-1}(s)\, \bar{F}(s)\, ds$
XBAR	sets up the position and velocity vector to the satellite given the orbital elements
ANOM	computes the true anomaly at any given time from the orbital elements.
BMAT	sets up the transformation matrix (3 x 3) B
EMAT	sets up the Euler matrix (3 x 3) and its partial derivative with respect to the azimuth angle s.
HMAT	sets up the H matrix (3 x 3)

PMOON	calculates the position and velocity vector to the moon at any given time from the tabulated values of the ephemeris

II. NAVIGATION GEOMETRIES AND PERFORMANCE

A. Ejected Particles

Neither of the two ejected particles (probes) furnished useful navigation information because of the short time interval over which each was observed; however, consideration will first be given to the geometry of the position of the probe as viewed from the spacecraft.

The salient characteristics of the probe motion are obtained by assuming that the only force acting on the satellite and probe is an inverse-square central force field.

In order to most conveniently describe the vector from the spacecraft to the probe, $\bar{R}_2$ (t) - $\bar{R}_1$ (t), a coordinate system is introduced which moves with the spacecraft (Figure 4-7). This system will be denoted as R, with unit vectors $\hat{r}$, $\hat{s}$, $\hat{z}$, such that $\hat{r} = \bar{R}_1$ (t)/$|\bar{R}_1$ (t)$|$, $\hat{s}$ is in the plane of the spacecraft so that $\dot{\bar{R}}_1$ (t) $\cdot$ $\hat{s} \geq 0$, and $\hat{z} = \hat{r} \times \hat{s}$.

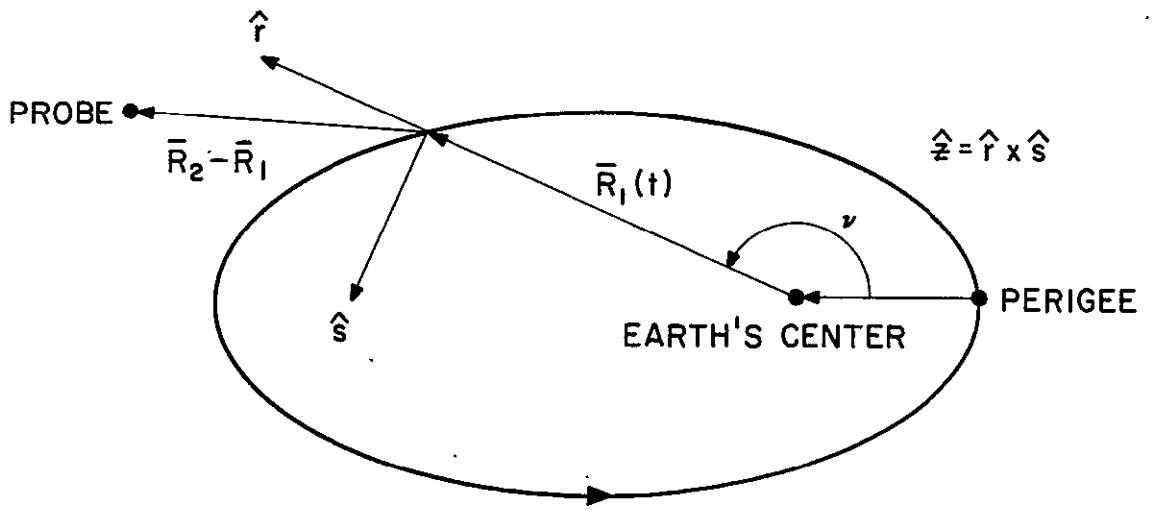

Figure 4-7: The Coordinate System R

Let the direction of ejection be determined with respect to R at the time of ejection, t_0, by the angles A_o and E_o shown in Figure 4-8 so that the velocity of ejection is

$$\overline{\Delta v} = \Delta v \, (\cos E_o \cos A_o \, \hat{r} \, (t_0) + \cos E_o \sin A_o \, \hat{s} \, (t_0) + \sin E_o \, \hat{z}).$$

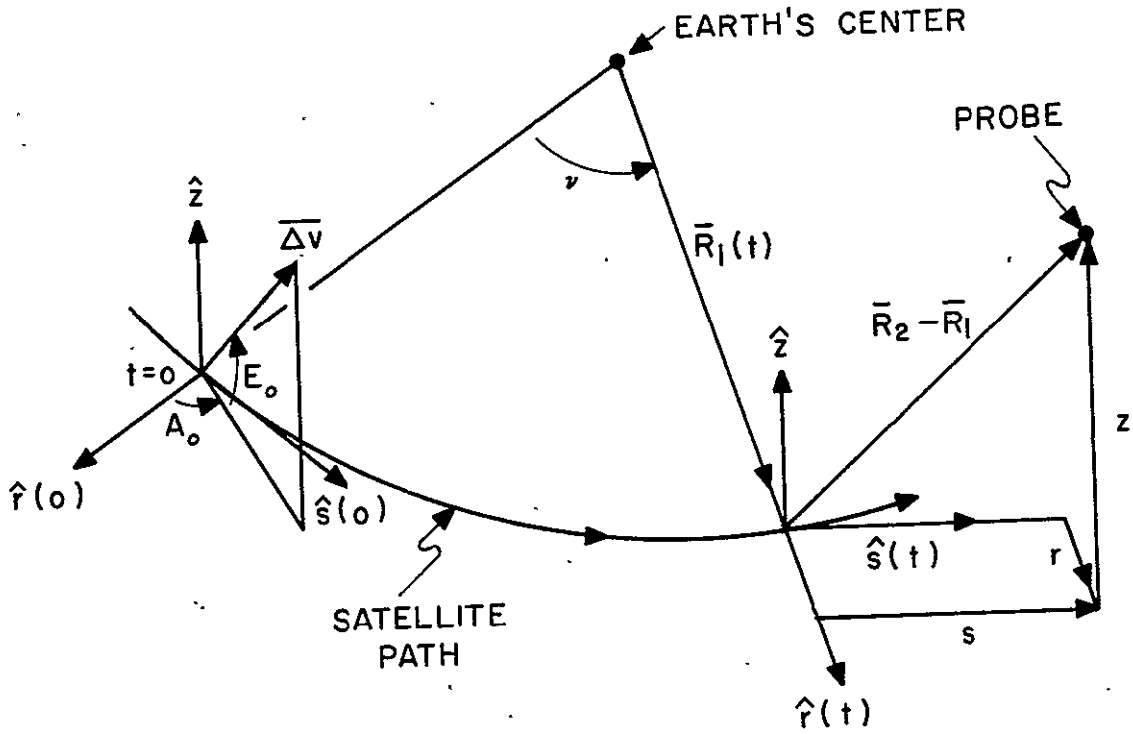

Figure 4-8: The Ejection Direction as Defined by A_o and E_o

Also, let the generic position of the probe with respect to the satellite be given

$$\bar{R}_2 \, (t) - \bar{R}_1 \, (t) = r \, \hat{r} \, (t) + s \, \hat{s} \, (t) + z \, z.$$

Then, if the orbit of the spacecraft is circular and Δv and t are small, it may be shown that

$$
\begin{aligned}
r &= \frac{\Delta v}{\dot{\nu}} \cos E_o \left(\cos A_o \sin \nu + 2 (1 - \cos \nu) \sin A_o\right) \\
s &= \frac{\Delta v}{\dot{\nu}} \cos E_o \left(-2 \cos A_o (1 - \cos \nu) + (4 \sin \nu - 3 \nu) \sin A_o\right) \\
z &= \frac{\Delta v}{\dot{\nu}} \sin E_o \sin \nu
\end{aligned}
\qquad (18)
$$

where ν = angle from $\hat{r}$ (0) to $\hat{r}$ (t) (Figure 4-8).

Figure 4-9 is a plot of the probe's path as viewed from the moving system, R, for ejection such that Δv = 1 mph, E_o = 0, A_o = 0 and 90^o (two cases). It is assumed that the orbital period of the satellite is 24 hours.

If A_o = 0, the ejection is in the radial direction. However, as the probe gains distance from the earth's center, its tangential velocity is insufficient to yield an angular rate equal to that of the satellite and it falls behind. After 6 hours, it achieves its maximum radial distance from the satellite, approximately 3 miles. At 12 hours, its radial distance is zero, but its tangential distance is -15 miles. At 24 hours it returns to its origin position. The motion of the particle in the moving system is an ellipse.

If $A_o = 90^o$, i.e., the ejection is in the tangential direction, then the ejection speed simply is added to the satellite speed to yield the particle speed. This results in an orbit of the probe whose major axis length and period are significantly greater than that of the satellite. Hence, the probe falls behind the satellite a distance which increases approximately linearly with time. After 24 hours its tangential distance is -72 miles. Since a small component of $\overline{\Delta v} \cdot \hat{s}$ (0) results in a large separation between the spacecraft and probe for $t \geq 12$, ejection must take place so that $\overline{\Delta v} \cdot \hat{s}$ (0) $\doteq$ 0.

From (18) the direction to the probe may be written

Figure 4-9: Position of Probe in the Orbital Plane for Ejection in the Radial and Tangential Directions. Δv = 1 mph

$$\tan A = \frac{-2 \cos A_o \ (1 - \cos \nu) + (4 \sin \nu - 3 \nu) \sin A_o}{\cos A_o \sin \nu + 2 \ (1 - \cos \nu) \sin A_o} = \frac{U}{V}$$

$$\sin E = \frac{W}{\sqrt{(U^2 + V^2) \cos^2 E_o + W^2}}, \quad W = \sin E_o \sin \nu \tag{19}$$

from small ν,

$$A = A_o - \nu + 0 \ (\nu^3)$$
$$E = E_o - \frac{4}{3} \nu^2 \tan \epsilon_o \cos^2 \alpha_o + 0 \ (\nu^3)$$

where

A = azimuth of $\overline{R}_2 \ (t) - \overline{R}_1 \ (t)$ with respect to $R \ (t)$,

E = elevation of $\overline{R}_2 \ (t) - \overline{R}_1 \ (t)$ with respect to $R \ (t)$.

From (18) and (19) the following general conclusions may be drawn:

1. The distance between the probe and spacecraft is a linear function of the ejection speed Δv.
2. $z \ (t)$ is a function of $\overline{\Delta v} \cdot \hat{z}$ but is independent of A_o. Moreover, $z \ (t)$ is a periodic function of t.
3. $r(t)$ and $s \ (t)$ are functions of $\overline{\Delta v} \cdot \hat{r} \ (t_0)$ and $\overline{\Delta v} \cdot \hat{s} \ (t_0)$ but are independent of $\overline{\Delta v} \cdot \hat{z}$.
4. $r \ (t)$ is a period function of t, but $s \ (t)$ is a period function of t only if $A_o = 0$ of 180°, i.e., ejection is in the plane defined by the earth's center and $\hat{z}$.
5. The direction to the probe is independent of Δv.
6. The azimuth at any time, A, is independent of the initial elevation, E_o.

Condition (5) is of particular interest. Recall that the proposed instrument measures transit times of targets, but these measurements are

quite similar to directional measurements. Hence, it must be inferred that the measurements are not effective in determining the ejection speed of the probe. Conversely, an error in assumed ejection speed has little effect upon the accuracy of the total system if the problem is formulated in terms of the eight unknowns $\delta \hat{X}_1$ (0), e_o, a_o.

Figure 4-10 gives the path of the probe as a function of time in terms of its right ascension, α_c, and declination, δ_c. Here it is assumed that the satellite's orbit is circular, equatorial, and has a 24 hour period. The elevation of ejection $E_o = -45^o$, various ejection azimuths are shown. Note that the path for $0 \leq t \leq 12$ hours is a weak function of A_o but a strong function of A_o for $24 \leq t \leq 36$ hours.

In order to detect the probe, ejection must take place when the satellite is sunlit. However, the sun then limits the portion of the celestial sphere over which the probe and stars can be observed. In fact, an azimuthal regional of approximately $\pm 100^o$ centered at the sun's right ascension is lost. This lost region is indicated in Figure 4-10. This figure shows that ejection must take place so that $-8^o \leq A_o \leq 8^o$ or $-172^o \leq A_o \leq 188^o$ if the probe is to be in the unblocked field of view for $24 \geq t \geq 36$ hours.

Figure 4-11 and 4-12 plots the instrument magnitude as a function of time for $\Delta v = 3$ ft/sec, $-8^o \leq A_o \leq 2^o$, $E_o = -45^o$, -40^o. In obtaining these figures, the attenuation of the optical system as a function of angle between the direction of the observed target and optic axis is taken into account. Also included is a correction for the a-priori estimate of instrument magnitude as a function of probe distance. It turned out that the a-priori estimate of instrument magnitude is approximately 0.5 magnitude too small.

The ejection mechanism was designed so that $\Delta v = 3$ ft/sec., and $E_o = -45^o$. The limiting instrument is approximately 3.0; hence, if the probe is to be observed for $t \geq 24$ hours, then Figure 4-12 implies that $-8^o \leq A_o \leq 2^o$.

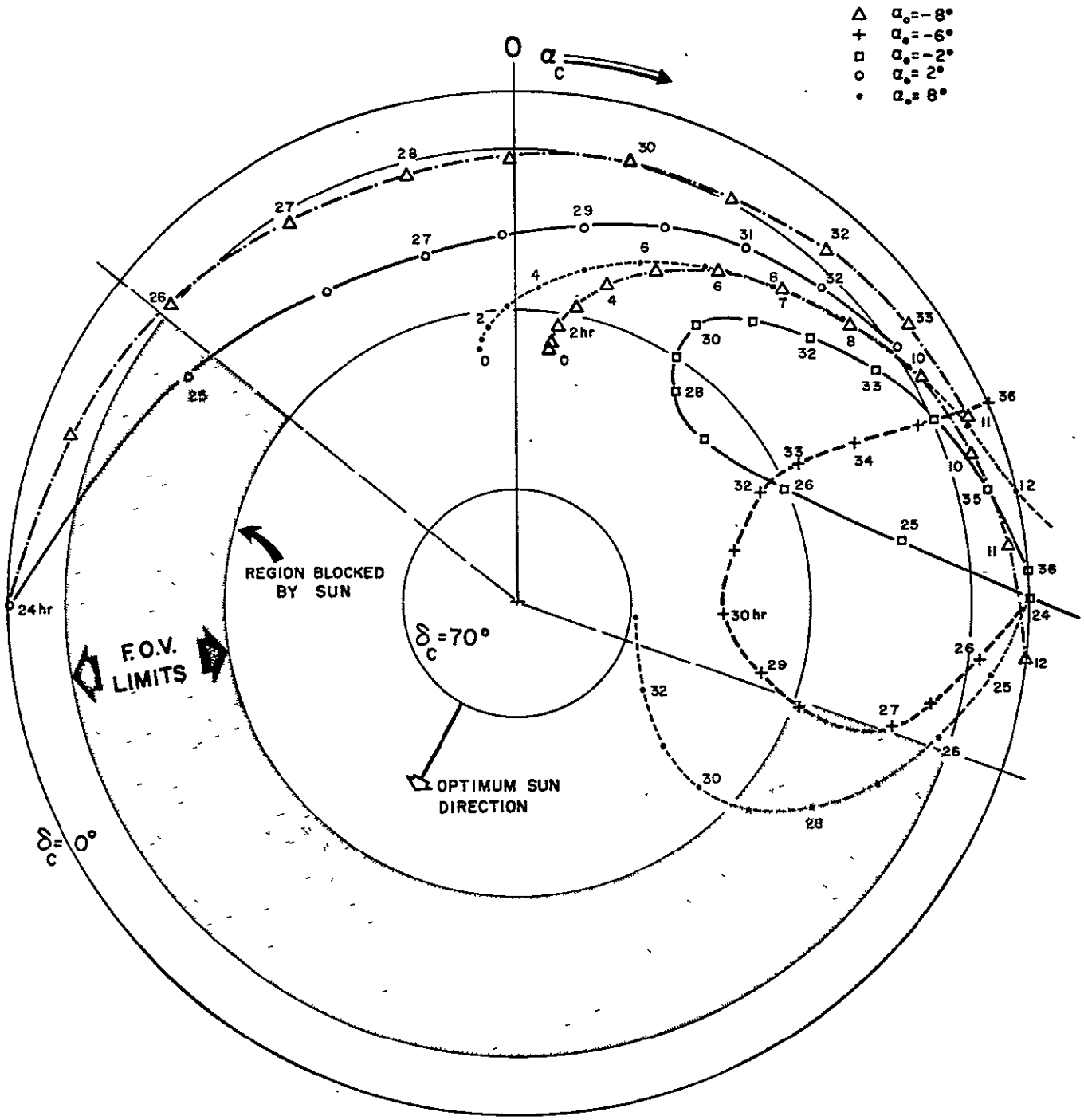

Figure 4-10: Path of Probe as a Function of Time for Various Initial Azimuths. E_o = -45°

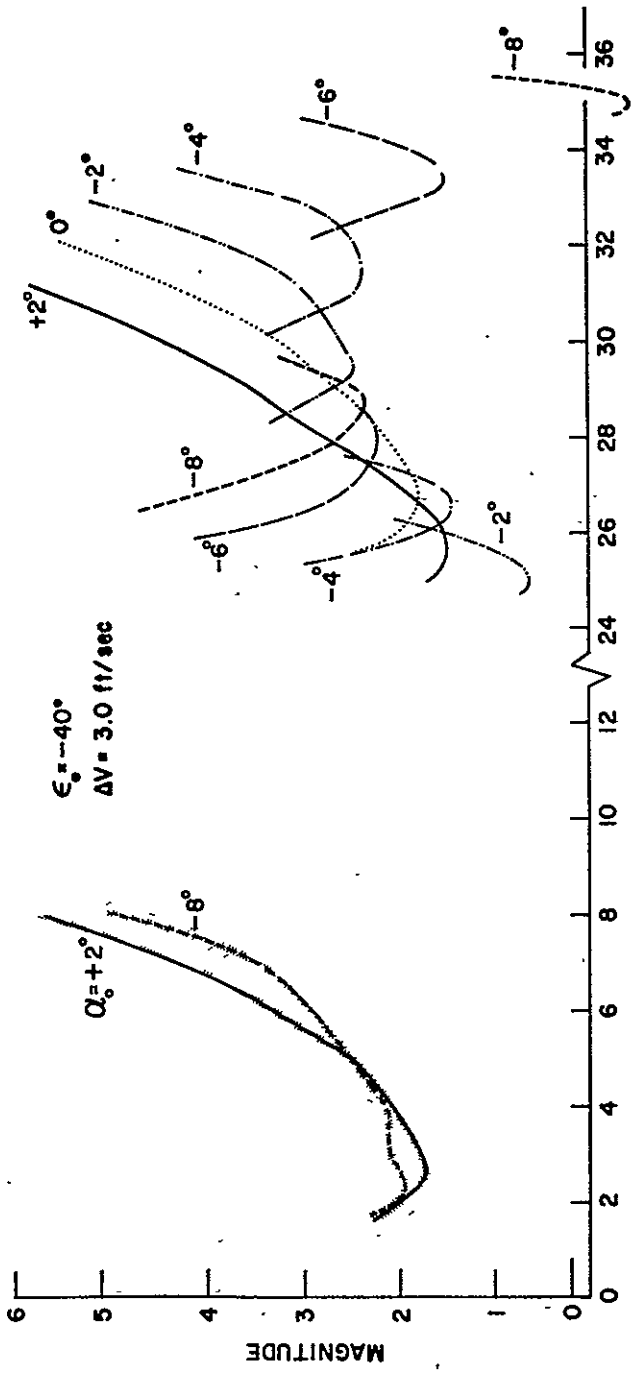

Figure 4-11: Magnitude of Probe as a Function of Time for Various Initial Azimuths, A_o. Full Phase. $E_o = -40^o$, $\Delta v = 3$ ft/sec

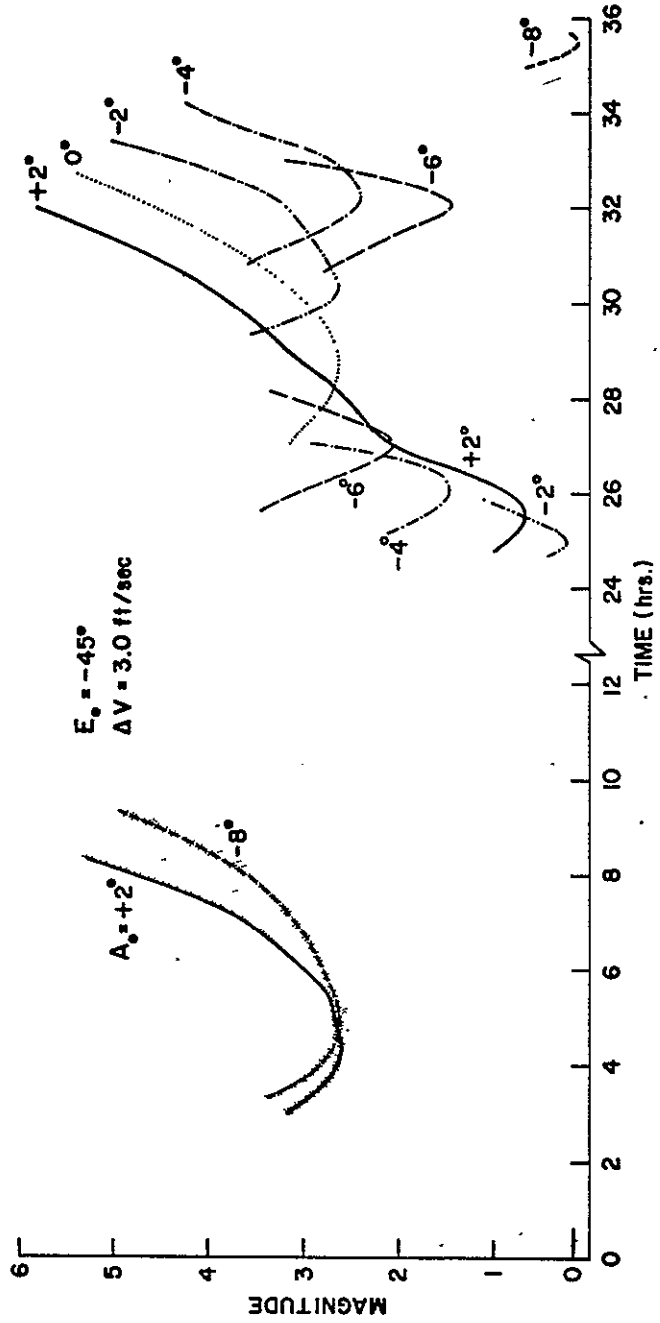

Figure 4-12: Magnitude of Probe as a Function of Time for Various Initial Azimuths, A_o 1 Full Phase. E_o = -45°, Δv = 3 ft/sec

If the probe could be ejected so that $\Delta v < 3$ ft/sec., then the allowable interval for A_o would be increased. However, if Δv is decreased, the azimuthal direction of ejection is more difficult to control. Conversely, if Δv is increased , the allowable interval for A_o decreases. $\Delta v = 3$ ft/sec. is optimum. However, comparison of Figures 4-11 and 4-12 shows that $E_o = -40^o$ generally yields greater probabilities of detection than does $E_o = -45^o$.

In summary, the ejection mechanism was designed so that $\Delta v = 3$ ft/sec., $E_o = -45^o$, and ejection direction was radial with respect to the satellite's center as shown in Figure 4-13. However, $E_o = -40^o$ is to be preferred. In any event, the allowable range of azimuthal directions imposed by the present optical system is narrow (10^o). Neither probe was ejected within this range and, hence, the observation time of each was small.

2. Navigation Performance

The first probe was ejected with $A_o = 50^o$ which is well outside the permissible azimuthal range for the experiment. No useful probe sightings were obtained.

The second probe was observed until 2.5 hours after ejection. At this time it was calculated to be about 8.6 miles from the spacecraft. All attempts to obtain navigation information from these sightings proved fruitless.

Using the position of the velocity of the satellite at the time of ejection as supplied by Goddard Space Flight Center, along with 149 probe transits $1^h\ 47^m$ (Day 202), the direction of the ejection was obtained as

$a_o = 261.274^o$ (right ascension)
$e_o = 22.672^o$ (declination).

The resulting directions in terms of the azimuth and elevation with respect to R (0) was

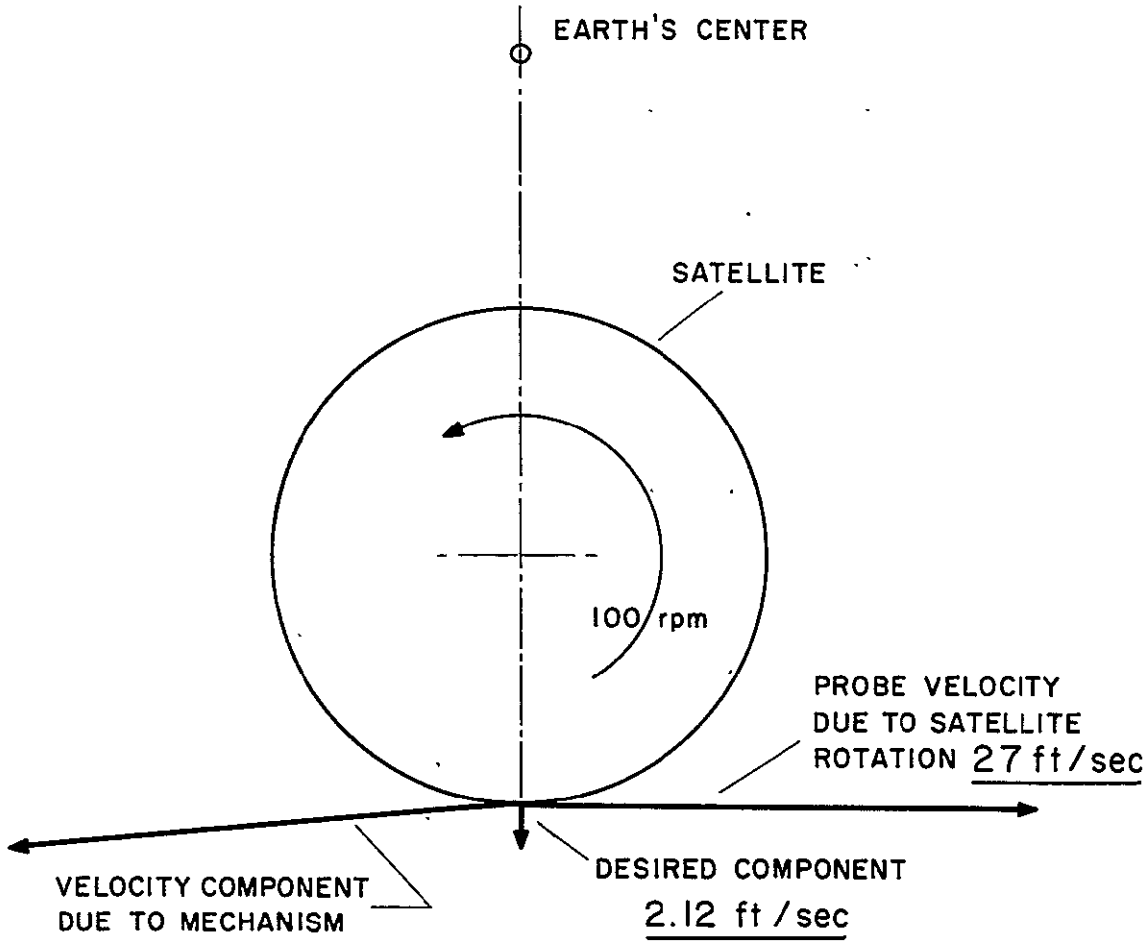

Figure 4-13: Probe Velocity Due to Satellite Rotation and Desired Ejection Component Perpendicular to Spin Axis

$A_o = 9.08^o$

$E_o = -22.76^o$.

A standard deviation of 34.4×10^{-6} seconds was obtained between the computed and measured times.

3. Simulated Navigation Results

Since no results were obtained using real data because each probe was ejected in an unfavorable direction, one is forced to rely upon simulated data to give some indication of the system's potential.

Since the satellite is presently spinning faster than the nominal 100 RPM (about 108 RPM), it is unlikely that the third probe could be ejected in such a manner that it could be seen on the spacecraft's second orbit. Hopefully, however, it will be ejected nearer to the desired direction than the first two probes. Assuming this to be the case, an error analysis for short arcs will be presented. The following is assumed:

1. Equatorial, 24 hour, circular spacecraft orbit (Kepler force field)
2. Ejection velocity given by

   $A_o = 9^o$

   $E_o = 40^o$

   $\Delta v = 3$ ft/sec.

With this information, a set of probe transits of three slits is constructed for $0 \leq t \leq 6$ hours. To each member of this set of correct times an error is added. Each error is chosen from a distribution which is normal with a mean of zero and a standard deviation of 40×10^{-6} seconds. These erroneous times are then used to compute the initial position and velocity of the spacecraft along with the direction of ejection. Errors in the initial position and velocity were then computed as true quantity minus erroneous quantity. Results are shown in Table 4-IV.

In Table 4-IV, Σ is the standard deviation of the difference between the input transit times and the computed transit times (computed with the converged solution). Note that Σ is less than 40×10^{-6} seconds, as it should be. n is the number of transits used, and the last column is the distance between the probe and spacecraft at the end of the sighting duration, T, given in the first column.

The greatest distance at which the second probe was sighted was 13.8 km. Hence, it is optimistic to assume probe sighting after 4 hours during the first orbit. Hence, if the probe is sighted only on the first orbit, and no additional information is given, then 800 km is a lower bound of the initial position error.

Table 4-V was constructed using similar assumptions to those used for Table 4-IV except that a near optimum ejection direction was chosen. Sightings were taken for $.5 \leq t \leq 6$ hours and for $24.4 \leq t \leq 26$ hours. Column 1 in Table 4-V is the time of the last sightings used, and the distance given in the last column is the maximum distance between the probe and spacecraft in the sighting interval. Note that considerable improvement in the position determination is afforded if sightings over the second orbit are obtained.

In both Tables 4-IV and 4-V, the errors in any component of position or velocity appear to be correlated when looked upon as a function of the sighting duration. This seeming correlation occurs because only one list of erroneous times was generated. This list was then truncated as the sighting duration was shortened.

It is also noted in Tables 4-IV and 4-V that the major error is in the direction perpendicular to the orbital plane. This conclusion is contradictory to an observer's intuition. A possible explanation may be related to the fact that the instrument is less efficient in determining elevation than azimuth. Tables 4-VI and 4-VII indicate the effect of errors in various

TABLE 4-IV

OUTPUT ERROR AS A FUNCTION OF PROBE SIGHTING DURATION. SIMULATED DATA

$A_o = 9^o$, $E_o = -40^o$, $\Delta v = 3$ FT/SEC

T(hrs)	Position (km)			Velocity (m/sec)			Ejection Dir.		Σ		Dist.
	δx	δy	δz	$\delta \dot{x}$	$\delta \dot{y}$	$\delta \dot{z}$	δa	δe	(sec x 10^{-6})	n	(km)
6	- 9.0	-27.4	- 71.6	3.0	5.0	3.6	.020	.009	24.4	639	21.6
5	-15.3	-16.9	-131.0	2.7	3.6	8.0	.020	.009	24.6	534	18.0
4	65.9	169.3	674.4	-35.2	28.5	21.5	.021	.004	23.7	429	14.3
3	No convergence									324	10.7

t = 0 is time of probe ejection

δx = true x (0) -- erroneous x (0) = error in x (0)

δa = error in right ascension of ejection direction

δe = error in declination of ejection direction

Σ = standard deviation of difference between input (true) times and computed times resulting from erroneous orbit

n = number of transits used

Dist. = maximum distance between probe and satellite in sighting duration

TABLE 4-V

OUTPUT ERROR AS A FUNCTION OF PROBE SIGHTING DURATION. SIMULATED DATA

$A_o = -2^o\ 19'$, $E_o = -40^o$, $\Delta v = 3$ FT/SEC.

T(hrs)	Position (km)			Velocity (m/sec)			Ejection Dir. (deg)		Σ	n	Dist.
	δx	δy	δz	$\delta \dot{x}$	$\delta \dot{y}$	$\delta \dot{z}$	δa	δe	(sec x 10^{-6})		(km)
26	- 5.6	9.7	46.3	.398	- .957	- .560	-.020	-.004	24.2	810	22.2
25	- 3.8	11.4	57.8	.561	- .970	- .652	-.020	-.006	24.4	693	22.2
24.5	- .35	- .42	54.7	- .049	.003	.060	-.020	-.006	24.4	639	22.2
6	34.0	54.1	104.2	2.41	9.25	2.75	-.021	-.002	24.9	594	22.2
5	- 59.7	66.8	- 151.6	- 6.75	-12.6	10.8	-.020	-.003	24.1	486	18.3
4	-224.0	524.1	-1660	-73.5	-94.4	-6.10	-.017	-.008	23.3	381	14.4
3	No convergence										10.6

TABLE 4-VI

EFFECT OF VARIOUS ERRORS IN ELEVATION FOR CROSSING OF SLITS 1, 2 AND SLITS 1, 3* δE (DEG)

Elevation of Target, E	Input Errors								
	$\delta\Gamma = .1^\circ$	$\delta\sigma = .1^\circ$	$\delta\xi_2 = .1^\circ$	$\delta\epsilon = .1^\circ$		$\delta t_1 = 40$ μsec		$\delta t_2 =$ 40μsec	$\delta t_3 =$ 40μsec
5°	0	-.100	-.010	0	0	-.121	Errors are ½ those of previous column	Negative those of sixth column	Negative those of seventh column
8°	.028	-.099	-.010	.001	0	-.119			
11°	.054	-.098	-.010	.002	0	-.117			
14°	.079	-.096	-.010	.003	0	-.115			
17°	.103	-.094	-.010	.004	0	-.112			
19°	.125	-.092	-.010	.005	0	-.108			
22°	.145	-.089	-.010	.006	0	-.104			
24°	.162	-.086	-.010	.007	0	-.100			
27°	.178	-.083	-.010	.008	0	-.096			
29°	.191	-.079	-.010	.008	0	-.092			
32°	.202	-.076	-.010	.009	0	-.088			
34°	.212	-.073	-.010	.010	0	-.083			
36°	.221	-.069	-.010	.011	0	.-079			
38°	.226	-.066	-.010	.011	0	-.075			
40°	.232	-.063	-.010	.012	0	-.071			
Slits Used	δE same for 1,2 or 1,3			1,2	1,3	1,2	1,3	1,2	1,3

* See Volume 3, Figure 2, for a definition of ξ_1 and ξ_2; Figure 3 for Γ, σ, ϵ; Figure 5 slit numbering and orientation.

TABLE 4-VII

EFFECT OF VARIOUS ERRORS ON AZIMUTH FOR CROSSING OF SLITS 1, 2 AND SLITS 1, 3 δA (DEG)

Elevation of Target, E	Input Errors							
	$\delta\xi_1 = .1^\circ$	$\delta e = .1^\circ$		δt_1 = 40 μsec		δt_2 = 40 μsec	δt_3 = 40 μsec	ξ_2, σ, Γ
5°	-.001	0	0	0	.012	.024	.012	Errors of $.1^\circ$ in
8°	-.001	-.005	-.005	0	.012	.024	.012	these parameters
11°	-.002	-.011	-.011	0	.012	.024	.012	yield negligible
14°	-.002	-.016	-.017	0	.012	.024	.012	azimuth errors
17°	-.003	-.021	-.022	0	.012	.024	.012	
19°	-.004	-.026	-.028	0	.012	.024	.012	
22°	-.004	-.032	-.033	0	.012	.024	.012	
24°	-.005	-.037	-.037	0	.012	.024	.012	
27°	-.005	-.042	-.044	0	.012	.024	.012	
29°	-.006	-.048	-.050	0	.012	.024	.012	
32°	-.006	-.053	-.055	0	.012	.024	.012	
34°	-.007	-.058	-.061	0	.012	.024	.012	
36°	-.007	-.063	-.066	0	.012	.024	.012	
38°	-.008	-.068	-.072	0	.012	.024	.012	
40°	-.008	-.074	-.078	0	.012	.024	.012	
Slits Used	1,2 or 1,3	1,2	1,3	1,2	1,3	1,2	1,3	1,2 or 1,3

inputs upon elevation and azimuth error respectively. In constructing these tables it is assumed that transits occur in Slits #1 and #2, also Slits #1 and #3 (#2 is center slit), but not in all three slits. The geometry of the slits and definition of symbols were discussed in Chapter 3.

The first three columns depicting the output error, δE, show the effects of errors of 0.1° in Γ, σ, and ξ_2 upon the elevation. For these parameters the same errors are obtained if Slits 1, 2, or 1, 3 are used. The next two columns show the effect of a 0.1° error in ϵ if Slits 1, 2 or 1, 3 are used. The fifth column is the resulting error if an error in t_1, the transit time pertinent to the first slit, of 40×10^{-6} seconds is made and Slits 1, 2 are used. If Slits 1, 3 are used, the errors are multiplied by one-half as indicated in the sixth column. The last two columns give the effect of 40×10^{-6} second errors in t_2 and t_3 respectively.

The columns in Table 4-VI may be interpreted in a manner similar to those in Table 4-VII. Note that time errors produce roughly five times greater error in elevations than in azimuth. Moreover, the elevation is more sensitive to slit parameter errors than is the azimuth.

4. Conclusions

Two probes were ejected, neither of which furnished information useful for navigation because of unsuitable ejection directions. Moreover, it is doubtful that the third probe, which is to be ejected in mid-summer of 1969, will yield good navigation results. This is because the spacecraft will be spinning faster than the nominal 100 rpm. Moreover, it is difficult to envision the ejection mechanism being improved with age.

Even though the navigation system was unable to obtain its goals, the system is potentially useful if the ejection direction can be controlled within $\pm 5^{\circ}$. This control would be more easily achieved if the spacecraft were spinning more slowly (say 50 rpm). Also more attention should be paid to obtaining an optical system whose response is more nearly uniform

throughout the field of view. The lens system used attenuated greatly the response from a target as this target was moved off the optical axis. The effect of this attenuation can be seen by comparing Figure 4-12 and Figure 4-14. Figure 4-12 was obtained by using the actual off-axis attenuation of the lens system. Figure 4-14 was obtained by assuming no off-axis attenuation. Note the improvement in probe detectability.

B. Moon

The moon was used as a secondary in the sightings listed in Table 4-VIII. These sightings yielded moderately accurate results. However, the accuracy of these results is about two orders of magnitude less than that which can be obtained by earth-bound radar. The situation would probably be reversed for orbits about Mars if the moons of Mars, Deimos and Phobos were used as secondaries.

No measurements were made 1 October 1968 because of a failure in the satellite-to-ground communications equipment. For the same reason, the measurement duration of 30 September 1968 is extremely short.

1. Geometry of Sightings

When the satellite is in the sunlight, approximately 190° of the azimuthal field of view is lost for all targets, including the moon. Also, the moon is sufficiently bright so that 50° of the azimuthal field is lost for stellar targets if the moon is in the field of view. Hence, if the satellite is sunlit, and the moon is in the field of view, then only 120° of the azimuthal field is available for stellar targets. A field this small is generally insufficient for an accurate attitude determination since the spacecraft attitude must be found before the orbit determination can be accomplished. The moon can be used as a secondary only if the satellite is in the earth's shadow. This was the case for all sighting times shown in Table 4-VIII.

Figure 4-15 gives the declination and right ascension of the moon for

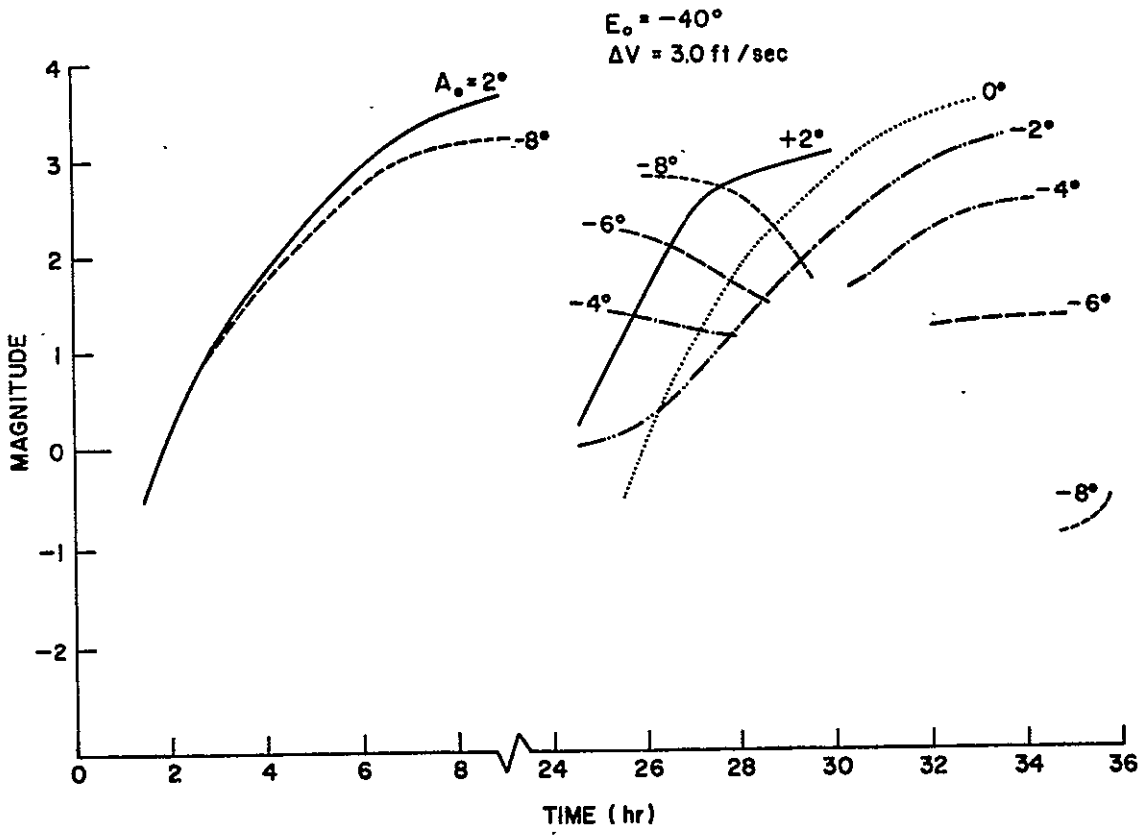

Figure 4-14: Magnitude of Probe as a Function of Time for Various Initial Azimuths, α_o. Full Phase. $\epsilon_o = -40^o$, $\Delta v = 3$ ft/sec. Lens Systems Assumes with No Off-Axis Attenuation

TABLE 4-VIII

TIMES AT WHICH SIGHTINGS OF THE MOON WERE MADE

Day	Initial Time	Final Time	Duration
5 Sept. 68	3.03 hr.	3.22 hr.	0.19 hr.
6 Sept. 68	2.95 hr.	3.03 hr.	.08 hr.
25 Sept. 68	2.93 hr.	3.43 hr.	.50 hr.
26 Sept. 68	2.78 hr.	3.43 hr.	.55 hr.
27 Sept. 68	2.66 hr.	3.41 hr.	.74 hr.
28 Sept. 68	2.68 hr.	3.41 hr.	.72 hr.
29 Sept. 68	2.54 hr.	3.39 hr.	.85 hr.
30 Sept. 68	3.26 hr.	3.28 hr.	.02 hr.
2 Oct. 68	2.63 hr.	3.29 hr.	.66 hr.
3 Oct. 68	2.95 hr.	3.35 hr.	.40 hr.

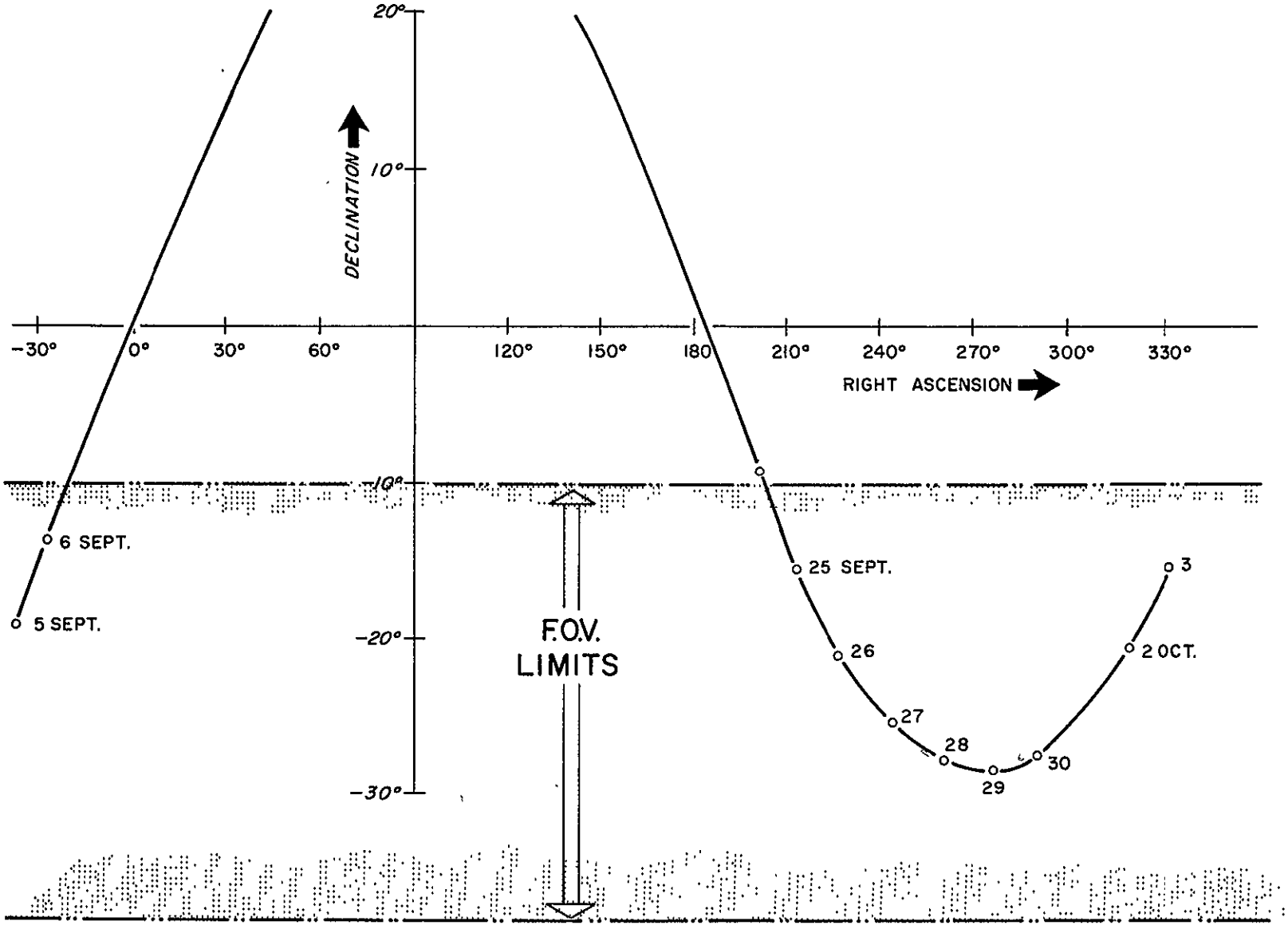

Figure 4-15: Path of Moon with Respect to Instrument Field of View

each of the 10 days on which sightings were made. No sightings were made from 7 September to 24 September because the moon was not within the instrument's field of view.

Figure 4-16 is a plot of the path of the moon and the orbit of the satellite as projected onto the plane of the moon's orbit. Also shown in this figure are the in-plane positions of the moon and satellite at the times of the sightings. Note that all sightings are made when the satellite is at approximately the same position with respect to inertial space. This occurs because all sightings were taken when the satellite was in the earth's shadow.

2. Correction to Transit Times

The photomultiplier output electronics are designed for optimum operation for stellar targets. Hence, these electronics are driven beyond the linear range of operation by a crossing of the moon. This results in a measured transit time which is dependent on the moon's intensity as viewed from the spacecraft. Therefore, the measured transit times must be corrected as a function of the moon's phase. In an actual application of the technique, this correction function must be obtained a-priori. This was not done. Instead, the positions of the moon and spacecraft were obtained from Goddard. From these positions a set of transit times was computed. This set was compared with the measured times to obtain the required corrections. A rationale was then given for these corrections and a correction was generated for each slit and each day. A more complete discussion of this point is contained in Chapter 2. It is mentioned here so that it is clear that a measure of hedging is present when these corrections are used. Results will also be shown for cases in which no corrections were used. In Table 4-IX these corrections are listed.

On September 5 and 6 the transits obtained for Slit 1 could not be used because of an improper trigger level setting.

TABLE 4-IX

TIME CORRECTIONS TO MOON TRANSIT TIMES

AS A FUNCTION OF DAY AND SLIT NUMBER

Day	Time Correction (Secs. x 10^{-6})		
	Slit 1	Slit 2	Slit 3
5 Sept. 68	Could not be used	101	75
6 Sept. 68	these days	150	150
25 Sept. 68	-90	-72	-43
26 Sept. 68	- 2	-30	-69
27 Sept. 68	15	-56	-60
28 Sept. 68	11	-62	-71
29 Sept. 68	- 4	-62	-73
30 Sept. 68	0	-20	-68
2 Oct. 68	75	50	17
3 Oct. 68	55	87	98

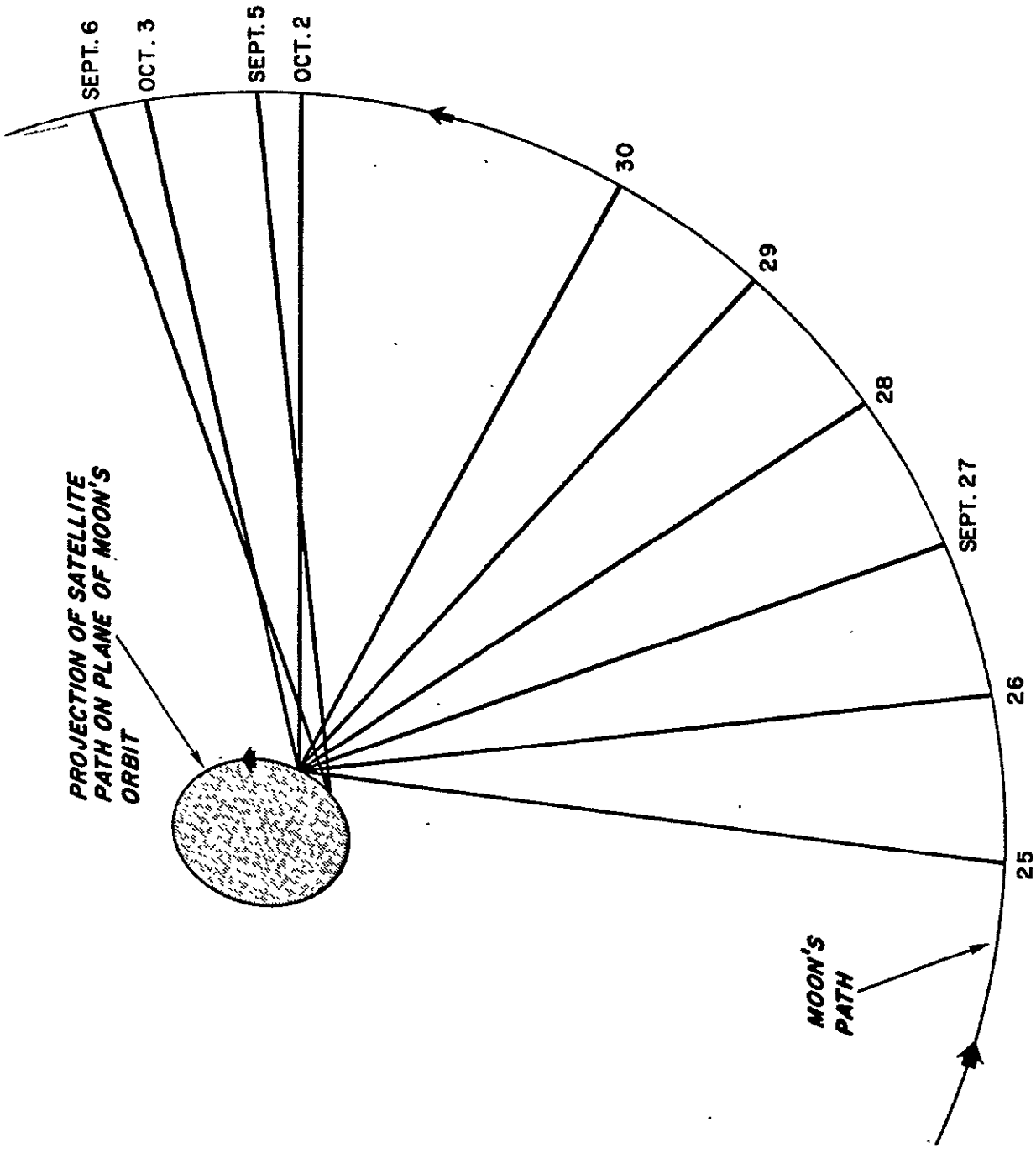

Figure 4-16: Moon's Position and Component of Satellite's Position in Plane of Moon's Orbit at the Times of Sightings

3. Position of Spacecraft as Obtained by Moon Transits

In this discussion, the moon's position is considered known (obtained from Ephemeris) and the spacecraft's position is to be determined. The moon was found to be a more useful target than the probe during the experiment, in that it was observable over a sufficiently long time interval to yield useful navigation data.

One point concerning the moon's use was disappointing. Data obtained on 5 and 6 September could not be used. First, attempts were made to use data from all 10 days and thus obtain a solution valid on the 28 day data gathering interval. Convergence to a solution could not be obtained. The difficulty occurs because of the 19 day interval from 6 September to the next day of data gathering, 25 September (refer to Table 4-IX).

The linearization of the differential equations of motion over this long interval introduces errors of sufficient magnitude to cause nonconvergence. Attempts were also made to use only the 5 and 6 September data to obtain a solution and again convergence was not obtained. This latter difficulty occurs because of the poor geometry defined by only these two days of sighting (Figure 4-16).

Results were obtained for data gathered from 25 September to 3 October. This data was used to obtain solutions valid over the 8 day interval.

Figures 4-17 and 4-18 give the components of spacecraft position error obtained from one set of 722 corrected moon transits. Define

δx = x component of spacecraft position obtained from Goddard Spacecraft Ephemeris minus x component computed from moon transits

with similar definitions for δy and δz. Also, in these figures are the periods over which the observations were made. Note that they comprise an

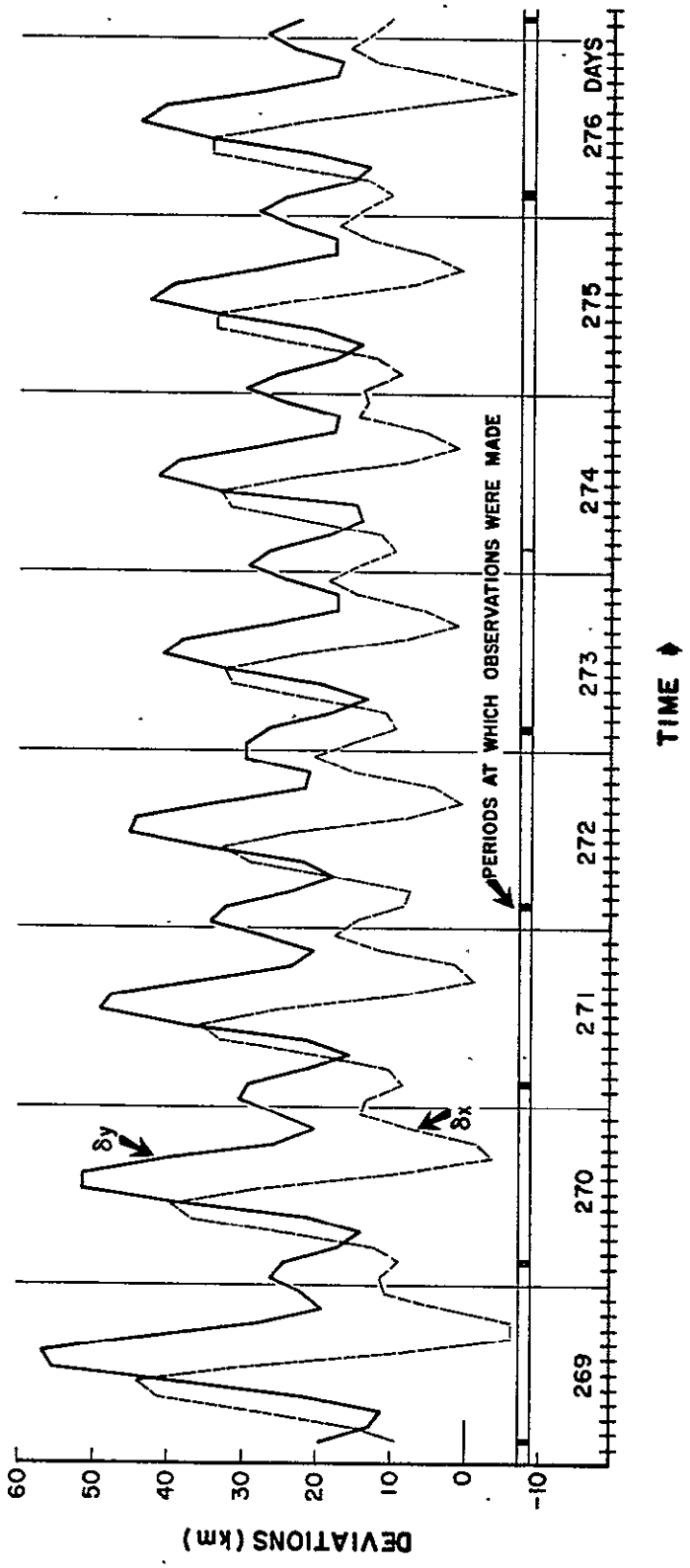

Figure 4-17: Error in x and y Components of Spacecraft's Position as a Function of Time. Moon Used as Target

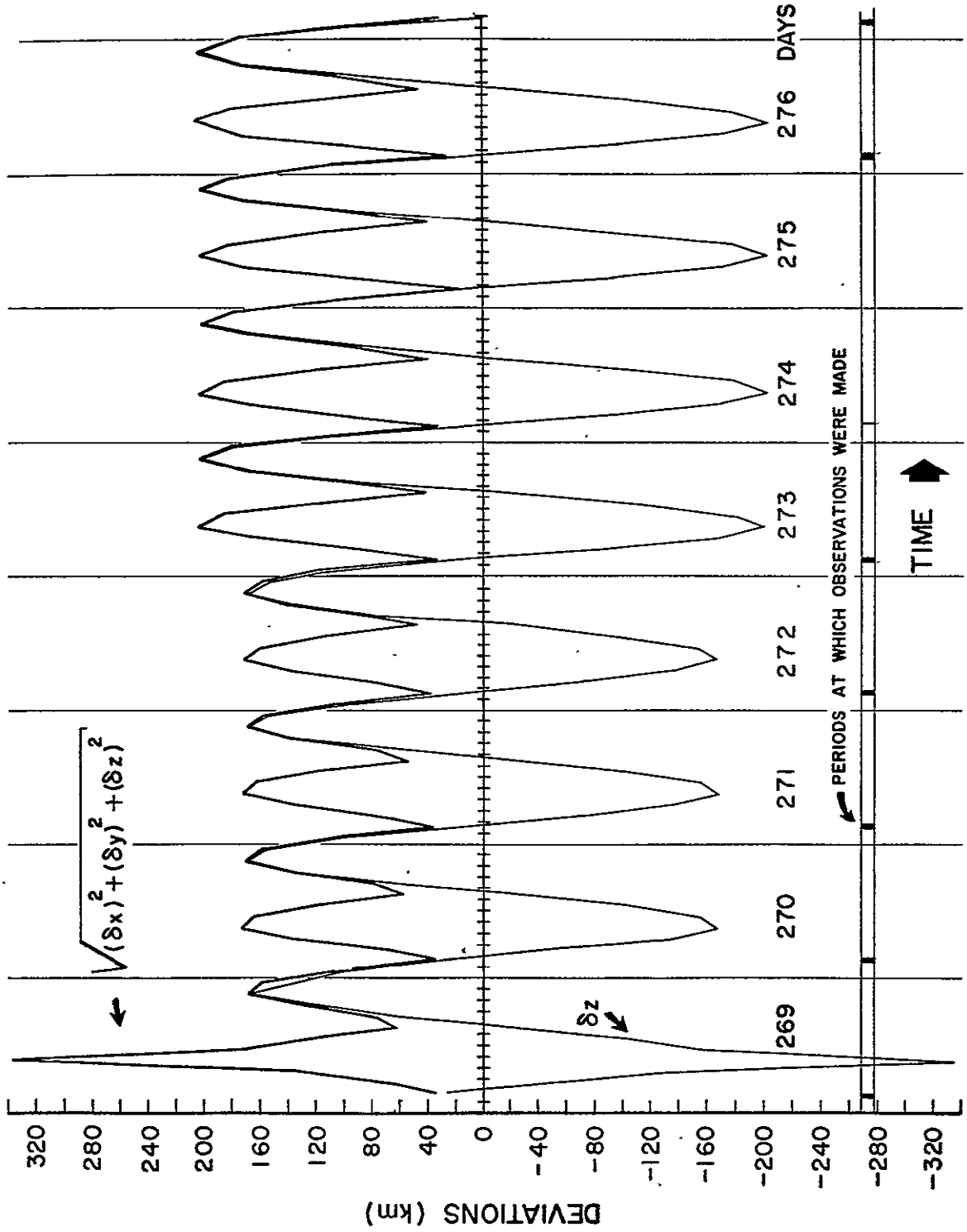
DEVIATIONS (km)
320
280
240
200
160
120
80
40
0
-40
-80
-120
-160
-200
-240
-280
-320
269
270
271
272
273
274
275
276 DAYS
TIME
PERIODS AT WHICH OBSERVATIONS WERE MADE
δz
√(δx)² + (δy)² + (δz)²

extremely small portion of the 8 day interval.

Figure 4-16 shows that $-6 \leq \delta x, \delta y \leq 58$ km in the 8 day interval. However, these errors are significantly smaller during the times observations were made, in that over these times $9 \leq \delta x, \delta y \leq 27$ km.

Figure 4-17 gives δz and $\sqrt{(\delta x)^2 + (\delta y)^2 + (\delta z)^2}$. Note that the error in δz dominates the other components of position error to the point that

$$|\delta z| \doteq \sqrt{(\delta x)^2 + (\delta y)^2 + (\delta z)^2}.$$

The fact that δz is the largest of the component errors is not too surprising in view of the geometry shown in Figure 4-16. Note that all the sightings were taken at approximately the same point along the orbital path. Hence, the orbital path may be rotated about a line joining this point and the earth's center without significantly affecting the transit times. Also note from Figure 4-18 that δz is small over periods at which observations were made and also mid-way between these periods.

Since transits were obtained on every revolution of the spacecraft during the observation periods, a sufficient number of transits were obtained so that three independent sets of transit times could be constructed. Figures 4-17 and 4-18 are based on Set 1. Figures 4-19, 4-20, and 4-21 show the results obtained from these three independent sets. Only the results for Day 269 (25 September) are shown.

Finally, Figure 4-22 is a plot of the position errors for Day 269, using Set 1 transit times, but without using the corrections shown in Table 4-VI. Note that when the correction for the moon's intensity is not applied, the errors increase by a factor of more than 10.

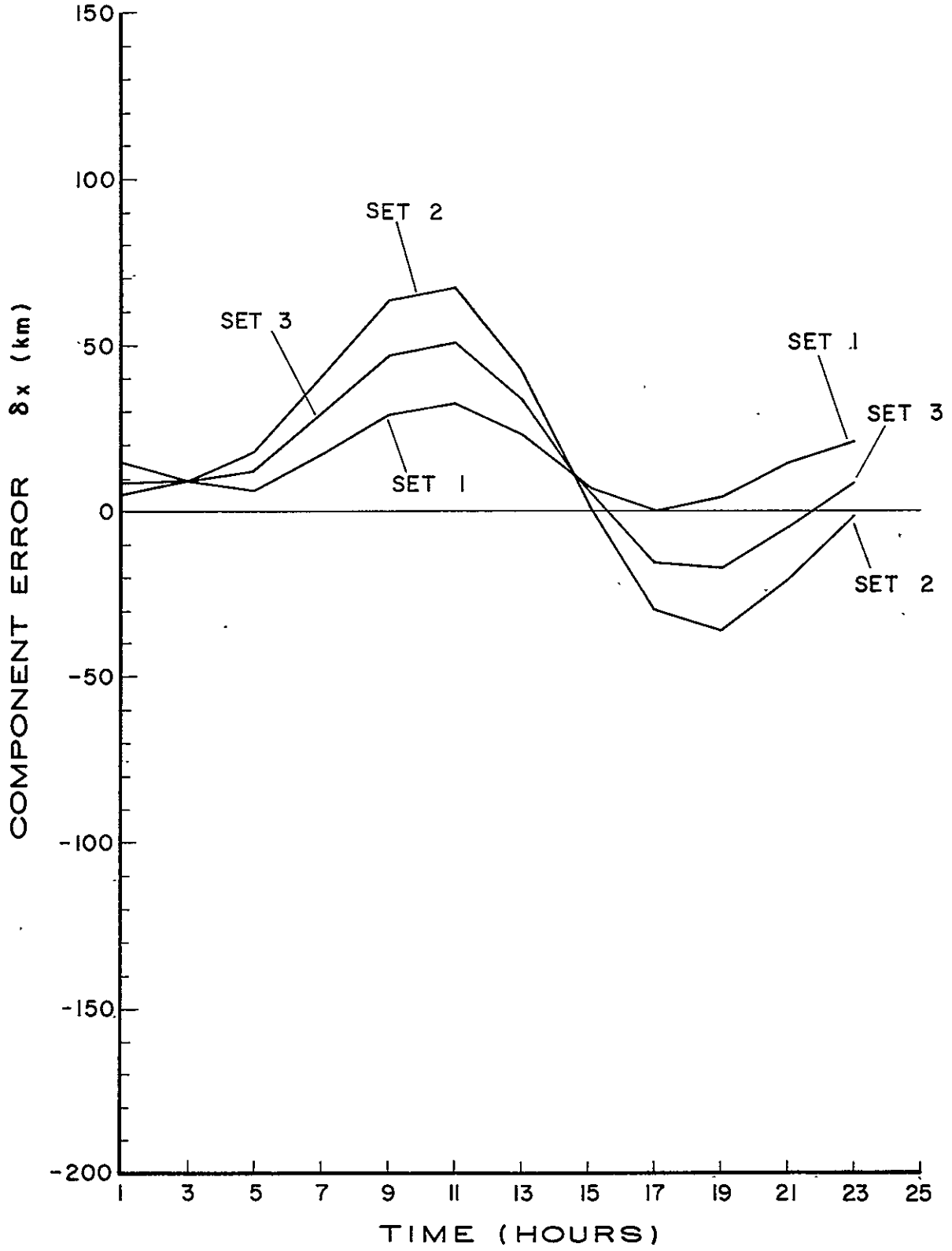

Figure 4-19: Error in x Component of Spacecraft Position for Day 269. Three Distinct Sets of Transit Times

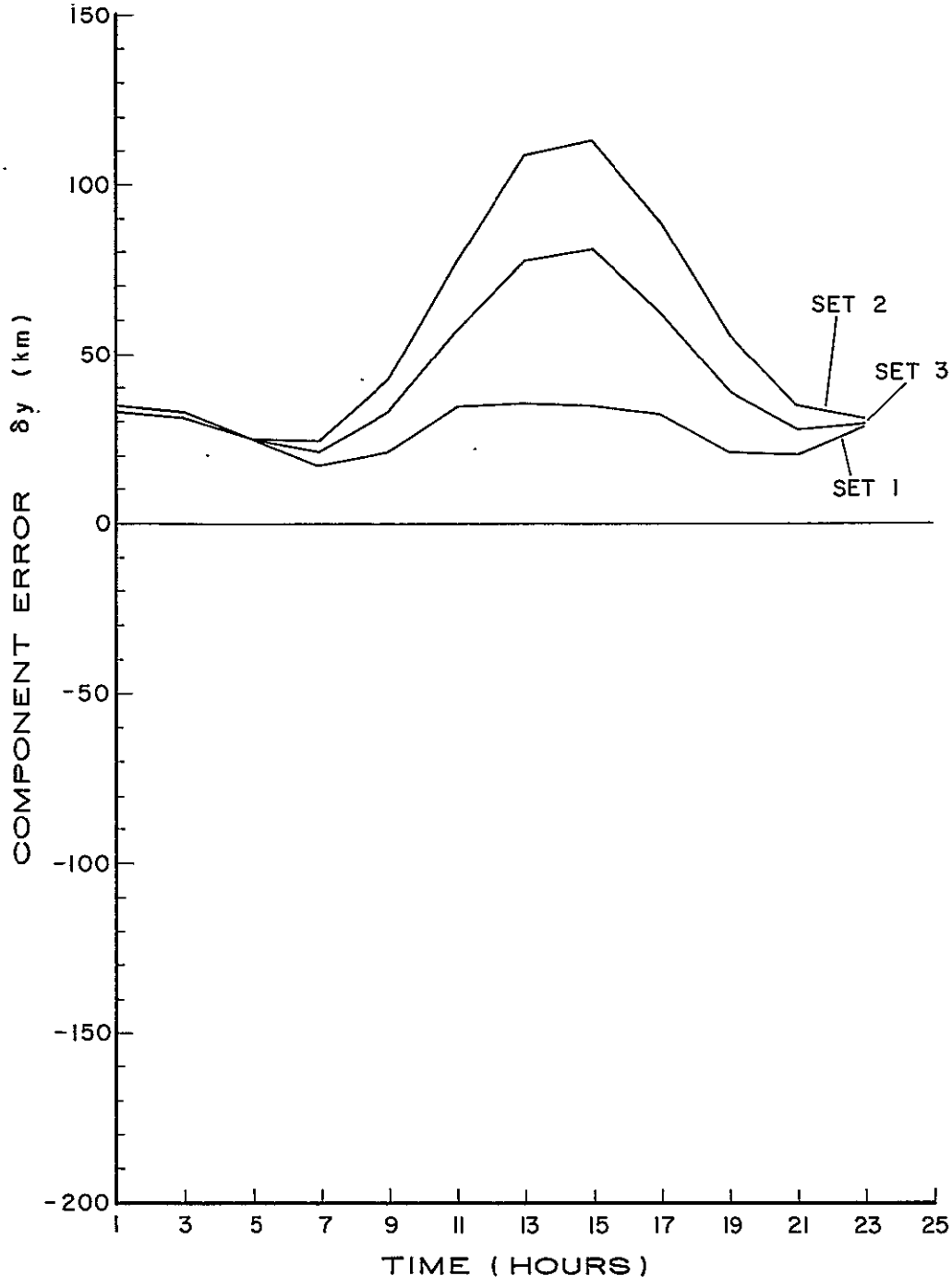

Figure 4-20: Error in y Component of Spacecraft Position for Day 269. Three Distinct Sets of Transit Times

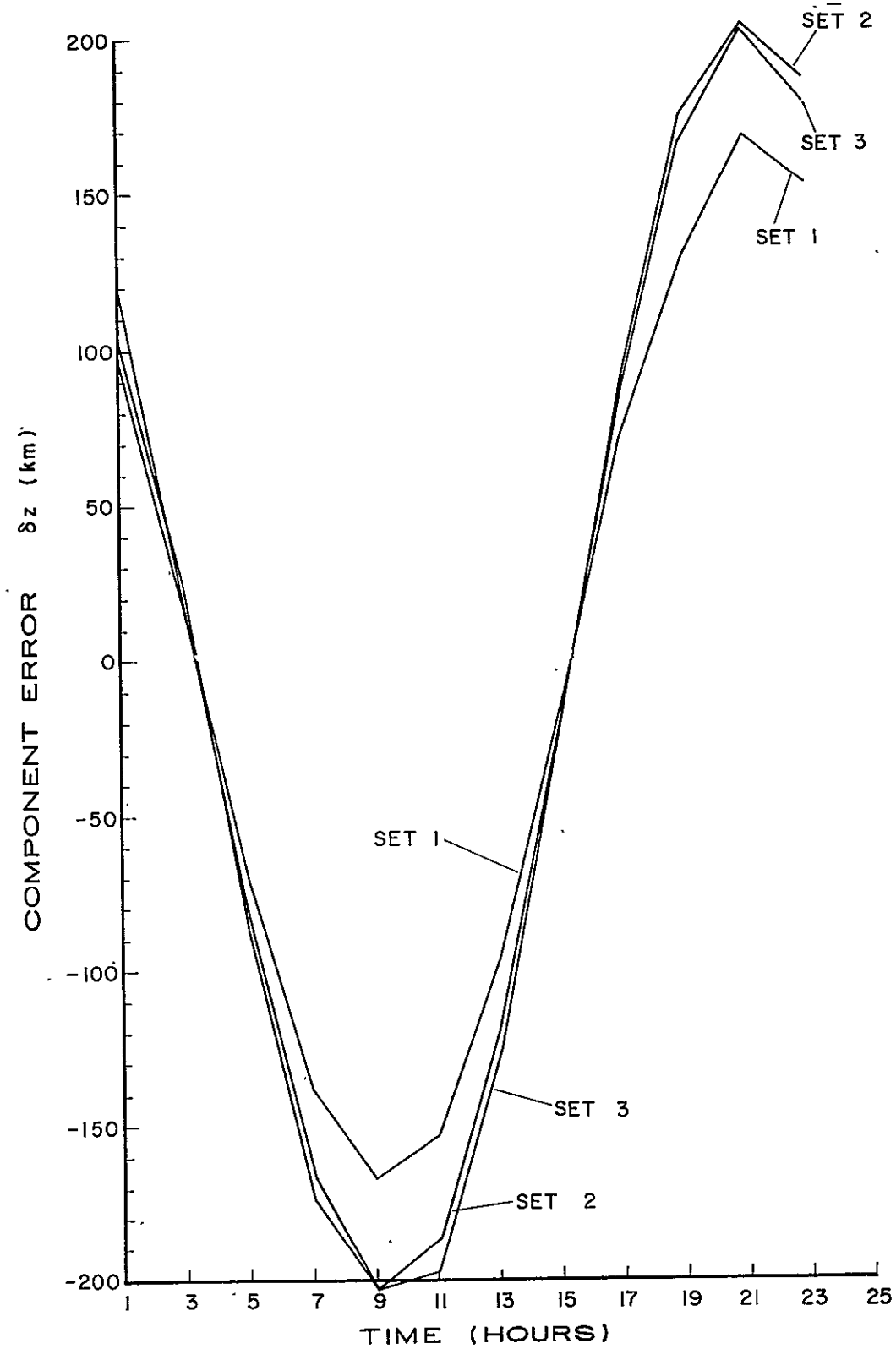

Figure 4-21: Error in z Component of Spacecraft Position for Day 269. Three Distinct Sets of Transit Times

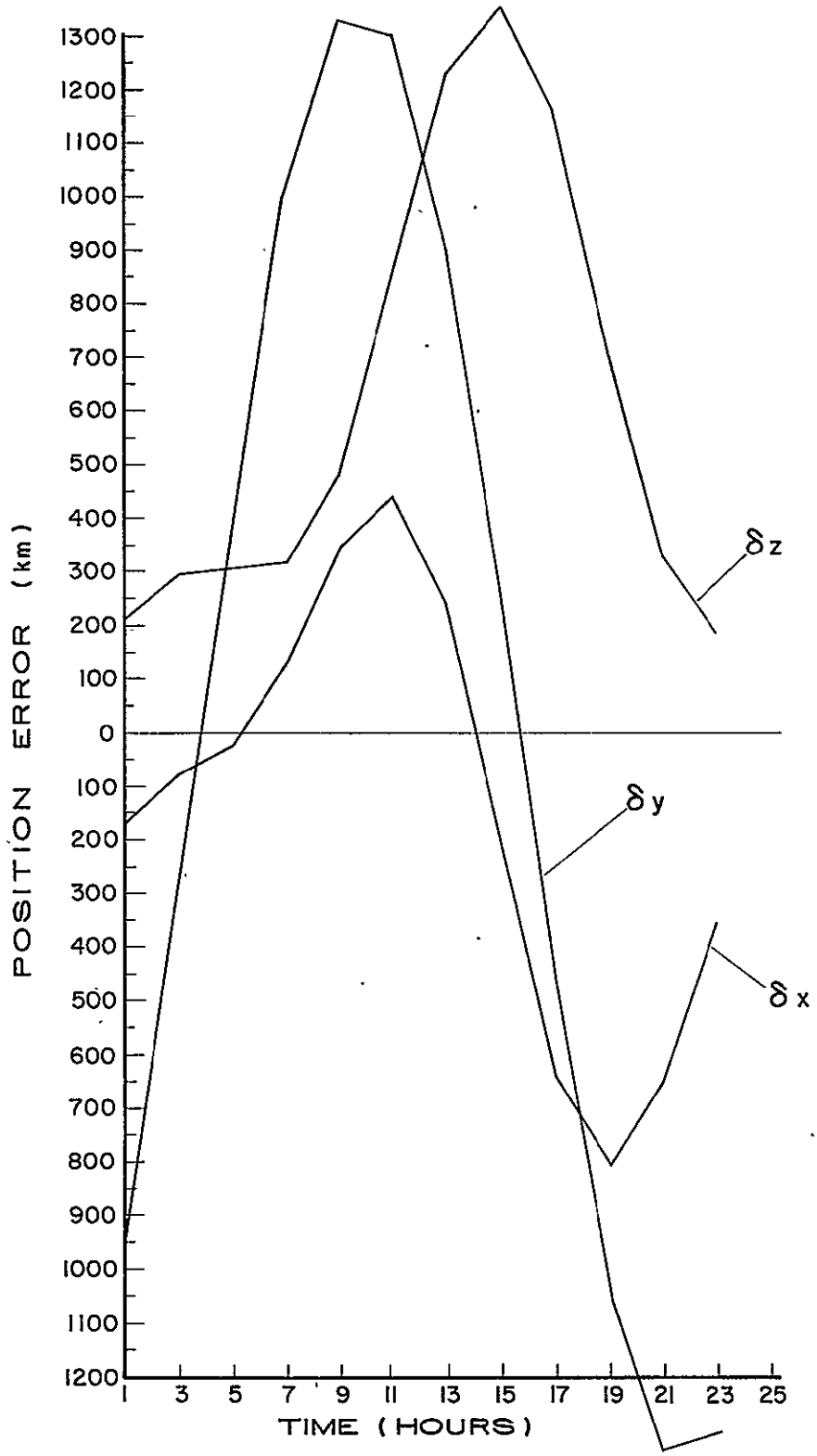

Figure 4-22: Error in Position Components of Spacecraft for Day 269. First Data Set. No Correction of Transit Times

4. Position of Moon as Obtained by Moon Transits

Because of the nature of the problem, it is easy to interchange the role of the primary and secondary satellites. Results will now be shown for such an interchange; i.e., the program will be formulated so that the position of the spacecraft is given, and the position of the moon is to be determined.

The geometry of Figure 4-15 indicates that the transits should "tie down" the moon's orbit better than the spacecraft's orbit. This is indeed the case. The convergence is excellent, in that initial guesses, several 1000 km from the solution led to the right solution.

A single solution was obtained from the data gathered over the 28 day data gathering interval. A comparison between the solution so obtained and the moon ephemeris supplied by Goddard could not be made over the complete interval because the Goddard ephemeris was incomplete.

Figure 4-23 is a plot of the difference between the position computed from the transits, and that obtained from the Goddard Moon Ephemeris. Three different days were chosen at which these position differences were computed. These days were at the beginning, middle, and end of the 28 day interval. Note that the difference lies between -50 and 40 kms. This difference is less than the difference between the Goddard Moon Ephemeris and the American Nautical Almanac Moon Ephemeris.

Finally, Figure 4-24 is a plot of the difference shown in the previous figure, except that no correction of transit times, due to the phase of the moon, were made. The position errors are increased for this case in that they lie between -50 and 480 km; however, they are still relatively small.

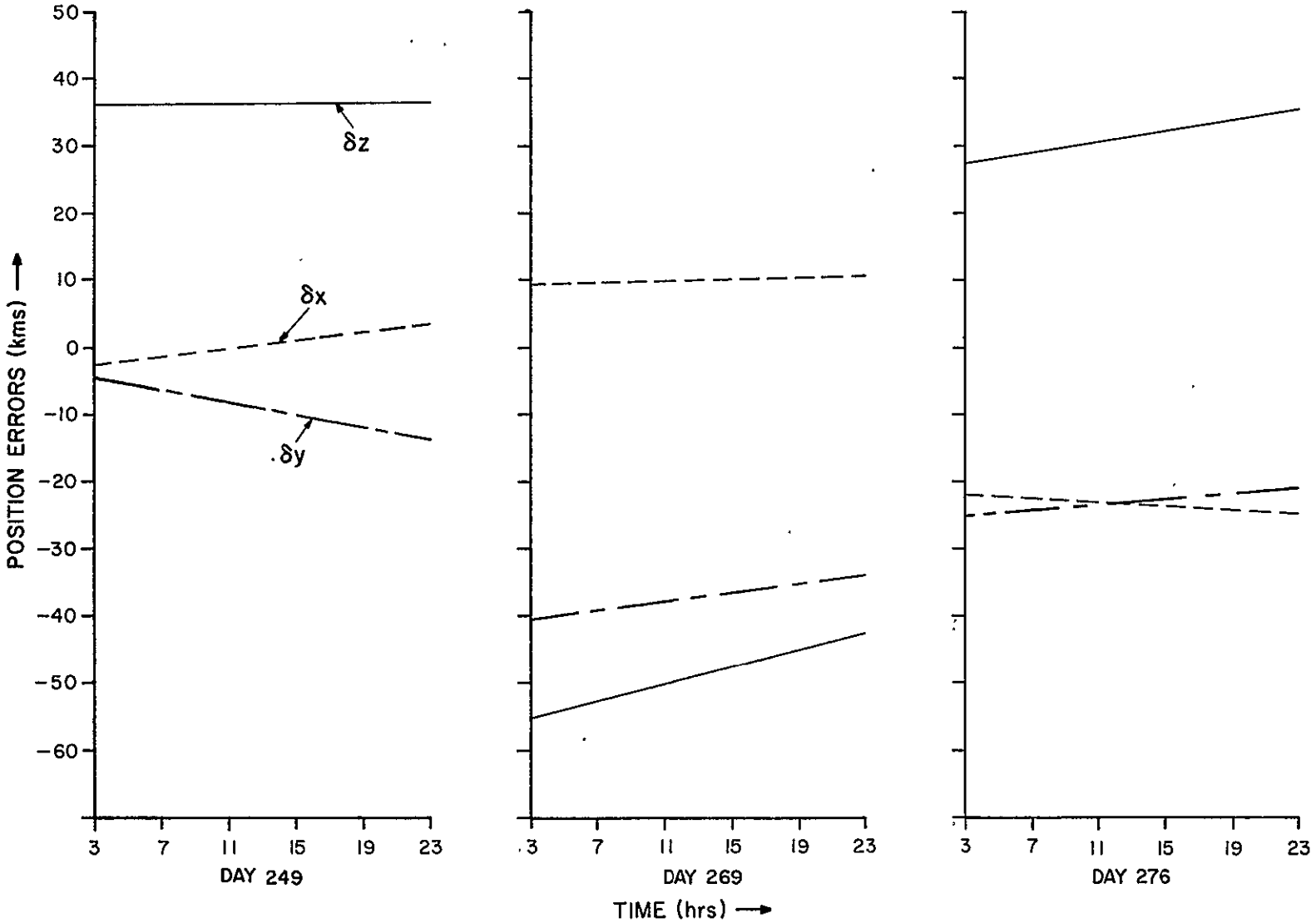

Figure 4-23: Position Errors of Moon for Three Different Days. Transit Time Correction Used

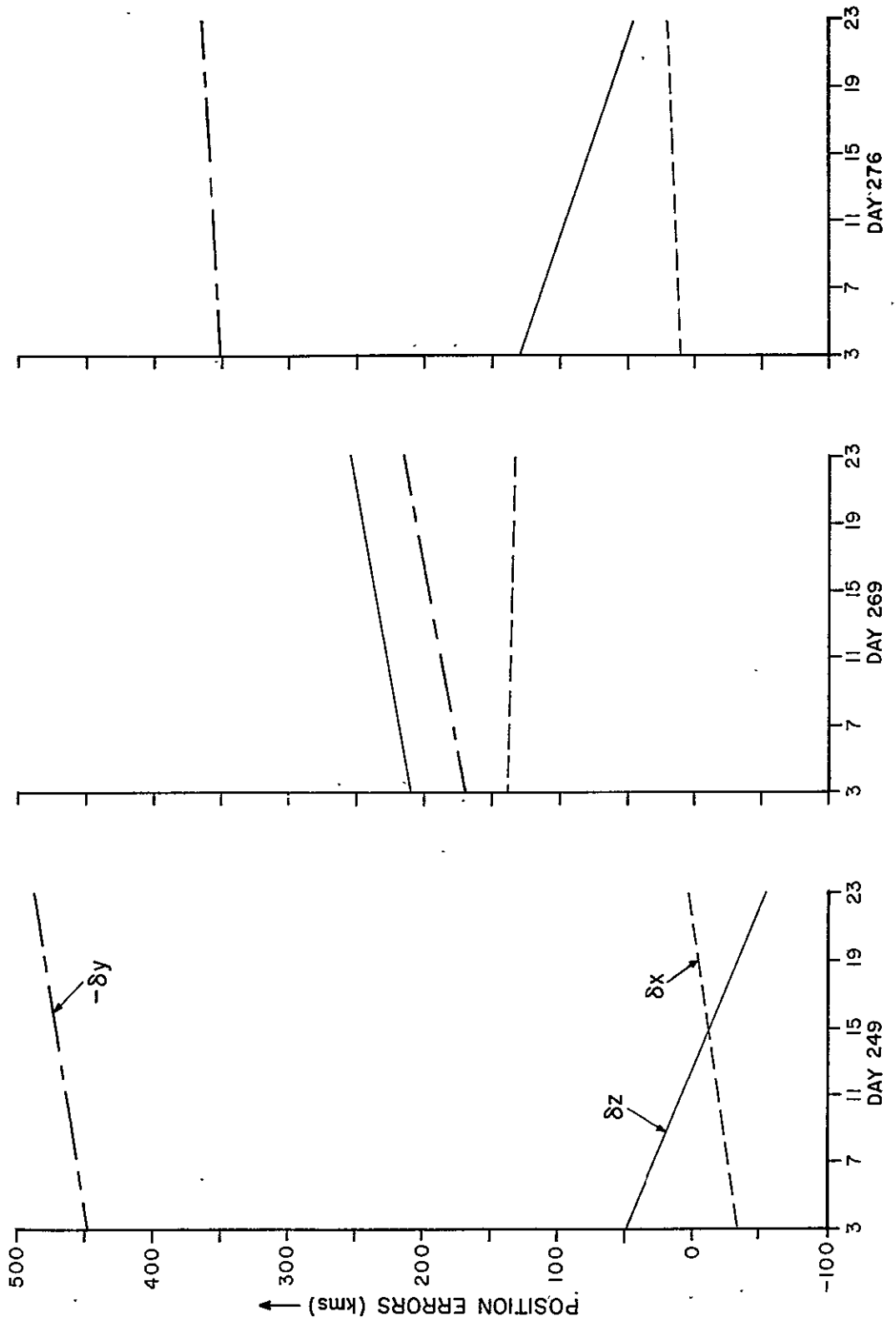

Figure 4-24: Position Errors of Moon for Three Different Days. Transit Time Correction Not Used

C. Ejection Mechanism Performance

As the ejector torque accelerates, the ball has an equal and opposite reaction force on the ejector, tending to keep the ball in the cup (shown as $\vec{F}_{b1}$ in Figure 1-7). When the ejector reaches its extended position at $\chi = 4.5$ degrees, this force decreases and the centripel force of the ejector becomes significant. The centrifugal reaction force of the ball $\vec{F}_{b2}$ is directed away from the pivot P_o. The resultant of these forces, $\vec{F}_{be}$ makes an angle η with the x axis such that $0^o \leq \eta \leq 90^o$. As long as $\vec{F}_{be}$ is directed against some portion of the ejector the relative static equilibrium between the ball and cup is maintained. However, for $\eta < \eta_c$, the static equilibrium is not maintained and the ball will pivot about the contact point P_f. Thus, in addition to the satellite tangential velocity and the accelerator velocity, the ball possesses a rolloff velocity about the retaining fingers.

The amount of rolloff velocity is a function of η_c, which in turn depends on the physical condition of the fingers. Since $\eta_c = \zeta_c + \chi^*$, η_c is well defined by ζ_c. For example, if a nominal finger length is assumed and contact between finger and ball is established at the finger midpoint located then $\zeta_c \simeq 15$ degrees, was shown in Figure 1-7. If this contact is at P_i, $\zeta \simeq 18$ degrees. Under these conditions the components of rolloff velocity would be

$\zeta_c = 15^o$; $v_x = 0.84$ ft/sec. $v_y = -1.67$ ft/sec.

$\zeta_c = 18^o$; $v_x = 1.46$ ft/sec. $v_y = -2.16$ ft/sec.

Tests were conducted using the SCNS spare flight model to evaluate the ability of the ejection mechanism to provide a desired ball velocity and launch angle During these test shots, made under laboratory conditions, the ejector stop angle and spring force were adjusted so that the resultant elevation and velocity approximated 45 degrees and 3 ft/sec. However, if the finger, shown in Figures 1-6 and 1-7, is bent out only slightly, then during ejector acceleration the ball will roll out to make contact with the fingers prior to the

time normally required for $\zeta = \zeta_c$. For example, if the ejector is originally calibrated at ζ_{cal} and the fingers are then bent such that ζ_c has a larger value, $\hat{\zeta}_c$, the resultant conditions are those listed in Table 4-X.

TABLE 4-X

BALL LAUNCH CONDITIONS DUE TO EJECTOR FINGER DEFECTS

ζ_{cal}	ζ_c	$v_{x\text{-roll}}$	$v_{y\text{-roll}}$	α	ϵ	$v_{resultant}$
15	20	1.94	2.43	-15.0	33.7	4.1 ft/sec
18	25	4.11	3.55	-16.3	23.6	5.7 ft/sec
19	24	3.25	3.24	-16.5	25.0	4.7 ft/sec

α - azimuth angle (degrees)

ϵ - elevation angle (degrees)

REFERENCES

1. ATS/SCNS Experiment Operational Handbook, prepared by Control Data Corporation by NASA under Contract NAS5-9683, July 1967.

2. Final Hardware Report, ATS Program, SCNS Experiment, prepared by Control Data Corporation for NASA under Contract NAS5-9683, September 1967.

3. Feasibility Study Report for Self-Contained Navigation System Experiment Contract NAS5-9683 GSFC (page 6 Mathematical Analysis), prepared by Control Data Corporation.

4. Solar and lunar ephemeris tape listing supplied by Goddard Space Flight Center.

5. ATS-III ephemeris tape listing supplied by Goddard Space Flight Center.

6. The American Ephemeris and Nautical Almanac, 1968.

APPENDIX A

SUMMARY OF OPERATIONAL CONDITIONS

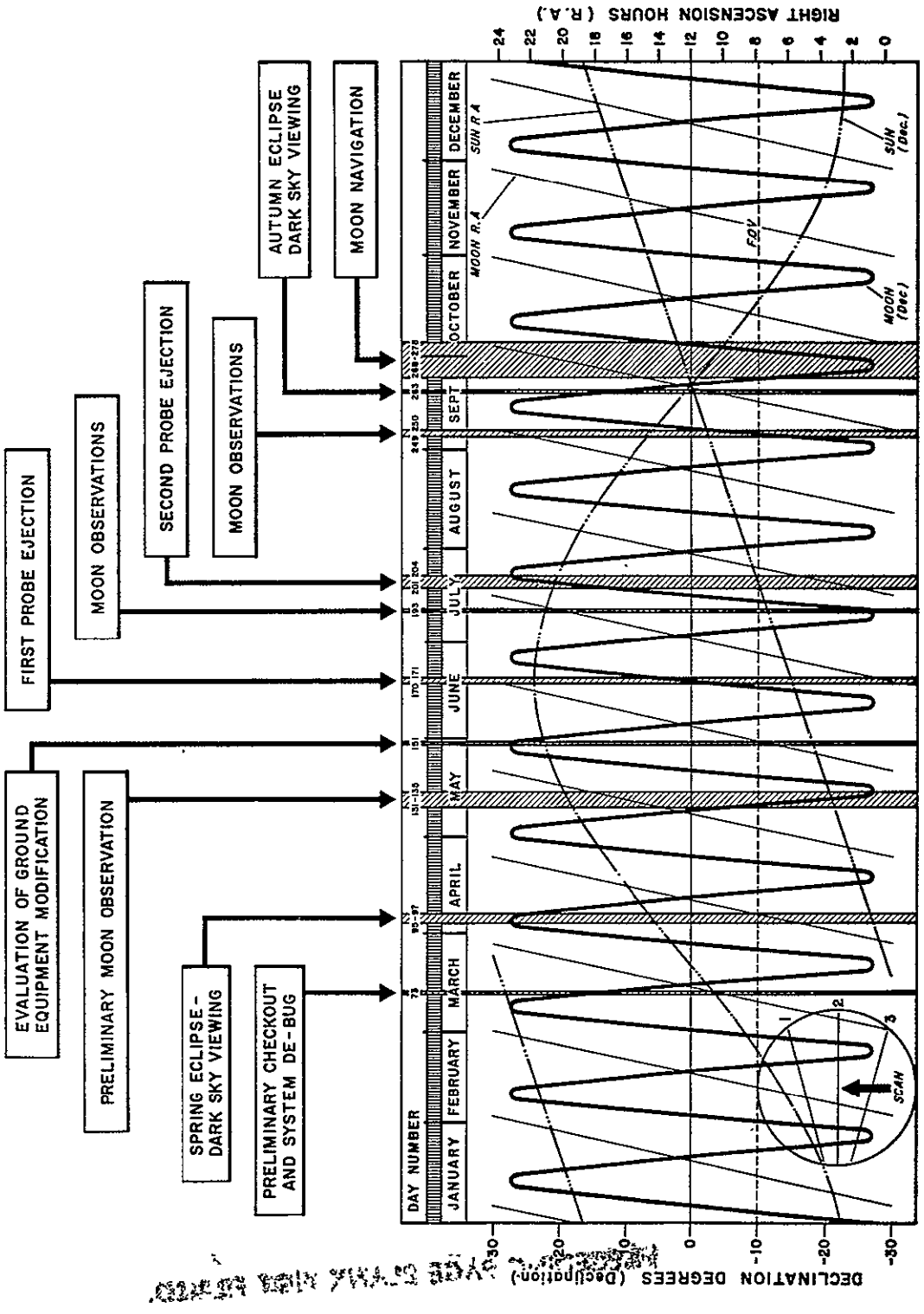
RIGHT ASCENSION HOURS (R.A.)
DECLINATION DEGREES (Declination)
DAY NUMBER
JANUARY
FEBRUARY
MARCH
APRIL
MAY
JUNE
JULY
AUGUST
SEPT
OCTOBER
NOVEMBER
DECEMBER
SUN R.A
MOON R.A
SUN (Dec.)
MOON (Dec.)
EQU
SCAN
EVALUATION OF GROUND EQUIPMENT MODIFICATION
PRELIMINARY MOON OBSERVATION
SPRING ECLIPSE - DARK SKY VIEWING
PRELIMINARY CHECKOUT AND SYSTEM DE-BUG
FIRST PROBE EJECTION
MOON OBSERVATIONS
SECOND PROBE EJECTION
MOON OBSERVATIONS
AUTUMN ECLIPSE DARK SKY VIEWING
MOON NAVIGATION

TABLE II
SUMMARY OF OPERATIONAL CONDITIONS

DAY	DATE	EXPERIMENT	ACQUISITION INTERVAL	CONDITIONS	CONSTRAINT GEOMETRY	REFERENCE
73	13 MAR	PRELIMINARY AND DEBUG	0500–0600 GMT	SPRING ECLIPSE FULL MOON S=14.3° SATELLITE IN EARTH'S SHADOW	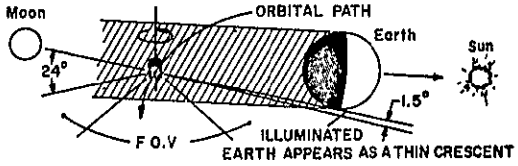	FIGURE 2
95 96 97	4 APR 5 APR 6 APR	ATTITUDE DETERMINATION	0500–0600 GMT	SPRING ECLIPSE MOON AT FIRST QUARTER δ=27.5°–28° SATELLITE IN EARTH'S SHADOW	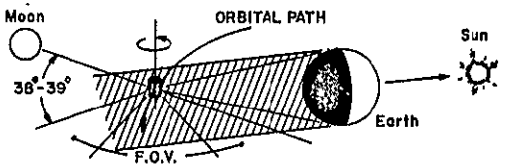	FIGURE 3
131 THRU 135	10 MAY THRU 14 MAY	(1) EQUIPMENT CHECK (2) MOON OBSERVATIONS	2300–0800 GMT	SATELLITE IN FULL SUNLIGHT MOON ENTERING THE FIELD OF VIEW AND FULL δ=5° (131) δ=26.7° (135)	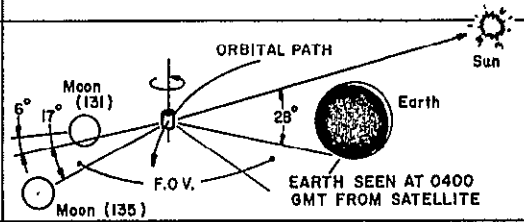	FIGURE 4
151	30 MAY	EQUIPMENT MODIFICATION CHECK (BASE FOLLOWING THRESHOLD DETECTION)	0000–0800 GMT	SATELLITE IN FULL SUNLIGHT MOON NOT IN FIELD OF VIEW δ=28°	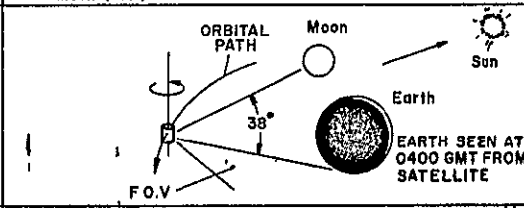	FIGURE 5
170 171	18 JUN 19 JUN	FIRST PROBE EJECTION	0000–0300 GMT	SATELLITE IN FULL SUNLIGHT MOON NOT IN FIELD OF VIEW δ=0°	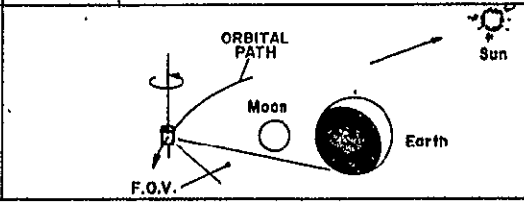	FIGURE 6

DAY	DATE	EXPERIMENT	ACQUISITION INTERVAL	CONDITIONS	CONSTRAINT GEOMETRY	REFERENCE
193	11 JUL	MOON OBSERATIONS		SATELLITE IN FULL SUNLIGHT MOON IN CENTER OF FIELD OF VIEW $\delta = -24.33°$		FIGURE 7
201 THRU 204	19 JUL THRU 22 JUL	SECOND PROBE EJECTION (ACTUAL FIRING ON 202:0000 GMT) ATTITUDE DATA ACQUISITION ON 201, 204	2300-0800 GMT	SATELLITE IN FULL SUNLIGHT MOON NOT IN FIELD OF VIEW $\delta = +13.8°$ (201) $\delta = +25.66°$(204)		FIGURE 8
249 250	5 SEP 6 SEP	MOON OBSERATION	0300-0400 GMT	AUTUMN ECLIPSE SATELLITE IN EARTH'S SHADOW 70 MINUTES EVERY 24 HRS FULL MOON IN FIELD OF VIEW		FIGURE 9
263	19 SEP	DETECTION COMPARISIONS WITH SPRING ECLIPSE DATA PMT AGING	0300- GMT	AUTUMN ECLIPSE MOON NOT IN FIELD OF VIEW		FIGURE 10
268 THRU 276	24 SEP THRU 4 OCT	MOON NAVIGATION EXP.	0000-0400 GMT	AUTUMN ECLIPSE MOON IN FIELD OF VIEW		FIGURE 11

APPENDIX B

SENSOR DETECTABILITY PERFORMANCE

		OPERATING STATE				STARS DETECTED		VISUAL MAGNITUDE FAINTEST STAR	THEORETICAL MAGNITUDE	NOISE FREQUENCY (PPS)	STAR FIELD GEOMETRY	SENSOR OUTPUT	NOTES
DAY	DATE	SYSTEM	VOLTAGE	GAIN	THRES.	REGULARLY	OCCASIONALLY						
73	3-13	2	H	0	50%	1, Venus	None (1)	-1.58	-0.05	-	Fig. 2	-	(1)
		2	H	3	50%	1, Venus	81 (2)	2.54	2.2	-		-	(2)
		1	H	0	50%	1, Venus	17, 23 (4)	1.63	2.0	-		-	(2) (3)
		1	H	3	50%	-	-	-	-	-		-	(4)
		1	L	5	50%	1, Venus	16, 17	1.29	1.30	-		-	
95	4-4	1	H	1	50%	1, 16, 17	48 (5)	2.14	2.40	20.0	Fig. 3		(5)
		1	H	2	50%	1, 16, 17	48 (5)	2.14	2.75	47.3			
		1	H	3	50%	1, 16, 17	130 (5)	2.91	3.10	119.6			
		1	H	4	50%	1, 16, 17	214 (5)	3.33	3.45	160.0			
		1	H	5	50%	1, 16, 17	81 (5)	2.54	3.80	194.4			
96	4-5	2	H	3	50%	1, 16, 17	-	1.29	2.20	10.5	Fig. 3		(5)
		2	H	4	50%	1, 16, 17	48 (5)	2.14	2.95	92.9			
		2	H	5	50%	1, 16, 17	130 (5)	2.91	3.70	241.7			
		2	L	4	12.5%	1, 16, 17	23 (5)	1.63	1.95	8.5			
97	4-6	2	L	5	12.5%	1, 16, 17	130 (5)	2.91	2.70	101.9	Fig. 3		
		2	L	6	12.5%	1, 16, 17	214 (5)	3.33	3.45	297.2			
		2	L	7	12.5%	1, 16, 17	81 (5)	2.54	4.20	383.2			
131	5-10	2	H	5	50%	16, 48	81, 115	2.84	3.7	109.4	Fig. 4		(6)
135	5-14	2	H	5	50%	None (7)	None (7)	-	-	-	Fig. 4		(7)
151	5-30	2	H	6	50%	16, 48, 81	208, 37	3.30	4.45	38.0	Fig. 5		(8)
170 171	6-18 6-19	2	H	6	50%	16, 48	81	2.54	4.45	-	Fig. 6	Fig. 12	

		OPERATING STATE				STARS DETECTED		VISUAL MAGNITUDE FAINTEST STAR	THEORETICAL MAGNITUDE	NOISE FREQUENCY (PPS)	STAR FIELD GEOMETRY	SENSOR OUTPUT	NOTES
DAY	DATE	SYSTEM	VOLTAGE	GAIN	THRES	REGULARLY	OCCASIONALLY						
193	7-11	2	H	6	50%	16, 17, 81	26, 125, 130	2.91	4.45	43.0	Fig. 7	Fig.13	
201-204	7-19-7-22	2	H	6	50%	16, 17, 48	37, 130, 95(9)	2.91	4.45	32.2	Fig. 8	Fig.14	(9)
249 250	9-5 9-6	2	H	6	50%	1, 16, 17, 23, 38, 39	73	2.43	4.45	-	Fig. 9		
263	9-19	2	H	4	50%	1, 16, 17, 23, 38, 39, 48	81, 190	3.21	2.95	12.1	Fig.10	Fig.15	
263	9-19	2	H	5	50%	1, 16, 17, 23, 38, 81, 102(9) 115(9), 73(9)	15, 26, 37, 39, 89, 125, 214	3.33	3.7	34.5	Fig.10	Fig.16	(9)
263	9-19	2	H	6	50%	1, 16, 17, 23, 38, 39, 48, 81, 73(9), 102(9), 115(9), 125(9), 173(9), 190(9), 214(9), 17	73, 247, 319, 373	3.82	4.45	28.5	Fig.10	Fig.17	(9)
268-278	9-24-10-4	2	H		50%	Venus 1, 16, 17, 23, 38, 39, 48, 81	-	-	-	-	Fig.11	Fig.18 19 20	

NOTES

(1) Regularly detected stars were the only targets detected.

(2) Detected more than 60% of time in one or more of slits.

(3) Gain fixed at 50%.

(4) No useful output information.

(5) Faintest star detected and identified. Magnitude of faintest star is based upon faintest star detected in all three slits at least 25% of time.

(6) Star identifications made through manual reduction of digital data.

(7) Due to interference from sun and moon, detection of sufficient bright stars to perform target identification was not possible. (Refer to Figure 4)

(8) Automatic determination of star identification and attitude was utilized.

(9) Detected more than 10% of the time in at least one slit.

APPENDIX C

THE DETERMINATION OF SPECTRAL ENERGY DISTRIBUTIONS AND INSTRUMENT MAGNITUDES FOR SOME SELECTED STARS

I. INTRODUCTION

Spectral energy distributions were determined using a black-body approximation and color index information for 96 bright stars in an annular field of view between declinations of -10 and -40 degrees. Instrument magnitudes for these stars are obtained using the black-body curves and the known spectral response of the SCNS-ATS III system.

Using a black-body distribution,

$$I(\lambda, T) = \frac{2\pi h c^2}{\lambda^5 (e^{hc/k\lambda T} - 1)}$$

$k = 1.38 \times 10^{-16}$ erg/^{o}K
$h = 6.62 \times 10^{-27}$ erg sec.
$c = 3 \times 10^{10}$ cm/sec.
T = temperature (^{o}K)
λ = wavelength (cm),

and blue (B) and visual (V) response curves the smoothed fluxes of radiation, $F_{\lambda V}$ and $F_{\lambda B}$, and given by

$$F_{\lambda V} = \int V_{\lambda} \cdot I(\lambda, T)\, d\lambda$$

and

$$F_{\lambda B} = \int B_{\lambda} \cdot I(\lambda, T)\, d\lambda$$

respectively, with the integrations over the effective bandwidths of the B and V curves. Generation of $F_{\lambda V}$ and $F_{\lambda B}$ values for various temperatures (T) and use of the relationship between color index (CI) and flux, Allen [1]

$$CI = -2.5 \log (F_{\lambda B}/F_{\lambda V}) + .71,$$

enables the determination of a temperature, T_o, for which the color index is zero. If a linear dependence of color index upon 1/T is assumed then the slope of the curve may be obtained by plotting the quantity

$$-2.5 \log (F_{\lambda B}/F_{\lambda V})$$

as a function of 1/T. Using the slope and the value of T_o yields a relation between temperature and color index of the form

$$T = 6533/CI + .51).$$

Black-body temperatures may now be determined for the stars solely from color index information. A characteristic constant, C, can be obtained for each star by solving for C in the equation

$$M_V = -2.5 \log (C \int V_\lambda \cdot I(\lambda, T)\, d\lambda),$$

where M_V is the visual magnitude of the star. Instrument magnitudes, M_I, are given by

$$M_I = -2.5 \log (C \int R_\lambda \cdot I(\lambda, T)\, d\lambda)$$

where R_λ is the system spectral response.

II. CALCULATION OF BLACK-BODY TEMPERATURES, ENERGY DISTRIBUTION AND INSTRUMENT MAGNITUDES

The spectral energy distribution of a star may be approximated by a black-body distribution (Planck function) in the region from 3800 Å to 9000 Å. The Planck function

$$I(\lambda, T) = \frac{2\pi h c^2}{\lambda^5 (e^{hc/k\lambda T} - 1)} \qquad (1)$$

where

$k = 1.38 \times 10^{-16}$ erg/^{o}k
$h = 6.62 \times 10^{-27}$ erg sec.
$c = 3 \times 10^{10}$ cm/sec.
T = temperature (^{o}K)
λ = wavelength (cm),

requires an estimate of the black-body temperature T. Since only color index and visual magnitude information are available a relationship between color index and temperature is necessary.

The color index of a star is dependent upon the fluxes of radiation in the blue and visual regions of the spectrum. If a black-body energy distribution is assumed and the blue and visual fluxes can be estimated, then the correct black-body temperature will make the measured and estimated color index agree.

The Arizona-Tonantzintla Catalogue[2], from which the color index and visual magnitude information for the stars was obtained, measures color index and visual magnitude with the Johnson and Morgan[3] UBV photometric system. Blue (B) and visual (V) response curves for this system are obtained by plotting the values as given by Allen with those from another source (unknown). All values are normalized to one at the peak. A smooth curve

is drawn through these points and response values are noted at 50 Å intervals over the range of response (Figure C-1).

The smoothed blue and visual fluxes for a star characterized by a black-body energy distribution can now be obtained by numerically integrating the following equations if the temperature, T, is known.

$$F_{\lambda B} = \int_{\lambda_1}^{\lambda_2} B_\lambda \cdot I(\lambda, T)\, d\lambda \qquad (2)$$

$$F_{\lambda V} = \int_{\lambda_1}^{\lambda_2} V_\lambda \cdot I(\lambda, T)\, d\lambda \qquad (3)$$

An approximate relation between color index and temperature is (Allen)

$$B - V \simeq 7300^{\circ}/T - .52. \qquad (4)$$

If this equation is solved for T the resulting function is as shown in curve A in Figure C-2. Black-body temperatures as given by Arp[4] are also shown (curve B). The values agree well for small color indices but the disparity becomes greater as the color index increases.

Using the color index values obtained from the Arizona-Tonantzintla Catalogue and Equation (4), black-body temperatures were estimated for several stars. Blue and visual fluxes were then calculated using Equations (2) and (3) and a two step Simpson's method of integration.

A constant, C, was then determined for each star such that the equation,

$$M_V = -2.5 \log \left(C \int V_\lambda \cdot I(\lambda, T)\, d\lambda\right), \qquad (5)$$

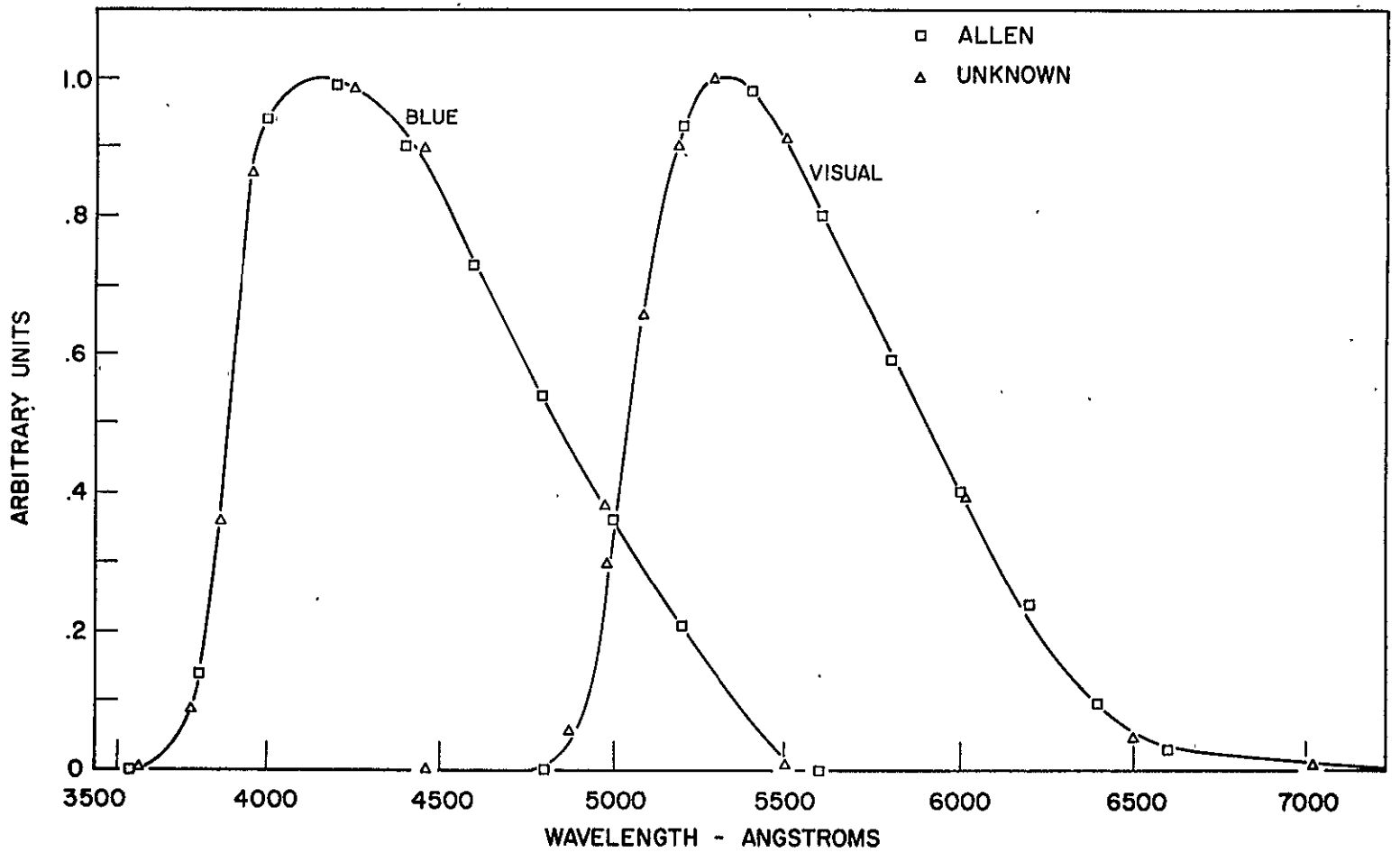

Figure C-1: Johnson and Morgan Blue and Visual Response Curves

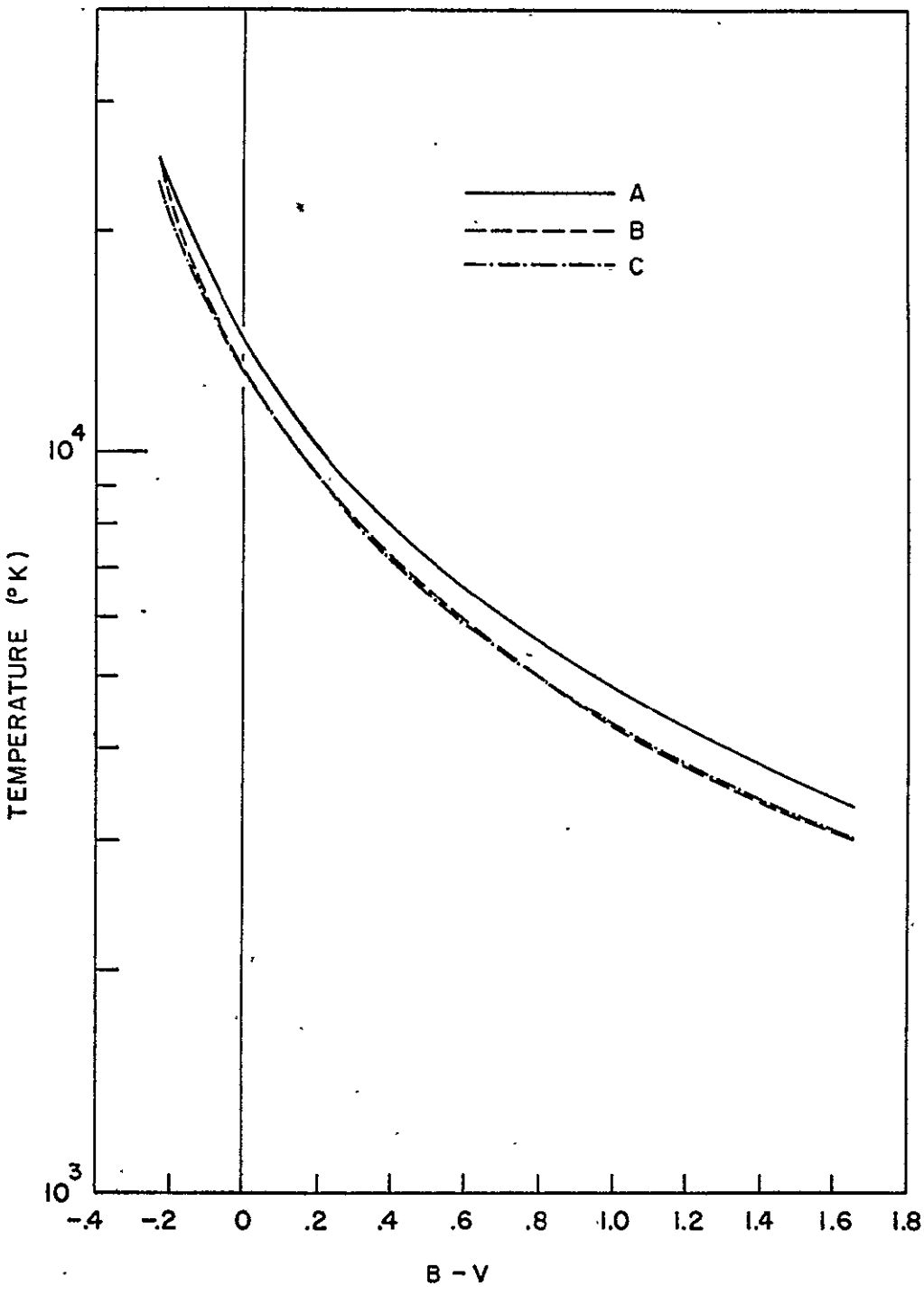

Figure C-2: Color Index-Temperature Relationships

was satisfied, where M_V is the measured visual magnitude of the star. A second constant, C', may also be computed for each star satisfying the equation,

$$M_B = -2.5 \log (C' \int B_\lambda \cdot I(\lambda, T)\, d\lambda). \quad (6)$$

For each star C' differs from C by a factor proportional to the peak value of the unnormalized blue response curve. The ratio, C'/C, is thus the same for all stars and needs only to be determined once. Using the star Sirius (B - V = .01, M_V = -1.45) the ratio, C'/C, was computed as C_s. For all stars Equation (6) now can be written as

$$M_B = -2.5 \log (C_s \cdot C \int B_\lambda \cdot I(\lambda, T)\, d\lambda) \quad (7)$$

where the value of C is obtained from Equation (5) for each star.

Blue magnitudes generated in the above manner are given in Table C-I for 32 stars in the field of view. Also given are measured blue magnitudes obtained from the Arizona-Tonantzintla Catalogue and the differences between the computed and measured values. The differences were found to vary approximately linearly with color index as shown in Figure C-3. To correct for the difference dependence upon color index a new relation between color index and temperature was determined.

A relation between color index and blue and visual flux (Allen)

$$B - V = 2.5 \log (F_{\lambda V}/F_{\lambda B}) + .71.$$

By computing the quantity G,

$$G = 2.5 \log (F_{\lambda V}/F_{\lambda B}),$$

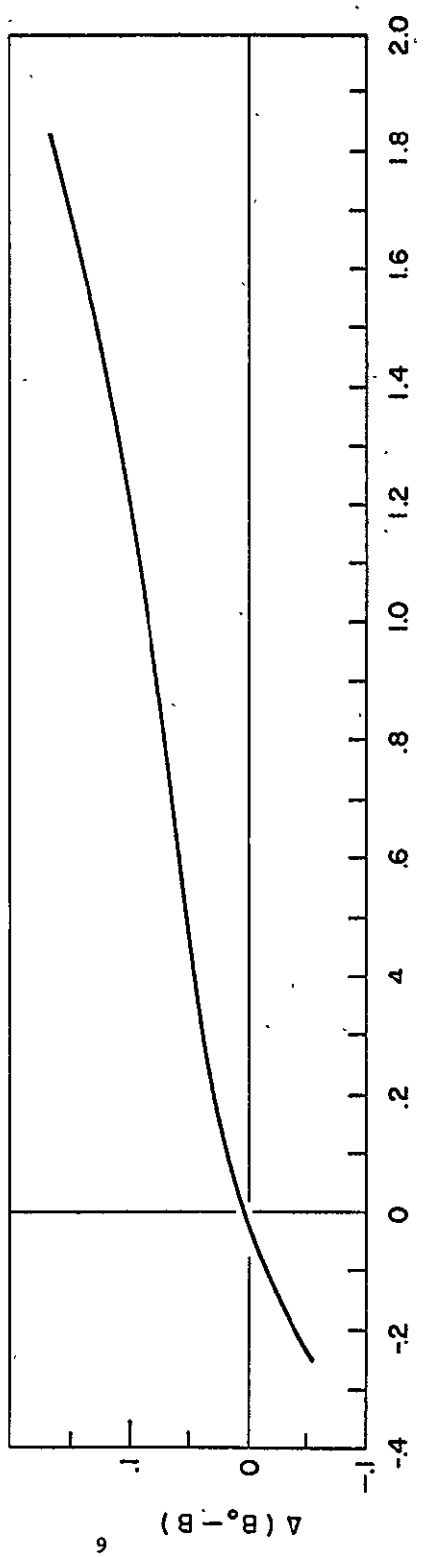

Figure C-3: Measured Minus Blue Magnitude as a Function of Color Index (Equation 7)

TABLE C-I

COMPARISON OF MEASURED AND COMPUTED BLUE MAGNITUDE(1)

Star No.	Color Index	Blue Magnitudes Tonantzintla	T = 7300/(CI + .52)	T = 6533/(CI + .51)	Col. 3-Col. 4	Col. 3-Col. 5
1	-.01	-1.46	-1.460	-1.475	0.000	.015
16	1.83	2.72	2.554	2.727	.165	-.006
17	.08	1.24	1.226	1.222	.014	.018
23	-.21	1.29	1.333	1.297	-.043	-.007
48	-.22	1.85	1.896	1.858	-.046	.008
81	-.10	2.23	2.247	2.222	-.017	.008
102	-.10	2.47	2.487	2.462	-.017	.008
107	-.22	2.48	2.526	2.488	-.046	-.008
115	.88	3.52	3.444	3.531	.076	-.011
124	.15	2.89	2.867	2.872	.023	.018
130	-.25	2.57	2.625	2.584	-.055	-.014
134	1.04	3.86	3.773	3.877	.087	-.017
144	.29	3.10	3.063	3.084	.037	.016
152	.33	3.20	2.159	3.186	.041	.014
166	-.23	2.79	2.839	2.800	-.048	-.010
182	-.10	2.90	2.917	2.892	-.017	.008
190	1.34	4.32	4.209	4.340	.111	-.020
198	1.20	4.40	4.301	4.419	.099	-.019
208	-.11	3.06	3.080	3.053	-.019	.007
214	.92	3.90	3.821	3.913	.078	-.013
229	1.20	4.51	4.411	4.529	.099	-.019
254	.06	3.32	3.309	3.303	.011	.017
275	1.18	4.67	4.572	4.689	.098	-.019
295	.72	4.22	4.153	4.224	.067	-.004
313	-.21	3.49	3.533	3.497	-.043	-.007
343	.95	4.53	4.449	4.544	.081	-.014
362	1.23	4.87	4.768	4.890	.102	-.020
375	1.00	4.61	4.526	4.625	.084	-.015
393	1.00	4.74	4.656	4.755	.084	-.015
409	1.01	4.78	4.695	4.796	.085	-.016
429	1.62	5.32	5.180	5.335	.140	-.015
441	1.18	5.06	4.962	5.080	.098	-.019

(1) Star numbers are obtained by consecutively numbering all stars of visual magnitude less than 4.0 ordered by visual (SAO) magnitude.

as a function of black-body temperature a value of T, T_o, for which the color index is zero may be determined by plotting T versus G as in Figure C-5. If the value of T for which G = -.71 is T_o then from Figure C-4, T_o is determined to be about 12750°K. If a linear dependence of color index upon temperature of the form,

$$B - V = \frac{A}{T} + C,$$

is assumed, the slope, A, can be obtained from a plot of G versus 1/T (Figure C-5. The constant A is evaluated to be 6533. C is thus equal to $-A/T_o$ or -.51. The new relation is therefore

$$B - V = \frac{6533}{T} - .51. \qquad (8)$$

Solving Equation (8) for T yields

$$T = 6533/(CI + .51). \qquad (9)$$

A plot of Equation (9) is shown as curve C in Figure C-2. These values agree more closely with Arp's values than do those of Allen.

Blue magnitudes were again computed using temperatures obtained from Equation (9), the technique employed being the same as before. The differences between the computed blue magnitudes and the measured blue magnitudes are shown in Figure C-6. The blue magnitudes and differences are tabulated in Table C-I. The values have a constant added to them so that the mean difference is approximately zero. The linear trend has been removed and the magnitudes of the differences are considerably less than those previously obtained. The discrepancy might be further improved by including higher order terms in the approximation of Equation (8).

For the present, the temperature-color index relation is significantly

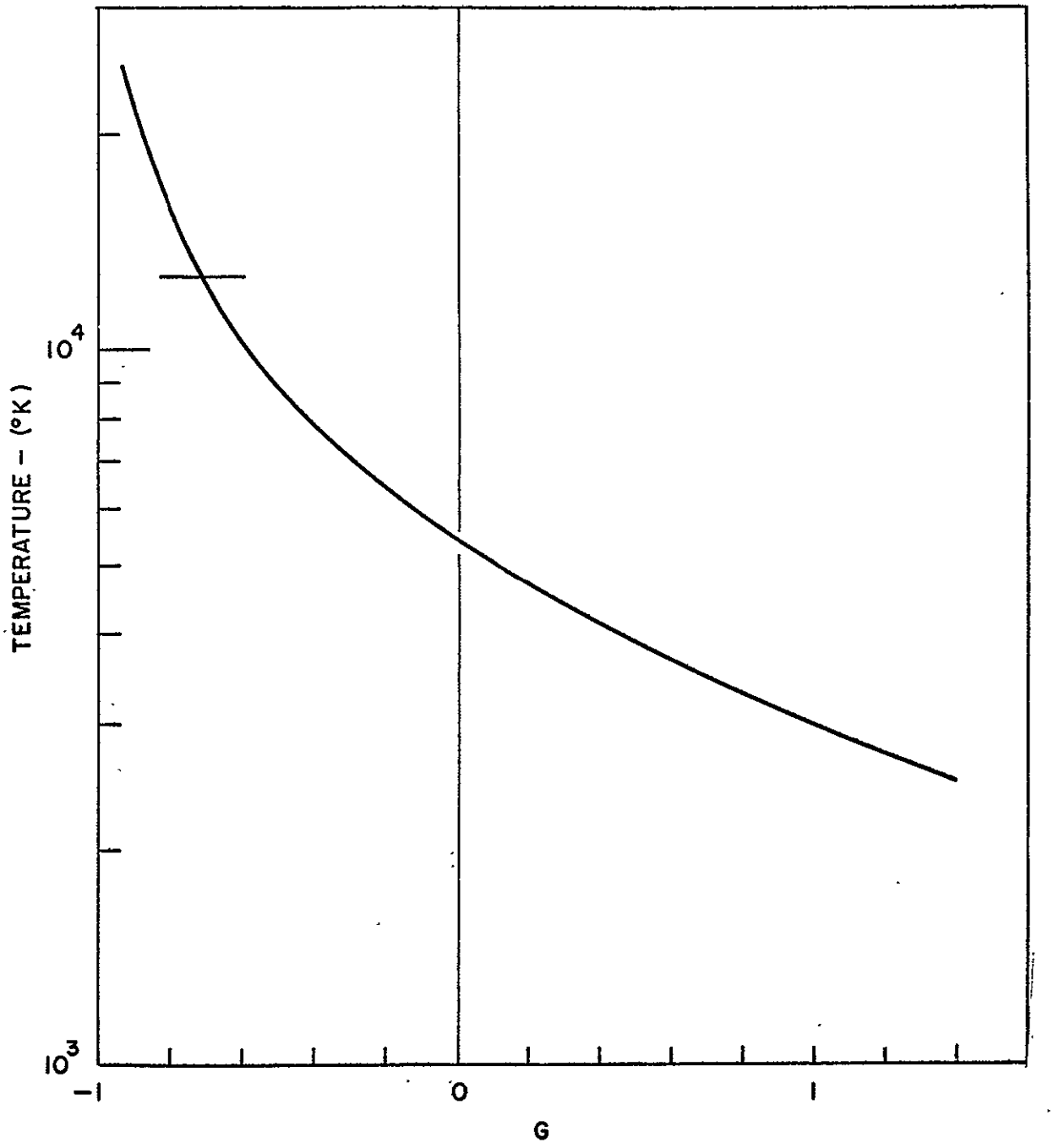

Figure C-4: Determination of T_o as the Value of T at which G Equals - .71

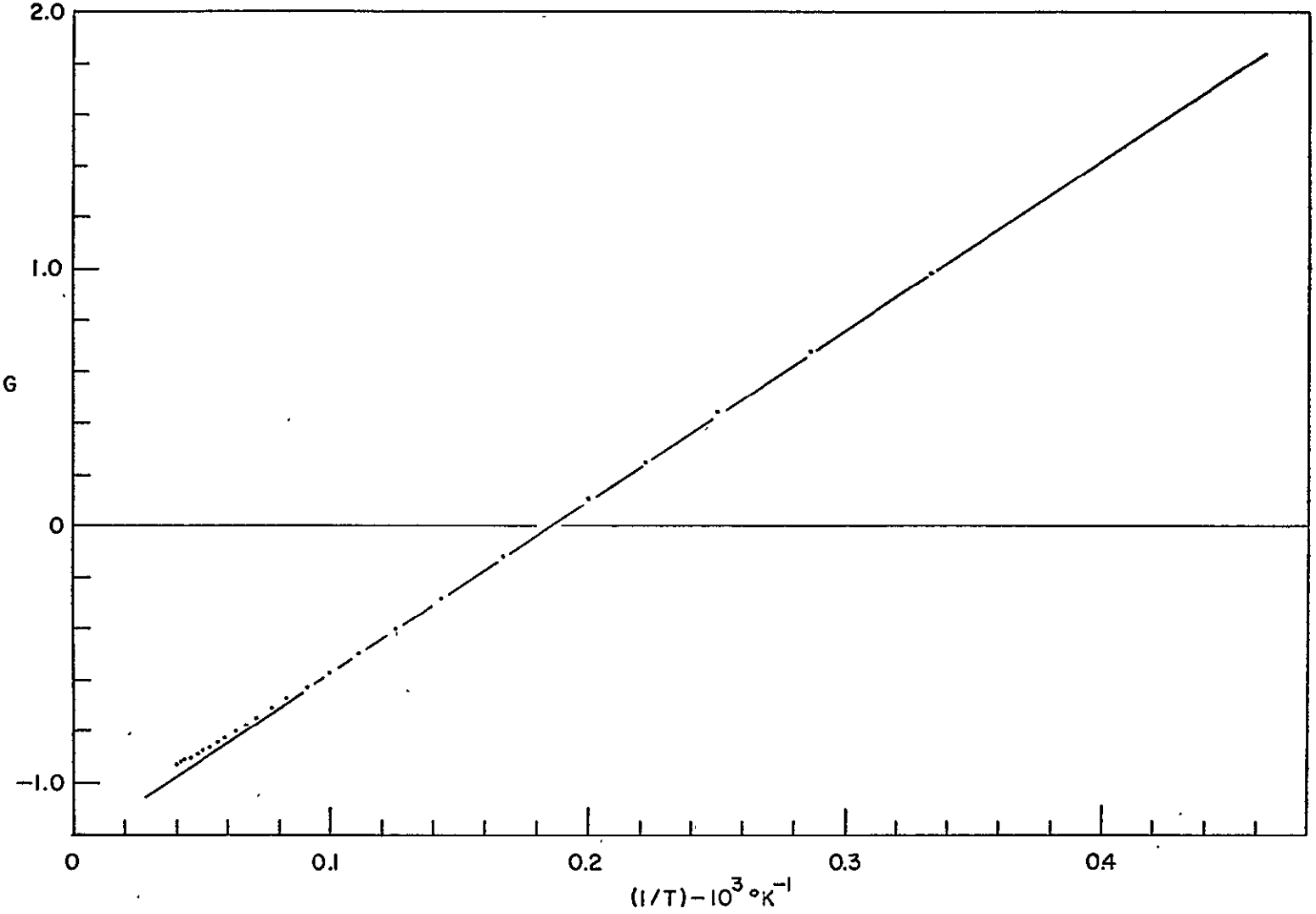

Figure C-5: Determination of Slope of G as a Function of Reciprocal Temperature

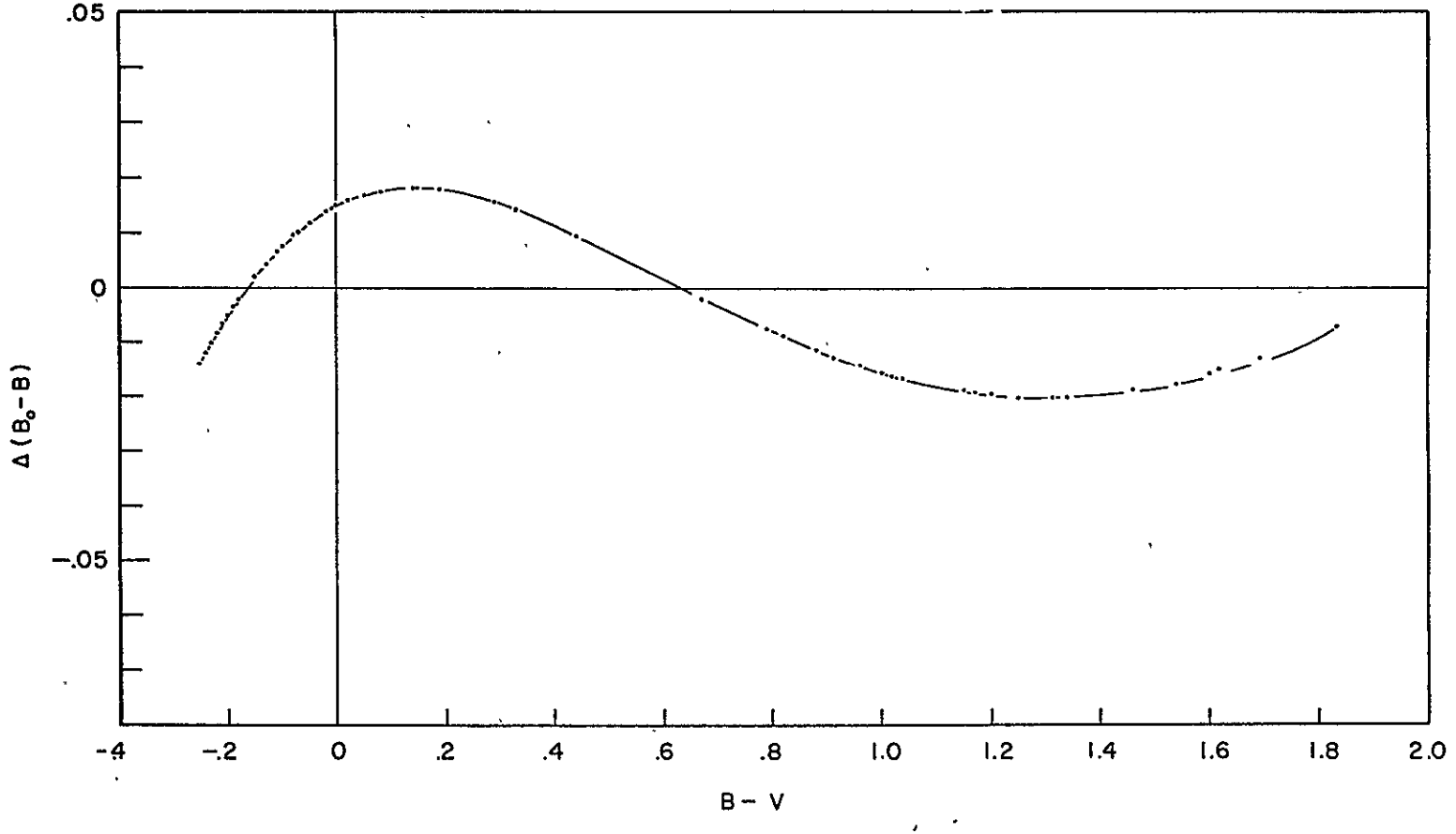

Figure C-6: Measured Minus Computed Blue Magnitude as a Function of Color Index (Equation 9)

accurate since the differences vary by less than $\pm$ .02 units of magnitude from the measured values. The black-body temperatures and constants, C, can now be computed for all stars of interest in the field of view. Instrument magnitudes are then calculated as follows:

The spectral response of the SCNS/ATS-III instrument photomultiplier is shown in Figure C-7. Instrument spectral response values, R_λ, are determined at 50 Å intervals. The response of the optical glass is approximated by a step function, rising at 3800 Å and constant to beyond 9000 Å. The instrument magnitudes are then obtained by numerically integrating the equation,

$$M_I = -2.5 \log \left(C \int_{\lambda_1}^{\lambda_2} R_\lambda \cdot I(\lambda, T)\, d\lambda\right) - Z \qquad (10)$$

$\lambda_1 = 3800$

$\lambda_2 = 8700$

where Z is the instrument magnitude of a zero color index, zero visual magnitude star. The instrument magnitudes are therefore relative. Instrument magnitudes and visual magnitudes taken from the Smithsonian Astrophysical Observatory (SAO) star catalogue [5] for the 96 stars in the field of view are shown in Table C-II.

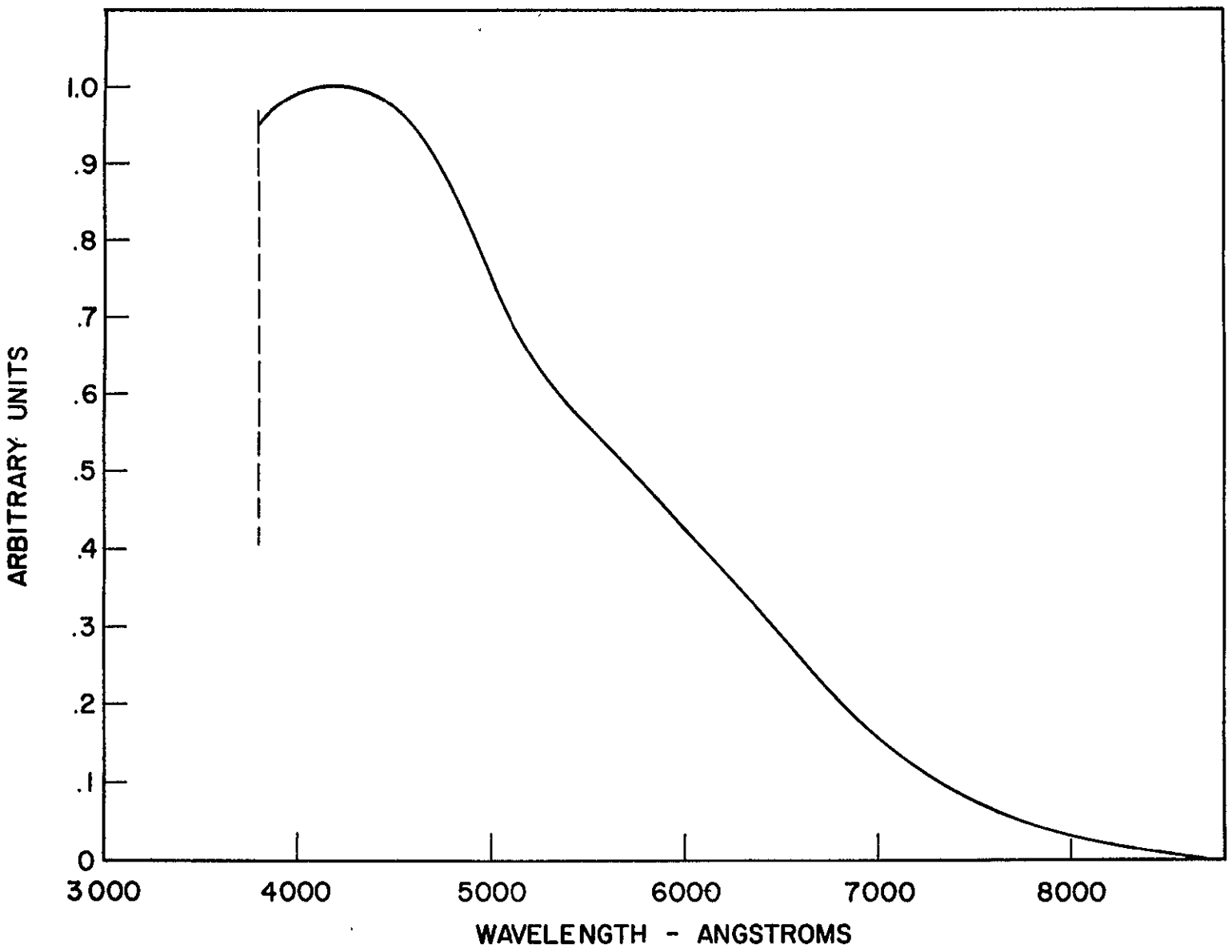

Figure C-7: Spectral Response of the SCNS Instrument (Photomultiplier and Optical System)

TABLE C-II

INSTRUMENT MAGNITUDES FOR STARS IN THE FIELD OF VIEW

No.	Mag (SAO)	Ins. Mag.	No.	Mag (SAO)	Ins. Mag.
1	-1.58	-1.45	203	3.29	3.83
15	1.21	.80	207	3.30	3.22
16	1.22	1.54	208	3.30	3.10
17	1.29	1.21	211	3.32	3.71
23	1.63	1.36	214	3.33	3.49
26	1.71	1.50	221	3.37	3.13
37	1.95	1.83	227	3.41	3.91
38	1.98	2.21	229	3.42	3.91
39	1.99	1.82	243	3.47	3.96
48	2.14	1.93	247	3.48	3.86
57	2.24	2.54	254	3.51	3.30
61	2.26	2.58	269	3.59	4.20
66	2.36	2.87	271	3.59	3.48
73	2.43	2.36	274	3.60	4.02
78	2.51	2.28	275	3.61	4.08
81	2.54	2.26	285	3.64	3.42
89	2.63	2.45	287	3.64	3.68
92	2.69	2.71	289	3.64	3.24
94	2.70	2.58	295	3.65	3.93
95	2.71	2.65	300	3.67	3.61
98	2.74	3.35	307	3.68	4.08
100	2.75	2.53	313	3.70	3.56
102	2.78	2.50	319	3.72	4.06
107	2.80	2.56	322	3.72	4.25
114	2.84	3.31	343	3.77	4.11
115	2.84	3.14	344	3.77	3.90
119	2.88	3.10	348	3.78	3.80
124	2.90	2.84	352	3.78	4.19
125	2.90	2.50	356	3.80	3.54
130	2.91	2.66	359	3.80	3.88
132	2.91	2.74	360	3.80	3.89
134	2.94	3.38	362	3.80	4.25
141	2.96	3.28	373	3.82	4.14
144	2.98	3.00	375	3.83	4.15
147	3.00	2.80	380	3.83	3.73
152	3.02	3.09	393	3.86	4.28
161	3.07	3.53	398	3.88	4.34
166	3.09	2.87	404	3.90	4.33
169	3.10	2.93	409	3.90	4.32
171	3.10	2.98	415	3.92	4.30
173	3.11	2.91	416	3.92	4.44
175	3.12	2.94	429	3.95	4.35
182	3.16	2.93	430	3.95	4.18
183	3.16	3.75	434	3.95	4.08
187	3.19	3.59	441	3.96	4.47
190	3.21	3.61	444	3.98	4.34
193	3.22	3.69	446	3.98	4.42
197	3.25	3.54			
198	3.25	3.80			

APPENDIX D

ATS-III/SCNS SLIT CHARACTERIZATION RESULTS

APPENDIX D

ATS-III/SCNS SLIT CHARACTERIZATION RESULTS

I. INTRODUCTION

In order to optimize the performance of the operational computer program for attitude determination, the characterization of the SCNS instrument and its relation to the satellite angular momentum vector must be as precise as possible.

From the data reduction results covering the various periods of SCNS operation, it is clear that a single time invariant set of slit parameters is not sufficient to characterize this relation. If a fixed set of slit parameters is employed, it is found that any set which yields essentially zero average residuals over all transits from each individual star/slit combination used in the attitude solution for one day will not give similar zero averages with data from another day. What this means, in effect, is that the known pattern of stars and the assumed relation between the spin axis (total angular momentum vector in this application) and the projection of the slits on the celestial sphere cannot be made to "fit" -- to be internally consistent. The most plausible "explanation" for this apparent discrepancy is that the spin axis of the vehicle has undergone slight shifts with respect to the gross geometrical or figure axis of the spacecraft. A small asymmetric mass displacement could account for such a change in the principal axis relative to the apparent geometric symmetry of the satellite. It is, of course, also possible that the geometrical figure of the spacecraft itself could warp; this, however, seems much less likely. In any event, it is possible for the parameters which characterize the projection of the slits on the celestial sphere to vary. This appendix will review the slit projection and document the results obtained from operational slit parameter investigations.

II. GEOMETRY OF THE SLIT PROJECTION

The basic geometry of the slit projection on the celestial sphere and parameters which characterize this projection are illustrated in Figure D-1. The three slit parameters are:

Γ = the slit-to-slit angle as seen from the projected slit vertex (measured on the celestial sphere),

σ = the angle from the spin axis to the projected slit vertex as seen from the center of the celestial sphere,

ϵ = the angle between the center slit (2) and the great circle arc from the spin axis to the projected slit vertex as seen from that vertex (measured on the celestial sphere).

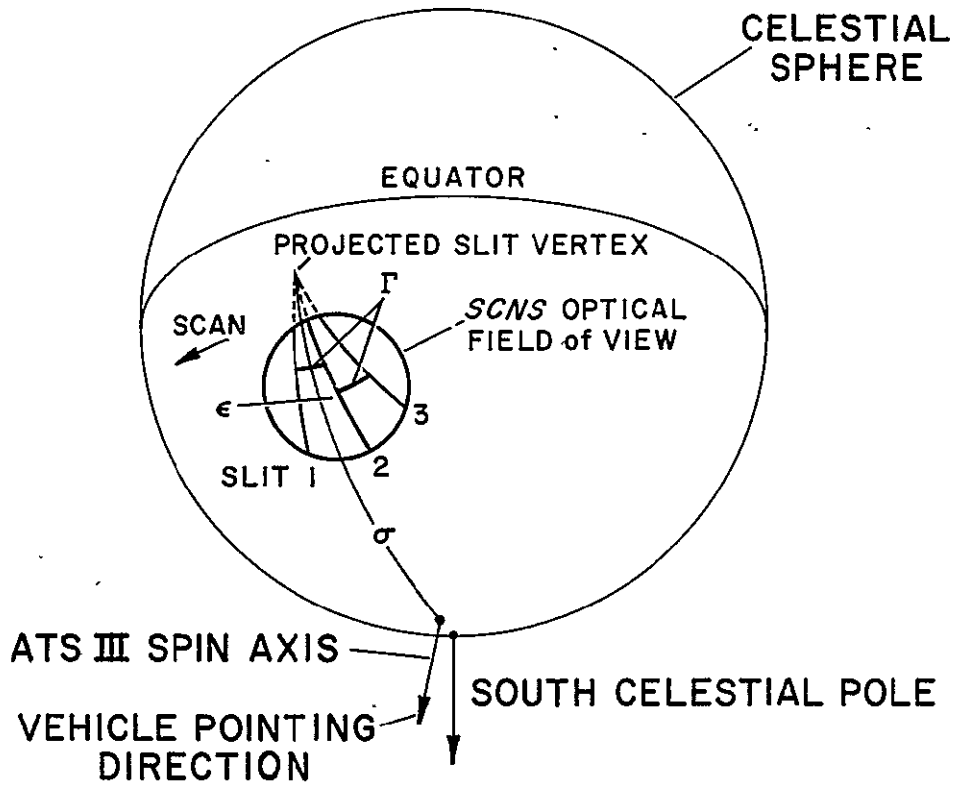

Figure D-1: Slit Configuration as Projected on the Celestial Sphere

It is important to note here that a shift in the spin axis relative to the figure axis can change ϵ, σ, or both. The slit separation Γ, on the other hand, is independent of the spin axis. Indeed, Γ depends only on the manner in which the slits are projected from the image or reticle plane onto the segment of the celestial sphere covered by the optical field. Unless the SCNS instrument undergoes significant internal displacements, Γ should be essentially time invariant.

Another observation may be made from reference to Figure A-1 and to Figure D-2 -- a SCNS star field plot on which the eight most solidly detectable stars are emphasized. These eight stars have significantly higher detection frequencies than the remainder of the stellar targets in the field. Thus the eight appear to represent the best set to use for a dynamic determination of the slit parameters directly from the operational data.

It turns out that there are reasons for discarding Sirius and these will be discussed later. Nevertheless, with or without Sirius, the azimuth distribution of the basic star set is excellent. However, it is seen that the stars lie in a very compact range in declination -- essentially a narrow band in zenith angle from the ATS-III spin axis. Thus the slit-to-slit separations will be about the same for each of the stars in the set. Under this condition σ and Γ appear to be highly interdependent; a change in σ coupled with a correlated change in Γ will leave the slit-to-slit separation in the center of the field almost unchanged. Turned around, this implies that a combination of locus in the (Γ, σ) plane can be accurately determined but that the specific point along that locus is only weakly determined in a simultaneous solution for all three slit parameters.

The problem of resolving Γ and σ is not particularly critical in the attitude determination task since large shifts along the Γ, σ locus will propagate to very much smaller shifts in the attitude solution -- at least in cases with many stars and good azimuth geometry. However, when the

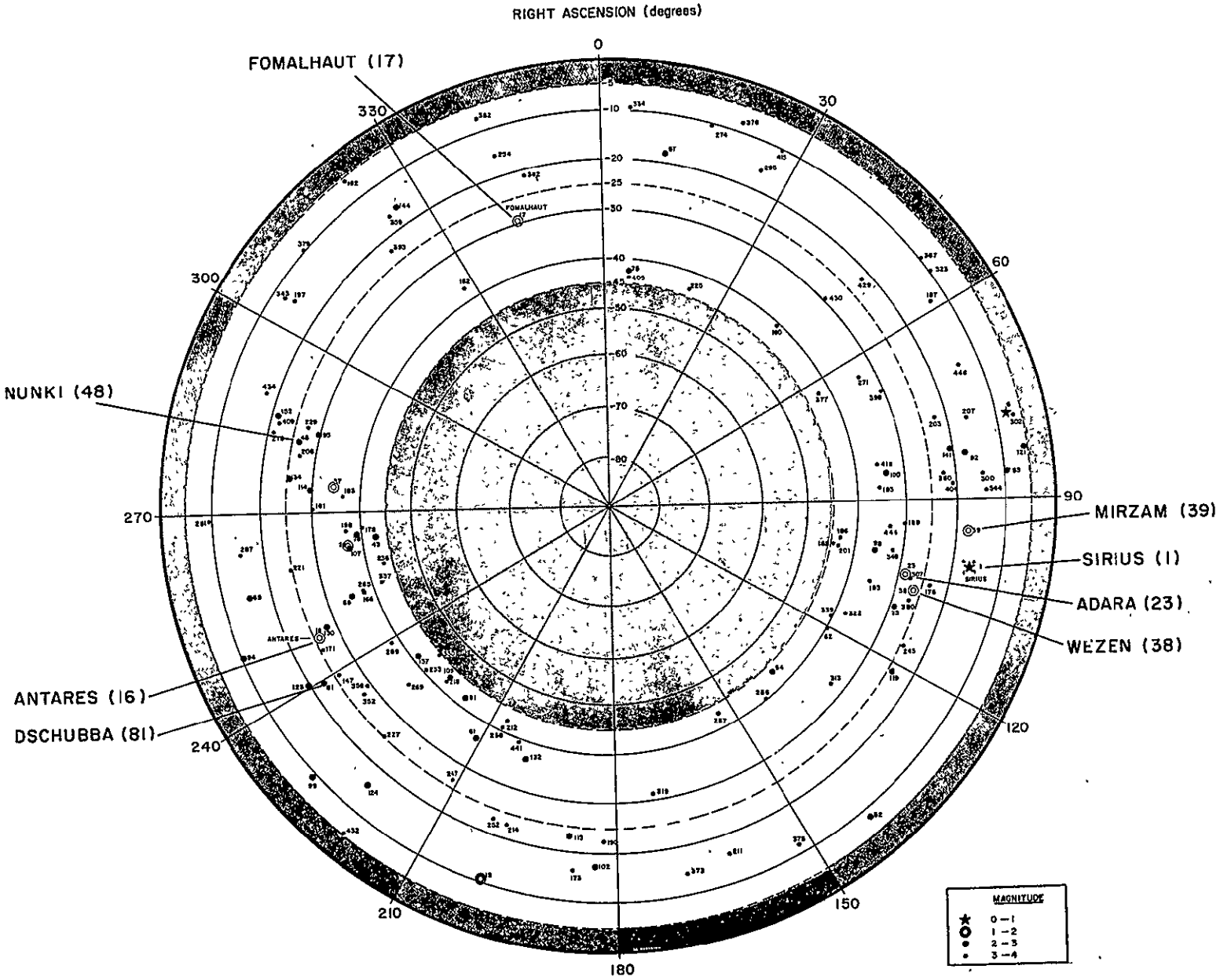

Figure D-2: SCNS Star Field with the Eight Most Solidly Detectable Stars Emphasized

position of a single navigation target (such as the moon) must be inferred and when this target may cross the slits well away from the center of the field, the individual values of Γ and σ become important. For this reason a single reliable value of Γ is established and used as a fixed parameter.

III. INDEPENDENT DETERMINATION OF Γ

One approach to this task is to project the known slit separation angle Γ' in the reticle (focal) plane through the optical system to infer the angle Γ on the celestial sphere. The geometry of this projection is shown in Figure D-3 below:

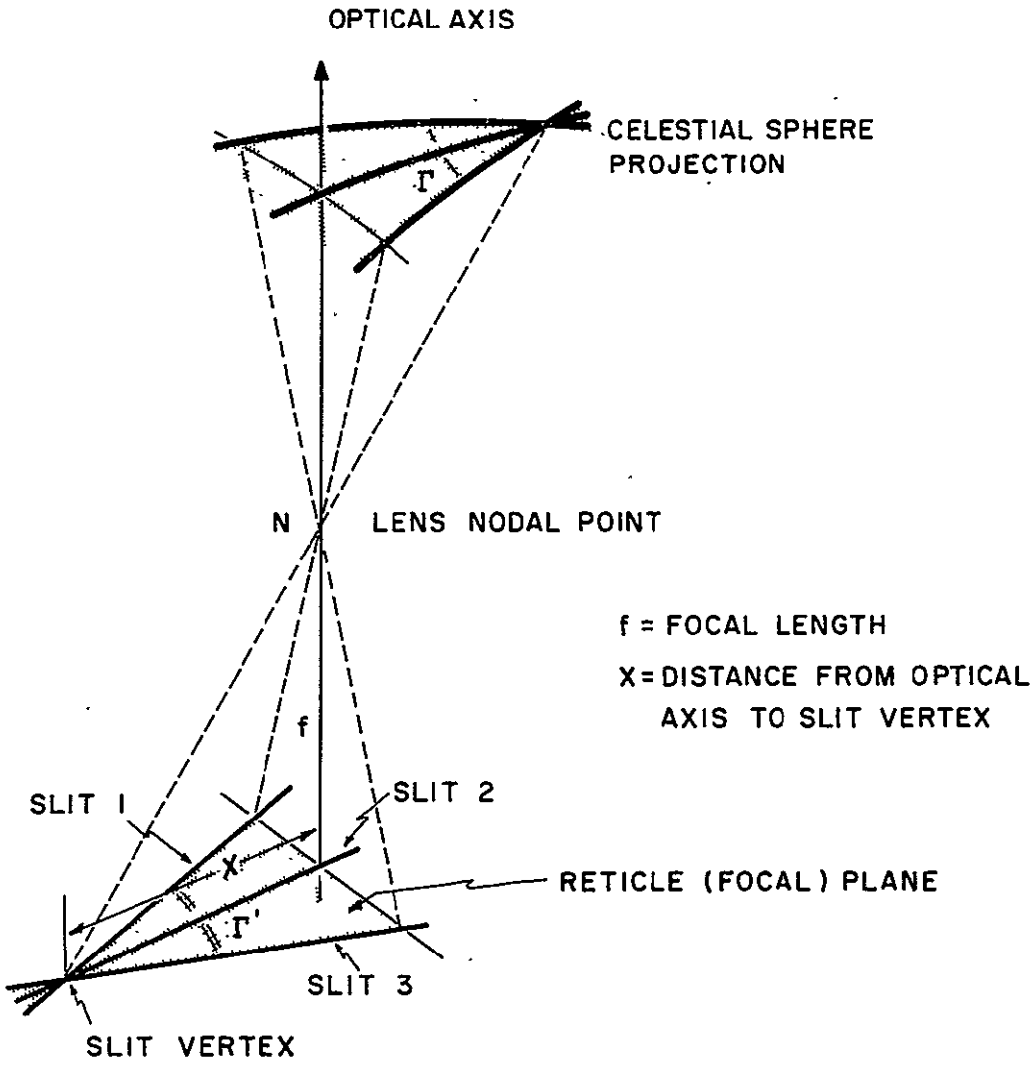

Figure D-3: Projection of the Slit Configuration from the Reticle Plane to the Celestial Sphere

The projected angle Γ depends on Γ', x, and f; it is determined by the relation

$$\sin \Gamma = \frac{\tan \Gamma'}{\sqrt{\tan^2 \Gamma' + \frac{f^2}{f^2 + x^2}}} = \sin \Gamma' \sqrt{\frac{\tan^2 \Gamma' + 1}{\tan^2 \Gamma' + \frac{f^2}{f^2 + x^2}}} \quad (1)$$

The design values for the reticle and optical variables are $\Gamma' = 10^{\circ}30'$, x = 1.0675 inches, and f = 76 mm. These yield $|\Gamma| = 11^{\circ}.13250$ as the projected slit-to-slit separation. The nominal values of the reticle dimensions are all subject to fabrication tolerances and measurement uncertainties. Since a spare reticle was available a careful validation of the measurements was performed. The reticles were all formed as photocopies from the same master so the results obtained should apply equally well to the flight unit.

The angle Γ' was measured with the aid of a sine table. The reticle was fastened to the table and the tilt angle adjusted with a planar gauge until the first slit was parallel to the motion of a 100 power travelling microscope on precision ways. The height of the planar gauge was then measured and reduced to an angle of the sine table. This procedure was repeated for each of the other slits with no change in the relative alignment of the table and the microscope motion. Note that this method has the advantage that motion of the microscope is required to be parallel to the slit over the entire slit length; this permits averaging over small fluctuations due to any slight random irregularities in the slit edges. The slit-to-slit angles from slit 1 to slit 2 and slit 2 to slit 3 were each determined and were found to agree within the uncertainty of the basic measurements. Thus, it appears that the assumption of slit symmetry is justified. The value of Γ' obtained was $10^{\circ}.454$ with an uncertainty of less than one minute of arc.

From this value of Γ' and a series of point settings with the measuring

microscope, four independent determinations of x were also made. These averaged to x = 1.075 inches with an uncertainty of approximately 0.003 inch.

A direct nodal slide measurement of the effective focal length f of the Super Farron lens in combination with the actual reticle glass path was also performed. The average value obtained from a series of measurements was f = 75.42 mm. With the extremes discarded, the measurement spread was 0.25 mm.

If the set of measured values {$\Gamma' = 10^{\circ}.454$, x = 1.075 inches, and f = 75.42 mm} is inserted in Equation (1), the resulting value of Γ, corrected for sign is

$$\Gamma = -11^{\circ}.1020 \ .$$

for the projected slit-to-slit separation. The minus sign is simply a consequence of the way Γ is defined. Evaluation of possible errors in the Γ determination was obtained by varying each of the independent variables in Equation (1) one at a time. The results are as follows:

$$\Delta\Gamma' = \pm 1 \text{ min } (\pm 0^{\circ}.0167) \rightarrow \Delta\Gamma = \pm 0^{\circ}.0176,$$

$$\Delta x = \pm 0.01 \text{ inches} \rightarrow \Delta\Gamma = \pm 0^{\circ}.0115,$$

$$4f = \pm 1 \text{ mm} \rightarrow \Delta\Gamma = \mp 0^{\circ}.016.$$

IV. SIMULTANEOUS SOLUTIONS FOR Γ, σ, AND ϵ FROM OPERATIONAL DATA

For two dates on which SCNS operations were conducted, the data acquisition conditions were ideal. On Day 96 (5 April -- spring eclipse) and again on Day 263 (19 September -- fall eclipse) the annular region scanned by the SCNS instrument is free of any major interference from the bright objects -- sun, earth, or moon. On these days, the base line of the SCNS video is unperturbed and all eight of the prime stellar targets are solidly detected. This data, then, represents the best available basis for a simultaneous dynamic solution for all three slit parameters -- Γ, σ, and ϵ.

Complete nine unknown attitude/slit solutions have been obtained for each day and the results are listed in Table D-I. On Day 96, a relatively small quantity of data (five 15 second data sets) is available and this was all processed as a single composite set containing approximately 1,000 identified transits. For Day 263, data was acquired over a much longer time span and it was partitioned and processed as five independent but interleaved composite data sets, each containing 1500 to 1800 identified transits. The spread in the results among these five solutions is a measure of the random component of the uncertainty in each unknown; these spreads are listed in parentheses under each corresponding average value.

The average value of Γ obtained from these solutions of the nine unknown problem (six attitude parameters plus the three slit angles) is $\Gamma = 11^{\circ}.0967$ where the results from Day 263 have been given a weighing factor of five relative to those from Day 96. This is in remarkably good agreement with the Γ obtained by projecting the reticle measurements through the optical system. These two independent Γ determinations differ by much less than the uncertainty inherent in either one of them. Since the reticle projection is the more certain of these two values, $\Gamma = -11.1020$ was adopted as the standard value. The dynamic solution is treated simply as strong corroboration.

TABLE D-I

ATTITUDE/SLIT SOLUTIONS FOR SCNS/ATS-III

Solution Type		Day	Number of Independent Solutions	Pointing Direction ξ_1	Pointing Direction ξ_2	Slit Parameters Γ	Slit Parameters σ	Slit Parameters ϵ
9 unknown	with Sirius	96	1	180.44242	0.09093	-11.07725	84.44870	0.23424
	w/o Sirius	96	1	180.44545	0.08541	-11.10606	84.38752	0.15668
	with Sirius	263	5	179.40277	-0.80276	-11.09409	84.21181	0.45998
				(0.00321)	(0.00302)	(0.00811)	(0.01469)	(0.00576)
	w/o Sirius	263	5	179.40753	-0.80552	-11.10133	84.19855	0.38148
				(0.00385)	(0.00448)	(0.05106)	(0.09971)	(0.05106)
8 unknown (σ, ϵ at fixed Γ)	with Sirius	263	5	179.40288	-0.80276	-11.0925	84.21488	0.45991
				(0.00309)	(0.00297)	fixed	(0.01055)	(0.00329)
7 unknown (Center slit, ϵ only)	with Sirius	263	5	179.39640	-0.80419	--	84.21181	0.47875
				(0.00627)	(0.00227)		fixed	(0.00962)
	w/o Sirius	263	5	179.40287	-0.80675	--	84.21181	0.38975
				(0.00835)	(0.00349)		fixed	(0.05508)

The detailed solutions of the nine unknown problem reveal the correlation between Γ and σ quite clearly. In Figure D-4 (Γ, σ) solution points are plotted for each of the twelve independent reductions in the nine unknown problem. Also plotted are the values of σ obtained at various fixed Γ values from eight unknown reductions of the data on Day 193 (11 July). Note that two independent interleaved data sets were reduced and exhibit excellent agreement with one another. Observe also that both lunar and solar interference were encountered on Day 193; the number and distribution of available solid stellar targets is insufficient to solve for all three slit parameters simultaneously but the solution for (σ, ϵ) for a fixed Γ goes very well. Finally, it is seen that the (Γ, σ) loci in Figure D-4 are all essentially straight lines on any given day and that the traces for the various days are parallel to one another. However, at fixed Γ, the zenith angle σ varies with time (Day) as expected.

An additional observation of some importance may be made with reference to Table D-I. The angles ξ_1 and ξ_2 describing the pointing direction are found to have much smaller uncertainty than do the slit parameters. In effect, the attitude solutions are somewhat better than the slit solutions provided that the slit solutions all fall on the correct (Γ, σ) locus. As a point of interest, the internal consistency of the five independent point direction determinations on Day 263 is better than 15 arc seconds.

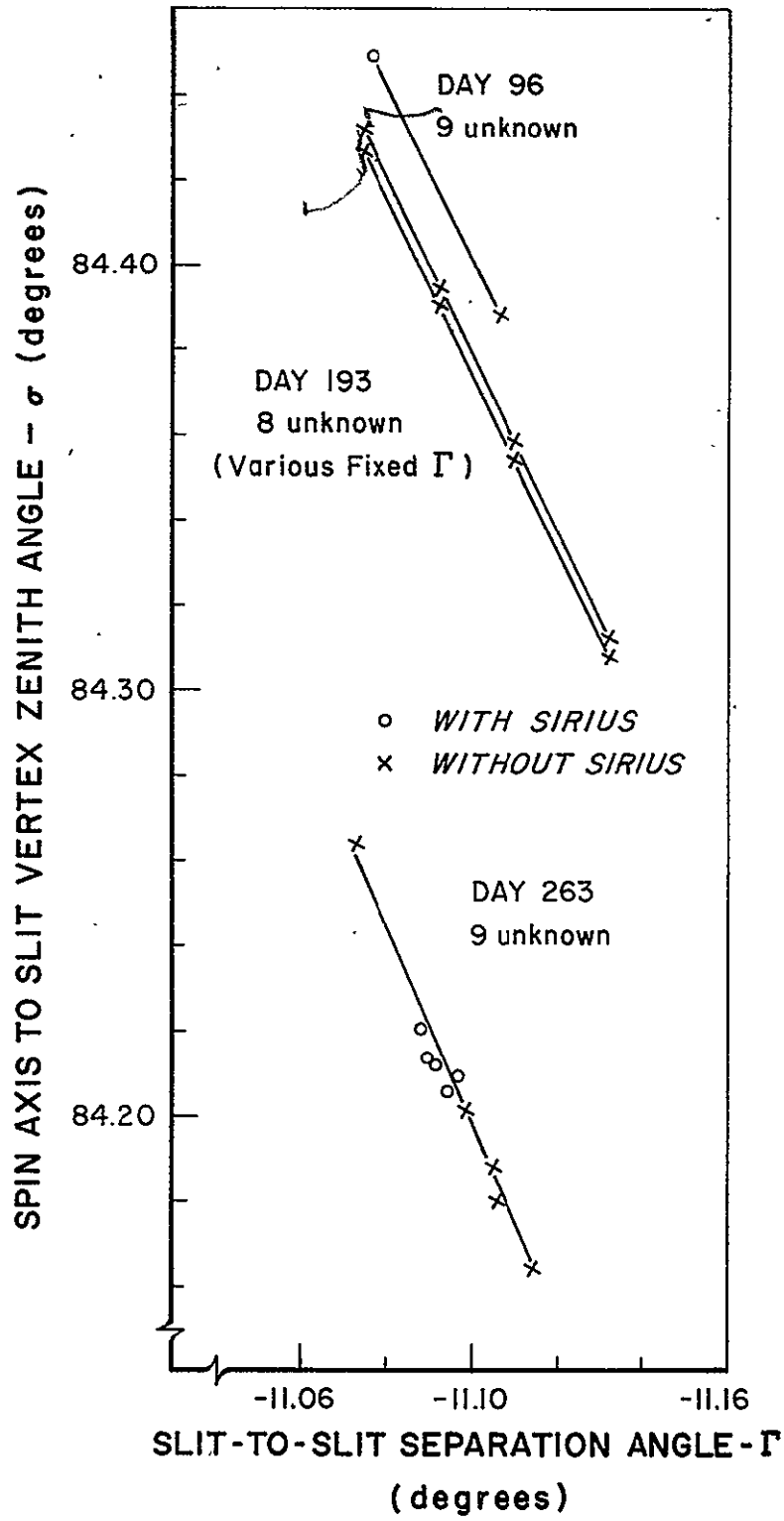

Figure D-4 (Γ, σ) Loci